



**HAL**  
open science

**Design, simulations and test of a Time-of-Flight spectrometer for mass measurement of exotic beams from SPIRAL1/SPIRAL2 and  $\gamma$ -ray spectroscopy of N=Z nuclei close to  $^{100}\text{Sn}$**

Pierre Chauveau

► **To cite this version:**

Pierre Chauveau. Design, simulations and test of a Time-of-Flight spectrometer for mass measurement of exotic beams from SPIRAL1/SPIRAL2 and  $\gamma$ -ray spectroscopy of N=Z nuclei close to  $^{100}\text{Sn}$ . Nuclear Experiment [nucl-ex]. Université de Caen Normandie, 2016. English. NNT : . tel-01469429

**HAL Id: tel-01469429**

**<https://in2p3.hal.science/tel-01469429v1>**

Submitted on 16 Feb 2017

**HAL** is a multi-disciplinary open access archive for the deposit and dissemination of scientific research documents, whether they are published or not. The documents may come from teaching and research institutions in France or abroad, or from public or private research centers.

L'archive ouverte pluridisciplinaire **HAL**, est destinée au dépôt et à la diffusion de documents scientifiques de niveau recherche, publiés ou non, émanant des établissements d'enseignement et de recherche français ou étrangers, des laboratoires publics ou privés.



Normandie Université

**THESE****Pour obtenir le diplôme de doctorat****Spécialité Physique****Préparée au sein de l'Université de Caen Normandie****Design, simulations and test of a Time-of-Flight spectrometer for mass measurement of exotic beams from SPIRAL1/SPIRAL2 and  $\gamma$ -ray spectroscopy of N=Z nuclei close to  $^{100}\text{Sn}$** **Présentée et soutenue par  
Pierre CHAUVEAU****Thèse soutenue publiquement le 18 Novembre 2016  
devant le jury composé de**

Pr. Gilles BAN	Professeur	Examineur
Dr. Bertram BLANK	Directeur de recherche	Examineur
Dr. Gilles DE FRANCE	Directeur de recherche	Directeur de thèse
Dr. Pierre DELAHAYE	Chargé de recherche	Examineur
Dr. Araceli LOPEZ-MARTENS	Directeur de recherche	Rapporteur
Pr. Lutz SCHWEIKHARD	Professeur	Rapporteur
Dr. Thierry STORA	Senior physicist	Examineur

**Thèse dirigée par Gilles de France, GANIL**



*À Nicolas*



# REMERCIEMENTS

L'heure est enfin venu d'écrire mes remerciements, exercice auquel je m'attelle avec grand plaisir, étant donné que c'est le seul chapitre de ce document qui ne sera pas relu avant impression et dans lequel je peux écrire à peu près n'importe quoi.

Et j'aime écrire n'importe quoi.

J'ajoute qu'en l'absence de relecture, il y aura probablement plus de fautes que dans le reste du rapport, de quoi occuper ma correctrice de mère et l'excité du Bescherelle qu'est Mathieu. C'est parti !

J'aimerai commencer par remercier de tout coeur mon encadrant, Pierre, pour son soutien sans faille au cours de ces trois années bien remplies. Tu m'as écouté et aidé pendant tout ce temps et toléré mes questions incessantes (et souvent redondantes) sans jamais perdre patience. Tu t'es toujours rendu disponible même quand tu étais surchargé de travail. Je suis ravi d'avoir travaillé avec toi et impatient de recommencer pour les tests de PILGRIM. Je veux également remercier mon directeur de thèse Gilles de France, pour son suivi tout au long de la thèse, son aide précieuse sur l'analyse de données EXOGAM et sa tolérance vis-à-vis de mon organisation douteuse. D'une manière générale, merci à vous deux pour m'avoir fait confiance pour ce projet de thèse et pour m'avoir accompagné et formé dans un domaine dans lequel je n'étais même pas capable d'évaluer mon ignorance avant mon arrivée. Maintenant c'est plus clair :) (oui, je met même des smileys). Merci également à Emmanuel Clément pour avoir quasiment fait office de second tuteur non-officiel sur la partie analyse de données, vu le nombre de fois où j'ai débarqué dans son bureau sans prévenir pour lui poser des questions.

En suivant l'ordre des différentes parties de ce document, je souhaite remercier les personnes qui m'ont aidé sur la source FEBIAD: Mickael, Pascal, Laurent, Olivier, Geoffrey et Jean-Charles pour avoir répondu à mes questions et m'avoir expliquer le fonctionnement de la source en début de thèse, ainsi que pour nos nombreuses interactions depuis. Je veux remercier pour PILGRIM l'équipe de Greifswald : Lutz, Robert et Marco pour leur nombreux conseils, leur suivi et leur participation aux tests du spectromètre. Je souhaite également remercier le personnel du LPC pour avoir entièrement construit le spectromètre et les systèmes associés (rien que ça !). Je pense en particulier à Jean-François, Yvan, Julien, Joel, Frederic et Christophe qui, en plus de nous avoir beaucoup aidé, sont carrément cools ! Je veux aussi dire merci aux personnes qui m'ont aidé sur le développement ou les simulations du déflecteur : Stephane,

Soufiane, Franck et Mehdi du CENBG et Luc de l'IPNO. Un grand merci enfin à Marcin pour sa participation à l'analyse de données EXOGAM et pour son aide en général.

Pour les aspects pragmatiques de cette thèse, j'adresse mes remerciements à Michel pour son aide sur plusieurs références bibliographiques, à Thierry pour l'impression des posters et des exemplaires de thèse, et à Sabrina et Virginie pour leur aide sur les **très NOMBREUSES** formalités administratives qui ont un jour échappé à ma compréhension.

Je voudrai également remercier mes camarades thésards et post-doc pour la très bonne humeur générale qu'ils ont contribué à apporter au GANIL, pour tous les repas, toutes les pause cafés, les rumeurs, les ragots. Un grosse pensée pour Mathieu, mon partenaire de crime pendant ces trois ans, le Starsky de mon Hutch, mon diable sur l'épaule. Merci également à Coralie, Lucas, Arek, Alexis, Bartholomé, Fabien, Quentin, Benoit, Aldric, Yung Hee, Alex, Marine, Dennis, Jose-Luis, Florent, Diego, Hong-Lian, Adrien, Simon et Hadrien. Bravo au nouveaux thésés, bonne chance aux suivants, bienvenu aux nouveaux et bisous à tout le monde !

Je souhaite remercier ma petite chérie Saba pour m'avoir laissé la draguer en conférence à Padoue il y a un peu plus de deux ans et pour m'avoir soutenu et fait rire tant de fois depuis, pour sa cuisine géniale, suffisamment épicée pour que personne ne pique dans mon assiette et pour son enthousiasme contagieux. Merci à ma maman pour m'avoir accompagné jusque là et m'avoir tellement aidé pour les formalités de la vie quotidienne pour lesquelles je suis nul (au fait, je peux t'amener du linge samedi ?). Merci enfin à mes grands parents pour m'avoir donné de la curiosité et le goût des sciences quand j'étais petit.

Pour finir je m'excuse auprès de ceux que j'ai pu oublié ou que je n'ai pu citer ici mais auquel je pense en écrivant ces lignes. Merci à tout le GANIL pour m'avoir aidé à me sentir chez moi pendant ces trois ans. Nous sommes aujourd'hui le mardi 12 décembre, il est 18h15 et je dois imprimer ce rapport sous peu. Afin de me motiver à écrire vite les dernières corrections et remerciements, j'écoute une boucle de "Nyan cat in space" depuis maintenant 2h. J'arrête donc avant de perdre la raison.

A plus,

Pierre/Pomy/P-Dawg/Mad P

# CONTENTS

CONTENTS	vii
INTRODUCTION	1
1 RATE MEASUREMENTS OF A FEBIAD-TYPE ION SOURCE	7
1.1 THE ISOL TECHNIQUE . . . . .	9
1.2 ION SOURCES . . . . .	9
1.3 CONTEXT OF THE SPIRAL1-UPGRADE . . . . .	11
1.4 DESIGN OF THE FEBIAD SOURCE . . . . .	12
1.4.1 Principle of this FEBIAD TISS . . . . .	12
1.4.2 First tests and design modifications . . . . .	12
1.5 EXPERIMENT OF DECEMBER 2013 . . . . .	15
1.5.1 Experimental setup . . . . .	15
1.5.2 Calibration of the HPGe . . . . .	15
1.5.3 Data analysis . . . . .	16
1.6 RESULTS . . . . .	21
1.6.1 Production rates . . . . .	22
1.6.2 Ionisation efficiencies . . . . .	23
1.6.3 Release efficiencies . . . . .	25
CHAPTER CONCLUSION . . . . .	25
2 INTRODUCTION TO MR-TOF MASS SPECTROMETRY	27
2.1 MASS SPECTROMETRY . . . . .	29
2.1.1 History of mass-spectrometry . . . . .	29
2.1.2 Important characteristics . . . . .	32
2.1.3 Types of spectrometer . . . . .	33
2.2 MR-TOF-MS . . . . .	40
2.2.1 Principles . . . . .	40
2.2.2 Theory . . . . .	45
2.3 EXISTING DEVICES: USAGE AND PERFORMANCES . . . . .	51
CHAPTER CONCLUSION . . . . .	54
3 SIMULATION AND DESIGN OF THE MR-TOF-MS PILGRIM	55
3.1 PILGRIM SIMULATIONS AND OPTIMIZATION . . . . .	57
3.1.1 SIMION and its accuracy . . . . .	57
3.1.2 Early geometries . . . . .	59
3.1.3 Optimization procedures . . . . .	59
3.2 SUCCESSIVE DESIGNS . . . . .	61
3.2.1 Early mechanical design and changes in the geometry . . . . .	61
3.2.2 Geometry of the mirrors . . . . .	63
3.2.3 Injection in the trap . . . . .	64



3.2.4	Final design . . . . .	65
3.2.5	Optical properties . . . . .	65
	CHAPTER CONCLUSION . . . . .	72
<b>4</b>	<b>FIRST TESTS OF PILGRIM AT LPC CAEN</b>	<b>73</b>
4.1	OBJECTIVES . . . . .	75
4.2	TEST SETUP AT LPC CAEN . . . . .	75
4.2.1	The ion source and its optics . . . . .	75
4.2.2	Vacuum system . . . . .	76
4.2.3	Electrical setup . . . . .	77
4.2.4	Timings . . . . .	78
4.2.5	Diagnostics and acquisition . . . . .	79
4.3	EXPERIMENT AND PARALLEL SIMULATIONS . . . . .	81
4.3.1	Beam tuning . . . . .	81
4.3.2	Bunching . . . . .	83
4.3.3	Beam characteristics and expected resolving power . . . . .	86
4.3.4	Shoot-through mode . . . . .	86
4.3.5	Trapping . . . . .	87
4.3.6	Measurement stability . . . . .	88
4.3.7	Search for the mass 40 doublet . . . . .	89
4.3.8	Towards higher resolving powers . . . . .	93
	CHAPTER CONCLUSION . . . . .	93
<b>5</b>	<b>OPTIMIZATION AND DESIGN OF THE 90° ELECTROSTATIC DEFLECTOR</b>	<b>95</b>
5.1	MOTIVATIONS . . . . .	97
5.2	OPTIMIZATION . . . . .	98
5.2.1	Deflector concepts and optimised parameters . . . . .	98
5.2.2	Criteria . . . . .	99
5.2.3	Method . . . . .	100
5.3	RESULTS . . . . .	102
5.4	DOUBLE DEFLECTOR . . . . .	103
5.4.1	U and S-configurations . . . . .	103
5.4.2	Comparison of double deflector performances . . . . .	105
5.5	REALISTIC BUNCHES . . . . .	107
5.6	PROPER USAGE OF THE DEFLECTOR. . . . .	109
5.6.1	Modelling the deflector in Mathematica . . . . .	109
5.6.2	Effect of the distance between deflectors . . . . .	111
5.6.3	Telescopic lenses . . . . .	112
5.7	DEFLECTOR DESIGN . . . . .	112
	CHAPTER CONCLUSION . . . . .	115
<b>6</b>	<b>DATA ANALYSIS OF THE EXOGAM/NWALL EXPERIMENT</b>	<b>117</b>
6.1	GOALS OF THE EXPERIMENT . . . . .	119
6.2	DESCRIPTION OF THE EXPERIMENT . . . . .	119
6.2.1	General description . . . . .	119
6.2.2	EXOGAM . . . . .	120
6.2.3	DIAMANT . . . . .	122
6.2.4	NWall . . . . .	123
6.2.5	Acquisition . . . . .	123
6.3	CALIBRATION OF THE DETECTORS . . . . .	126

6.3.1	EXOGAM . . . . .	126
6.3.2	DIAMANT . . . . .	137
6.3.3	NWall . . . . .	137
6.4	PRE-ANALYSIS . . . . .	138
6.4.1	Expected reactions and contaminations (Ar and C) . . . . .	138
6.4.2	Background reduction and scattering rejection in EXOGAM	138
6.4.3	Neutron identification in NWall . . . . .	140
6.4.4	Scattering rejection in NWall . . . . .	141
6.4.5	Charged particles identification in DIAMANT . . . . .	141
6.5	SPIN AND POLARITY ASSIGNMENTS . . . . .	144
6.5.1	DCO ratios and polarisation asymmetries . . . . .	145
6.5.2	$^{94}\text{Pd}$ . . . . .	148
	CHAPTER CONCLUSION . . . . .	151
	THESIS CONCLUSION	153
	LIST OF FIGURES	155
	BIBLIOGRAPHY	165
	NOTATIONS AND ACRONYMS	179



# INTRODUCTION

OVER a century ago, Rutherford paved the way for nuclear physics studies. Today nuclear physics is a very active field of research and nuclear facilities around the world are leading researches on isotopes far from the line of stability. Nuclei with  $N/Z$  ratio much bigger or much smaller than those of stable nuclei found on Earth are called exotic nuclei. These nuclei are of primary interest in the description of astronuclear phenomena in stars, supernovae or neutron stars, where extreme conditions of temperature and pressure favour the capture of free protons or neutrons. Especially in the last two cases, nucleon capture reactions can breed a seed-nuclei into a highly exotic one. For a given  $N$ , a nucleus can be enriched with protons up to the point where no proton bound state is available anymore, and any proton forcefully added to the structure of the nucleus would "leak" or "drip". This  $N$ -dependent limit on the proton-rich side of the valley of stability is called the proton drip line and similarly, a  $Z$ -dependent neutron drip line is expected on the neutron-rich side of the valley as shown in [Fig. 1](#). These drip lines put a physical limit to crucial astronuclear reactions such as  $r$  and  $rp$  nucleosynthesis in supernovae or the neutron-enrichment process in neutron stars. Therefore, the position of these drip lines and the properties of the nuclei in their vicinity have a strong impact on the astrophysical properties of these celestial bodies.

More fundamentally, exotic nuclei bring important constraints in fundamental nuclear physics. Similarly to the atomic structure, the nuclear structure has been observed to be especially stable (i.e. long lived) for certain numbers of protons and neutrons, the so-called "magic numbers". In the simple single-particle shell model, the nuclear shells defined by these numbers arise from the quantic orbital behaviour of nucleons trapped in a nuclear potential well and from the effect of the spin-orbit coupling. The shell model accurately predicts the magic numbers to be 2, 8, 20, 28, 50, 82 and 126 near the valley of stability but fails to explain the loss of magicity of certain numbers in exotic regions of the chart of the nuclides. Among the main challenges of theoretical models are the prediction of the evolution of shell closures far from the valley and the quest for new high magic numbers which define the centre of an "island of stability" of super-heavy nuclei.

Because of the extreme complexity of the nuclear interaction for nuclei of  $A > 10$ , most theoretical models are phenomenological models fitted on experimental data. The capacity of these models to predict nuclear properties rarely extends far beyond the nuclei which were used to constrain it. Thus measurements of the nuclear properties of highly

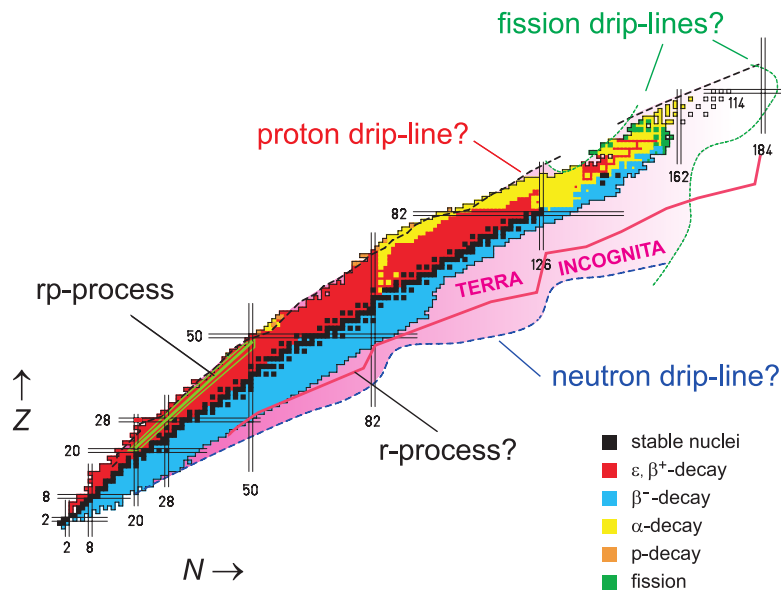


Figure 1 – Chart of nuclides showing the stable elements forming the valley of stability, the limits of the known nuclei, the estimated positions of the drip lines and path of the r-process and the magic numbers [1].

exotic nuclei, possibly close to the drip lines, and super heavy nuclei are extremely important to constrain these models and extend their range of predictability. This necessity raised new technological challenges, as the study of short-lived exotic nuclei requires intense production of these nuclei and fast measurement of their properties. Most of the important nuclear laboratories around the world have already started to address these challenges by building a new generation of accelerators, radioactive ion production systems and measuring instruments. The acceleration of intense radioactive ion beams in new facilities will allow to produce exotic nuclei through various nuclear reactions (fragmentation, fusion-evaporation, transfer reaction) for which cross-section was a limiting factor in prior installations.

The SPIRAL1 Upgrade project [2] and the future SPIRAL2 facility [3, 4] at GANIL are part of the common effort in the nuclear physics community to produce radioactive beams of competitive or even unprecedented intensity. Fig. 2 shows the current GANIL and SPIRAL1 facilities and the two planned construction phases of SPIRAL2. The LINear ACcelerator (LINAC) [5] will accelerate deuteron beams for the creation of neutron beams in the NFS (Neutron For Science) experimental room, and also nuclei ranging from Carbon to Uranium to energies from 2 to 14.5 MeV/u and intensities up to  $10^{14}$  pps for heavy ions. The Super Separator Spectrometer S3 [6] is an in-flight separator designed to operate with the high intensity beams delivered by the LINAC followed by a Low Energy Branch (S3-LEB) to study of the ground properties of exotic or super-heavy nuclei. S3 is part of the phase 1 of SPIRAL2 and will focus on shell evolution in the  $N = Z$  region near the exotic doubly magic  $^{100}\text{Sn}$

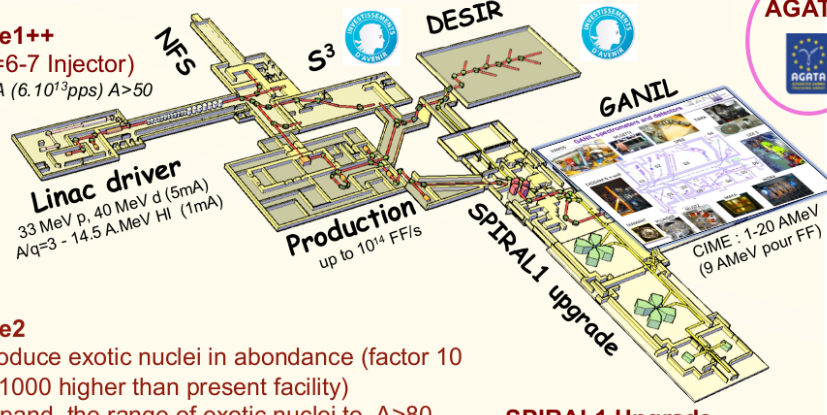
**Phase1**

Increase the intensity of stable beams by a factor 10 to 100 + High intensity neutron source

$10\mu\text{A}$  ( $6 \cdot 10^{13}$ pps)  $A < 50$

**DESIR Phase1+**  
(low energy facility)

**Phase1++**  
( $A/Q=6-7$  Injector)  
 $\geq 10\mu\text{A}$  ( $6 \cdot 10^{13}$ pps)  $A > 50$

**Phase2**

- Produce exotic nuclei in abundance (factor 10 to 1000 higher than present facility)
- Expand the range of exotic nuclei to  $A > 80$
- Post-acceleration of high intensity RIB

**SPIRAL1 Upgrade**  
New light n-deficient nuclei from beam/target fragmentation

Figure 2 – Future layout of the SPIRAL2 facility. Phase 1: linear accelerator and NFS and S3 experimental rooms. Phase 1+: low energy experimental room DESIR receiving beams from S3 and SPIRAL1. Phase 1++:  $A/Q = 7$  injector. Phase 2: production of radioactive ions at high intensity. The CIME cyclotron is used to post-accelerate radioactive ion beams from SPIRAL1 and will do so for the beams from SPIRAL2 as well.

and on nuclear shape and stability in the very heavy and super heavy regions during the "day 1" experiments. The presence of this doubly magic nuclei near the proton drip line provide opportunities to investigate the evolution of the  $N = Z = 50$  shell closure for highly exotic nuclei. The DESIR (Désintégration, Excitation et Stockage des Ions Radioactifs) [7] experimental room will receive the high intensity low energy radioactive beams from SPIRAL1 and from the S3 experimental room in phase 1+, and from the SPIRAL2 ISOL facility in phase 2.

The main objective of the present thesis work is to design a Multi-Reflection Time-of-Flight Mass Spectrometer (MR-ToF-MS) for mass separation and mass measurement of short-lived nuclei in S3-LEB. Such a spectrometer could later be duplicated for DESIR. Because of the reaction mechanisms involved in the production of S3 beam (mainly fusion-evaporation), the chosen ion of interest for a given experiment will be produced alongside many other isotopes. Though the S3 spectrometer will filter a part of these contaminants, it is likely to be unable to separate all isobaric contaminants, i.e. nuclei with the same  $A$  as the ion of interest but a different  $Z$ . Also, if the ion of interest is very exotic it is likely to have a short lifetime and the isobaric contaminants could have a greater production cross-section. Thus a fast high resolution spectrometer is needed in the LEB. MR-ToF devices have been reported to achieve resolving power above 200000 in a few tens of milliseconds, which would be highly profitable to purify beams before they reach the decay station of S3. In DESIR, a MR-ToF-MS could also be used for beam purification before mass measurement in the double Penning-trap PIPERADE, since

such traps have been reported to be very sensitive to contaminants.

In addition to being an excellent auxiliary beam purifier, such a spectrometer could also be used to perform fast high precision mass measurement of exotic or super-heavy nuclei and hence become a powerful tool to constrain nuclear models in these regions. The nuclear binding energy, or the mass difference between a nucleon at rest and the sum of the masses of its constituents, accounts for the sum of all nuclear forces inside this nuclei. Thus the rest mass is a fingerprint of the nuclei and the direct mass measurement of a radioactive ion is a deep insight on its binding energy. In particular, it can be used to study the evolution of shell closures. MR-ToF spectrometers in ISOLDE and RIKEN have achieved fast mass measurement with a precision of the order of  $10^{-7}$  [8, 9].

Many aspects of the technical and physics research which take place in a nuclear physics facility have been explored in the course of this thesis, including the test of an ion source for radioactive beams, the design and test of beam manipulation devices (bending, trapping) and the participation to a data analysis on a proton-rich exotic nucleus. This report is organised following the typical scheme of a nuclear physics experiment: from the creation of radioactive ions in a target-source system, to using these ions in an experimental apparatus, followed by an analysis of the experimental measurements.

We will start the present report by studying the production rates of a FEBIAD-type ion source designed for the Upgrade of the SPIRAL1 ISOL facility. Chapter 1 first introduces the ISOL technique and the sources most commonly used to ionise radioactive atoms, then present the successive designs and low-intensity tests of the present FEBIAD source for SPIRAL1. The main part of this chapter describes the first experimental test of this source at high beam power ( $\sim 1200$  W) and the data analysis from which the production rates of many radioactive ions, including metallic ones, are deduced.

The second chapter is an introduction to MR-ToF mass spectrometry. We start with a brief history of mass spectrometry highlighting the key features expected from a mass spectrometer. This chapter introduces and compares the performances of various types of mass spectrometers, before describing its latest state-of-the-art implementation and operation. A few theoretical aspects of the optics of charged particles trapped in a MR-ToF-MS are then developed, and the chapter concludes by reviewing the existing prototypes worldwide and their usage.

Chapter 3 summarises the simulations and optimisations of our MR-ToF-MS named "Piège à Ions Linéaire du GANIL pour la Résolution des Isobares et la Mesure de masse" (PILGRIM) using the ion-flight simulation software SIMION 8.1. The chapter is introduced by a discussion on the accuracy of SIMION for a long time-of-flight. We then present the optimisation procedures used to maximise the resolving power and transmission efficiency of PILGRIM, and provide details about the optical and

mechanical constraints that led to its final design. The optical properties of this design are investigated using realistic beams.

In chapter 4 we present the first off-line tests of PILGRIM which took place during the summer of 2016. We introduce the different technical aspects of the test bench located at LPC Caen. We focus on the production of short bunches of low emittance, using a pair of deflecting blades and a collimator to chop the continuous beam produced by a thermal ion source. Next, we describe the successful trapping of ion bunches and the first results of optimised resolving power. We conclude the chapter with the description of the first attempt to separate the  $^{40}\text{K}/^{40}\text{Ca}$  stable isobaric doublet.

The fifth chapter is dedicated to the design and optical study of a multi-direction electrostatic deflector. This deflector has been optimised to avoid spoiling the ToF properties of an input bunch as it will be used in both S3 and DESIR experimental areas to bend radioactive beam at  $90^\circ$  before or after mass separation into PILGRIM. The method of optimisation is described and several electrode-configurations are compared. The possibility to use two deflectors in a row to reduce the optical aberrations is also discussed. The final optical properties of this deflector are tested by simulating the deflection of realistic beams. Chapter 5 also determines the ideal beam conditions before deflection and introduces the principle of an auxiliary telescopic lens system which is yet to be designed. The chapter concludes on the deflector's mechanical design.

The last chapter describes the  $\gamma$ -ray spectroscopy of  $^{94}\text{Pd}$  in the vicinity of the  $^{100}\text{Sn}$  nucleus (double shell closure  $N = Z = 50$ ). This region could be an experimental field for mass measurements with PILGRIM during the commissioning of S3 in 2018. This chapter first introduces the effect of isoscalar coupling on the excited level scheme of even-even nuclei on the  $N = Z$  line, which was the subject of the experiment E623. We describe the experimental setup and its different particle and  $\gamma$  detectors and detail their calibration for amplitude, time and efficiency. We then explain the different conditions of event-selection or rejection to enhance the ratio of events of interest compared to fortuitous ones. Finally we use the EXOGAM segmented  $\gamma$ -array to measure the Directional Correlation from Oriented state (DCO) ratios and polarisation asymmetries of well known  $^{94}\text{Ru}$  and  $^{95}\text{Rh}$ , and of  $^{94}\text{Pd}$  for which polarisation asymmetry had not been measured yet. We deduced from these measurements the multipolarities and electromagnetic nature of several  $\gamma$ -transitions of these nuclei.





# RATE MEASUREMENTS OF A FEBIAD-TYPE ION SOURCE

1

## CONTENTS

2.1	MASS SPECTROMETRY . . . . .	29
2.1.1	History of mass-spectrometry . . . . .	29
2.1.2	Important characteristics . . . . .	32
2.1.3	Types of spectrometer . . . . .	33
2.2	MR-ToF-MS . . . . .	40
2.2.1	Principles . . . . .	40
2.2.2	Theory . . . . .	45
2.3	EXISTING DEVICES: USAGE AND PERFORMANCES . . . . .	51
	CHAPTER CONCLUSION . . . . .	54

**T**HIS chapter details the analysis of the data from the experiment of December 2013 on the FEBIAD ion source. This source is part of the SPIRAL Upgrade planning to extend the range of radioactive ion beams available at GANIL.



## 1.1 THE ISOL TECHNIQUE

The production of radioactive ion beams is necessary to explore nuclear regions far from the valley of stability. Radioactive ions can be produced via natural or induced fission in nuclear reactors, or by high energy nuclear reactions in accelerators. Two major production techniques prevail among accelerators: Isotope Separation On Line (ISOL) and In-Flight. The target-source system described here has been developed for an ISOL facility and we will therefore focus on this method. The production of radioactive ions with this technique follows these steps:

- I. Production and acceleration of a stable ion beam.
- II. Impact of the beam on a thick target and production of radioactive atoms through various nuclear reactions (fragmentation, fission, etc). With this technique reaction products are stopped in the target.
- III. Diffusion of the radioactive atoms through the bulk material and effusion towards the ion source.
- IV. Ionisation of the radioactive atoms.
- V. Extraction of the radioactive ions.
- VI. Mass separation of the ions, usually with a magnetic dipole.
- VII. If needed, charge breeding and post-acceleration of the ions.

In an In-Flight facility, the primary beam of heavy ions impinges on a thin target of light element, producing radioactive ions by fragmentation of the incoming beam ions. In comparison an ISOL facility has a better beam quality and a lower energy dispersion as the secondary beam is produced using similar methods as for stable beams. This also makes the mass separation easier as a single magnetic dipole is required to separate ions of different mass number  $A$ . Moreover the fact that the reaction products escape the target in the atomic state allows to chemically favour or suppress the ionisation of certain elements and enables a  $Z$  selection. However, the time requested by the release<sup>1</sup> of the atoms from the target to the source, the ionisation, the low energy beam transport and the post-acceleration can limit the intensity of short lived secondary beams. In addition, the production rate of a given element will depend on its chemistry and elements with a high potential of first ionisation will prove harder to produce.

## 1.2 ION SOURCES

Several types of ion sources are used in ISOL facilities, all of which have their own strengths and limitations. An ion source for the production of radioactive ion beams must meet several requirements:

---

<sup>1</sup>In the following, we define the release efficiency as the transport efficiency for a given isotope from the target to the ion source.

- It must be fast to limit the losses by radioactive decay.
- It needs a high overall efficiency (including the release and ionisation efficiencies) to reach a high beam intensity.
- Selectivity is important to limit the isobaric contamination.
- Universality or the source ability to produce a wide range of chemical elements is also an important criterium. We may notice that these two requirements seem contradictory as one is usually chosen over the other, depending on the source type.
- The source must be capable of withstanding months of operation at high temperature ( $\simeq 2000$  K) for both efficiency and safety reasons. The high temperature is necessary to prevent radioactive ions from sticking to the walls of the source.
- The source must be close to the place of production of the radioactive atoms in order to achieve a fast and efficient transport from the target to the source. For this reason, both are gathered in a unique Target Ion Source System, or TISS.

The choice of the source will depend on the relative importance of the previous criteria. The sources most commonly used in ISOL facilities are introduced in the following.

**Electron Cyclotron Resonance (ECR) sources** use a permanent magnetic field and an oscillating electric RF field to induce a cyclotron motion among charged particles. The electric field frequency is set at the electron cyclotron frequency in order to excite electrons. As they are accelerated, they gather enough energy to snatch other electrons from the electronic cloud of passing atoms, thus ionising them and creating a plasma. As electrons can easily have a kinetic energy well over the potential of first ionisation of any element, this source is in principle not limited by the chemistry of the element of interest, as long as it is in its gaseous state. The ECR source is also capable of producing multiply charged elements and even completely stripping light atoms of their electrons. Finally, this source can be used as a "charge breeder" on  $1^+$  ions to increase their charge before acceleration.

**Surface ion sources** are able to produce positive and negative ions. In positive surface ionisation, atoms of low first ionisation potential (alkaline/alkaline earth elements) are desorbed by a hot surface of high work function. In a single-particle approach, this means that the ground state energy of an outer electron of an atom is close to or higher than the Fermi energy on the surface, which favours the transfer of this electron from the atom to the surface material. Negative surface ion sources use materials with a low work function to foster the electron transfer to atoms of high electron affinity (usually halogens).

Positive surface ion sources are widely used to produce alkaline elements in ISOL facilities. Their principles (heating and high work function)

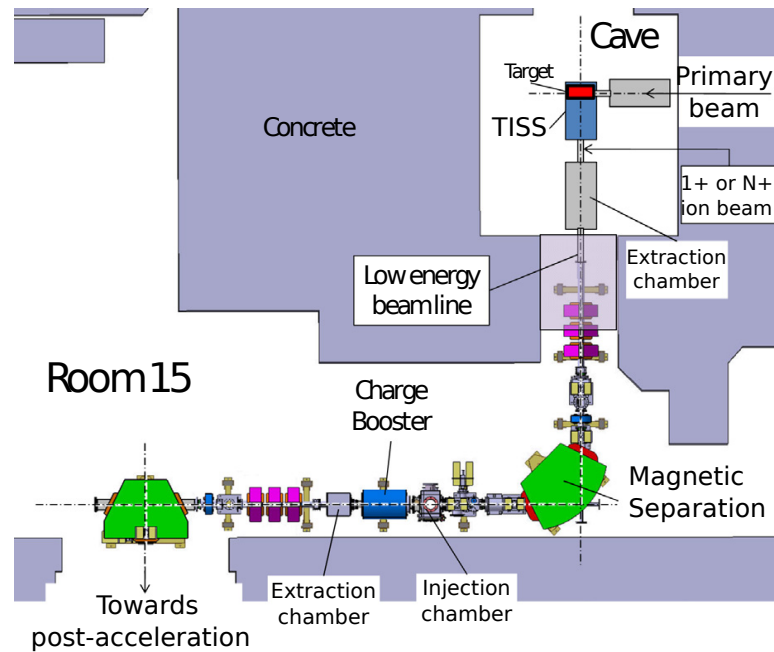


Figure 1.1 – SPIRAL1 upgrade layout. Image from [10]

also apply to the reduction of the effusion time between the target and the source and the enhancement of the release efficiency.

**Resonant ionisation Laser Ion Sources (RILIS)** combine high selectivity and a large panel of acceptable elements. Resonant laser ionisation consists in the successive excitation of electrons of the valence band until they reach an energy higher than the ionisation potential. As the transition from the ground state to the first excited state is quantified, only a precise laser frequency can excite a ground level electron, thus the selectivity. Some elements possess transitions outside the laser tuning range and therefore cannot be ionised with a RILIS source (Noble gases, some halogens, nonmetals).

**Forced Electron Beam Ionisation by Arc Discharge (FEBIAD) sources** ionise atoms by electronic impact. Electrons are accelerated from a hot cathode towards a grid anode. As for the ECR source, they snatch electrons from atoms and create a plasma which is confined by a magnetic field. The energy of the accelerated electrons is high enough to ionise any element, making it quite universal, though poorly selective. The electron beam energy is generally not sufficient to knock off more than one electron per atom, making it a  $1^+$  ion source as surface and RILIS sources.

### 1.3 CONTEXT OF THE SPIRAL1-UPGRADE

The SPIRAL facility (Système de Production d'Ions Radioactifs Accélérés en Ligne) at GANIL is an ISOL facility which has been delivering radioactive beams of gaseous elements of high intensity and purity for physics experiments since 2001. Radioactive atoms are produced by fragmentation of the primary beam on a thick carbon target, then ionised in a compact

Nanogan III ECR ion source. The range of produced ions was not limited by the ionisation capabilities of the source, but by (1) the cold transfer tube connecting the target to the source and (2) by the cooled surfaces of the plasma chamber, protecting the permanent magnets from the heat of the target and the plasma, respectively [11]. This practically restrains the range of operation of the source to elements in a gaseous state at room temperature. The upgrade of SPIRAL1 [2, 12] aims at extending the production of radioactive ions to condensable elements. It consists of the installation of new sources and of a charge booster, and of the upgrade of the production cave. The cave can now support three different ion sources:

- I. The existing Nanogan III ECR ion source capable of producing multi-charged gaseous ions.
- II. The monoNaKE source which couples a surface ion source to the SPIRAL targets to produce 1+ alkali ions.
- III. The FEBIAD ion source discussed in this part. This source is based on the VD5 design of the Versatile Arc Discharge Ion Source (VADIS) series from ISOLDE at CERN [13].

A PHOENIX type ECR ion source used as a charge booster will also be installed after the first magnetic separator (see Fig. 1.1) in order to breed the charge state of the ions from the 1+ to the  $n+$  charge state required by the post-accelerator CIME at SPIRAL.

## 1.4 DESIGN OF THE FEBIAD SOURCE

### 1.4.1 Principle of this FEBIAD TISS

The principle of operation of the VD5 source is shown Fig. 1.2. The primary beam impinges on a thick carbon target as before. The reaction products diffuse from the target bulk material then effuse inside a transfer tube towards the anode in which they are ionised. The plasma is confined by a solenoid magnet surrounding the source to reduce the effect of the space charge. The target oven, transfer tube, cathode and anode are heated at  $\sim 2000^\circ\text{C}$  to desorb condensable elements and enhance the release time. Because of this, surface ionisation also happens in the TISS. Alkaline and alkaline-earth elements have generally higher ionisation efficiency than the other elements. The entire TISS is at a high voltage of 10 to 20 kV, so as to reach a good extraction efficiency.

### 1.4.2 First tests and design modifications

This FEBIAD source has experienced several tests at reduced power described in details in [14, 15]. We only give a quick overview of the preliminary tests as they explain the evolution of the design and the elements and ionisation rates to be expected.

#### First beam test: May 2011

The TISS was tested at SIRa (Separator d'Ions Radioactifs) in GANIL under a  $^{58}\text{Ni}^{28+}$  beam accelerated at 72 MeV/A. The SIRa installation is used

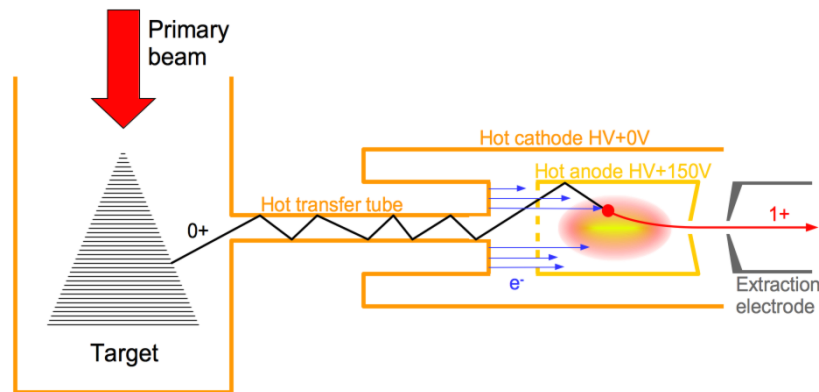


Figure 1.2 – Principle of operation of the VD5 FEBIAD ion source.

for the development and test of new TISS. As this installation was not adapted to high neutron flux, the beam intensity was limited, and the beam power did not exceed 40 W.  $^{38}\text{K}$ ,  $^{38\text{m}}\text{K}$ ,  $^{53}\text{Fe}$ ,  $^{53\text{m}}\text{Fe}$ ,  $^{58}\text{Mn}$ ,  $^{58}\text{Cu}$ ,  $^{59}\text{Cu}$  and  $^{60}\text{Cu}$  were successfully produced during this test, proving the possibility for this source to ionise metallic elements. Their rates could be extrapolated at high intensity to infer their production in SPIRAL [16]. At the end of the experiment the cathode broke due to the high mechanical constraints generated by thermal expansion. Also the drift tube, which was supposed to slide along its axis in a guiding part to compensate its own thermal expansion ( $\sim 2$  mm at  $2000^\circ\text{C}$ ), stuck to the guiding part. It was decided to install a bellow on the transfer tube to absorb the expansion.

### Second beam test: June-July 2011

This experiment also took place at SIRa, with a beam of  $^{36}\text{Ar}^{18+}$  accelerated at 95 MeV/A. The power was limited at  $\sim 13\text{W}$ . Though the source lacked conditioning time to reach its nominal efficiency,  $^{23}\text{Mg}$ ,  $^{33}\text{Cl}$ ,  $^{35}\text{Cl}$ ,  $^{37}\text{K}$ ,  $^{38}\text{K}$  and  $^{38\text{m}}\text{K}$  were observed [16].

### Third beam test: July 2012

During this test, an upgraded TISS with 2 bellows on the transfer tube and a few minor modifications was tested offline. After several heating cycles the bellows lost their flexibility and became rigid. This caused the target container to enter in contact with the target oven as the thermal expansion of the tube was not compensated anymore. This created a short circuit that destroyed the target resistor. It was ultimately decided to use a mobile source to address this issue. The final design of the TISS can be seen in Fig. 1.3. The target container is now fixed to the target resistor so as to avoid unwanted short-circuit [15].



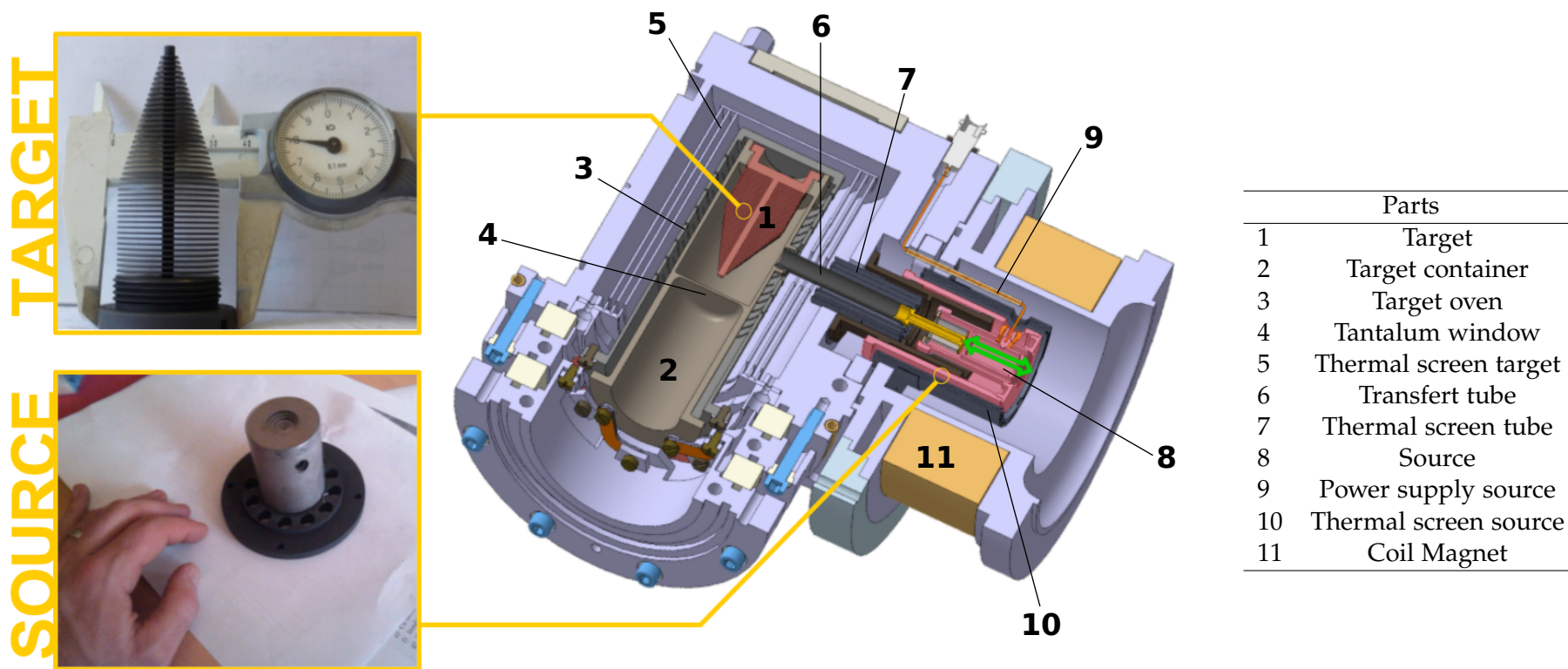


Figure 1.3 – Mechanical design of the FEBIAD source in SPIRAL1.

## 1.5 EXPERIMENT OF DECEMBER 2013

### 1.5.1 Experimental setup

The commissioning of the TISS was performed at the SPIRAL1 low energy identification station (Fig. 1.4), a full description of which can be found in [17]. Low energy ions produced in the FEBIAD source were separated by sequential dipole magnets and guided to this identification station where they were implanted into an aluminized-polyethylene-terephthalate (PET) collection tape. A first High-Precision Germanium detector (HPGe) was located in front of the implantation point at  $0^\circ$  with respect to the beam axis and was used to measure the purity of the beam and the respective yields of various isotopes. After irradiation, the tape can be moved to a decay chamber equipped with a fast plastic scintillator and another HPGe measuring coincident  $\beta$ -particles and 511 keV  $\gamma$ -rays respectively. This chamber is used for Half-life measurements. The commissioning of the FEBIAD TISS aimed to produce radioactive metallic ions at nominal power ( $\sim 1500$  W). We used a primary beam of  $^{36}\text{Ar}$  at 95 AMeV. A description of this experiment and of the following analysis and results have been published [18].

### 1.5.2 Calibration of the HPGe

Though several half-lives were measured during this experiment, the present work only focuses on the determination of the production rates. We will therefore not give here any detail on the calibration or analysis related to the decay chamber and its detectors, which can be found in [19, 20].

The HPGe of the collection chamber was calibrated in energy using the 511 keV  $\gamma$ -ray from positron-electron annihilation and the 2231 keV from the  $\beta^+$  of  $^{32}\text{Cl}$ . These  $\gamma$ -peaks were fitted to determine their position in channel. The gain and offset are easily determined by doing a linear interpolation between the channel positions of the 2 peaks and their known energies. This is of course a very coarse energy calibration. Nevertheless, the energy spectra are solely used for identification of the radioactive ions and photopeak integration (for rate calculation). A coarsely calibrated spectrum will not affect the first and induce an error on the second which is negligible in comparison to the efficiency error ( $\sim 1\%$ ).

The efficiency calibration of the HPGe was performed using 3 well known sources of  $^{152}\text{Eu}$  on the 122, 245, 344, 779 and 1408 keV peaks. The energy dependant efficiency of a given peak can be measured as follow:

$$\epsilon_{HPGe}(E_\gamma) = \frac{N_{meas}(E_\gamma)}{N_{calc}(E_\gamma)BR(1 - DT)} \quad (1.1)$$

where  $N_{meas}$  is the number of counts in a peak measured in a given amount of time,  $N_{calc}$  is the number of nuclear decays feeding this transition that supposedly occurred in the same amount of time,  $BR$  is the branching ratio of the  $\gamma$ -transition and  $DT$  is the averaged dead-time of the acquisition over the measurement time. The measured efficiencies for

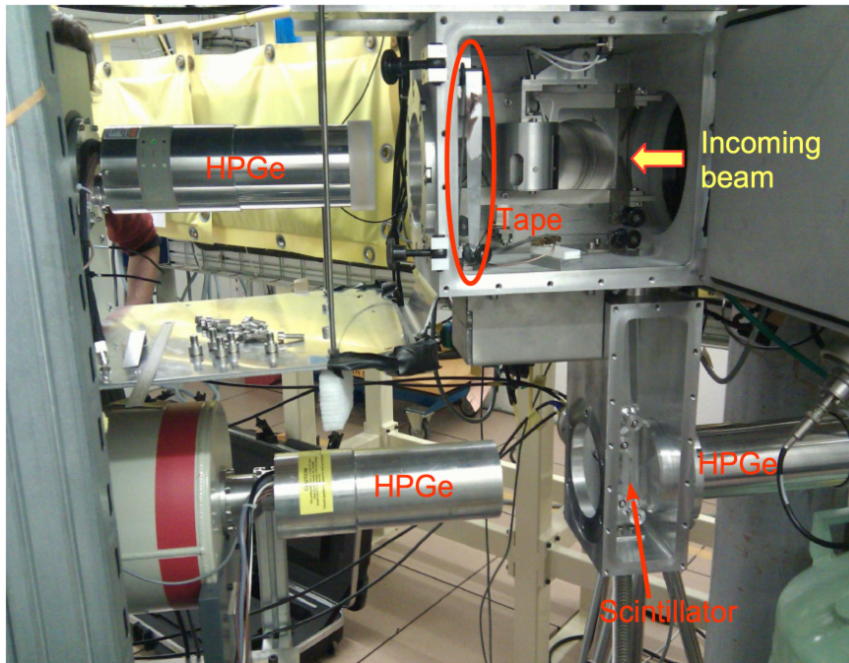


Figure 1.4 – Identification station in SPIRAL, including a collection chamber (top) and a decay chamber (bottom). During the test of the FEBIAD source, only one of the 2 bottom HPGe was used. See description in text.

all important  $\gamma$ -transitions of the 3 sources are then fitted with a first order Gray function [21] taking the expression:

$$\epsilon_{HPGe}(E_\gamma) = \frac{a_0 + a_1 \ln(E_\gamma)}{E_\gamma} \quad (1.2)$$

with  $a_0$  and  $a_1$  being the fit parameters. Measurements of the efficiency and their fit were performed for 3 positions of the HPGe, corresponding to distances of 85, 260 and 590 mm between the implantation point on the tape and the front end of the germanium detector. The fits of the efficiencies for the 3 positions can be seen in Fig. 1.5.

### 1.5.3 Data analysis

#### Principles

The analysis was performed using the Root software and aimed to estimate the production rates of different isotopes produced in SPIRAL. At the end of each run the mobile Faraday Cup (FC) was inserted in front of the beam and the tape was moved to avoid contamination of the next run. At the beginning of each run, the FC was removed and the beam was irradiating a clean part of the tape. The number of disintegration per second  $Y_{dis,AZ}$  of a given element on the implantation point is:

$$Y_{dis,AZ} = Y_{prod,AZ}(1 - e^{-t/\tau}) \quad (1.3)$$

where  $Y_{prod,AZ}$  is the  $^AZ$  element's production rate,  $\tau$  its lifetime and  $t$  the time since the FC has been removed. At saturation, the disintegration and production rates are equal. When the FC is inserted again in

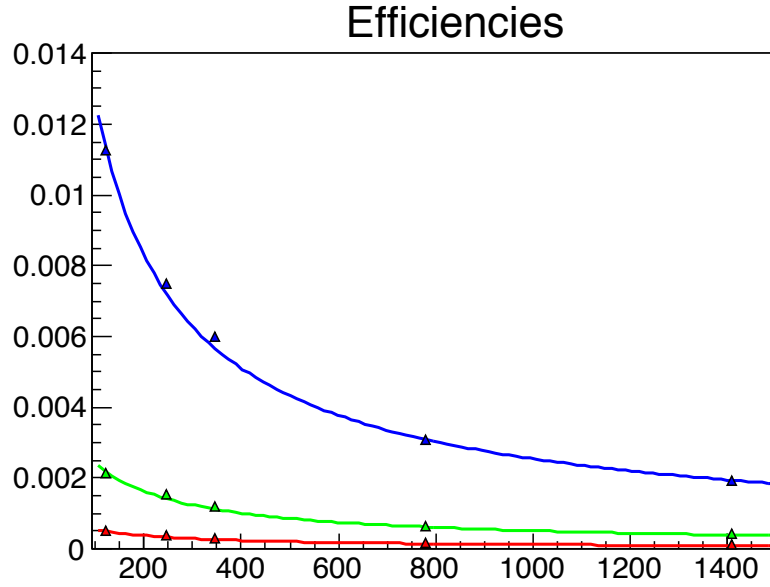


Figure 1.5 – Fit of the  $\gamma$ -efficiency at 85 mm (blue), 260 mm (green) and 590 mm (red). The error bars are not represented here since they are typically smaller than the dots.

the beam axis the activity decreases following a simple exponential decay. The production rate of the element is calculated with the saturated activity  $Y_{dis,AZ,sat}$  as follows:

$$Y_{prod,AZ} = Y_{dis,AZ,sat} = \frac{I_{sat,\gamma}}{BR_{\gamma}(1 - DT)\epsilon_{HPGe}(E_{\gamma})} \quad (1.4)$$

where the saturated intensity  $I_{sat,\gamma}$  is the number of counts per second in a  $\gamma$ -peak at saturation. This value has been determined with either of the 2 methods presented next, depending on the half-life of the considered species.

**I.** In case of a short lived isotope (or a long run time), the saturation is reached rapidly and the Germanium detectors experience a constant intensity for all the decay  $\gamma$ -rays of the concerned isotope. By gating in time over the saturation period, one can obtain  $I_{sat,\gamma} = N_{\gamma}/T_{gate}$ , with  $N_{\gamma}$  being the number of counts in the  $\gamma$ -peak of the time-gated energy spectrum and  $T_{gate}$  being the size of the time gate. The  $\gamma$ -peak in the energy spectrum is fitted by a simple gaussian curve with a linear background. See Fig. 1.6, top.

**II.** If the activity did not reach the saturation before the end of a run or if the saturation time is too short to make a precise measurement, we apply a gate in energy to one or several  $\gamma$ -peaks of a given element and fit the time profile of the energy-gated activity with Eq. 1.3. In order to suppress the background due to Compton scattering in the time spectrum in coincidence with the peak, we correct it by removing the time spectrum in coincidence with the energy background on both sides of the peak. The size of the energy gate on the peak must match the sum of the sizes of the two background gates on either side of the peak. If not, the background time spectra must be normalised by the ratio of the gates sizes. See Fig. 1.6, bottom.

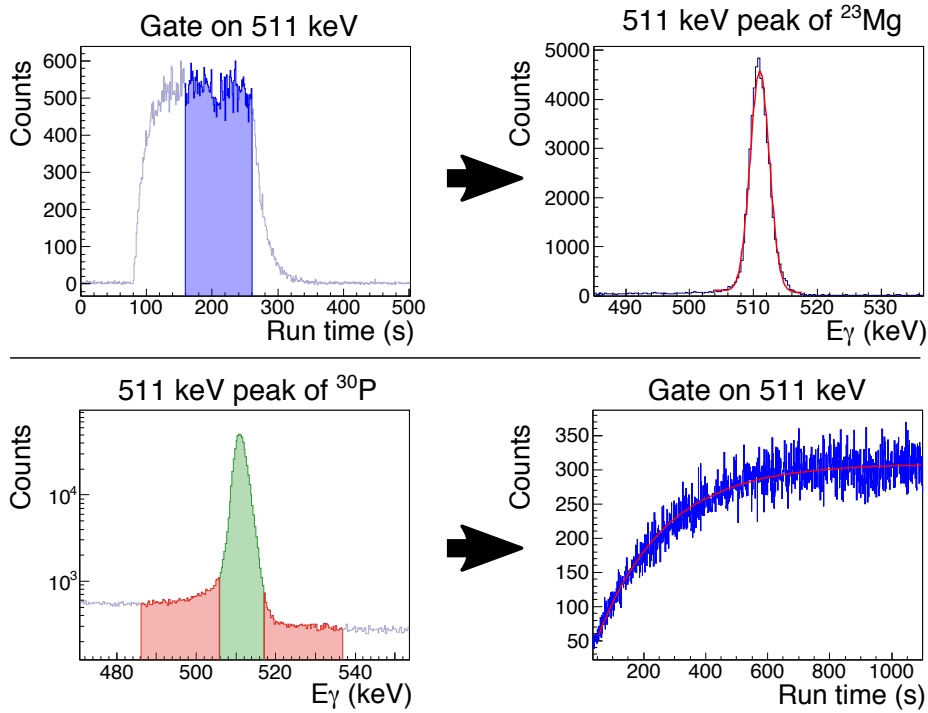
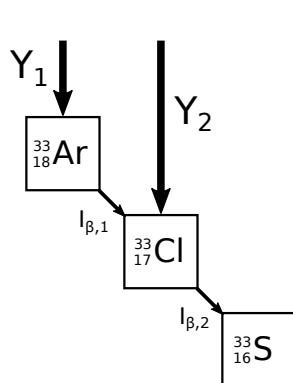


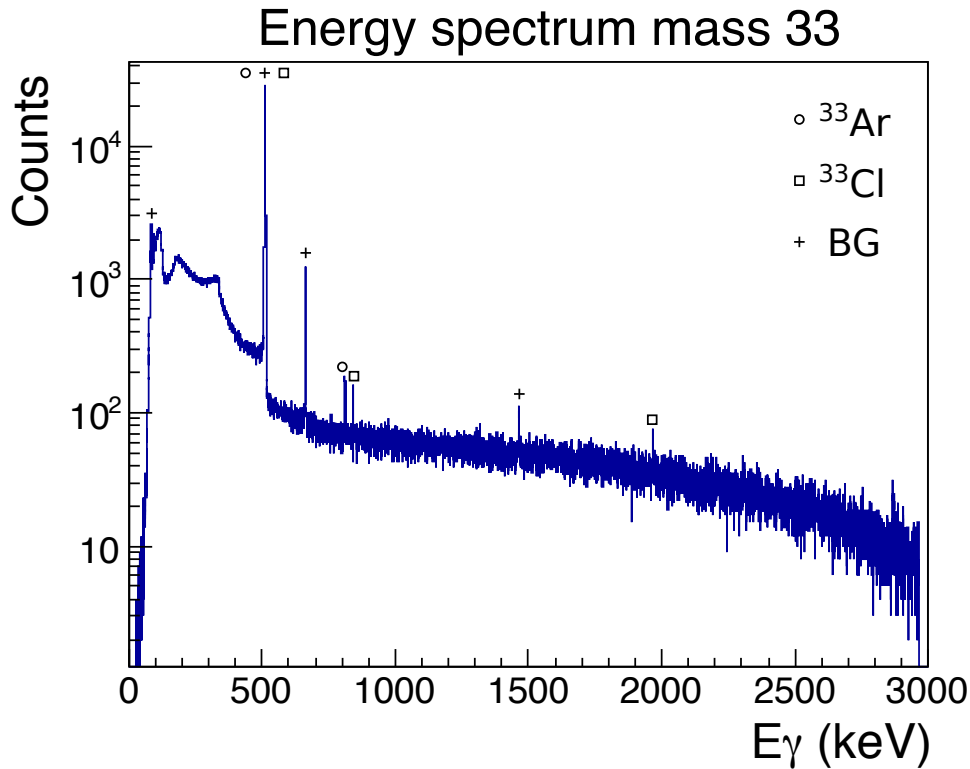
Figure 1.6 – **Top:** fitting a  $\gamma$ -peak in time-gated energy spectrum. **Bottom:** fitting a saturation curve in an energy-gated time spectrum. The green and red areas are the peak and background gates, respectively.

The dead-time  $DT$  of the acquisition rises with the sum of the activities of the different species. Therefore it evolves as a function of time, like  $I_\gamma$ . The dead-time was estimated for a given time window by comparing the number of counts received by the acquisition with and without a condition of anti-coincidence on the "inhibit" signal. The ratio of these two numbers gives the live time  $(1 - DT)$ . Whichever method is used to determine  $I_{sat,\gamma}$ , we measure the dead-time and correct the intensities every second. The following two examples highlight a few subtleties in the analysis.

#### First example: run 47 (mass 33)



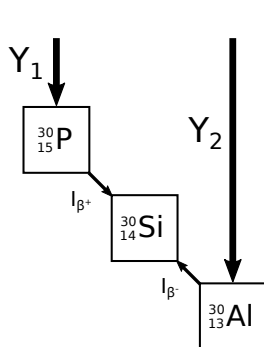
The magnetic dipole was tuned for  $\frac{A}{q} = 33$ . The energy spectrum showed several peaks, all of which have been identified as decay of  $^{33}\text{Ar}$  (810 keV),  $^{33}\text{Cl}$  (841, 1967 keV) or background radiation (see Fig. 1.7). Both  $^{33}\text{Ar}$  and  $^{33}\text{Cl}$  are sufficiently short lived to use the first method and the rate of  $^{33}\text{Ar}$  is easily determined with Eq. 1.4. We have to take into account that the  $^{33}\text{Ar}$   $\beta$ -decays to the  $^{33}\text{Cl}$  which in turns  $\beta$ -decays to a stable element (see the scheme). The production rate of  $^{33}\text{Cl}$  calculated with Eq. 1.4 has to be corrected by the rate of  $^{33}\text{Ar}$ . We can also use the 511 keV peak corresponding to the  $\beta^+ / e^-$  disintegration to increase the precision of the measurement on the rate of  $^{33}\text{Cl}$ . This peak is populated by all  $\beta^+$  emitters ( $^{33}\text{Ar}$ ,  $^{33}\text{Cl}$  and a few background emitters). Therefore the intensity of the 511 keV line is  $I_{511} = I_{\beta,1} + I_{\beta,2} + BKG_{511} = Y_1 BR_1 + (Y_1 + Y_2) BR_2 + BKG_{511}$ . We deduce:

Figure 1.7 –  $\gamma$  spectrum of run 47, for mass 33.

$$Y_2 = (I_{511} - Y_1(BR_1 + BR_2) - BKG_{511})/BR_2 \quad (1.5)$$

The background contribution to the 511 keV peak is estimated by fitting a constant line on the time spectrum gated on the 511 keV before the removal of the faraday cup from the beam axis. The errors on all rates take into account the statistical error of  $I_{sat,\gamma}$  fits and efficiency, and the error on the branching ratios from the literature. A special attention has been given to the error whenever a subtraction of  $\gamma$ -intensity was involved. Should we have the choice to estimate either of the rates of 2 isotopes feeding the same  $\gamma$ -line, we always use the one on which we have the best precision to measure the rate of the one with the biggest error.

#### Second example: run 90 (mass 30)



For this run the dipole has been tuned to accept  $\frac{\Delta}{q} = 30$ . The peaks of the  $\gamma$  spectrum of Fig. 1.8 belong to the decay lines of  $^{30}\text{Al}$  and  $^{30}\text{P}$  (1263 and 2235 keV),  $^{21}\text{F}$  (351 and 1396 keV) and to the background. The  $^{21}\text{F}$  is observed at this mass selection because it was bonded with stable Beryllium in the  $^9\text{Be}^{21}\text{F}^+$  molecular ion. Indeed, while heating the source, some of the Beryllium contained in the BeO insulators of the TISS was evaporated and created molecular bonding with all Fluor isotopes. Thanks to its short half-life (4.16 s), the production rate of  $^{21}\text{F}$  was estimated by

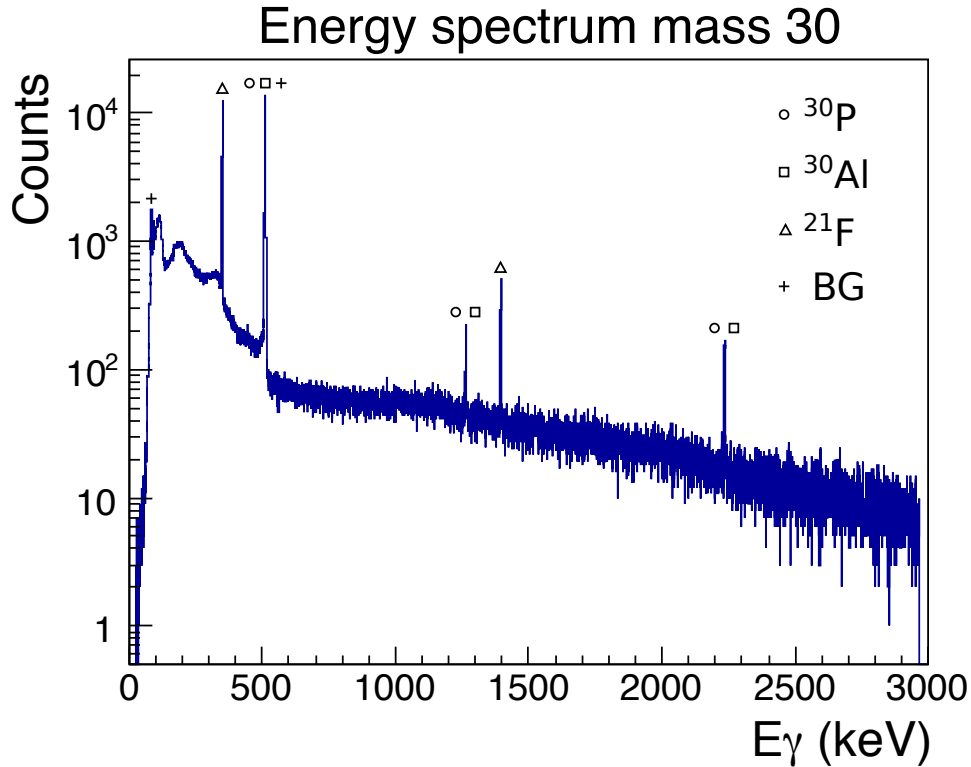


Figure 1.8 –  $\gamma$  spectrum of run 90, for mass 30.

the first method applied on its two visible peaks.  $^{30}\text{P}$  and  $^{30}\text{Al}$  are mirror nuclei decaying on the same stable nuclei ( $^{30}\text{Si}$ ) by  $\beta^+$  and  $\beta^-$ -decay respectively. This implies that these two nuclei can feed the same  $\gamma$ -lines in  $^{30}\text{Si}$ . This time the 511 keV line is only populated by the decay of  $^{30}\text{P}$  and the background. After correcting for the background as in the first example, we determine the rate of this relatively long-lived isotope (2.498 min) with the second method. We then use this rate to deduce the production rate of  $^{30}\text{Al}$ . For example the intensity of the 351 keV  $\gamma$ -line is given by:

$$I_{351} = Y_{Al}BR_{Al,351} + Y_PBR_{P,351} \quad (1.6)$$

Which leads to an easy deduction of  $Y_{Al}$ .

### Analysis of the 511 keV missing counts

It was observed for  $\beta^+$  emitters with at least one  $\gamma$ -line that the rate calculated with the 511 keV line was systematically lower than the rates calculated with other  $\gamma$ -lines. The difference between this line and other  $\gamma$ -lines is that  $\gamma$ -decay radiations are emitted from the nucleus itself, trapped in the tape at the implantation point while the 511 keV photons are emitted from the point of disintegration of a positron. We can consider that in case of a proton rich nucleus implanted in the tape, its  $\beta^+$  particles are emitted isotropically from the implantation point and disintegrate only when they meet an electron, most likely on the walls. Therefore, while the source of decay  $\gamma$ -rays and  $\beta^+$  particles is "point-like", the source of the 511 keV photons is the whole vacuum chamber, not counting the background. The bias is calculated as

$$B = \frac{\frac{N_\gamma}{\epsilon_{\text{HPGe}}(E_\gamma)BR_\gamma} - \frac{N_{511}}{\epsilon_{\text{HPGe}}(E_{511})BR_{511}}}{\frac{N_\gamma}{\epsilon_{\text{HPGe}}(E_\gamma)BR_\gamma}} \quad (1.7)$$

with  $N_\gamma$  the number of direct  $\gamma$  hits from the implantation point, and  $N_{511}$  the number of hits coming from positron disintegration. Because of its geometric origin, it is expected that this 511 keV bias will depend on the position of the Germanium detector and that there will be three biases for when the HPGe is at 590, 260 and 85 mm from the tape. The 511 keV bias of several isotopes at distance 590 mm was measured and plotted in [Fig. 1.9](#). As the dispersion and error on the bias is rather high for several measurements, the estimated bias at this distance was calculated as the mean of all biases at 20.1(10)%. Only 3 values of the bias were measured at a distance of 260 mm, all three being approximately 45%. The only two measurements at 85 mm exhibited no bias, though it is likely that these runs were contaminated in 511 keV radiations by a long-lived  $\beta^+$  emitter created in a previous run. In the end, the few isotopes whose rate was estimated solely on the 511 keV line, and thus needed correction, were only studied at 590 mm distance. Rates given later in [Tab. 1.1](#) are already the corrected ones.

Simple C++ simulations were done to reproduce the observed bias. In the first place, we simulated the isotropic emission of  $\gamma$ -rays from a point-like source at the tape position and observed how many of them reached the HPGe, depending on its position. The active diameter of the HPGe was taken to be 6 cm. We then simulated the isotropic emission of  $\beta^+$  particles from the same point and collision onto the walls of the vacuum chamber. The geometry of the chamber was reproduced in the routine including the walls, the beam tube, the entrance and exit tubes of the tape, and the mobile Faraday Cup in off-beam position. Once a positron reaches a wall/tube/FC, its point of impact is in turn considered as a point-source for two 511 keV photons, emitted at  $180^\circ$  from one another. The simulations used  $10^7$   $\beta$  particles. We calculated biases of 10.3 % at 590 mm, 24.6 % at 260 mm and 45.8 % at 85 mm. The simulations confirmed that with increasing distance of the detector, the difference between a point-like and a finite-size source, lessen. Though the simulations do not quantitatively reproduce the values of the bias, they give the good order of magnitude and explain the phenomenon.

## 1.6 RESULTS

The FEBIAD TISS successfully produced radioactive ions of non-metals (O, F, P, Cl), rare gases (Ne, Ar), alkalines (Na, K) and metals (Mg, Al) at close-to-nominal power. The experiment nevertheless encountered few issues:

- The presence of Beryllium gas, mentioned earlier, indicated the dissociation of the BeO insulators at high temperatures. This was not observed at ISOLDE for similar temperatures of the cathode. In particular the wire bringing the 150 V to the anode is mechanically held on the cathode with



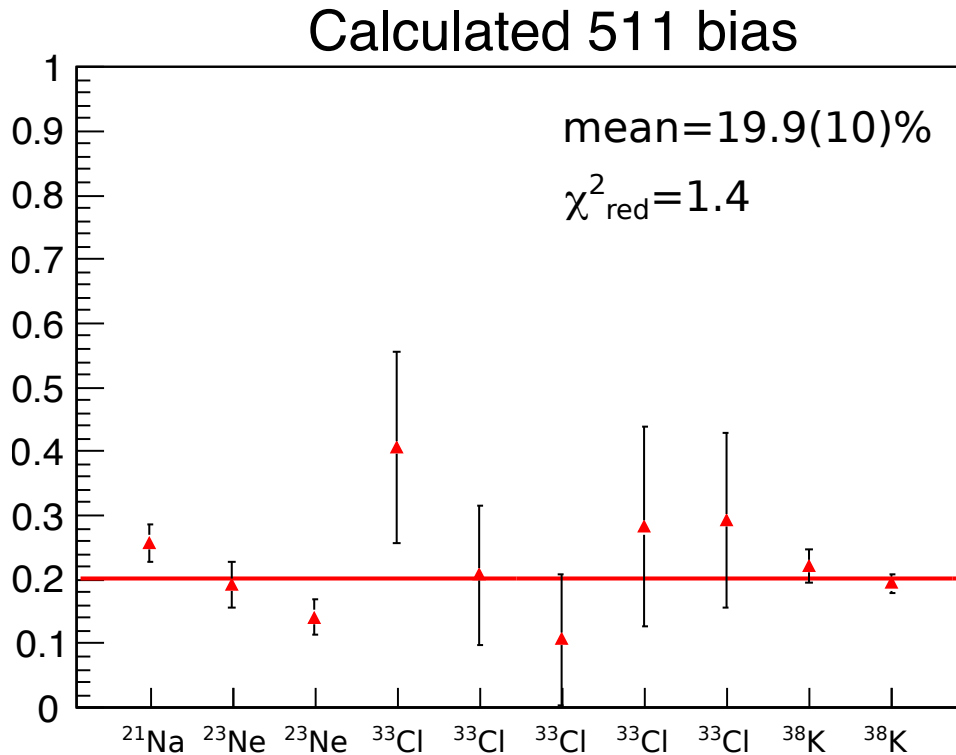


Figure 1.9 – Calculated 511 keV bias for several isotopes and several runs at a distance of 590 mm from the implantation point.

one of these BeO insulators. The better heat shielding of the source in SPIRAL could induce a higher temperature on this specific insulator compared to the ISOLDE source.

- The power of the primary beam was rather unstable, restraining the analysis to sometimes very short time frames with a constant power.
- The ionisation efficiency was found to be lower than what was measured with this source at ISOLDE.

In addition to the test of the TISS, the physical goal of this experiment was to perform high precision half-life measurements. After implantation of radioactive nuclei, the tape was moved to the decay station mentioned earlier. The half-lives of  $^{21}\text{Na}$ ,  $^{17}\text{F}$  and  $^{33}\text{Cl}$  were determined by J. Grinyer *et al.* in [19] and [20], but are not detailed in this work.

#### 1.6.1 Production rates

Tab. 1.1 shows the production rates calculated in this analysis and their extrapolation at 1200 W as well as the rates expected from the previous experiments described in [14, 16] and projected for the SPIRAL Upgrade. One can notice that several ions heavier than  $^{36}\text{Ar}$  have been produced. This is mainly due to transfer reactions involving a few nucleons from the carbon target. Fig. 1.10 summarises the elements and isotopes observed during the experiment. Silicon and sulfur were not observed, the first being refractory and therefore very hard to desorb from a surface, and the second being chemically very reactive and thus likely to being neutralised

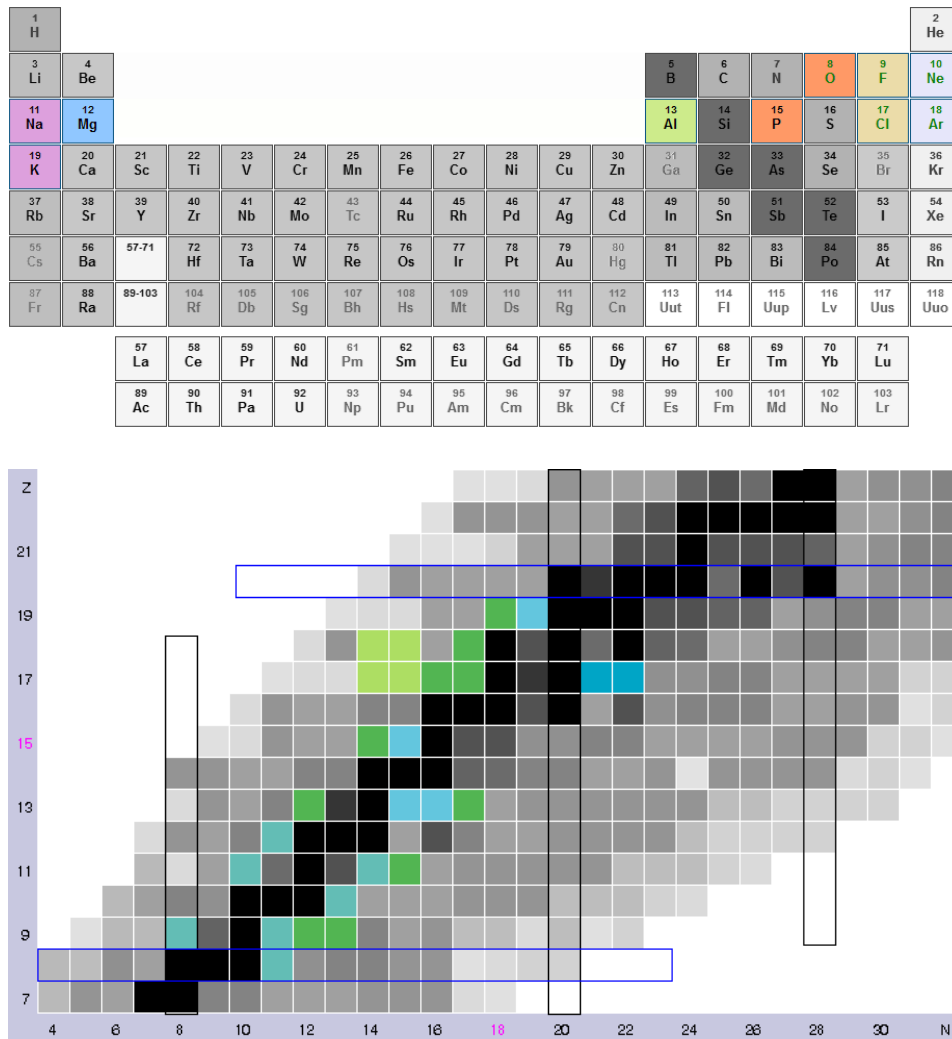


Figure 1.10 – Colored elements of the periodic table (top) and isotopes of the nuclide chart (bottom) have been observed during the commissioning of the FEBIAD TISS. The colors of the chart only account for the half-life of the isotopes (from [22]).

onto the transfer tube surface. We did not try to observe masses under 17 and over 42.

### 1.6.2 Ionisation efficiencies

The ionisation efficiency was estimated during the off-line commissioning of the TISS using a calibrated argon gas leakage and during the on-line experiment using calibrated leakages of neon, argon and krypton. The ionisation efficiency measured for argon during this experiment was  $\sim 4$  times lower than the one measured with the FEBIAD source of ISOLDE [13]. It was believed that the Be vapour lowered the ionisation efficiency and that several measured rates could have been higher once this problem was solved. However, tests were repeated offline with other insulator materials than BeO and no sizeable improvement could be achieved. The efficiencies were reproducible and still down by a factor of 4 compared to ISOLDE. Reasons for these comparatively lower efficiencies are still

Type	Isotope	Power (W)	Measured rates (this work)	Extrapolated rates (1200W)	Expected from previous experiments
Alkalines	$^{21}\text{Na}$	984	$3.0 \cdot 10^7$	$3.7 \cdot 10^7$	$3.0 \cdot 10^7$
	$^{25}\text{Na}$	964	$2.2 \cdot 10^7$	$2.7 \cdot 10^7$	$2.9 \cdot 10^7$
	$^{26}\text{Na}$	939	$1.5 \cdot 10^6$	$1.9 \cdot 10^6$	$2.6 \cdot 10^6$
	$^{37}\text{K}$	823	$4.7 \cdot 10^7$	$6.9 \cdot 10^7$	
	$^{38}\text{K}$	1214	$6.4 \cdot 10^7$	$6.3 \cdot 10^7$	
Metals	$^{23}\text{Mg}$	1299	$1.6 \cdot 10^7$	$1.5 \cdot 10^7$	$3.2 \cdot 10^6$
	$^{25}\text{Al}$	964	$1.1 \cdot 10^5$	$1.4 \cdot 10^5$	$1.8 \cdot 10^5$
	$^{26m}\text{Al}$	939	$1.9 \cdot 10^5$	$2.4 \cdot 10^5$	
	$^{28}\text{Al}$	981	$1.6 \cdot 10^7$	$2.0 \cdot 10^7$	$4.2 \cdot 10^6$
	$^{29}\text{Al}$	1355	$1.2 \cdot 10^7$	$1.1 \cdot 10^7$	$2.4 \cdot 10^6$
	$^{30}\text{Al}$	1247	$4.2 \cdot 10^4$	$4.0 \cdot 10^4$	$2.6 \cdot 10^4$
Nonmetals	$^{29}\text{P}$	1355	$1.7 \cdot 10^4$	$1.5 \cdot 10^4$	
	$^{30}\text{P}$	1300	$4.0 \cdot 10^5$	$3.7 \cdot 10^5$	
	$^{31}\text{Cl}$	1337	$3.1 \cdot 10^3$	$2.8 \cdot 10^3$	$5.9 \cdot 10^3$
	$^{32}\text{Cl}$	891	$1.2 \cdot 10^5$	$1.6 \cdot 10^5$	$2.4 \cdot 10^5$
	$^{33}\text{Cl}$	1235	$1.3 \cdot 10^7$	$1.3 \cdot 10^7$	$1.8 \cdot 10^7$
	$^{38}\text{Cl}$	1013	$4.4 \cdot 10^3$	$5.2 \cdot 10^3$	
	$^{38m}\text{Cl}$	1013	$5.9 \cdot 10^2$	$7.0 \cdot 10^2$	
Rare gases	$^{23}\text{Ne}$	1299	$1.4 \cdot 10^6$	$1.1 \cdot 10^6$	
	$^{32}\text{Ar}$	891	$1.9 \cdot 10^3$	$2.6 \cdot 10^3$	
	$^{33}\text{Ar}$	1235	$2.1 \cdot 10^5$	$2.0 \cdot 10^5$	
	$^{35}\text{Ar}$	703	$5.56 \cdot 10^7$	$9.5 \cdot 10^7$	
Molecules	$\text{C}^{19}\text{O}$	1337	$1.3 \cdot 10^3$	$1.2 \cdot 10^3$	
	$\text{Be}^{17}\text{F}$	939	$9.0 \cdot 10^7$	$1.2 \cdot 10^8$	
	$\text{Be}^{20}\text{F}$	1355	$2.5 \cdot 10^6$	$2.2 \cdot 10^6$	
	$\text{Be}^{21}\text{F}$	1247	$1.8 \cdot 10^5$	$1.7 \cdot 10^5$	
	$\text{Be}^{22}\text{F}$	1337	$1.5 \cdot 10^4$	$1.3 \cdot 10^4$	
	$\text{H}^{38}\text{Cl}$	1013	$4.2 \cdot 10^3$	$5.0 \cdot 10^3$	
	$\text{H}^{38m}\text{Cl}$	1013	$5.9 \cdot 10^2$	$7.0 \cdot 10^2$	
	$\text{Be}^{33}\text{Cl}$	941	$3.1 \cdot 10^5$	$4.0 \cdot 10^5$	
$\text{O}^{23}\text{Mg}$	1013	$4.3 \cdot 10^2$	$5.1 \cdot 10^2$		

Table 1.1 – Measured rates (in pps) and compared with expected ones.

Element	$t_0(s)$	alpha
Na	2.06	1.36
Mg	2.76	0.97
Al	152	1.16
P	470000	0.61
Cl	3.5	1.27
Ar	0.277	0.97

Table 1.2 – Estimation of the fit parameters  $t_0$  and  $\alpha$  for different elements.

actively debated. Possible explanations invoked are: (1) a rather large C vapour from the target in SPIRAL, (2) different heating configurations in SPIRAL and ISOLDE.

### 1.6.3 Release efficiencies

The measured rates were also used to determine the release efficiencies of different isotopes. The release efficiency depends both on the half-life of the concerned isotope, its diffusion properties and its average sticking time on hot walls.  $\epsilon_{release}$  is therefore a specific value to each isotope. The ion rate in the main chamber of the SPIRAL identification station can be expressed as:

$$Y_{ion} = Y_{target} * \epsilon_{release} * \epsilon_{ionisation} * \epsilon_{transport} \quad (1.8)$$

The isotopic production rate in the target  $Y_{target}$  can be calculated using the EPAX cross-section parametrisation. The ionisation efficiency  $\epsilon_{ionisation}$  has been measured on rare gases as explained before and extrapolated to other elements. The transport efficiency  $\epsilon_{transport}$  ( $\simeq 80\%$ ) between the FEBIAD source and the implantation point on the tape was calculated by comparing the current of the HV power supply and the current of the Faraday Cup in the implantation room. The release efficiency of an isotope depends on its chemical nature and half-life. The calculated  $\epsilon_{release}$  for Al isotopes are shown in Fig. 1.11, and are fitted using the empirical function used in [23]:

$$f(T_{1/2}) = \frac{1}{1 + (\frac{t_0}{T_{1/2}})^\alpha} \quad (1.9)$$

where  $t_0$  and  $\alpha$  are the fit parameters that depend on the element.  $\alpha$  describes the behaviour of the efficiency as a function of half-life for short  $T_{1/2}$  and contains the information of the release mode (diffusion, effusion or both).  $t_0$  is the half-life above which the release efficiency reaches its maximum value. The release efficiencies of several isotopes have been calculated with the data from our experiment, and the fitted values of  $\alpha$  and  $t_0$  are listed in Tab. 1.2. A more detailed treatment will be given in a forthcoming publication on the SPIRAL<sub>1</sub> Upgrade.

## CONCLUSION

The FEBIAD TISS developed at GANIL successfully produced alkaline, alkaline earth, metallic and gaseous radioactive ions at nominal power, and

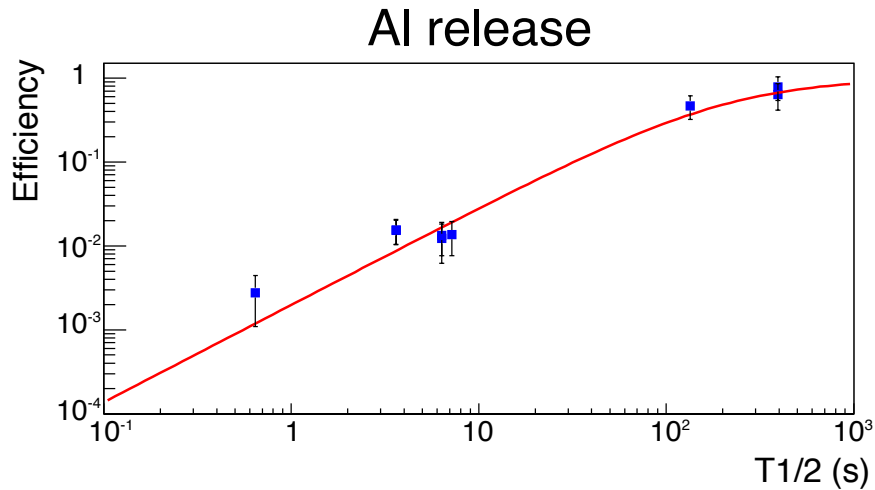


Figure 1.11 – Release efficiencies of aluminium as a function of the half-life of the isotope, fitted by the empirical equation Eq. 1.9 (in red).

a wider range of elements is expected for different target/beam combinations. Production rates of different elements were measured are generally as good as expected. The upgrade of the SPIRAL1 facility is still on going and should be delivering radioactive beam of competitive intensity by mid of 2017. SPIRAL1 beams could benefit from the development of the MR-ToF-MS PILGRIM for both mass separation and mass measurement in the LIRAT (Ligne d'Ions Radioactifs A Très basse énergie) facility as S3 will not be commissioned before 2018.

# INTRODUCTION TO MR-TOF MASS SPECTROMETRY

# 2

## CONTENTS

3.1	PILGRIM SIMULATIONS AND OPTIMIZATION . . . . .	57
3.1.1	SIMION and its accuracy . . . . .	57
3.1.2	Early geometries . . . . .	59
3.1.3	Optimization procedures . . . . .	59
3.2	SUCCESSIVE DESIGNS . . . . .	61
3.2.1	Early mechanical design and changes in the geometry . .	61
3.2.2	Geometry of the mirrors . . . . .	63
3.2.3	Injection in the trap . . . . .	64
3.2.4	Final design . . . . .	65
3.2.5	Optical properties . . . . .	65
	CHAPTER CONCLUSION . . . . .	72

**I**N this chapter we introduce several techniques of mass spectroscopy and spectrometry before focussing on the rather recent MR-ToF-MS technique. We develop some state-of-the-art aspects of its practical implementation and expose a simple theoretical model explaining the main optical properties and effects encountered in the later simulation phase. We also give a brief overview of the development of MR-ToF spectrometry worldwide.



## 2.1 MASS SPECTROMETRY

Mass spectrometry is an ensemble of micro-analysis techniques used in chemistry, particle physics and nuclear physics to determine the mass, nature and abundance of one or more elements in a sample. The species considered, ranging from single particles to molecules, are far too light to be measured at rest (i.e. weighted). These species have to be accelerated to observe their dynamical properties, from which we deduce their mass. This practically limits the range of mass spectrometry to charged particles (electrons, ions, molecular ions for the least exotic part) accelerated by electromagnetic fields in vacuum. As a consequence the real data measured is never directly the mass, but the mass-over-charge ratio  $\frac{m_0}{q}$ , as shown in the relativistic expression of the Lorentz law:

$$\frac{d(\gamma\mathbf{v})}{dt} = \frac{q}{m_0}(\mathbf{E} + \mathbf{v} \times \mathbf{B}) \quad (2.1)$$

where  $\mathbf{v}$  is the speed of a charged particle in the laboratory frame,  $t$  is the time in the laboratory,  $\gamma$  is the Lorentz factor,  $q$  is the charge of the flying particle,  $m_0$  is its rest mass, and  $\mathbf{E}$  and  $\mathbf{B}$  are the electric and magnetic fields, respectively. The first mass spectrometers date back from over a century ago and several techniques have been developed and improved since, increasing the performances of these aparati.

### 2.1.1 History of mass-spectrometry

We just give here the key steps of the emergence and development of this science. A more detailed version of the history of mass spectrometry can be found in [24] and in the special issue of the Nature milestones dedicated to mass spectrometry [25]. More details about the working principles of the different mass spectrometers are given in the next sections.

It was theorised by Prout in the early 19th century that atomic masses of all elements were integer multiples of the atomic mass of the lightest element known, hydrogen. At this time, the absolute values of the masses could not be measured and only relative weights were inferred by considerations such as: "The weight of a volume of atmospheric air being 1, the weight of the same volume of  $X$  is  $W_X$ ". The so-called Prout's hypothesis seemed to be disproved later by more accurate measurement of the atomic masses, e.g. boron ( $m_B = 10.72m_H$ ) or chlorine ( $m_{Cl} = 35.17m_H$ ). Just as the first step for any type of mass-spectrometry or spectroscopy is to create a sample of charged particles, the history of this science starts with the creation of the first ion beams. In 1886, as the famous "cathode rays" had already been studied for more than 2 decades, Eugen Goldstein used a perforated cathode and observed rays on the side of the cathode opposite to the anode. He named the phenomenon "canal rays" since the rays were coming from the canal in the cathode. Noticing that they were traveling in the opposite direction to the negative cathode rays, he concluded that these rays must be positively charged. He had created the first ion beam.



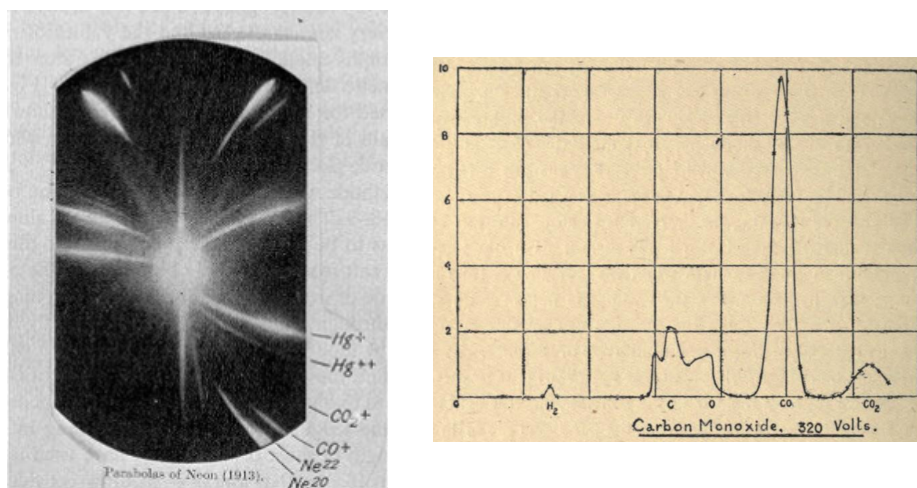


Figure 2.1 – Left: parabolae of neon and other elements printed on a photographic plate [26]. Right: mass spectrum sorting several elements and molecules. The abscissae are the values of the magnetic field used to deflect the ions, while the ordinates are the values of the deflection of the foils of an electroscope used to measure the current [27].

In 1897, Thomson discovered the electron and measured its mass-to-charge ratio during his three historic experiments. In 1898, Wien used a similar apparatus combining a magnet and an electrostatic deflector to apply a velocity-dependent deflection to canal rays. Velocity filters working on the same principle came to be known as Wien filters. Wien confirmed the positive nature of the rays and noticed that the velocity of the canal rays was much lower and its mass-to-charge ratio much higher than these of the cathode rays. In 1911, Thomson used a slightly different apparatus: the electric and magnetic fields which were perpendicular to each other in Wien's experiment, were now parallel to each other and both perpendicular to the flight path of the canal rays. Under these conditions, the rays of same mass-to-charge ratio were deflected on the same parabola and their position on the parabola is determined by their velocity. By using a photographic plate at the end of his apparatus, Thomson could visualise these parabolae and made the first qualitative separation of ions of different mass. This quickly led to the discovery of different stable isotopes for the same element, neon (Fig. 2.1, left). Nevertheless, the parabola pictures given by the photographic plate were quantitative in terms of  $\frac{m}{q}$  value, but qualitative in terms of intensity of the parabolic lines, meaning the first apparatus was "only" a spectrograph. By 1912 he upgraded the principle of his experimental setup by removing the photographic plate and replacing it with a metal plate with a parabolic slit and a Faraday Cup behind it. By changing the magnetic field, Thomson could select ions crossing the metal plate according to their mass-to-charge ratio and therefore scan the  $\frac{m}{q}$  spectrum, while measuring the ion intensity at a given  $\frac{m}{q}$  value. This was the first ever mass spectrometer. One of the first mass spectra, dating from 1913 can be seen on Fig. 2.1, right.

The First World War interrupted Thomson's work. At the end of the conflict, *Aston*, a previous research assistant of Thomson, built a new spectrograph in 1919, trying to explain the 2 lines of Neon in Thomson's

spectrum. The apparatus used successive electric and magnetic fields, perpendicular to the axis and to each other and a photographic plate to visualise the results. By doing so he managed to reach velocity-focussing, i.e. to focus all ions of same mass but different velocity on the same point of the photographic plate. This design and its later improvements helped Aston identifying 212 of the 287 naturally occurring isotopes. In 1918, Dempster developed a new type of spectrometer using a directional-focussing  $180^\circ$  magnetic sector with which he discovered isotopes of magnesium, zinc and calcium in the early 1920's. He developed later a new version of his apparatus, following the calculations of Bartky [28], in which the magnetic sector was preceded by a  $90^\circ$  electrostatic deflector to perform velocity-focussing in addition to directional-focussing. This instrument led to the discovery of the  $^{235}\text{U}$  isotope of uranium in 1935. Dempster had established the theory and first designs of a type of mass spectrometer which is still widely used to this day in many research facilities. The design was improved in the next decades with technological progress and the development of the first electron impact ion sources. Notably, a magnetic sector, the Calutron, was used as a trajectory separator to perform industrial scale nuclear enrichment of uranium during the Manhattan project.

In 1946 Stephens described for the first time the principle of Time-of-Flight (ToF) mass spectrometry. He proposed in his article [29] to generate ion pulses and to compare the ToF of different ions in a vacuum tube. Stephens argued that such a device could display the whole mass spectrum almost in real time with a high repetition rate. In 1948 the first proof-of-principle ToF spectrometer was built by Cameron and Eggers. It had a rather poor resolving power and was not capable of separating stable isotopes of the same elements. In 1955 Wiley and McLaren built an enhanced version with improved optics of the ion source, so as to reduce the ToF spread due to the initial spatial distribution of the ions which limited the resolving power in the case of Cameron and Eggers. Nevertheless, the resolving power was still severely limited by the energy distribution. This problem was solved in 1973 by Mamyrin and collaborators who introduced the reflectron [30], an electrostatic mirror that induced greater delay on ions of higher energy and created a ToF focus at the position of the detector. The ToF-spectrometry would not meet a great popularity until the early 1990's when progresses on pulsed ion source and in fast-timing acquisition made the concept competitive.

In parallel, other types of mass spectrometry were developed in the second half of the 20th century. In 1949, Hipple and collaborators introduced the first Ion Cyclotron Resonance (ICR) mass spectrometer in which ions of a given  $\frac{m}{q}$  are selectively excited and collected on a fixed detector. In 1953, Paul described for the first time the Quadrupole Mass Spectrometer which was capable of selecting masses on the criteria of ion motion stability in an oscillating electric field. In 1959, Dehmelt built the first magnetron trap, or Penning trap, using a combination of static magnetic and electric field to confine the ions. The apparition of ion traps brought about the renewal of mass spectrometry, as extended ion flight times and dis-

tance could then be achieved in a limited apparatus. In 1974, Comisarow and Marshall used emerging trapping techniques to trap ions and observed the frequency signature these ions left while passing next to an electrode [31]. More recently in 2000, Makarov introduced the orbitrap, an orbital trap using only electrostatic fields to trap ions, on which he used a similar detection technique [32]. Many variations and combinations of these different techniques have been reported through the years but won't be introduced here.

### 2.1.2 Important characteristics

This short historical review highlights several crucial characteristics for a mass spectrometer. First and most obviously the resolving power must be high. It is defined as  $R = \frac{m}{\Delta m}$ , with  $\Delta m$  being the minimum mass difference that can be resolved by the spectrometer. In order to achieve this high resolving power, the spectrometer has to be separative in mass but focussing in all other respects. Let  $O(m, p_i)$  be the observable (final position, direction, ToF, frequency ...) of the spectrometer depending on the mass  $m$  and other variables  $p_i$  (energy, momentum, initial position and direction ...). Then we need:

$$\frac{\partial O}{\partial m} \neq 0, \quad \frac{\partial O}{\partial p_i} \simeq 0, \forall i \quad (2.2)$$

Whatever the observable is, it must vary with mass but should not depend on any other variable. The dependency of  $O$  to  $m$  gives the sensitivity of the spectrometer, while the dependency of the observable to the other variables limit the precision of the device, i.e. its statistical variability. Both have influence on the resolving power. A spectrometer should also be able to treat high yields of input species (chemical, nuclear or corpuscular) with high efficiency in order to reach high statistics. In case of a pulsed beam (ToF and frequency methods), the spectrometer also needs to be fast; firstly because the speed of the measurement affects the repetition rate and therefore the time to accumulate a certain quantity of data, and secondly because the measurement time limits the capability of the spectrometer to analyse short-lived species. In his book "Recollections and Reflections" [33], Thomson wrote:

*"The rays are registered on the photograph within much less than a millionth of a second after their formation, so that when chemical combination or decomposition is going on in the gas in the tube, the method may disclose the existence of intermediate forms which have only transient existence, as well as that of the final product, and may thus enable us to get a clearer insight into the processes of chemical combination"*

Though Thomson was writing here about transient chemical compounds in fast reactions, the point still stands for any transient species including radioactive isotopes. Known decaying nuclei have half-lives ranging from billions of years to a few tens of nanoseconds, making fast spectrometry very important for a wide variety of isotopes. Also important are the universality and the selectivity of the spectrometer. The univer-

sality denotes the capability of the spectrometer to work on a wide part of the mass spectrum. The range would of course depend on the field of study (particle physics, nuclear physics, chemical analysis). The selectivity characterise the spectrometer's ability to scan a short range of the mass spectrum. Though these two characteristics can seem conflicting, most of modern spectrometers have a broad-band mode and a scanning mode.

### 2.1.3 Types of spectrometer

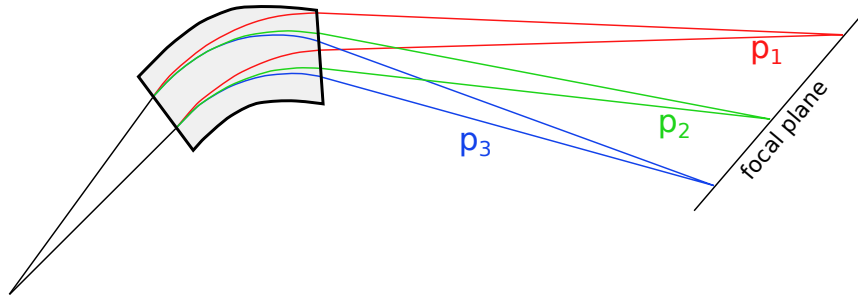
We only focus here on the main types of spectrometers that are used in nuclear physics and their operating and detection principles.

#### Sector spectrometers

**Magnetic sectors:** a charged particle of mass  $m$ , charge  $q$ , and velocity  $v$  in a constant magnetic field  $B$  (perpendicular to the motion) is deviated following a radius of curvature  $\rho$ . Using the formulation of the Lorentz force it follows:

$$B\rho = \frac{mv}{q} \quad (2.3)$$

Magnetic sectors therefore separate ions on the basis of their momentum. The expression  $\frac{mv}{q}$  is purely beam dependent and is called the magnetic rigidity. Owing to the geometry of the magnet, ions taking the outer (resp. inner) turn remain longer (resp. less) in the magnetic field and are more (reps. less) deflected. This result in focussing the input beam as shown in the drawing below.

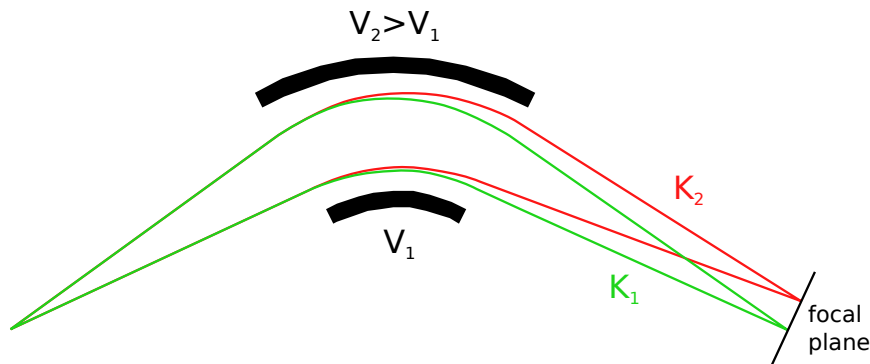


When the magnetic sector is part of a larger apparatus, the focal plane might not be reached after only one sector. Ideally, at the focal plane, the focus point depends only on the magnetic rigidity of the beam and not on the initial dispersion in direction and transverse position. A slit can be placed at the position of the focal plane to select a given momentum.

**Electrostatic sectors:** these sectors are usually made of 2 spherical blades of different potential following the beam line (see drawing). This way the electric field is always roughly perpendicular to the trajectory. Following again the expression of the Lorentz force:

$$E\rho = \frac{mv^2}{q} \quad (2.4)$$

This means that electrostatic sectors separate the ions with respect to their kinetic energy. Quite alike magnetic spectrometers, it is possible to perform angle and position focussing. Due to the geometry of such an arrangement, the electric field is rather constant between the blades, both in longitudinal and transverse direction, meaning that ions taking the outer turn are more deflected than others mostly because they spend more time in the sector.

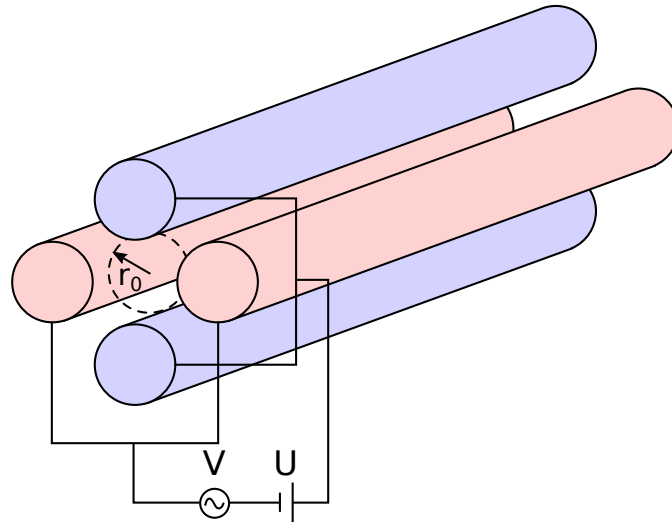


Some combinations of magnetic and electrostatic sectors, the so-called double-focussing mass spectrometer, make use of the properties of both sectors to create achromatic focus planes. The position of the focus point in this plane does not depend on the initial angle, position or speed of an ion, but solely on its mass. The idea of double-focussing spectrometers comes from the original idea of Bartky and Dempster, mentioned earlier [28]. This kind of spectrometer is very popular in chemical analysis, using low energy ions ( $10^2 - 10^4$  eV). The resolving power of sector spectrometers ranges from  $10^2$  to  $10^3$  for single focussing devices and can reach several  $10^4$  for double focussing ones. Sector spectrometers generally have a high acceptance and are fast ( $\sim 10^{-5}$  s at a few keV) but are very expensive.

Sector instruments are widely used in nuclear physics for fragment separation or identification in In-flight facilities. Magnetic sectors are generally preferred due to the high energy of the fragments (1 – 100 MeV). The separator is tuned to have a rather large momentum acceptance for fragment of interest but so that the primary beam is out of the  $B\rho$  acceptance of the sector. Examples of such separators are LISE at GANIL [34], FRS at GSI [35], A1900 at NSCL [36] and RIPS at RIKEN [37]. The resolving power in fragment separators reach typically a few hundreds.

### Quadrupole Mass Spectrometer (QMS)

QMS are arrangements of 4 electrodes, either hyperbola-shaped or simply cylindrical, on which a sum of DC and RF potentials is applied. Two opposite rods have a potential of  $+(U + V\cos(\omega t))$ , while the other two rods have a potential of  $-(U + V\cos(\omega t))$  (see drawing). This arrangement creates an oscillating hyperbolic field.



The motion of charged particles in the resultant field follows Mathieu's equations:

$$\frac{d^2x}{dt^2} = -\left(\frac{q}{m}\right) \frac{(U + V \cos(\omega t))}{r_0^2} x \quad (2.5)$$

$$\frac{d^2y}{dt^2} = \left(\frac{q}{m}\right) \frac{(U + V \cos(\omega t))}{r_0^2} y \quad (2.6)$$

$$\frac{d^2z}{dt^2} = 0 \quad (2.7)$$

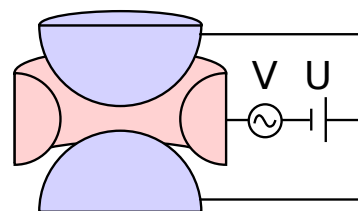
$r_0$  being the radius of the opening between the 4 electrodes and  $z$  being the beam axis. While solving these equations, two important factors  $a_u$  and  $q_u$  emerge:

$$a_u = \frac{8qU}{mr_0^2\omega^2} \quad q_u = \frac{4qV}{mr_0^2\omega^2} \quad (2.8)$$

with  $q$  the charge state of the ion. These equations do not have an analytical solution but they define stable  $X$  or  $Y$  regions of the  $a_u$  vs  $q_u$  plot (see Fig. 2.2). Mathematically, "stable" means that the motion has a real solution in  $X$  or  $Y$ . Ions can go through the mass filter if they belong to the intersection of  $X$  and  $Y$  stable regions. The mass selection is done by changing either  $\omega$  of  $U$  and  $V$ . This kind of spectrometer is roughly as fast as a sector spectrometer, but is much cheaper and very compact, owing to the absence of the magnet. However the resolving power is limited to a few thousands and depends on the mass.

### Ion traps

**The Quadrupole Ion Trap (QIT)** or Paul trap is a 3-dimensional extension of the QMS, enabling dynamic trapping of the ions. The trap consists of a hyperbolic (or cylindrical, or spherical) ring electrode and 2 hyperbolic (or spherical) end cap



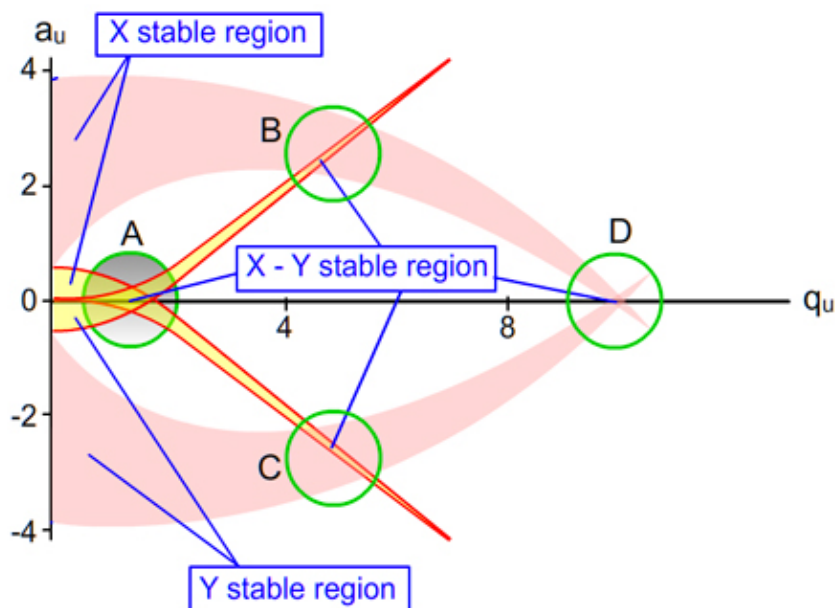
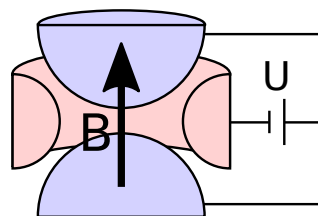


Figure 2.2 – Mathieu stability diagram. Mathieu's equations define regions in the  $a_u$  vs  $q_u$  plane in which the motion of the charged particle along the X or Y axes is stable. The intersections of X- and Y-stable regions are circled in green. Drawing from [38]

electrode. Both end-caps have one or several holes to inject and eject ions. Like for the QMS, only ions with the right  $\frac{m}{q}$  ratio maintain a stable flight path. The main difference between this spectrometer and the QMS is the longer flight path that guarantees a larger sensitivity and therefore a larger resolving power. Like other ion traps, the QIT is very sensitive to space charge, owing to the extended flight path in a small area. The resolving power of the QIT is generally limited to a few  $10^4$  and is mass-dependent, like for the QMS. The Paul trap can also be used to trap transient species for extended periods of times to observe their decay properties. The LPC-trap for example is a Paul trap dedicated to the study of  $\beta - \nu$  angular correlation at GANIL [39]. The Paul trap also exist in a linear version comparable to a QMS on which is superimposed a set of DC potentials forming an electrostatic well in the axial direction. In nuclear physics, this version of the Paul trap is generally used to cool ions beams and not as a spectrometer.

**The Penning trap** is very close to the QIT in geometry with one fundamental difference: a magnetic field ensures the radial confinement and therefore no RF potential is needed between the ring and the end-cap electrodes. The ring electrode is at a lower potential compared to the end-cap electrodes to create an axial confinement. The motion of an ion in the 3D trap that is the Penning trap can be described by 3 eigen-motions:



1. The *axial motion* of frequency  $\nu_z = \frac{1}{2\pi} \sqrt{\frac{qU}{md^2}}$ .  $d$  is a parameter depending on the trap's geometry.

- II. The *magnetron motion* of frequency  $\nu_- = \frac{1}{2}(\nu_c - \sqrt{\nu_c^2 - 2\nu_z^2})$
- III. The *reduced cyclotron motion* of frequency  $\nu_+ = \frac{1}{2}(\nu_c + \sqrt{\nu_c^2 - 2\nu_z^2})$

where  $\nu_c = \frac{qB}{2\pi m}$  is the free space cyclotron frequency, i.e. the frequency of the motion without the electric field. One can notice that in this case  $\nu_- = 0$  and  $\nu_+ = \nu_c$ . The magnetron and reduced cyclotron motions can be excited using a dipolar/quadrupolar/octupolar RF electric field. In order to generate this field the ring electrode is segmented in 2/4/8 segments on which the RF potential is applied. Both end-cap electrodes are perforated for admission and extraction of the ions. This versatile ion trap can be used both as a high resolution beam separator/purifier and high precision mass measurement device.

In mass separation or purification mode, the exit electrode usually has a single, small and centred exit hole and the trap is filled with neutral gas (usually Helium) to cool the ions inside the trap by successive collisions. In the widely used sideband cooling technique [40], the magnetron motion of the ions is excited by applying a dipolar RF excitation at the magnetron frequency. Usually, the values of  $U$ ,  $B$  and the geometric parameters are such that  $\nu_c \gg \nu_z$ . Under this assumption, the Taylor development of the magnetron frequency is, at first order:

$$\nu_- \simeq \frac{\nu_z^2}{2\nu_c} = \frac{U}{4\pi Bd^2} \quad (2.9)$$

Therefore the magnetron excitation does not depend on the mass at first order. Ions inside the trap are excited until the radius of their trajectory inside the trap is larger than the exit aperture (so they would all crash if extraction were attempted). Then a quadrupole excitation is applied at the free space cyclotron frequency  $\nu_c = \nu_+ + \nu_-$ . At this frequency (also called the sideband frequency or the coupling frequency) the magnetron motion can be converted in reduced cyclotron motion by resonant excitation. Unlike the magnetron excitation, the cyclotron excitation is very mass-selective, so only ions of the right  $\frac{m}{q}$  ratio have their motion converted into reduced cyclotron. While ions are losing energy in the cooling gas, the radius of the reduced cyclotron motion gets smaller and the radius of the magnetron motion gets bigger [40]. However the gas pressure and the amplitude of the quadrupolar excitation are chosen so the magnetron radius shrink due to motion conversion for the selected species is faster than the magnetron radius blow-up. By applying the excitation for an appropriate time, it is possible to recenter only the chosen  $\frac{m}{q}$  ratio with a very high resolution before extraction. Resolving powers of a few  $10^5$  have been obtained for trapping times of  $\sim 5 * 10^{-1}$  s. With the buffer gas, the trapping time is limited by the damping of the trapped bunch.

The mass measurement mode is somewhat similar, except for the very low pressure ( $10^{-8}$  mbar) which allows longer trapping time. Like for the purification mode, the ions are excited at the magnetron frequency and their motion is then converted by a quadrupolar excitation at cyclotron



frequency. The excitation time is calculated to match one full conversion from magnetron to reduced cyclotron motion for the ions excited at the exact cyclotron frequency. Ions whose cyclotron frequency is slightly different from the RF frequency have their motion only partially converted to the reduced cyclotron motion. Therefore, the radial energy of the ions depends on their  $\frac{m}{q}$  ratio. Upon extraction, the ions experience a strong magnetic field gradient with a component perpendicular to the beam axis. Because of this they experience an axial acceleration depending on their radial motion. The  $\frac{m}{q}$ -dependent time-of-flight is measured by a detector at the exit of the trap. By varying the frequency of the RF excitation, one can plot a ToF vs frequency plot and observe resonances at very precise frequencies from which the mass can be deduced. This method is referred to as the ToF-ICR technique. In this mode the resolving power can reach up to  $10^7$  for extended trapping times ( $\sim 10$  s) and the mass uncertainty can be lower than  $10^{-8}$ . The long trapping time can be a limiting factor for mass measurement of radioactive isotopes. In this mode, especially for long flight times, the spectrometer is extremely sensitive to the Coulomb interaction between the ions inside the trap. Reducing the contamination is therefore crucial. In order to partially address this issue, one can use a two-stages Penning trap with a purification trap to remove the isobaric contamination and a precision trap for precision mass spectrometry and mass measurement. This double Penning trap system was pioneered at ISOLDE with ISOLTRAP, and inspired other comparable apparatus such as SHIPTRAP at GSI, TITAN at TRIUMF and MLL-trap and PIPERADE for the DESIR setup at SPIRAL2.

### Time-of-Flight spectrometers

The underlying principle of time-of-flight mass spectrometry is probably one of the simplest of all types of mass spectrometry. Ions (or other charged particles) are initially accelerated under a potential  $U$  at the kinetic energy  $K = qU$ . The ToF needed for the ions to travel a certain distance  $D$  in a field-free region is:

$$T = \frac{D}{v} = D \sqrt{\frac{m}{2qU}} \quad (2.10)$$

The ToF is indeed mass-dependent. This also makes sense from an inertial point of view as heavier ions will be slower than the lighter ones. As this technique requires a time reference, it cannot be used with a continuous beam. The ToF is measured as a *STOP* – *START* difference, where the *STOP* is the detection time of the ions and the *START* is usually the time of acceleration of the bunch. The resolving power of any ToF based spectrometer is given by:

$$R = \frac{m}{\Delta m} = \frac{T}{2\Delta T} \quad (2.11)$$

It should be emphasised that  $\Delta m$  is more a statistical spread in the measurement of  $m$  due to the statistical spread in ToF than a spread in  $m$  itself. A slight mass spread does exist, owing to the different energy of ions of same rest mass, but is very small:  $\sim 1$  per  $A 10^8$  for a ion of  $A$

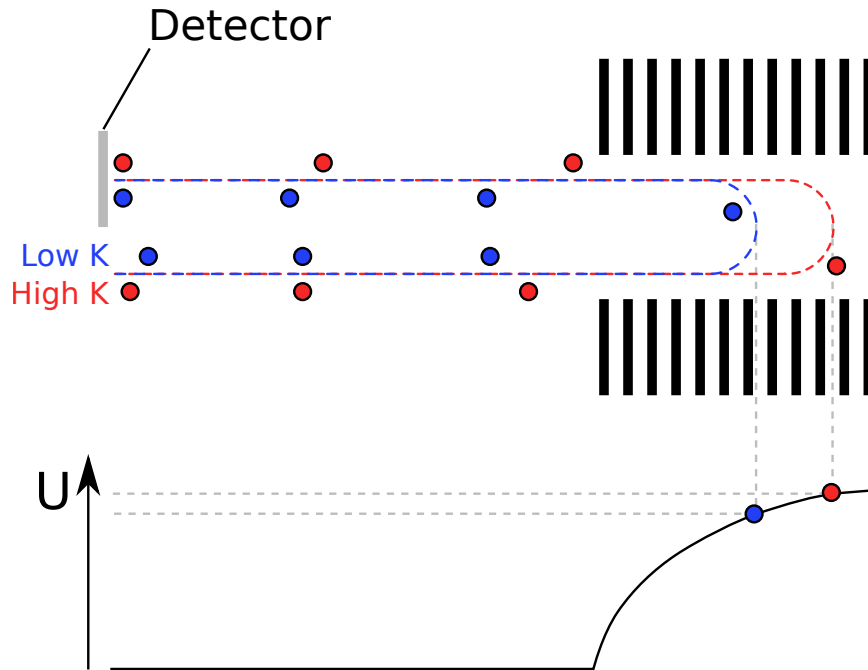


Figure 2.3 – Principle of operation of the reflectron.

nucleons with an energy spread of 10eV and an energy in the keV range. ToF spectrometers are essentially limited by the kinetic energy dispersion of the ions as:

$$(\Delta T)^2 = (\Delta T_0)^2 + \left(\frac{T}{2K} \Delta K_0\right)^2 \quad (2.12)$$

Where  $\Delta T_0$  is the part of the time dispersion uncorrelated to the energy dispersion. Therefore, the resolving power in a pure drift section is practically limited to  $R < \frac{K}{\Delta K_0}$ , i.e. a few  $10^2$ . This  $K$  dispersion takes its origins in the bunch acceleration. In low energy applications, the bunch is accelerated through a potential gradient. Due to the inevitable dispersion in position at the time of the acceleration, ions closer to the exit of the acceleration field are accelerated less than those deep in the potential gradient.

The reflectron [30] solves the problem by giving an energy-dependent delay to the ions of the bunch. The reflectron is an electrostatic mirror consisting of several blades of different potentials (see Fig. 2.3). The ensemble creates a very precisely defined potential gradient inside the mirror. Ions of higher energy go deeper inside the mirror and have a higher turning-back time than ions of lower energy. The potentials are defined to reach a ToF focus on a precise plane. The shape of the potential and its amplitude matter. For example a potential with a quadratic dependance to axis position would not induce any mass-dependent delay (case of the harmonic oscillator).

The resolving power of a ToF spectrometer with a reasonably-sized drift section is less than  $10^3$  without a reflectron and  $10^4$  with one. Assuming we are able to create a ToF-focus plane regardless of the ToF, then the dispersion in energy, initial position and initial direction are not factors

limiting the resolving power anymore. Indeed, the resolving power in free space can be expressed using Eq. 2.12 as:

$$R = \frac{1}{\sqrt{\left(\frac{\Delta K_0}{K}\right)^2 + \left(\frac{2\Delta T_0}{T}\right)^2}} = \frac{T}{2\sqrt{\Delta T_s^2 + \Delta T_0^2}} \quad (2.13)$$

Where  $\Delta T_s$  is the increase of ToF dispersion that occurs during a drift of duration  $T$  at energy  $E$  with an energy dispersion  $\Delta E$ . The reflectron induces an energy-dependent delay that compensates exactly  $\Delta T_s$ , cancelling the overall ToF dependency to the energy. This means that as long as we have a perfect ToF-focus at the position of the detector, the resolving power increases almost linearly with the time of flight (or the distance). This is of course a first order approximation and resolving power eventually meets second order limitations. The simplest solution then consists in increasing the flight path to increase the ToF. In nuclear physics, the resolving power necessary to separate most isobars ranges from a few  $10^3$  to several  $10^5$ . Assuming an initial ToF bunchwidth of 50 ns (at FWHM), a bunch of mass 40 ions at 2 keV, the distance needed to reach  $R = 10^5$  is  $\simeq 1000$  m. Thus there is no choice but to fold the ion path in an ion trap to obtain the highest resolving powers. This can be done in low energy traps or pseudo-traps as the ones discussed in [41] and shown in Fig. 2.4. At high energy, long apparati [42] and even traps [43] dedicated to time of flight spectrometry have also been reported.

Among ToF traps, the Multi-Reflection Time-of-Flight Mass Spectrometer (MR-ToF-MS) is a rather simple yet effective trap that has met increasing popularity since its introduction by Wollnik and Przewłoka in 1990 [44].

## 2.2 MR-ToF-MS

The main work of this thesis is the simulation, design, construction and test of the PILGRIM MR-ToF-MS. The following introduces the basic concepts associated with this technique. An overview of MR-ToF spectrometry can be found in [41].

### 2.2.1 Principles

**Geometry of the trap:** The Laplace law in vacuum  $\Delta V = 0$  forbids static trapping of charged particles by purely electrostatic fields. However it theoretically allows static trapping by oscillating electric fields and dynamic trapping by electrostatic fields. The MR-ToF-MS is a linear ion trap in which ions maintain a stable trajectory by bouncing back and forth between 2 electrostatic mirrors. These mirrors are reflectron-like arrangement of electrodes aiming to achieve a ToF focus on the detection plane. Between the mirrors lies a middle field-free section where the ToF separation takes place (see Fig. 2.6-top). The apparatus is also equipped with focussing elements to maintain the stability of the ions. In all existing prototypes, either an additional lens electrode or one or several electrodes of the mirrors are set at a strongly accelerative potential. The number

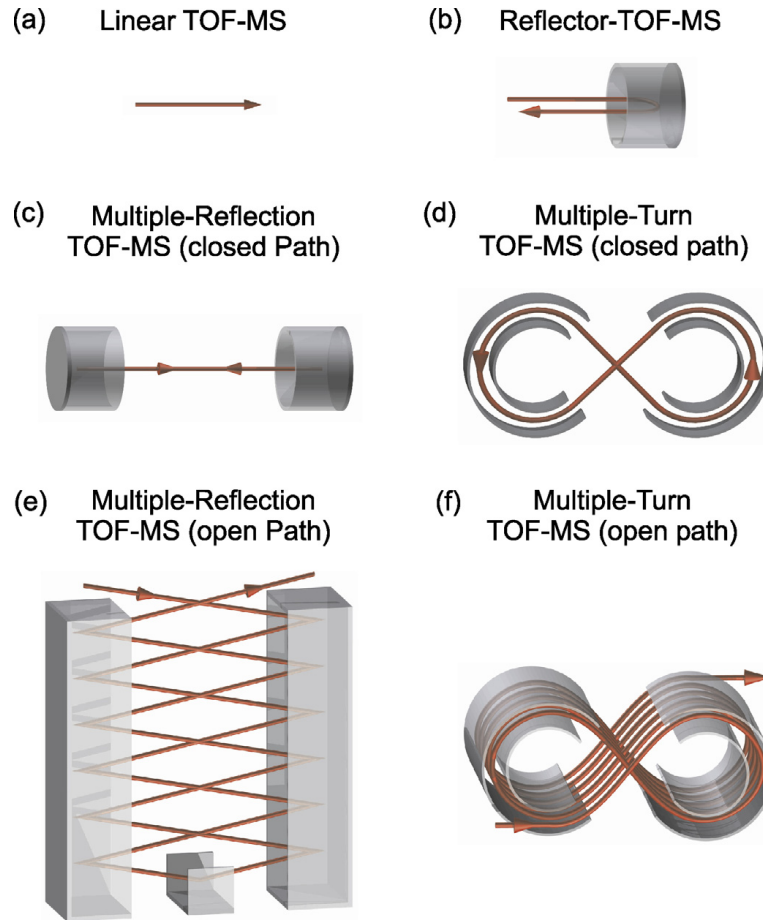


Figure 2.4 – Several types of low energy folded path ToF spectrometer. In trap ToF spectrometers (c,d), there is no real limit to the flight path, but the mass range that can be analysed in one cycle is limited by the opening time-window of the trap, and the trapping time itself. This problem is solved in open path spectrometers (e,f) at the expense of the maximum flight path. See [41] and reference therein for more details.

of mirror electrodes and the symmetry of the potentials vary from one prototype to the other.

**Vacuum:** The spectrometer requires a very good level of vacuum due to the very long flight path of the ions inside the trap (up to several kilometers). Taking a simple kinetic description, the mean free path of an ion in vacuum can be expressed as:

$$l = \frac{k_B T}{\sqrt{2} \pi d^2 P} \quad (2.14)$$

With  $k_B$  the Boltzmann constant,  $T$  the temperature,  $P$  the pressure (in Pa) and  $d$  the kinetic diameter of a gas molecule. Taking  $T = 300$  K and  $d = 350$  pm (gross average for atmospheric air), the mean free path is  $l = 0.0072/P$ . Therefore, a vacuum of at least  $5.10^{-8}$  mbar is necessary to achieve a mean free path of 1.4 km. Assuming a classic exponential decay of the efficiency with the flight path, pressures of  $10^{-8}$  mbar or below are necessary to reach the km range while losing less than 10% of the beam by collision. As we enter the domain of ultra-high vacuum, high-level vacuum systems involving CF standard, differential pumping and second

stage turbo-molecular pumps are required.

**Potential and mechanical stability:** The HV sources connected to the mirrors must have a very high stability. Fast variations ( $> 0.1$  Hz) of the voltage supply limit the resolving power while slow variations would affect the repeatability of the results and hence complicate mass measurement applications. Indeed, the ToF after trapping depends on the potential of the mirror electrodes, especially those near the ions turning back point. For example in [45] the ToF varies with the potential of a specific electrode by 0.5 ppm for a variation of 1 ppm on the voltage. This means that a jitter of 10 ppm on this voltage supply ( $\sim 0.02$  V) limits  $R$  to  $\sim 10^5$ . Furthermore, it has been reported that the ToF to the detector changes with the temperature either because the voltage supplies are temperature-sensitive [45, 46] or because it induces thermal expansion in the spectrometer itself [47].

**Beam preparation:** The formation of the bunch plays a crucial role in the final resolving power of the spectrometer. The ToF bunchwidth must be as low as possible as it directly impacts the resolving power, and the dispersions of this bunch in energy, position and direction must be as low as possible to minimise the optical aberrations. Transverse and longitudinal emittances both impact the final resolving power, and a high transverse emittance reduces the trapping efficiency. It has been noticed that this efficiency rapidly drops in the first few hundred turns then remains quite stable [45, 48], though the MR-ToF device of RIKEN seems to avoid this effect [49]. This behaviour does not match the expected exponential drop of the efficiency due to the imperfect vacuum and most likely shows the acceptance limits of such devices at a large number of turns. Several techniques have been developed to create high quality bunched beams with low transversal and longitudinal emittances [50]. The most widely used of these techniques is to accumulate and cool the ions in a gas filled linear RFQ trap also called RFQ Cooler-Buncher (RFQCB). The RF potential is constant on the full length of the trap and ensures transversal trapping, while the DC potential forms a well to trap the ions in the axial direction. This position-dependent DC potential is achieved by using either segmented electrodes to which the potential  $U_{DC}(x) + V_{RF}(t)$  is applied (e.g. [51, 52]) or a combination of RF-only rods and segmented DC blades (as in [53]). Once the ions have been cooled, the DC potential on the exit side is lowered to free the so-formed ion bunch. A pulsed drift tube can be added behind the RFQCB to bring the ions to the chosen energy (see Fig. 2.5). The transverse emittance at the exit of such a trap is  $\epsilon_{95\%} \sim 2 - 8 \pi$ .mm.mrad and the ToF and energy dispersions are expected to be around 50 ns and 15 – 20 eV at FWHM, respectively. More advanced RFQ traps have shown bunchwidths of 20 ns [54] and even less than 10 ns [49] at ToF-focus (FWHM values).

We define here the incompressible time  $\Delta t_{inc}$  as the part of the ToF dispersion which is not correlated to the energy or the geometric parameters and thus cannot be corrected in any static field. In any bunching technique based on a pulsed dipolar acceleration field,  $\Delta t_{inc}$  is due to the velocity

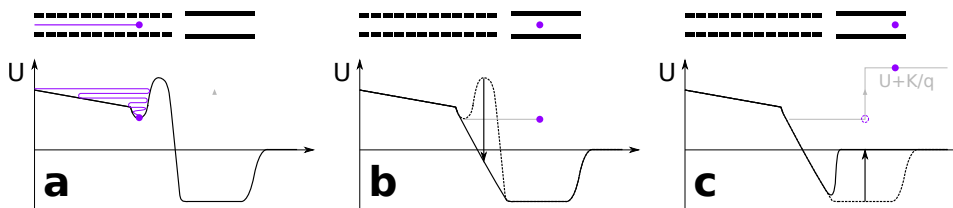


Figure 2.5 – Schematic overview of a RFQCB and a pulsed drift tube for bunch preparation with the associated voltage pulsing. **a**: cooling of the ion in the buffer gas. **b**: ejection of the bunch. **c**: Increasing the energy in a pulsed drift tube.

spread in the direction of the acceleration field at the time of ejection. Indeed the ions with an initial momentum opposite to the acceleration field at the switching time first need to turn around before being accelerated. In the case of the RFQ-Cooler-Buncher, this velocity spread is due to the residual energy of the ions in the cooling trap. As a first approximation in the RFQCB, the energy spread after acceleration depends on the linear position dispersion at the time of the ejection and the acceleration field, while the incompressible time depends on the acceleration field and the momentum of the ions (see for example [52]):

$$\Delta t_{inc} = \frac{m\Delta v}{qE_{acc}} \quad (2.15)$$

$$\Delta K = qE_{acc}\Delta z \quad (2.16)$$

Where  $v$  and  $z$  are the axial speed and position of the ions in the RFQCB just before extraction. As the ToF spread due to the incompressible time cannot be corrected by any electrostatic field,  $\Delta t_{inc}$  limits the minimum ToF bunchwidth and thus the maximum resolving power. The two previous equation show that one could obtain a reduced  $\Delta t_{inc}$  at the expense of an increased  $\Delta K$ .

**Important note:** What we call incompressible time throughout this report is referred to as "turn-around time" in [52] and several other publications, following the initial notation of Wiley [55]. However we found this notation confusing here, as in the case of the MR-ToF-MS the ions do turn around many times. Thus we will use the expression "turn around" to describe the reflections of the ions in the mirrors and will keep the notation "incompressible time" to refer to the minimal achievable bunchwidth at ToF focus.

**Injection/Ejection:** In order to be trapped the ions must have a kinetic energy below the maximum potential of the mirrors :  $K < qU_{max}$ . However, they also need to cross the mirror's potential for the injection/ejection phases. In order to achieve both, two solutions have been used (see Fig. 2.6-bottom) :

**I.** The potential of one [47, 46] or several [52, 56] electrodes of the mirrors can be switched down to let the ions go inside the spectrometer, then up for trapping and down again for ejection. This case requires switching the potentials of all the electrodes of the mirror at once, which is not much of a constraint if all potentials are defined by a single voltage supply and a resistor bridge [57].

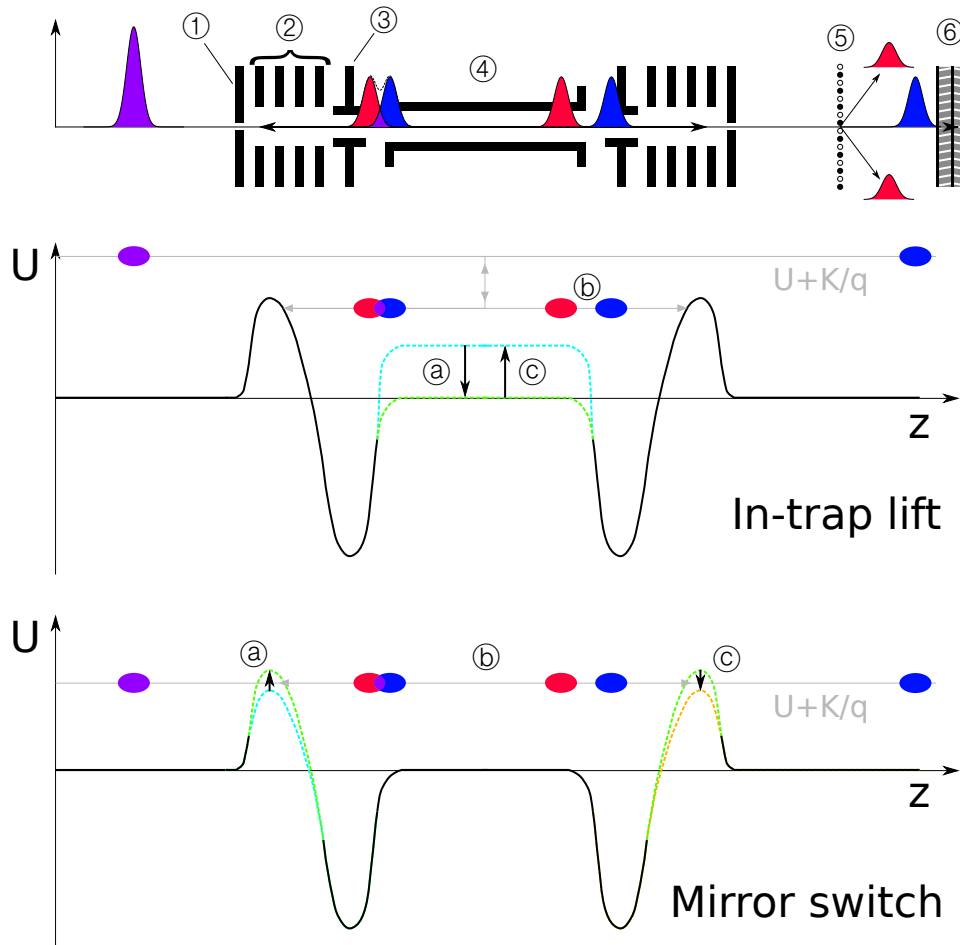


Figure 2.6 – **Top:** typical layout and operation of an MR-ToF-MS apparatus. **1:** end mirror. **2:** mirror electrodes. **3:** Einzel-lens (to keep the bunch focused in the trap). **4:** Pulsed drift-tube. **5:** Bradbury-Nielsen Gate. **6:** Micro-Channel Plate. **Bottom:** the two injection principles are represented by the two potential curves. The colors represent the potentials that are switched, both before and after the switch. The grey lines represent the total mechanical energy (kinetic + potential) of the ions, normalised by  $q$ . **a:** trapping. **b:** separation. **c:** ejection.

**II.** The ions are injected with an energy higher than the potentials of the mirrors  $K > qU_{max}$ . The middle section, consisting of a drift tube, is pulsed at ground potential when the ions reach the middle of the device. This lowers the potential energy of the ions so their re-acceleration in the lens is not sufficient to go through the mirrors [58]. Upon ejection, the pulsed drift tube's voltage is brought back to its high value, which gives back energy to the ions and allows them to leave the trap.

The first method allows injection and ejection of a wider mass range, but requires extremely advanced voltage supplies on the mirrors capable of being switched at  $10^2 - 10^3$  Hz while maintaining a high voltage stability. With the second method however, the potential of the drift tube only affects the energy of the ions inside the trap. The voltage stability of this supply is therefore not critical, if limited to a few  $10^{-1}$  V, i.e. for variations of energy 100 times smaller than the energy spread itself.

**Gate and detection:** In case the spectrometer needs to achieve not only

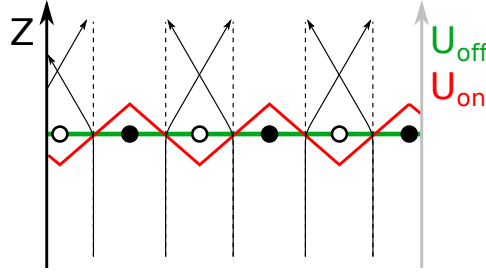
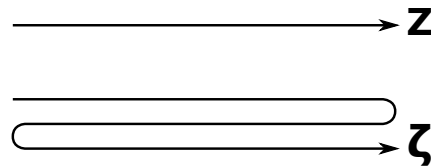


Figure 2.7 – Principle of operation of a Bradbury-Nielsen Gate. Shows the trajectories of the ions when the gate is off (dashed lines, green potential) or on (full lines, red potential).

isobaric separation but also purification, e.g. for subsequent injection into a Penning trap, a fast beam-cutting gate has to be installed after the spectrometer. Classic electrostatic dipolar deflectors effectively cut the beam at low-energy, but have a large spatial range which is not suited for the selection of one isobar among others. The Bradbury-Nielsen Gate (BNG) [59] is a planar arrangement of parallel wires perpendicular to the beam axis. When the gate is powered, the wires are alternately at positive and negative potential. The ions near the wires therefore experience a strong deflecting field and end up crashing onto the walls (see Fig. 2.7). However at distances  $D > 2d$ ,  $d$  being the wire spacing, the field becomes almost negligible. The time resolution of the gate at ion speed  $v_i$  is given by  $\tau = 2d/v_i$  [45]. This gate is therefore very time-selective and is used in most setups [60, 45, 46, 61, 62]. The ion detection is performed with a Micro-Channel Plate (MCP). These detectors consist of one or several slabs with a very dense array of microscopic tubes, the micro-channels. Because of the high potential difference between the front and rear end of the slab(s), any ion entering a micro-channel triggers an electron avalanche. Because of the layout of the micro-channel array, the geometric efficiency of such detectors is typically  $\sim 50\%$ .

### 2.2.2 Theory

The ion-optics theory of MR-ToF devices has already been studied in many publications [44, 57, 63, 64, 65, 66]. We first define the notations of any optical system. Let  $z$  be the optical axis and  $\zeta$  the curvilinear axis following the path of a reference ion perfectly aligned on the optical axis  $z$ . The difference between  $z$  and  $\zeta$  is that  $\zeta$  is the coordinate of an axis which can be folded and as such will have a different value for a different number of turns in a trap. We define  $x$  and  $y$  the coordinates of an arbitrary ion in the plane perpendicular to the  $\zeta$ -axis, as well as  $a = \frac{dx}{d\zeta}$  and  $b = \frac{dy}{d\zeta}$ , the slopes of this ion in the planes  $(x, \zeta)$  and  $(y, \zeta)$ , respectively. The reference ion has a mass  $m_r$ , an energy  $K_r$  and crosses a given plane  $\zeta = Z$  at the time  $t_r$ . The energy  $K_r$  is chosen to be the mean energy of a bunch with a realistic energy spread. Likewise, the arbitrary ion has a mass  $m$ , and energy  $K$  and crosses the same plane at the time  $t$ . We define the relative energy and ToF of the arbitrary ion as:





$$\delta_K = \frac{K - K_r}{K_r} \quad \delta_t = \frac{t - t_r}{t_r} \quad (2.17)$$

The position of any ion in the 6-dimensional phase space is given by  $\Phi = (x, a, y, b, \delta_K, \delta_t)$ . Other systems of coordinate can be equivalently defined, e.g.  $(x, a, y, b, \delta_p, \delta_\zeta)$  or  $(x, a, y, b, \delta_{p_z}, \delta_z)$ . One can notice that under all these conditions, the reference ion is defined by  $x_r = y_r = a_r = b_r = \delta_{K,r} = \delta_{t,r} = 0$ , i.e. the origin of the phase space. Let  $A$  be the transfer function of an optical system (magnetic sector, electric sector, drift section, RF-field ...) and  $\zeta_0$  and  $\zeta_1$  the  $\zeta$ -positions just before and just after this system, respectively. We have:

$$\Phi(\zeta_1) = A(\Phi(\zeta_0)) \quad (2.18)$$

And by definition :  $\Phi_r(\zeta_1) = \Phi_r(\zeta_0)$ . Let us temporary rename the phase space coordinate vector in  $\Phi = (\phi_1, \phi_2, \phi_3, \phi_4, \phi_5, \phi_6)$  for the sake of the unicity of the following equation. Each coordinate  $\phi_{i,1}$  at the coordinate  $\zeta_1$  can be expressed as a function of the  $\phi_{i,0}$  at the coordinate  $\zeta_0$  by means of expansion into Taylor series:

$$\begin{aligned} \phi_{i,1} = & \sum_{j=1}^6 (\phi_i | \phi_j) \phi_{j,0} + \frac{1}{2} \sum_{j=1}^6 \left\{ \sum_{k=1}^6 (\phi_i | \phi_j \phi_k) \phi_{j,0} \phi_{k,0} \right\} \\ & + \frac{1}{6} \sum_{j=1}^6 \left\{ \sum_{k=1}^6 \left\{ \sum_{l=1}^6 (\phi_i | \phi_j \phi_k \phi_l) \phi_{j,0} \phi_{k,0} \phi_{l,0} \right\} \right\} \quad (2.19) \\ & + \dots \end{aligned}$$

where

$$(\phi_i | \phi_j) = \left( \frac{\partial \phi_{i,1}}{\partial \phi_{j,0}} \right)_{\phi_{j,0}=0} \quad (2.20)$$

$$(\phi_i | \phi_j \phi_k) = \left( \frac{\partial^2 \phi_{i,1}}{\partial \phi_{j,0} \partial \phi_{k,0}} \right)_{\phi_{j,0}=\phi_{k,0}=0} \quad (2.21)$$

$$(\phi_i | \phi_j \phi_k \phi_l) = \left( \frac{\partial^3 \phi_{i,1}}{\partial \phi_{j,0} \partial \phi_{k,0} \partial \phi_{l,0}} \right)_{\phi_{j,0}=\phi_{k,0}=\phi_{l,0}=0} \quad (2.22)$$

Depending on the optical system, some relations between the coefficients of the Taylor series may arise. In the case of the MR-ToF-MS, let us consider the optical system to be one revolution inside the spectrometer. First the kinetic energy does not change, meaning  $(\delta_K | \delta_K) = 1$  and  $(\delta_K | \phi_j \dots) = 0$ . The whole MR-ToF apparatus has a cylindrical symmetry implying that:

**I.** The  $x$  and  $y$  axes are equivalent. We can narrow the description of the optics to the set of parameters  $(x, a, \delta_K, \delta_t)$ . In addition, the planes defined by  $(x, a)$  and  $(y, b)$  are independent and all terms of the Taylor expansion that mix parameters of these planes (e.g.  $(\dots | xy)$  or  $(\dots | xxb)$ ) vanish.

ii. Because of the cylindrical symmetry, all odd order derivatives of  $\delta_t$  with respect to  $x$  or  $a$  or both are zeroed, i.e.  $\frac{\partial^{i+j}\delta_t}{\partial x^i \partial a^j} = 0$  if  $i+j$  odd. Therefore, the first order expansion of the relative ToF is simply:  $\delta_{t,1} = \delta_{t,0} + (\delta_t|\delta_K)\delta_{K,0}$ .

At first order, the transfer function of the MR-ToF spectrometer (1 turn) can be expressed by a transfer matrix:

$$\begin{pmatrix} x_1 \\ a_1 \\ \delta_{K,1} \\ \delta_{t,1} \end{pmatrix} = \begin{pmatrix} (x|x) & (x|a) & (x|\delta_K) & 0 \\ (a|x) & (a|a) & (a|\delta_K) & 0 \\ 0 & 0 & 1 & 0 \\ 0 & 0 & (\delta_t|\delta_K) & 1 \end{pmatrix} \begin{pmatrix} x_0 \\ a_0 \\ \delta_{K,0} \\ \delta_{t,0} \end{pmatrix} \quad (2.23)$$

It is possible to tune the geometry and the potentials of the mirrors to achieve the so-called "point-to parallel" conditions [65], i.e. a point like source will give a parallel beam after 1 reflexion (1/2 turn) and vice-versa. This is translated mathematically by:

$$B_{1/2} = \begin{pmatrix} 0 & -\alpha \\ \frac{1}{\alpha} & 0 \end{pmatrix} \quad (2.24)$$

where  $B_{1/2}$  is the upper-left part of the total transfer matrix  $A$  for 1/2 turn, and  $\alpha = -(x|a) = 1/(a|x)$ . For one full turn:  $B = B_{1/2}^2 = -I_2$ . This also means that such device rotates the emittance profile by  $\frac{\pi}{2}$  at each reflexion. In addition, assuming that the mirrors can be tuned to achieve a laterally achromatic system after one turn, we have  $(x|\delta_K) = (a|\delta_K) = 0$  [44]. Under all these conditions, we have at first order:

$$x_n = (-1)^n x_0 \quad (2.25)$$

$$a_n = (-1)^n a_0 \quad (2.26)$$

With  $n$  the number of turns. Assuming reasonably that the initial distribution of the ions in  $x$  and  $a$  is symmetric, this means that the purely geometrical part of the beam is invariant by an integer number of turns at first order. In [65], further considerations allow to fulfil the achromaticity at second order as well, but this is not the case for the present work. This arrangement allows one to inject the ions at one end of the spectrometer and eject them at the other end, while approximately conserving their transverse emittance profile. This 4-fold symmetry of the emittance causes some oscillations in the transmission efficiency [49] and resolving power [67]. However if one wishes to inject and eject the ions at the same end or to choose the ejection side, the following solution can be envisioned: if we manage to tune the mirrors so the emittance doesn't rotate by  $\frac{\pi}{2}$  but by  $\frac{\pi}{3}$ , i.e. the transfer matrix is:

$$B_{1/2} = \begin{pmatrix} \cos\frac{\pi}{3} & -\alpha \sin\frac{\pi}{3} \\ \frac{1}{\alpha} \sin\frac{\pi}{3} & \cos\frac{\pi}{3} \end{pmatrix} \quad (2.27)$$

Then the emittance is reversed by 1.5 turns in the MR-ToF, and invariant by 3. This means it is possible to eject the ions at the injection end after  $\frac{3}{2} + 3n$  turns or at the opposite end after  $3n$  turns without changing the emittance profile at first order.

The conservation of the emittance profile after a given number of turns finds its interest in the final efficiency of the MR-ToF device. Of more primary importance are the conditions of ToF-focus. The  $\delta_t$  after one reflexion can be expressed up to the third order as:

$$\begin{aligned}
\delta_{t,1/2} = & \delta_{t,0} + (\delta_t|\delta_K)\delta_{K,0} + \frac{1}{2}(\delta_t|\delta_K\delta_K)\delta_{K,0}^2 + \frac{1}{6}(\delta_t|\delta_K\delta_K\delta_K)\delta_{K,0}^3 \\
& + \frac{1}{2}(\delta_t|xx)x_0^2 + \frac{1}{2}(\delta_t|ax)a_0x_0 + \frac{1}{2}(\delta_t|aa)a_0^2 \\
& + \frac{1}{2}(\delta_t|yy)y_0^2 + \frac{1}{2}(\delta_t|by)b_0y_0 + \frac{1}{2}(\delta_t|bb)b_0^2 \\
& + \frac{1}{6}(\delta_t|xx\delta_K)x_0^2\delta_{K,0} + \frac{1}{6}(\delta_t|ax\delta_K)a_0x_0\delta_{K,0} + \frac{1}{6}(\delta_t|aa\delta_K)a_0^2\delta_{K,0} \\
& + \frac{1}{6}(\delta_t|yy\delta_K)y_0^2\delta_{K,0} + \frac{1}{6}(\delta_t|by\delta_K)b_0y_0\delta_{K,0} + \frac{1}{6}(\delta_t|bb\delta_K)b_0^2\delta_{K,0} \\
& + \dots
\end{aligned} \tag{2.28}$$

other first, second and third degree contributions vanish either due to the aforementioned symmetry conditions, or because all derivatives with respect to  $\delta_{t,0}$  but the first must be equal to zero. In [65], the mirrors were optimised to suppress the geometrical dependencies up to second order and the pure energy dependency up to third order to minimise the ToF spread due to any source. However we will see that in our case, it is interesting to keep a linear dependency of the ToF to the energy. By limiting the problem to the second order, the relative ToF after  $N$  reflexions (or  $N/2$  turns) is:

$$\begin{aligned}
\delta_{t,N/2} = & \delta_{t,0} + N \left( (\delta_t|\delta_K)\delta_{K,0} + \frac{1}{2}(\delta_t|\delta_K\delta_K)\delta_{K,0}^2 \right) \\
& + \frac{1}{2} \sum_{i=0}^{N-1} \left\{ (\delta_t|xx)x_{i/2}^2 + (\delta_t|ax)a_{i/2}x_{i/2} + (\delta_t|aa)a_{i/2}^2 \right. \\
& \left. + (\delta_t|yy)y_{i/2}^2 + (\delta_t|by)b_{i/2}y_{i/2} + (\delta_t|bb)b_{i/2}^2 \right\} + \dots
\end{aligned} \tag{2.29}$$

Assuming now that the emittance profile rotates with each reflexion and is left unchanged at first order by  $M$  reflexions, we can choose  $N$  as a multiple of  $M$ . Under this assumption, all geometric parameters become periodic with a period of  $M$  half-turns, i.e.  $x_{(i+M)/2} = x_{i/2}, \dots$ . We then define the second order ToF aberration due to geometric considerations,  $\delta_{t,G1/2}$ , as the average geometric aberration for 1 reflexion, knowing the geometric aberration for  $M$  reflexions:

$$\begin{aligned}
\delta_{t,G1/2} = & \frac{1}{M} \sum_{i=0}^{M-1} \left\{ (\delta_t|xx)x_{i/2}^2 + (\delta_t|ax)a_{i/2}x_{i/2} + (\delta_t|aa)a_{i/2}^2 \right. \\
& \left. + (\delta_t|yy)y_{i/2}^2 + (\delta_t|by)b_{i/2}y_{i/2} + (\delta_t|bb)b_{i/2}^2 \right\}
\end{aligned} \tag{2.30}$$

Then Eq. 2.29 becomes simply:

$$\delta_{t,N/2} = \delta_{t,0} + N \left( (\delta_t|\delta_K)\delta_{K,0} + \frac{1}{2}(\delta_t|\delta_K\delta_K)\delta_{K,0}^2 + \delta_{t,G1/2} \right) + \dots \quad (2.31)$$

as long as  $N$  is a multiple of  $M$ . In addition, in order to achieve the ToF focus at the detector plane, one has to take into account the flight from the RFQ Cooler-Buncher to the middle of the trap and the flight from the middle of the trap to the detector. We introduce  $\delta_{t,RFQ}$  and  $\delta_{t,MCP}$  the relative ToF after the ejection of the RFQCB and at the detection plane, respectively. We have at second order:

$$\delta_{t,RFQ} = \delta_{t,inc} + (\delta_t|\delta_K)_{RFQ}\delta_{K,0} + \frac{1}{2}(\delta_t|\delta_K\delta_K)_{RFQ}\delta_{K,0}^2 + \dots \quad (2.32)$$

$$\delta_{t,0} = \delta_{t,RFQ} + (\delta_t|\delta_K)_i\delta_{K,0} + \frac{1}{2}(\delta_t|\delta_K\delta_K)_i\delta_{K,0}^2 + \delta_{t,Gi} + \dots \quad (2.33)$$

$$\delta_{t,MCP} = \delta_{t,N/2} + (\delta_t|\delta_K)_e\delta_{K,0} + \frac{1}{2}(\delta_t|\delta_K\delta_K)_e\delta_{K,0}^2 + \delta_{t,Ge} + \dots \quad (2.34)$$

where  $\delta_{t,inc}$  is the relative time difference between the considered ion with a given momentum in the RFQ-trap at the time of extraction and an ion of reference which is at rest at the same time. We use the index *inc* as this time difference is the origin of the incompressible time spread  $\Delta t_{inc}$ . The other notations are the same as before, with the indexes *RFQ*, *i* and *e* referring to the ToF coefficients due to the RFQ, the beam line before injection in the MR-ToF spectrometer and the beam line after the ejection, respectively. Equations 2.31, 2.32, 2.33 and 2.34 simply state that the relative ToF at the end of a step (transport to the trap, trapping, transport to the MCP) is equal the relative ToF at the end of the previous step plus some kinetic and geometric aberrations. The overall relative ToF from the ejection of the bunch from the RFQCB to the MCP can be expressed as:

$$\delta_{t,MCP} = \delta_{t,inc} + \delta_{K,0}C_1 + \frac{\delta_{K,0}^2}{2}C_2 + \delta_{t,Gi} + \delta_{t,Ge} + N\delta_{t,G1/2} + \dots \quad (2.35)$$

With

$$C_1 = (\delta_t|\delta_K)_{RFQ} + (\delta_t|\delta_K)_i + (\delta_t|\delta_K)_e + N(\delta_t|\delta_K) \quad (2.36)$$

$$C_2 = (\delta_t|\delta_K\delta_K)_{RFQ} + (\delta_t|\delta_K\delta_K)_i + (\delta_t|\delta_K\delta_K)_e + N(\delta_t|\delta_K\delta_K) \quad (2.37)$$

By definition the geometric aberrations  $\delta_{t,G1/2}$ ,  $\delta_{t,Gi}$  and  $\delta_{t,Ge}$ , and the incompressible time  $\delta_{t,inc}$  are all independent with each other and with the relative energy  $\delta_{K,0}$ . Thus the ToF spread of an ions bunch is given by:

$$\begin{aligned} \left(\frac{\Delta t}{T_0}\right)^2 &= \frac{1}{T_0^2} \left\{ \Delta t_{inc}^2 \right. \\ &\quad + C_1^2(\Delta\delta_k)^2 + 2C_1C_2(\Delta\delta_k\delta_k^2)^2 + C_2^2(\Delta\delta_k^2)^2 \\ &\quad \left. + \Delta t_{Gi}^2 + \Delta t_{Ge}^2 + N^2\Delta t_{G1/2}^2 + \dots \right\} \end{aligned} \quad (2.38)$$

and

$$T_0 = T_i + T_e + NT_{1/2} \quad (2.39)$$

where  $T_i$ ,  $T_e$  and  $T_{1/2}$  are the ToF before injection, after ejection and for half a turn in the trap respectively, and  $T_0$  is the overall ToF. There is no cross correlation term in Eq. 2.38 because of the variable independence, except for the correlation between  $\delta_k$  and  $\delta_k^2$ , which varies with the mean of  $\delta_k$ . Eq. 2.38 and Eq. 2.39 enable several interpretations. First even assuming we are able to produce a perfectly energy isochronous ensemble at a high number of turns (i.e.  $C_1 = C_2 = 0$ ), the resolving power can be approximated by:

$$R \simeq \frac{T_{1/2}}{2\Delta t_{G1/2}} \quad (2.40)$$

This shows simply that the maximum  $R$  is eventually limited at high number of turns by the second order geometric aberrations. Higher orders, either purely geometric or mixed energy-geometric also affect  $R$  in lighter proportions. The ToF for which this maximum is obtained depends mainly on the ToF dispersion due to the incompressible time. Furthermore, the expression of  $C_1$  implies that we can change the position of the ToF-focus only by changing the energy of the ions inside the trap. This was suggested by Wolf and collaborators in [58] and tested in [68]. The idea is based on the fact that near the isochronic-trap configuration, i.e.  $(\delta_t|\delta_K) = 0$  inside the trap, the ToF vs energy plot is often shaped like a well (see Fig. 2.8), which is confirmed by simulations [65] and by experiments [68, 62] (we will see in the next chapter that other shapes are also possible). Thus by tuning the energy of the ions inside the trap, it is possible to tune the sign and even the amplitude of  $(\delta_t|\delta_K)$  in order to cancel  $C_1$ . Changing the in-trap ion energy is easily achieved in the case of the in-trap lift injection described earlier, as the mean energy of the ions inside the trap becomes completely decoupled from their mean energy outside the trap. This allows an easy control of the position of the ToF-focus by changing only the injection potential. This also means that it is possible up to a certain extent to find a ToF-focus for different number of turns. Indeed, one can change the number of turns inside the spectrometer, thus loosing the ToF-focus, then change the injection potential to find it back.

Eq. 2.38 and Fig. 2.8 also hint the limits of this technique. The first three parameters of  $C_2$  in Eq. 2.37 are very weak, meaning that if one wishes to reduce or even cancel  $C_2$ ,  $(\delta_t|\delta_K\delta_K)$  must be close to 0 as well, especially at high number of turns. However, a very small  $(\delta_t|\delta_K\delta_K)$  means that the position of the ToF focus is little sensitive to a change of injection potential. We can choose on the contrary to increase  $(\delta_t|\delta_K\delta_K)$  in order to enhance the sensitivity at the expense of the quality of the ToF-focus and thus the resolving power. A simple solution to this second order ToF aberration would be to reduce the kinetic energy spread. This is more efficient at the second order than at the first. For instance, if one divides all  $\delta_K$  by a factor  $a > 1$ , the second order contribution is reduced by  $a^2$ .

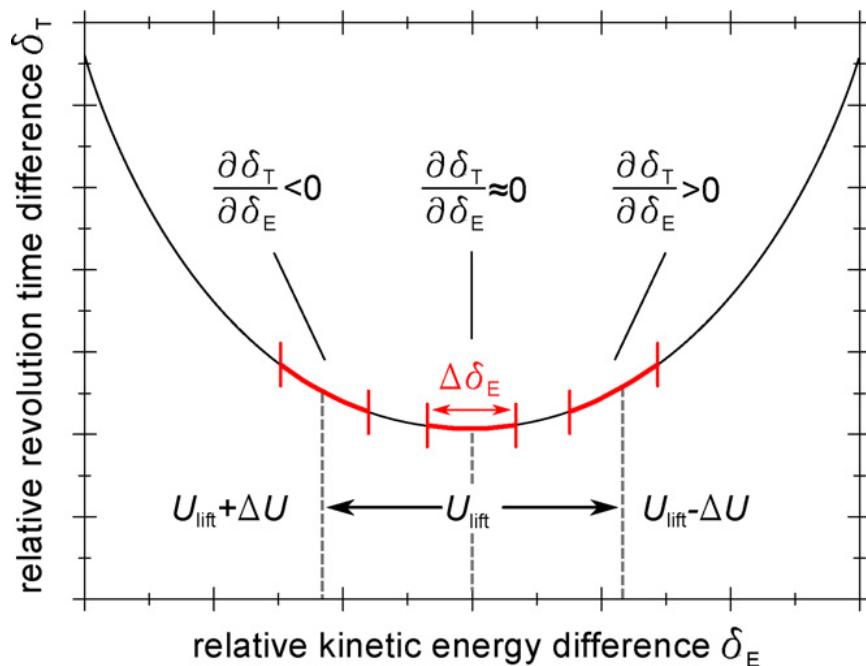


Figure 2.8 – Schematic example of the relative ToF dependency to the relative energy for one revolution. The first order ( $\delta_t|\delta_K$ ) coefficient can be tuned by changing the energy of the ions inside the trap. Figure from [58].

Equations 2.15 and 2.16 show that the ToF dispersion at the extraction of the RFQCB can be reduced at the expense of the energy dispersion and vice versa by changing the acceleration potential. If a high order of energy-isochronicity can be guaranteed at the position of the detector, a low ToF spread and high energy dispersion would be preferable. However, if the setup is only first-order energy-isochronic, a compromise has to be found between the initial ToF spread due to the incompressible time and the aforementioned second-order energy-dependent aberrations.

### 2.3 EXISTING DEVICES: USAGE AND PERFORMANCES

Sector mass spectrometers for high energy radioactive beams have achieved mass resolving powers of a few thousands and mass measurements with a precision  $\delta m/m$  of several  $10^{-6}$  when used in combination with ToF spectrometry for flight times of the order of the  $\mu s$  [42]. On the other hand the Schottky Mass-Spectrometry technique for high energy beams trapped in a storage ring have shown impressive resolving powers over  $10^6$  and mass precision down to  $\delta m/m = 2 \cdot 10^{-7}$  but electron cooling times of several seconds (see e.g. [69]). Similarly at low energy, Penning trap mass spectrometers achieve similar resolving powers and mass precisions for a trapping time ranging from hundreds of ms to seconds. The success of MR-ToF spectrometry over the last decade owes to the fact that it is a convenient compromise between high mass resolution and good mass precision on the one hand and low trapping time on the other hand, which is crucial for the study of short lived radioactive ions. A complete cycle from the production of a radioactive element to its ToF measurement after a MR-ToF device lasts a few tens of ms, and resolving powers of  $10^5$

and above have been reported in many articles. Though the Isochronic Mass Spectrometry (IMS) technique in storage ring achieves comparable performances for shorter times (high energy), MR-ToF devices are much cheaper and more compact. MR-ToF mass spectrometry has a higher resolving power than Penning Trap mass spectrometry for equal trapping time up to  $\sim 100$  ms. Performance comparisons of these 2 techniques are discussed in [68, 70]. In addition, such devices are single-particle sensitive, allowing study of exotic beams with very low intensity, either because of a fast decay or a low initial production rate. Fast and efficient beam purification and mass measurement will become crucial in the next generation of RIB facilities which will deliver more intense and exotic beams and also produce more contaminants.

MR-ToF-MS prototypes are already fully operational at the FRS ion-catcher/GSI in Darmstadt, Germany [52], at ISOLTRAP/ISOLDE/CERN in Geneva [68], Switzerland and at SLOWRI/RIBF/RIKEN in Wako, Japan [49]. New prototypes are also being developed or tested in most of the other major RIB facilities: at TITAN/TRIUMF in Vancouver (Canada) [61], at CARIBU/ANL in Argonne (USA) [62], in HRIBF/ORNL in Oak Ridge (USA), at the University of Notre Dame (USA) [67], at MLLTrap/MLL in Garching (Germany) and in RISP/RAON in Daejeon (South Korea) [56]. PILGRIM<sup>1</sup>, the MR-ToF-MS device discussed in the present work, will be installed at the low energy branch of the Super Separator Spectrometer (S3) at SPIRAL2/GANIL in Caen for isobaric separation and mass measurements. A copy of this spectrometer should also be built at the DESIR installation from SPIRAL2, also for isobaric purification. The spectrometer from GSI has been developed by the Justus-Liebig University in Gießen and was initially developed for FRS and the low energy branch of Super-FRS in the future Facility for Antiproton and Ion Research (FAIR). A duplicate of this MR-ToF-MS has been built for MLLTrap [71]. The spectrometer of TITAN, also based on the same design, was built and commissioned at Gießen as well. The prototype installed at ISOLDE has been designed, built and tested at Greifswald University [72] and inspired the work of Hirsh *et al* for CARIBU [62], Yoon *et al* for RISP [56] and Nicoloff *et al* and Schultz *et al* for the Notre Dame University [73, 67], as well as the present work.

A summary of the usage of the different spectrometers can be found in Tab. 2.1. Functional MR-ToF devices have been used on-line for mass spectroscopy, high resolution isobaric purification by coupling the spectrometer with a BNG and recently mass measurement of ground states of exotic nuclei. The MR-ToF-MS from FRS recently performed mass purification of both isobars and an isomer of the heavy  $^{211}\text{Po}$  nucleus (see ref. in table). In ISOLTRAP, the MR-ToF-MS is specifically used to perform an additional purification stage to facilitate precision mass measurements in the double Penning-Trap. It is intended to do the same for the MR-TOF-MS at TITAN with the MPET Penning trap, for the device at CARIBU with CPT and for the PILGRIM installation at DESIR with the double Penning Trap PIPERADE. The ISOLDE spectrometer has recently been used in

<sup>1</sup>Piège à Ions Linéaire du GANIL pour la Résolution des Isobares et la Mesure de Masse

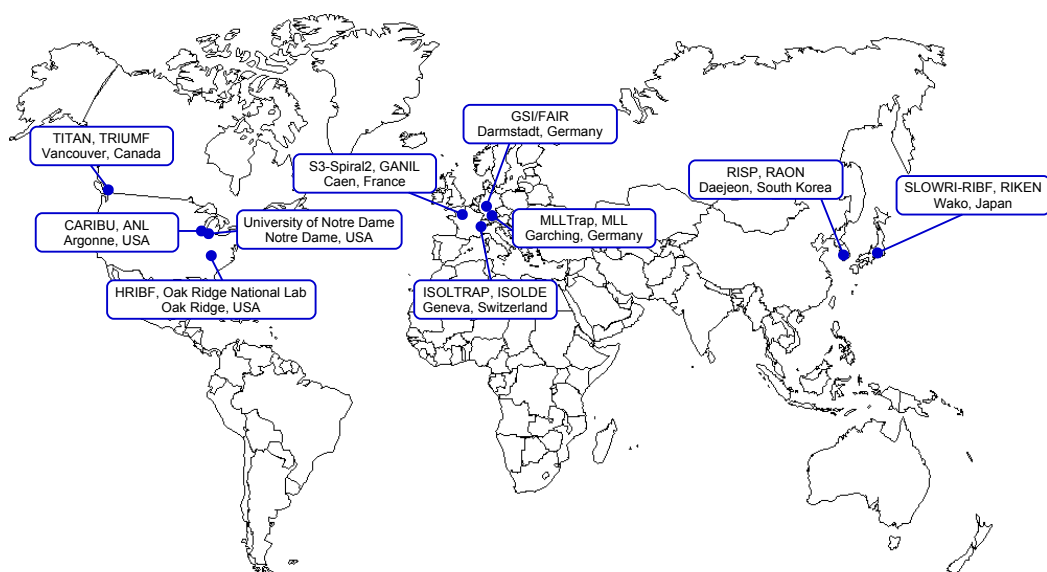


Figure 2.9 – The MR-ToF-MS worldwide. See text for citations and details.

Device	Status	Beam purification	Direct mass measurement		Max R
			Known	First time	
ISOLTRAP	On-line	yes [75, 8]	yes [76]	yes [8, 77, 76]	up to 300k [78]
SLOWRI	On-line	—	yes [9, 79]	planned	150k-200k [9]
GSI/FAIR/MLL	On-line	yes [80]	yes [52]	planned	up to 600k [52]
TITAN	Commissioned	planned		planned	50k
CARIBU	Commissioned	yes		planned	68k
HRIBF	Commissioned	planned		—	up to 110k [46]
UND	Designed	planned		—	130k
RISP	Simulated	planned		planned	110k
PILGRIM	In Commissioning	planned		planned	see next chapter

Table 2.1 – Usage of the different MR-ToF-MS prototypes. Citations are given when different from the ones in text. *Experimental* or *simulated* resolving powers of different facilities according to the recent literature are also given.

combination with ISOLTRAP's RFQCB to test the feasibility of lifetime measurements [74] for fast resolution of the isobars after trapping the decaying species of interest and its isobaric contaminants in the RFQCB.

In terms of optical design, the spectrometers from ISOLTRAP and SLOWRI and from the present work, have been optimised to reach ToF focus at the plane of detection by a MCP or mass separation by a BNG. The spectrometers from FRS, TITAN and CARIBU however have been optimised to achieve energy isochronicity of the trap itself. The spectrometer of FRS is equipped with a post analyser reflector, which is basically a reflectron. Thus the MR-ToF-MS can be isochronic and the energy-related ToF-spread due to the flight from the RFQ trap to the BNG in "shoot through" mode is simply compensated by the reflector. The spectrometer at TITAN has no reflector but the flight path from the RFQCB to the linear trap is very short. In this installation, isobars are not purified by a BNG but are selected by dynamic re-trapping of a resolved bunch into the



injection trap. Thus the path outside the spectrometer is twice the path from the injection trap to the middle of the MR-ToF-MS, which quickly becomes negligible for long flight path. The CARIBU spectrometer was only optimised this way to facilitate the optimisation procedure. However after optimisation, the potential of the pulsed drift tube was changed to move the position of the ToF focus at the detector plane.

## CHAPTER CONCLUSION

MR-ToF spectrometry has been successfully tested in three of the world's major RIB facilities over the past decade. Its reduced size and cost, simple usage and interpretation and its high measurement speed allowing spectrometry on short-lived radioactive ions made it a vanguard technique for the study of ground states and isomeric states of exotic nuclei. A new generation of MR-ToF-MS instruments are being built all over the world and will be used mainly for either direct mass measurement or beam purification for subsequent analyses, such as precision mass measurement in a Penning trap, laser spectroscopy, in-trap decay spectroscopy or contamination-free life-time measurement.

# SIMULATION AND DESIGN OF THE MR-TOF-MS PILGRIM

CONTENTS	
4.1	OBJECTIVES . . . . . 75
4.2	TEST SETUP AT LPC CAEN . . . . . 75
4.2.1	The ion source and its optics . . . . . 75
4.2.2	Vacuum system . . . . . 76
4.2.3	Electrical setup . . . . . 77
4.2.4	Timings . . . . . 78
4.2.5	Diagnostics and acquisition . . . . . 79
4.3	EXPERIMENT AND PARALLEL SIMULATIONS . . . . . 81
4.3.1	Beam tuning . . . . . 81
4.3.2	Bunching . . . . . 83
4.3.3	Beam characteristics and expected resolving power . . . . . 86
4.3.4	Shoot-through mode . . . . . 86
4.3.5	Trapping . . . . . 87
4.3.6	Measurement stability . . . . . 88
4.3.7	Search for the mass 40 doublet . . . . . 89
4.3.8	Towards higher resolving powers . . . . . 93
	CHAPTER CONCLUSION . . . . . 93

**T**HIS chapter describes the simulations, optimisations and mechanical design of PILGRIM. We explain how the geometry and potentials were chosen and modified to meet both the optical and mechanical requirements. An optical analysis of the final geometry using realistic beams is also given.



The PILGRIM spectrometer is largely based on the design from Greifswald university that has been developed for ISOLDE [72]. We use the same in-trap lift principle for injection/ejection from the trap, the same voltage sources, a comparable vacuum system and plan to build a comparable Bradbury-Nielsen [45] gate for beam purification. We also used the same algorithm to optimise the transmission and resolving power of PILGRIM. The differences between the present separator and the one from Greifswald reside mainly in design choices described in this chapter, including:

- hollow mirror electrodes
- mechanically independent mirrors
- efforts to keep the field cylindrical symmetry
- a pulsed drift tube divided in 3 parts

We detail in this chapter the simulations and optimisation cycles performed and the subsequent design choices.

### 3.1 PILGRIM SIMULATIONS AND OPTIMIZATION

#### 3.1.1 SIMION and its accuracy

All PILGRIM simulations were performed with SIMION 8.1 software [81, 82]. SIMION is an ion optics simulation program that models ion flights in 2D or 3D electrostatic and/or magnetic potential arrays. SIMION numerically calculates these potential arrays by a finite element method over a 2D/3D meshed space. When relevant, SIMION may use a Poisson solver to calculate electric potential array in regions with space charge or even magnetic potential arrays. Outside these special cases, SIMION solves the Laplace law in free space:

$$\Delta V = \nabla^2 V = 0 \quad (3.1)$$

In a 3D finite element space composed of cubes and in which the coordinates  $x$ ,  $y$  and  $z$  correspond to the number of a given cube on each axis, this condition is replaced by:

$$V_{x,y,z} = \frac{V_{x+1,y,z} + V_{x-1,y,z} + V_{x,y+1,z} + V_{x,y-1,z} + V_{x,y,z+1} + V_{x,y,z-1}}{6} \quad (3.2)$$

Which is to say that the Laplace law is numerically satisfied at second order on the node of coordinates  $(x, y, z)$  when the potential of this node is defined by the average of the potentials of the 6 nodes surrounding it. The numerical solver, or array refining, aims to achieve this condition on every node of the mesh. After the refining, the potential is defined not only on the nodes but at any spatial point. The potential in a point is then interpolated from the potentials of the closest nodes. A first limitation, common to all numerical models, appears: the accuracy of the potential array (or PA), from which is deduced the force applied to ions, is limited

by the node spacing, i.e. the size of a SIMION grid unit. For this reason, we used a grid unit size of 0.1 mm throughout all simulations of the MR-ToF-MS. Because each electrode with an adjustable potential needs the creation of its own potential array, 0.1 mm seemed to be the smallest "reasonable" step size, beyond which the size of the potential array files becomes difficult to manage. All the potentials of all geometries described in this manuscript (including the deflector) have been refined to 0.1 ppm, which is the maximum precision available in SIMION.

Furthermore, an ion's motion into this numerical field is also determined numerically by applying changes of trajectory every time step. These changes are calculated every time-step, using the Lorentz force law and the previously calculated potential array(s). The time step varies with the speed of a particle and is usually set so this particle advances by about one grid-unit per time step (see e.g. [83]). It is possible to enhance SIMION's accuracy by lowering the time step through a "trajectory quality factor" available in SIMION's GUI. However once the time step is lower than the time needed to travel one grid unit, the simulation accuracy is eventually limited by the interpolation of the potential between nodes, and thus again by the size of a grid unit.

An analysis of SIMION inaccuracies can be found in [81]. In particular, it appears that the fractional error on some parameters of the motion (energy, speed, radius of curvature, ToF . . .) is higher for non-linear complex electrostatic or dynamic fields (e.g. RF potentials) than for electrostatic linear potential gradients. The reported fractional error in this article can be as high as a few  $10^{-4}$  for complex electrostatic fields, which is typically the case of the fields inside the mirror of an MR-ToF-MS. In addition, these errors have been measured for rather simple and short simulations, but in a multi-turn flight path system like PILGRIM, the errors could be stacked. It was reported in [84], that the energy deviation could be as high as 2.5% at 42 keV for a long ToF of 500  $\mu$ s. However in our case, we tested the energy conservation with a beam of 1800 eV trapped between the mirrors for 4 ms and got an average deviation of  $2 \cdot 10^{-5}$ . We also noticed an increase of the deviation with respect to the run time (or the number of turns). Without further details on the simulations from [84], we assume the very thin meshing and the low energy to be responsible for this difference.

To conclude this discussion, we tried to minimise the SIMION relative inaccuracy in our simulation and measured a rather low energy dispersion. However, assuming a similar inaccuracy on the energy and the ToF it is difficult to give high credit to any simulated resolving power above a few  $10^5$ . Of course it is possible, though hard to prove, that the ToF deviations would occur accordingly for every ion, changing the overall ToF but not the resolving power. Thus in this chapter, we will use the simulation results as proofs of principle and the estimate of PILGRIM's final performances as well as the optimal mirror potential as a starting point for a live optimisation of the real spectrometer.

Before jumping into the details of the SIMION simulations, we should

mention that we did not consider the effect of the space-charge on the ions' trajectory inside the trap throughout this study, as we expect the beam-intensity in S3-LEB to be limited to a few  $10^3$  ions per bunch. In [85] for instance, Rosenbusch *et al.* noticed that the effect of the space charge is clear for 50000 ions trapped for 80 turns but does not appear for 12000 ions. Should the space-charge not be negligible in S3, Rosenbusch and collaborators propose a method to limit its effect for extended trapping times using the pulsed drift tube.

### 3.1.2 Early geometries

First investigations of the geometry were done during the Master Thesis of B. Kansal [86]. The main geometries investigated then can be seen in Fig. 3.1. The first geometry is inspired from the first design of the ISOLTRAP MR-ToF-MS made by the Greifswald team [72], where the mirror's electrodes are blades close to the optical axis, which helps defining precise potentials on the axis (much like the blades of a reflectron). In this simplified geometry, only 3 mirror electrodes are used, instead of 5 in the MR-ToF-MS of ISOLDE. There is a grounded electrode before the first mirror electrode in order to shield the potentials of the mirror and separate the inside and the outside of the trap from the electric field point of view. The inner Einzel lens (or E-lens) consists of a large, close to axis electrode and is followed by a grounded plate.

This plate prevents the usually high potential of the E-lens to penetrate inside the drift tube, which facilitates the injection. In the second geometry the blades were replaced by thick electrodes far from the axis. The first mirror electrode is still equipped with a plate to prevent the ground potential of the shield plate to penetrate in the mirror. In the third geometry, even the inner E-lenses are far from the axis. The potentials of the mirrors in each case were optimised in order to benchmark the geometries. Comparative simulations with beams of realistic emittances (transversal and longitudinal) seemed to favour the second geometry, which we used as a starting point for the present work. In order to minimise both the field asymmetry and the size of the potential array in the memory, all geometries of PILGRIM created during this PhD work have been simulated in SIMION with a cylindrical symmetry. Thus the refining of the potential array was limited to 2 dimensions.

### 3.1.3 Optimization procedures

As Greifswald's team and others since, we use the built-in Nelder-Mead [87] (or downhill simplex) optimiser of SIMION 8.1 to optimise the potentials of the different electrodes. A short review of the usage of this method applied to SIMION can be found in [88]. The algorithm consists in minimising the size of a polygon of  $N + 1$  corners (the simplex) in the  $N$ -dimensions parameter space. In our case each parameter will be the potential of an electrode. At each iteration, the algorithm replaces the least optimal point by another one, usually by its symmetric with respect to the centroid of the remaining  $N$  points, but this can vary according

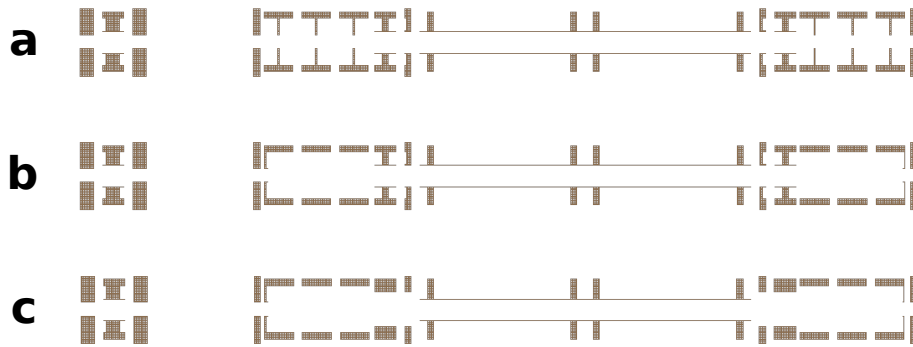


Figure 3.1 – Several geometries simulated by B. Kansal. *a*: Greifswald-like lenses and mirrors. *b*: hollow mirrors. *c*: hollow mirrors and lenses.

to a set of rules. In the recent versions of this algorithm, the simplex is capable to stretch in the direction of the greater slope, making it very fast. Like any numerical optimiser, this method can find a non-absolute local minimum. For many parameter systems like the MR-ToF-MS (5-10 parameters including the analyser and the injection optics), this is very likely due to the high density of local minima. In order to increase our chances of finding a better local minimum, we take the potential values found by the optimisation, randomise them to a value close to the optimal one and use the randomised parameter set as an input for a new optimisation cycle. After a couple of randomisation, we keep the best optimal set. The Nelder-Mead method is widely used for non-linear optimisation problems and though the algorithm is heuristic, it gained credit over the years in practical application as it is simple to use and very fast in finding a local minimum.

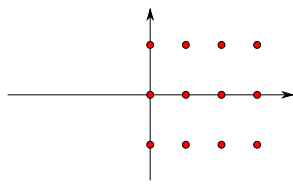
The most important part of the configuration of the optimiser is the choice of the goal function (or minimisation function). As we are trying to optimise a mass spectrometer/separator, one could try to minimise  $1/R_{FWHM}$ . However, experience showed that it was more convenient to aim for beam stability inside the trap in the first place and then optimise the resolving power after a high transmission has been achieved. We used in total 4 goal functions (see Tab. 3.1) depending on the number of ions crashing on the electrodes during the simulation  $N_{crash}$ , the mean of the transverse speed  $\overline{V}_y$  and its dispersion  $\sigma_{V_y}$ , the resolving power and a constant  $A$ . All these minimisation functions are arbitrary and have been chosen after several variants of the 4 functions have been tested. At very low number of turns, the first goal function aims at conserving the beam inside the trap but also to keep parallel. Thus, depending on the number of turns the system is optimised on, the trap will not necessarily achieve the "point-to-parallel" condition mentioned in the previous chapter, but could achieve a "parallel-to-parallel" condition. Of course in this case the settings of the mirrors could be suboptimal in terms of  $R_{FWHM}$  but this is of no concern yet. For a few turns or tens of turns, the second function introduces the resolving power in the optimisation and is much more severe with the number of ions lost in the trap. Up to 100 turns, the third goal function releases the stress on the trap efficiency in order to increase the relative importance of  $R_{FWHM}$ . At this point it is considered that the

goal function	number of turns
$(N_{crash} + 1)(\overline{V}_y + 2.35\sigma_{V_y})$	< 5 turns
$(N_{crash} + 1)^3(\overline{V}_y + 2.35\sigma_{V_y} + (A/R_{FWHM})^2)$	5-25 turns
$(N_{crash} + 1)(\overline{V}_y + 2.35\sigma_{V_y} + (A/R_{FWHM})^2)$	25-100 turns
$(N_{crash} + 1)(A/R_{FWHM})^2$	> 100 turns

Table 3.1 – Different goal functions from optimisation phase and the numbers of turns for which they were used.

beam is stable within PILGRIM for long trapping times and for longer ToF, the parallelism condition is removed in the fourth goal function.

The initial state of beam we chose for the simulation is also important. First the simulations have to be repeatable, thus we cannot take a random beam for each run. We could of course use the same random distribution for all runs. However the number of ions needed to have a statistically homogeneous filling of the phase space is around 1000, which would take a very long time to simulate for a high number of turns. Instead we chose to simulate a very low number of ions regularly spaced in the phase space. The chosen beam is:



- 48 ions of mass 133
- 4 transverse positions: 0, 0.5, 1 and 1.5 mm
- 3 directions:  $-0.7$ ,  $0$  and  $0.7^\circ$
- 4 energies: 4970, 4990, 5010 and 5030 eV

Owing to the symmetry of the system, it is unnecessary to simulate the other half of the beam phase space. The beam emittance of this beam in full phase space is  $39.9 \pi \text{mm.mrad}^1$ . In addition, it is useless to take a initial ToF spread in the simulations. Indeed the incompressible time is not correlated with the energy of the ions nor is it with the transverse position and direction. The increase in ToF spread after several turns in the MR-ToF device can be expressed as:

$$\Delta t_{tot} = \sqrt{\Delta t_{optical}^2 + \Delta t_{inc}^2} \quad (3.3)$$

Therefore we only need to get  $\Delta t_{optical}$  and the overall ToF from the simulation to determine the final resolving power. Unless specified, the resolving powers mentioned in the following sections take into account a incompressible time of 50 ns FWHM.

## 3.2 SUCCESSIVE DESIGNS

### 3.2.1 Early mechanical design and changes in the geometry

At this point the optimised resolving power was  $\simeq 26000$  at 250 turns considering the previous pessimistic beam, and was increasing almost

<sup>1</sup>By default, we call "emittance" the 90% emittance, or the area containing 90% of the bunch in the transverse phase space.



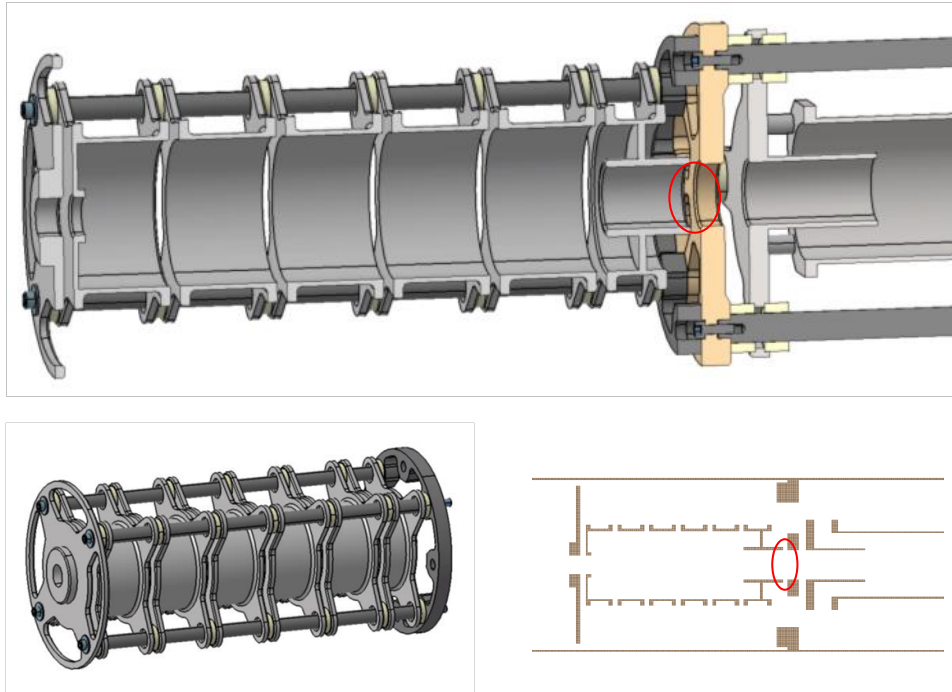


Figure 3.2 – Early mechanical design of the mirror. The bottom-right figure is a SIMION view. The red ellipses pinpoint the region of highest potential gradient.

linearly with the number of turns. The beginning of the mechanical design brought important modifications to the current geometry. In order to explain these changes from SIMION's point of view we must give now some details about the design of the trap (see Fig. 3.2). We chose to have a versatile design so the full mirror ensemble could be removed and exchanged in case a better geometry would be found. In the mirror ensemble, the electrodes are axially guided by 4 invar rods and maintained into position by the outer grounded shield plate on one side, and a grounded ring on the other side. The ring is then fixed to the inner shield plate. In order to achieve a good alignment of the ensemble, the mirror electrodes, the E-lens and the 2 grounded plates were lightened but the sides of the electrodes directly facing the beam were preserved.

Also the 4 rods and the fixing lugs of each electrode were breaking the cylindrical symmetry of the ensemble. If the electric potential does not fulfil this symmetry, ions may not have the same revolution time depending on the plane they evolve in. Because they are trapped for many turns, even a slight asymmetry could increase the final ToF bunchwidth. However the mechanical design can be non-symmetric as long as the field inside the trap is. In order to ensure this we reduced the spacing of the mirror electrodes to shield the effect of the rods. A special attention was paid to the region between the E-lens and the inner ground plate. Indeed this region has the strongest gradient in the whole setup and the fixing lugs of the plates (and the asymmetry they carry) are much closer to the beam axis than those of the mirror electrodes (see the red ellipses in Fig. 3.2). We therefore made a 3D modelling of this part of the spectrometer to investigate the asymmetries (see Fig. 3.3-left). In this model we compared

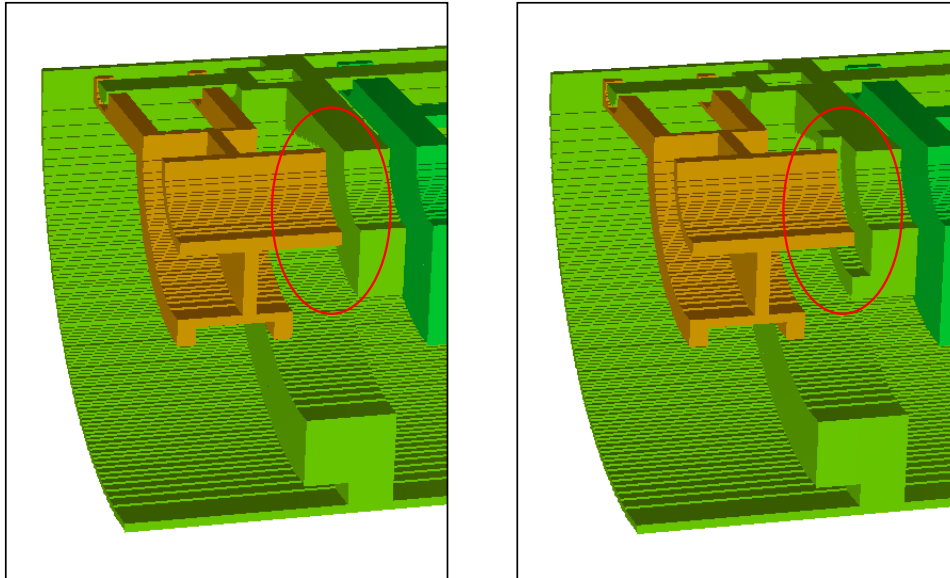


Figure 3.3 – 3D models of the interface between the inner Einzel lens and the inner ground plate. The left (resp. right) figure shows the model without (resp. with) a small collar shield.

the potentials at the coordinates  $(10, 0, Z)$  and  $(0, 10, Z)$  in mm,  $Z$  being the axial position of a point right between the back end of the E-lens and the front end of the ground plate. The difference of potential resulting from the asymmetry is 0.04 V or 15 ppm. We then added a small collar to the shield plate, as shown on Fig. 3.3-right, reducing the potential asymmetry to 0.07 ppm. We considered that this was the only critical point since the other electrodes are far from the axis and less sensitive to the rods. We checked that the asymmetry between two mirrors electrodes was below 0.01 V.

### 3.2.2 Geometry of the mirrors

In order to enhance the maximum resolving power, we tried several mirror configurations:

- I. 3 electrodes of 24 mm long
- II. 3 electrodes of 40 mm long
- III. 5 electrodes of 24 mm long
- IV. 5 electrodes of 40 mm long

We compared the results of these mirrors for the optimised sets of potential after 25 turns, using the third goal function. At such a low time of flight, the incompressible time can be much bigger than the ToF dispersion due to the beam optics in the trap. This means that the configuration with the highest resolving power at 25 turns is not necessarily the one with the best optics. For a very long ToF,  $R_{FWHM}$  reaches a limit because the incompressible time becomes negligible compared to the ToF dispersion due to geometrical aberrations, which is to say that the upper limit of a

Electrodes	3 short	3 long	5 short	5 long
$R_{FWHM}$	1146	4942	5418	2726
$R_0$	1170	9296	16120	3033

Table 3.2 – Comparison of  $R_{FWHM}$  and  $R_0$  for the 4 mirror configurations.

MR-ToF device is independent from the incompressible time. In order to evaluate the trap optics quality, we define  $R_0$  as the resolving power the spectrometer would have if the incompressible time was 0. The optimised results are shown Tab. 3.2. The best optical properties are found for 5 short electrodes.

### 3.2.3 Injection in the trap

We define  $\sigma_x$ ,  $\sigma_a$  and  $\sigma_K$  the RMS spreads in transverse position, transverse angle and kinetic energy respectively. During the preliminary optimisation phase we noticed that the optimal resolving power and efficiency were depending on the initial axial position of the ions, its occupancy of the phase space while keeping the  $\sigma_x\sigma_a$  product constant (i.e. keeping the same emittance) and the position of the injection Einzel lens. This can be explained qualitatively if we assume that the bunch needs to have a special emittance profile in the middle of the trap for the spectrometer to achieve a high resolving power. For example the point-to-parallel configuration mentioned in 2.2.2 would not be achieved if the beam was focused before or after the middle of the trap. The emittance profile in the middle of the trap depends on 4 parameters:

- the initial emittance profile at the beginning of the simulation
- the drift length (thus it depends on the starting position of the bunch)
- the injection E-lens position
- the injection E-lens potential

On the basis of the previous assumption, changing any of these parameters would affect the resolving power, as observed. Tuning the E-lens potential is the most obvious way to change the emittance profile inside the trap. It can be optimised along the mirror electrodes in SIMION's optimiser. Then changing the position of the E-lens allowed to enhance further the resolving power by adding a degree of freedom to the optimisation of the injection. At this point of the simulation work on PILGRIM, it was not known what the bunch emittance profile after the RFQCB or what the final layout of S3-LEB would be. Thus we decided to change the position of the injection E-lens in order to adapt the emittance profile for optimising the performances of PILGRIM. We used the same standard beam of emittance  $\sim 40 \pi \cdot \text{mm} \cdot \text{mrad}$  as defined earlier. We scanned 20 positions by steps of 10 mm then 5 mm and tried to reach the maximum number of turn for which none of the 48 ions of our standard bunch was lost on the walls. After changing the position by 195 mm compared to the initial position, we achieved a loss-less 250-revolutions flight with optimised resolving power of  $\simeq 36000$ .

### 3.2.4 Final design

Fig. 3.4 shows the mechanical and optical design of PILGRIM as it was built. The drift tube is equipped with shields of smaller aperture to limit the penetration depth of the ground potential when the drift tube is at the lift potential. However the drift tube itself has a large radius to ease the pumping of the drift section. The tube itself is divided into two sections for the same reason. Between the two sections stands a pickup electrode that will be used to monitor the round trip frequency of the ions inside the trap. In the mean time this electrode is put to the same potential as the rest of the drift tube. The invar rods holding together the different electrodes are all grounded. The potentials of the mirror electrodes are separated with one another and the potential of the rods by  $\text{Al}_2\text{O}_3$  rings. The whole separator ensemble is supported inside the main vacuum chamber through the two inner grounded plates (see the SIMION view) and the precision of the mechanical alignment of the mirrors is 0.1 mm or better. The injection E-lens has been lightened like the mirror electrodes, and is supported by a flange of the first vacuum chamber. A similar E-lens, symmetric to the first one has been built on the other side of the spectrometer to tune the ejection optics. The two 6-ways vacuum crosses on the sides are used to insert diagnostics and beam-damping grids on the beam line. PILGRIM's vacuum system, diagnostics and acquisition electronics are detailed in the next chapter.

### 3.2.5 Optical properties

We investigated the optical properties of this final design for more realistic beams. The optical setup for the following simulation included the electric deflector (detailed in chapter 5) in shoot through mode and 2 additional E-lenses. The injection is thus not the same as in the previous simulations, but the new E-lenses bring 2 degrees of freedom so the emittance profile at the time of trapping is somewhat similar. Compared to the first simulations by B. Kansal, and according to the recommendations of the Greifswald team, we reduced the energy of the injected and trapped ions by a factor 5/3. With an ion kinetic energy of 3 keV outside of the trap instead of the 5 keV previously, it is much easier to deflect the unwanted contaminants by a Bradbury-Nielsen Gate, which is intrinsically limited by the maximum voltage such gate can stand ( $\pm 250\text{V}$  for the ISOLTRAP design). Under these conditions, the ToF, but also the bunchwidth are increased, leaving the resolving power unchanged. We optimised the whole voltage set for 250 revolutions, still using an unrealistic beam, but this time with a realistic emittance of  $4 \pi \text{mm.mrad}$ , defined as:

- 84 ions of mass 133
- 3 transverse positions:  $-0.15, 0$  and  $0.15 \text{ mm}$
- 7 directions from  $-0.7$  to  $0.7^\circ$
- 4 energies: 2982, 2994, 3006 and 3018 eV

We then proceeded to test the spectrometer for a realistic beam of same emittance:  $\sigma_x = 0.111 \text{ mm}$ ,  $\sigma_a = 0.517^\circ$  and  $\sigma_K = 8.5 \text{ eV}$ , using

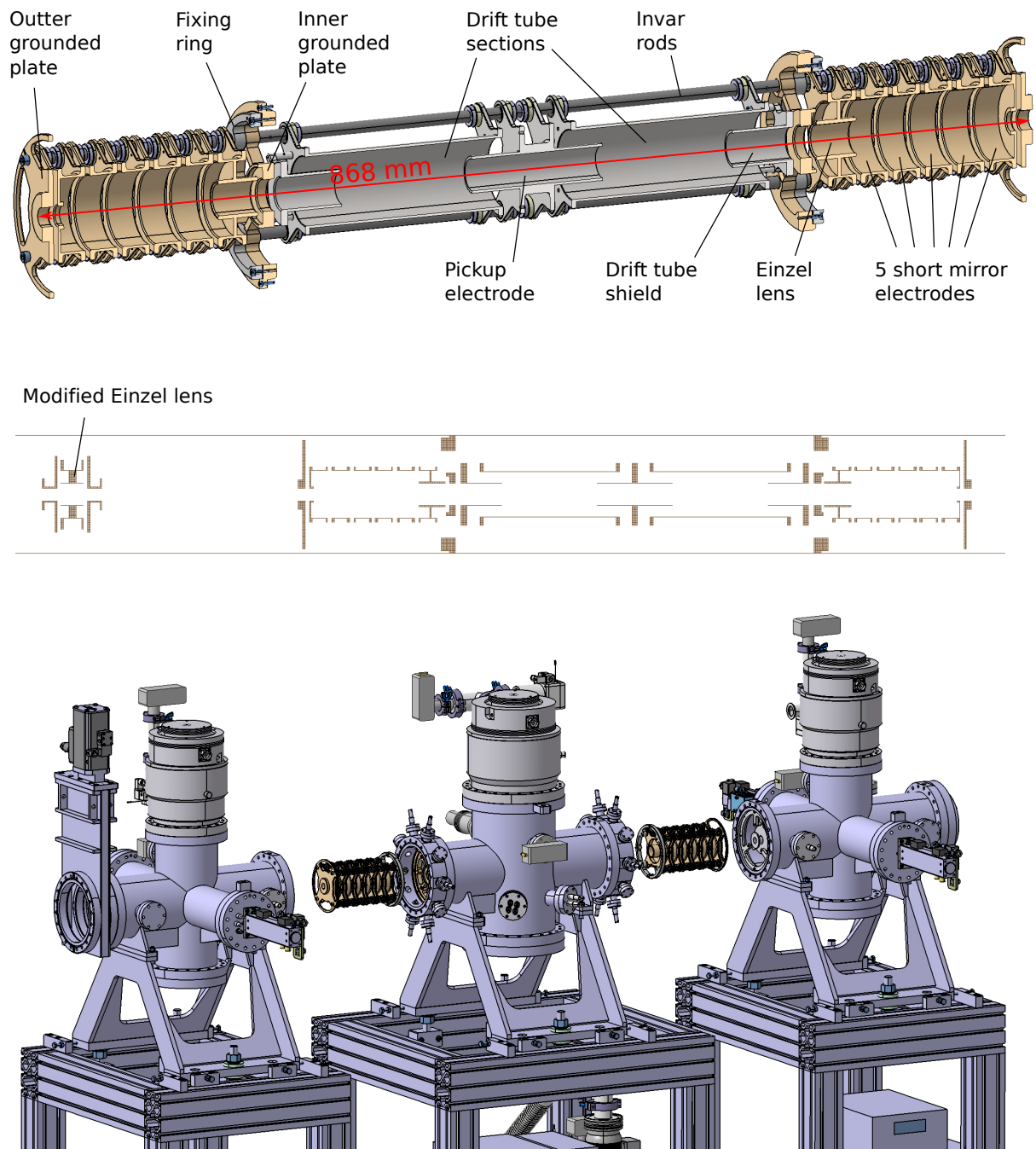


Figure 3.4 – **Top:** mechanical design of the separator ensemble and its parts. **Middle:** SIMION version used for simulations. **Bottom:** mechanical design of PILGRIM showing the vacuum chambers and the turbo-pumps. The mirrors can be taken out and, if needed, exchanged without removing the drift tube from its chamber.

1000 ions. Once again we did not put an initial incompressible time and we only measured the ToF spread increase at the end of the simulation. Fig. 3.5 shows the resolving power of this bunch (in blue) as a function of the number of turns, as estimated by simulation. The resolving power is calculated for different incompressible times of 7, 20 and 50 ns matching the bunchwidths found in [49], [54] and [89]. In order to estimate the sensitivity of  $R$  to the initial parameters of the bunch, we also calculated the resolving power as a function of time for 3 other bunches with either double  $\sigma_x$  (2), double  $\sigma_a$  (3) or double  $\sigma_K$  (4) compared to the initial bunch (1). The bunch characteristics, maximum resolving power ( $R_{max}$ ) and transmission efficiency ( $\epsilon_{trans}$ ) are summarised in the table of Fig. 3.5.

These figures hold several interpretations. First the general shape of the  $R$  lines indicate clearly the existence of the expected ToF-focus and matches the predicted shape in [58]. Secondly, bunches with higher spread on  $x$ ,  $a$  or  $K$  have larger ToF aberrations due to the geometric parameters or the energy and thus have a lower resolving regardless of the ToF. Lower emittances were also tested and led, as expected, to higher resolving powers. Thirdly, for a very low incompressible time the geometric aberrations become predominant over  $\Delta t_{inc}$ . This can be guessed by the fact that the beam emittance has a high impact on the resolving power at  $\Delta t_{inc} = 7$  ns but a very low influence when  $\Delta t_{inc} = 50$  ns. However if we were to perform the ToF focus at a much higher number of turns, even the 50 ns would eventually become negligible before the geometric aberrations, and the second order term ( $\delta_t|\delta_K\delta_K$ ). If we make the assumption that we are capable of changing the position of the ToF focus to a very high number of turns without changing these aberrations, we can estimate that the limit of the resolving power at saturation (for a high number of turn) is equal to the resolving power at 250 turns with  $\Delta t_{inc} = 0$ , which is  $\simeq 314000$ .

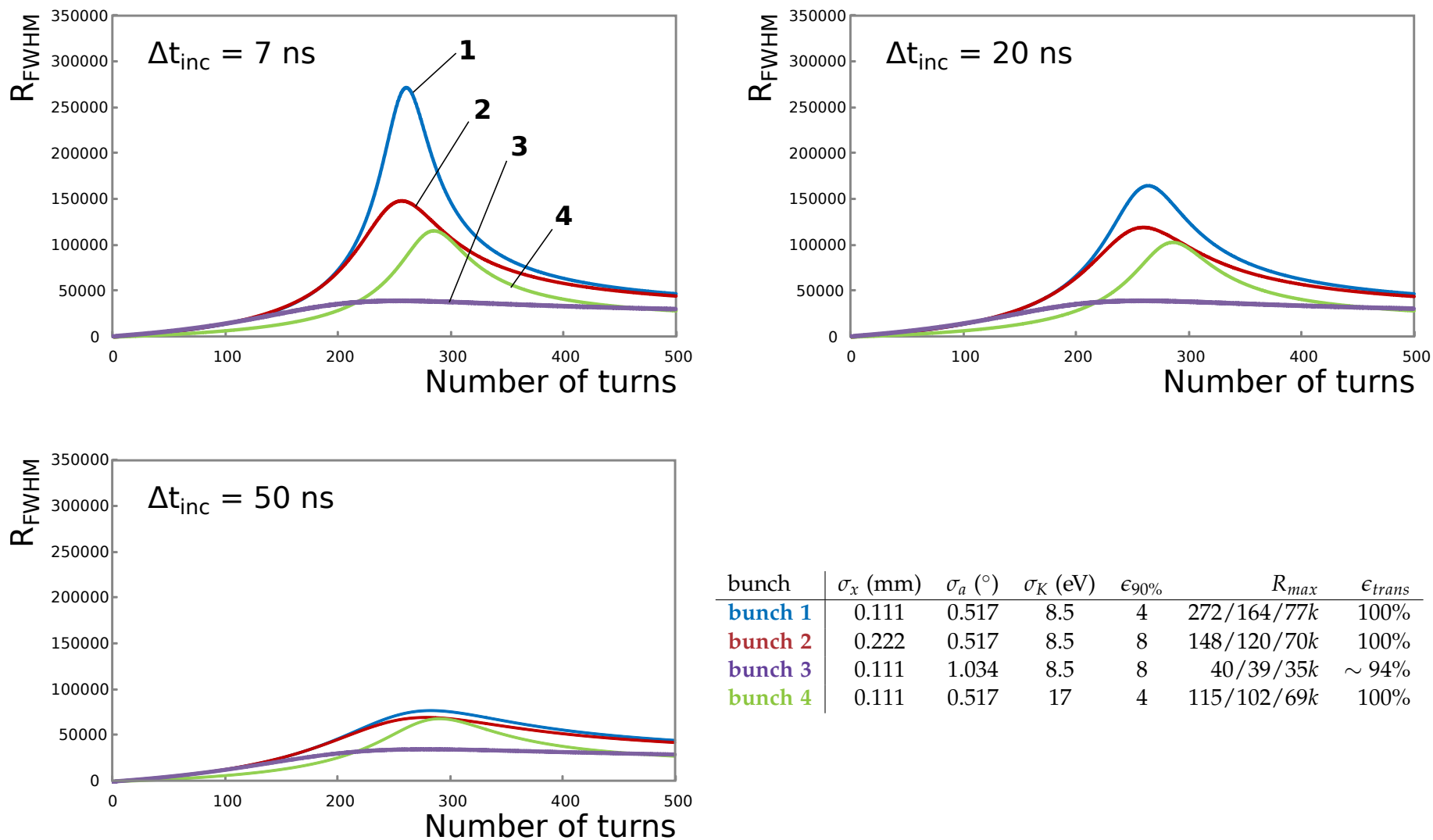


Figure 3.5 – Comparative resolving powers as a function of the number of turns for 4 different beams (4 colours in the graphs and the table) and for 3 different incompressible times  $\Delta t_{inc}$  at the ejection from the RFQ.  $\epsilon_{90\%}$  is the 90% emittance. At mass 133, the ions make one revolution in  $\simeq 29.2 \mu s$ .

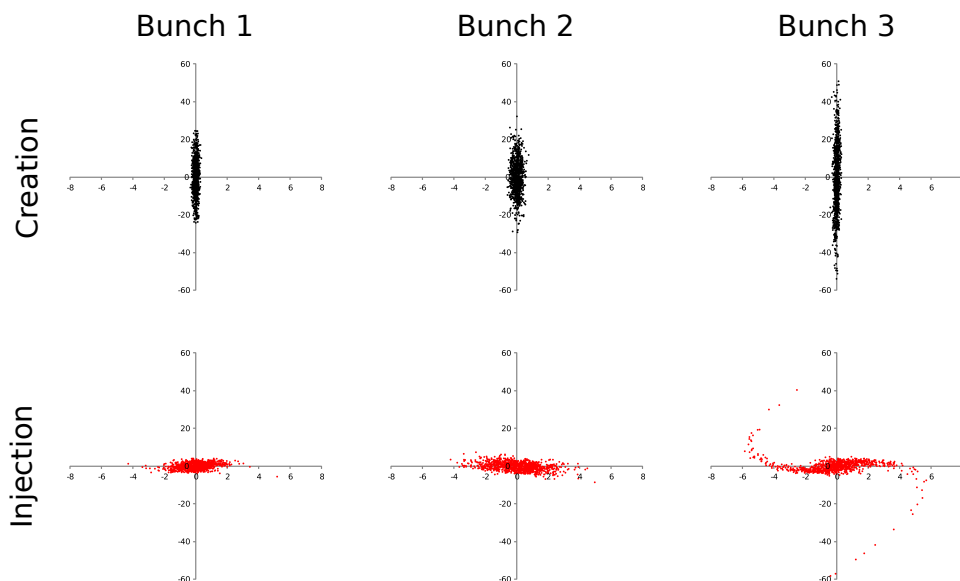


Figure 3.6 – Emittance plots for the bunches 1, 2 and 3. X axis is the transverse position  $x$  in mm and Y the transverse angle  $a$  in mrad. We compare the shape of the emittance profile at the creation of the bunch (top, black) to the profile in the middle of the MR-ToF-MS, just before switching the in-trap lift (bottom, red).

The resolving power plots also raise 2 issues:

- I. The bunches 2 and 3 have the same emittance but lead to very different resolving powers. This confirms that the resolving power is very sensitive to the injection, but hints that the set of potentials for the injection optics that we optimised for an unrealistic beam might not be optimal for a realistic beam. In addition the larger  $\sigma_a$  of bunch 3 lead several ions to crash on the walls of the spectrometer. This gives a semi-quantitative estimate of the MR-ToF-MS acceptance as ions start crashing at  $\sigma_a = 0.45^\circ$  ( $\simeq 1\%$  crash).
- II. The position of the ToF focus changes for a larger energy spread, which could be due to the effect of a second (or more) order component on the time of flight.

We try to develop and understand these issues in the following.

Fig. 3.6 shows the effect of the injection optics on the emittance profile of the bunches 1, 2 and 3. By increasing the initial  $\sigma_x$  (bunch 2) we increase both  $\sigma_x$  and  $\sigma_a$  by similar factors. The emittance profile being wider, the observed resolving power drop is no surprise. However, the bunch 3, with increased  $\sigma_a$ , sees its emittance profile strongly distorted. In this case the emittance profile is filamenting due to strong optical aberrations along the path of the beam. The very strong decrease of the resolving power in this case (at least a low  $\Delta t_{inc}$ ) can be explained by the fact that the distortion of the emittance profile populates regions of the phase space far from the origin.

Also, because the injection optics have previously been optimised to maximise the resolving power in PILGRIM, the transformation of the



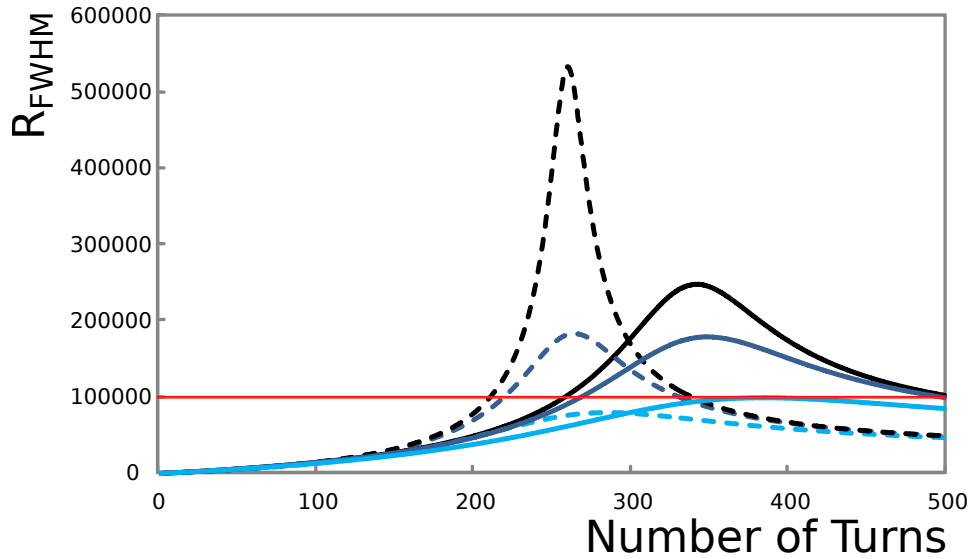


Figure 3.7 – Resolving powers as a function of the number of turns for an incompressible time of 50 ns (light blue), 20 ns (dark blue) and for no incompressible time (black). The dashed lines show  $R_{FWHM}$  for a ToF focus at 250 turns. The full lines show  $R_{FWHM}$  after changing the ToF focus by changing the potential of the drift tube. The red line show the 100k limit.

emittance on the bunch 1 shows clearly that PILGRIM works better if the injected bunch is parallel at the time of the trapping. Since the bunch has a finite emittance, the  $\sigma_a$  can only be made lower by increasing the  $\sigma_x$ , which would decrease the aberration due to  $a$  but increase the one due to  $x$ . Again, because the injection optics have been optimised, we should have reached a compromise between  $\sigma_a$  and  $\sigma_x$  so that the overall geometric aberrations are minimum. However, as stated before, it was unsure if the optimisation on the unrealistic beam gave the best results. By manually tuning  $\sigma_x$  and  $\sigma_a$  while keeping a constant emittance of  $4 \pi \text{mm.mrad}$ , we could increase the maximum resolving powers at 250 turns to 382k, 182k and 79k for incompressible times of 7, 20 and 50 ns, respectively. This was obtained for  $\sigma_x = 0.133 \text{ mm}$  and  $\sigma_a = 0.431^\circ$ . The theoretical limit of the resolving power at high number of turns when  $\Delta t_{inc}$  becomes negligible is  $\simeq 532000$  (see Fig. 3.7, dashed lines).

We then tried to test the change of ToF focus by changing the potential of drift tube to change the energy of the ions inside the trap as suggested in [58]. Fig. 3.8-left shows the revolution time with respect to the energy of the ions inside the trap. We should notice that the optimisation of the potentials in PILGRIM, in particular the one of the drift tube, centred the energy distribution of the bunch at the position of the inflexion point of the ToF vs K curve (Fig. 3.8-top right). At this point, the high order aberration due to the energy  $((\delta t|\delta K), (\delta t|\delta K\delta K) \dots)$  are minimum. By changing the energy inside the trap, we change the average slope of the distribution thus the  $(\delta t|\delta K)$  for one turn and the position of ToF focus. Given the shape of the ToF vs K curve, any small change in the mean energy of the ions inside the trap will increase the ToF for which the ToF focus is obtained. Unlike in [58], we chose to increase the energy of the ions, as it led to higher resolving powers than when decreasing it. The resolving

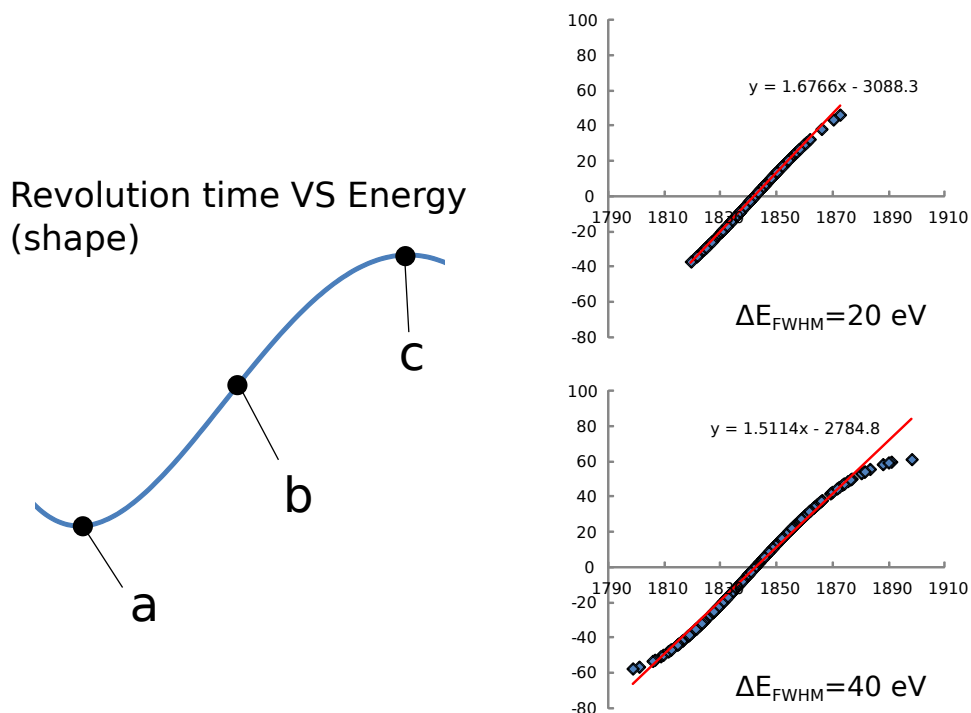


Figure 3.8 – *Left*: shape of the  $\Delta t$  vs  $\Delta K$  dependency after one revolution in the MR-ToF-MS. The points *a* and *c* are isochronous configuration for which PILGRIM does not induce any dispersion or correction of the ToF correlated to the energy. The point *b* is an inflexion point for which the ToF depends quasi linearly on the energy with very little contribution of the higher orders. *Right*: ToF (in  $\mu\text{s}$ ) as a function of the energy inside the trap (in eV) for two different energy spreads. All 3 curves have been drawn by considering a bunch without transverse emittance ( $x = a = 0$ ) to simplify the interpretation.

powers obtained by changing the potential of the drift tube by  $-25 \text{ V}$  are shown in Fig. 3.7. We should note that the maximum resolving power is obtained at a higher number of turns. The maximum  $R_{FWHM}$  considering a  $50 \text{ ns}$  incompressible time has increased to  $\simeq 100000$ , while it is left almost unchanged for  $t_{inc} = 20 \text{ ns}$  and is even reduced for  $t_{inc} = 0$ .  $R_{FWHM}$  is balanced between the increasing ToF  $t$  and the increasing  $\Delta t$ . In the case  $t_{inc} = 50 \text{ ns}$ ,  $\Delta t$  is dominated by  $t_{inc}$  until a very high ToF, explaining why  $R_{FWHM}$  grew. In contrast, the resolving powers for  $t_{inc} < 50 \text{ ns}$  are decreasing because the change of kinetic energy inside the trap increases the geometric and/or kinetic aberrations affecting  $\Delta t$ .

In order to explain the change of the ToF focus position for the bunch 3, we looked at the dependency of the revolution time of the trapped ions to their energy inside the trap (see Fig. 3.8 again). Increasing the energy spread allows some ions to reach non-linear parts of the curve, thus the reduced resolving power. Finally, by fitting the graphs of the right of Fig. 3.8 by a linear curve, we estimate an average linear correlation which is slightly modified by the orders 2 and higher. The ToF focus is achieved when the mirrors compensate the ToF spread due to the energy spread during the drift from the RFQCB to the detector. Since the linear coefficient of the ToF-E correlation in PILGRIM is lower for a  $40 \text{ eV}$  dispersion than for a  $20 \text{ eV}$  one, the ToF focus will occur for a higher number of turns. The ToF focus for the bunch 1 occurs at 260 turns. We thus deduce

that the ToF focus for the bunch 3 will occur at  $260 * 1.677/1.511 = 289$  turns, which matches very nicely what we see in simulation.

## CONCLUSION

In this chapter, we detailed the different optimisation steps and changes of geometry that led to the current design. We studied the possibility to use 3 and 5 lenses of different lengths and paid attention to the possible sources of field asymmetry. The resolving power was then optimised for 250 turns with a conservative beam and tested with several more realistic ones. We also tested in simulation the impact of the different beam parameters on the final resolving power. Finally we tested the effects of changing the ToF focus point with the in-trap lift technique and manage to reach a resolving power of 100k or more for 3 reported values of the bunchwidth taken as an incompressible time in our calculations.

# FIRST TESTS OF PILGRIM AT LPC CAEN

# 4

## CONTENTS

5.1	MOTIVATIONS . . . . .	97
5.2	OPTIMIZATION . . . . .	98
5.2.1	Deflector concepts and optimised parameters . . . . .	98
5.2.2	Criteria . . . . .	99
5.2.3	Method . . . . .	100
5.3	RESULTS . . . . .	102
5.4	DOUBLE DEFLECTOR . . . . .	103
5.4.1	U and S-configurations . . . . .	103
5.4.2	Comparison of double deflector performances . . . . .	105
5.5	REALISTIC BUNCHES . . . . .	107
5.6	PROPER USAGE OF THE DEFLECTOR. . . . .	109
5.6.1	Modelling the deflector in Mathematica . . . . .	109
5.6.2	Effect of the distance between deflectors . . . . .	111
5.6.3	Telescopic lenses . . . . .	112
5.7	DEFLECTOR DESIGN . . . . .	112
	CHAPTER CONCLUSION . . . . .	115

**I**N this chapter, we will describe the setup for the commissioning of PILGRIM and explain the different tests performed as well as their results. We give a detailed description of the beam tuning, bunching, trapping and ToF measurements.



## 4.1 OBJECTIVES

This experiment ultimately aims at proving the possibility of isobaric separation with PILGRIM. We tried to separate  $^{40}\text{Ca}$  from  $^{40}\text{K}$  as in [47, 67] which requires a resolving power of  $\sim 30000$ . This is a good middle range R-aim to prove the capabilities of PILGRIM before stepping up to the  $> 10^5$  final goal. The first goal of this experiment was to test the vacuum system, voltage supply, control and monitoring of PILGRIM.

## 4.2 TEST SETUP AT LPC CAEN

The test setup is composed of PILGRIM's mechanical assembly introduced in the previous chapter and an ion source mechanical ensemble as well as their respective vacuum systems and power supplies. The PILGRIM setup is almost identical to the one planned for S3 except for the vacuum gate valve (Fig. 3.4) that we skipped in the present experiment.

### 4.2.1 The ion source and its optics

The ion source and its optical elements were initially designed for the Magneto-Optical Trap (MOT) of LPC-Caen [90] (see Fig. 4.1). It is a surface ionisation source, which limits the available elements for this test to alkaline and alkaline-earth elements (see chapter 1). Ions are emitted by heating a small pellet of the chosen composition. We decided to use a calcium pellet model 101139 from HeatWave Labs [91], knowing that it would be naturally contaminated by potassium during the source manufacturing, as stated in the documentation from Heatwave. We did not ask for the optional cleaning of HeatWave's source oven. The pellet was therefore very likely to contain a cocktail of alkaline elements. Potassium has an ionisation rate much higher than calcium in a thermal ion source, because its lower ionisation potential. We planned to take advantage of the presence of K and its high production rate to obtain a mixture of  $^{40}\text{Ca}$  (96.94% of natural abundance) and  $^{40}\text{K}$  (0.0117% of natural abundance) with comparable intensities. The same source was considered for the same reason by Schultz *et al.* [67], independantly from the present work. In [49], Schury and collaborators used an unreferenced calcium thermal ion source to produce the same isobaric doublet and were able to see and separate both isobars.

In our setup, the source is put at the acceleration potential  $V_{acc}$ , meaning the ions will be accelerated to the energy  $qV_{acc}$ . A small conical electrode near the source is put at extraction potential  $V_{ext}$  and helps to extract and guide the ions before their real acceleration. The source is also equipped with numerous optical elements. Two Einzel lenses are used to tune the convergence on the beam. Following are two tunable slits aligned in  $X$  and  $Y$  perpendicularly to the beam axis. Each slit consists of two mobile blades cutting the beam in the corresponding transverse axis. In case the beam does not follow the axis of the setup, its direction can be adjusted using 4 quarter-circle deflecting electrodes. We usually apply low opposite potentials to opposite electrodes (of the order of 10V for a

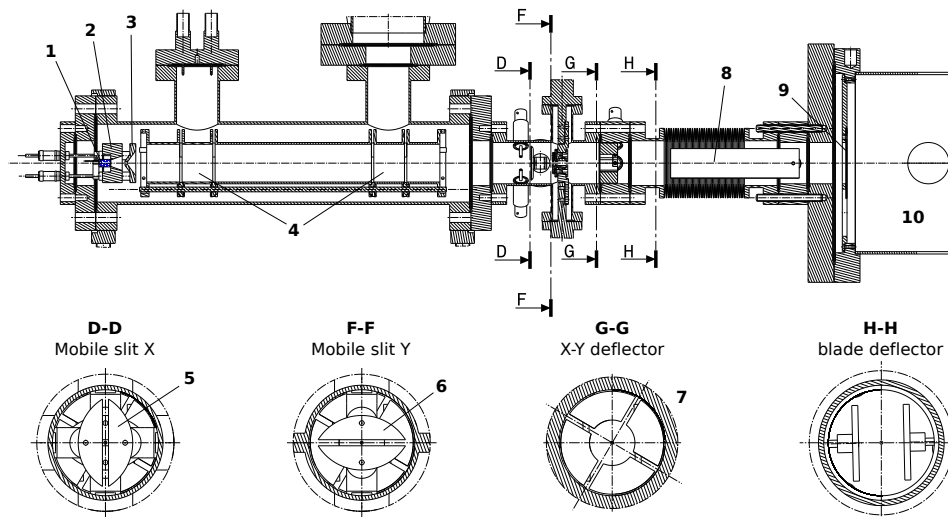


Figure 4.1 – Mechanical drawing of the source. (1) Ca/K pellet, (2) acceleration electrode, (3) extraction electrode, (4) Einzel lenses, (5) and (6) mobile slits, (7) X-Y deflectors, (8) blade deflector, (9) collimator, (10) first vacuum chamber of the PILGRIM ensemble.

3keV beam). Finally two deflecting blades are used to chop the beam. We bunched the beam by setting one of these blades at ground potential and pulsing the other from a few 100V down to 0V for a short time during which the ions can fly towards PILGRIM. Unlike the cooler buncher trap, this setup actually deflects the beam for most of the time and let it go for very short time windows. This is only viable because we used a stable beam of rather high intensity. In addition to the source optics, a collimator has been installed between the beam-chopper and the first diagnostics in order to cut into the emittance profile of the beam so PILGRIM receives a low emittance beam, as would be delivered by the S3 RFQCB.

#### 4.2.2 Vacuum system

A drawing of the vacuum system can be found in Fig. 4.2. A scroll pump model XDS35i from Edwards is used to ensure a primary vacuum. The ultra high vacuum is achieved with several turbo-molecular pumps:

- A small 60L/s pump on the source.
- A 1000L/s Agilent pump model Turbo-V 1001 Navigator on the main vacuum chamber of PILGRIM.
- Two 750L/s Agilent pump model Turbo-V 750 Twistorr on the 6ways crosses on the sides of PILGRIM.
- An additional 80L/s booster pump on the 1000L/s pump to reach even better vacuum in the trap.

Several valves are used in combination with the pumps either for the pumps safety or to switch between pumping modes (primary, secondary, boosted secondary), or again for leakage detection. The vacuum setup is completed by a handful of Pfeiffer primary and secondary gauges. Without activating the booster pump we reached the lower limit,  $5 \cdot 10^{-9}$  mbar,

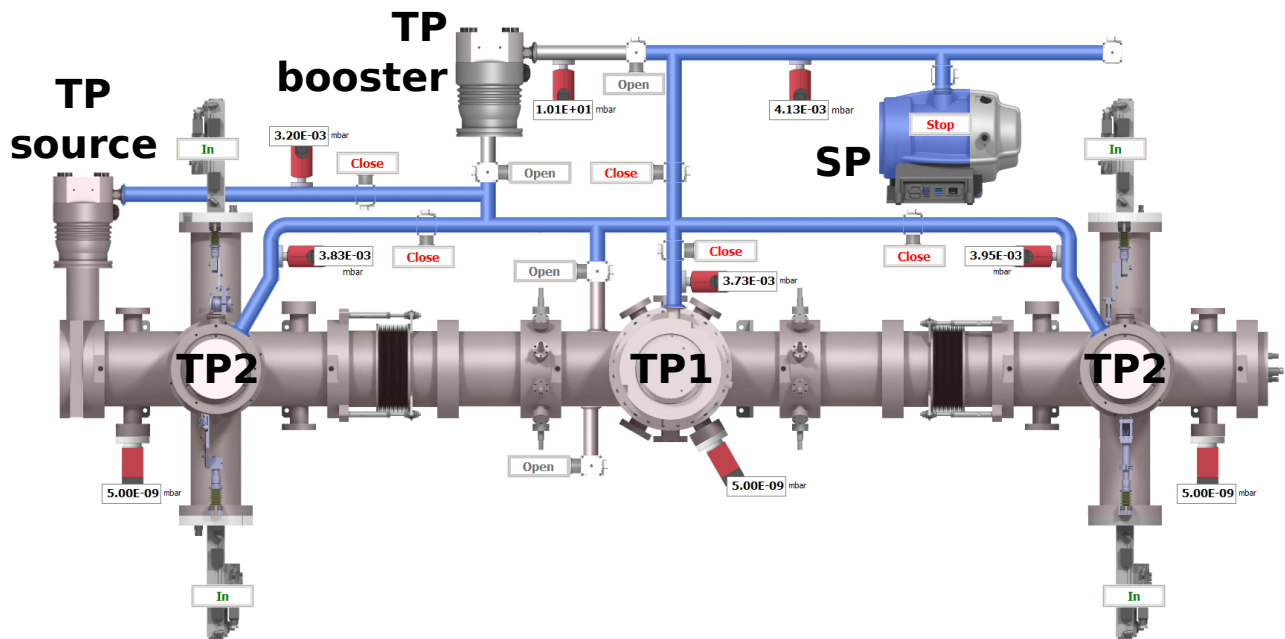


Figure 4.2 – Vacuum setup of the PILGRIM test. The drawing is part of the software interface for monitoring and control of the vacuum system. It shows the scroll pump (SP), the turbo-molecular pumps (TP), the valves, primary and secondary gauges as well as their respective readings. The pressure values read are the real measurements performed after  $\sim 4$  weeks of pumping. This interface is also used to control the insertion of the diagnostics in the beam-line (see section 4.2.5).

on every full range gauge, including the one close to the source. By using an additional gauge of Bayard-Alpert type, we could measure a pressure below  $3 \cdot 10^{-9}$  mbar in the middle of the trap when the ion source is being used. According to Eq. 2.14 from chapter 2, the mean free path of ions at this pressure should be near 24 km. The flight path length in PILGRIM typically ranges from a few hundreds meter to  $\sim 3$  km (for 2000 turns). In the latter case the transmission efficiency due to collisions with remnant gas is estimated to  $\simeq 92\%$ .

### 4.2.3 Electrical setup

All PILGRIM electrodes but the drift tube (5 mirror electrodes, 3 E-lenses and 2 MCP) use a static potential and are powered with 4kV or 6kV HV power supplies of the DPS series from ISEG. These power supplies have a good voltage stability (below  $10^{-5}$ ) which is crucial for any electrostatic trap application. They are gathered in a dedicated ISEG rack in the electronic rack of PILGRIM (see Fig. 4.4) and their potentials are controlled through the software interface from Fig. 4.3. MCP detectors don't need a precise voltage to operate, but it is convenient to group and control their power supplies along with the other ones in the ISEG rack. The potentials from the source and its optics are provided by miscellaneous power supplies from LPC-Caen and are controlled manually on their front panel (see Fig. 4.4). As the ions make only one pass next to the electrodes from the source, the voltage precision is not as critical as for the mirrors. These power supplies are also conveniently gathered in the PILGRIM electronic



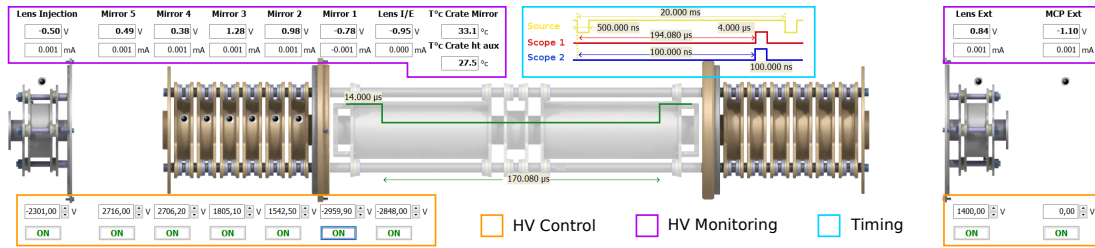


Figure 4.3 – Control and monitoring user interface for the high voltage power supplies and the pulse generation.



Figure 4.4 – All non-pulsed power supplies of PILGRIM (left) and the source (right).

rack even if they do not belong to the PILGRIM setup, as intended for S3.

PILGRIM's drift tube and the source blade deflector (and later the ejection E-lens) are being pulsed. It so happens that the high precision ISEG power supplies perform poorly while being pulsed because of the high current driven by the switching. Thus we use Ortec power supplies, more stable in these conditions. We use high voltage push-pull switches from Behlke with a typical switching time of 100 ns. Each switch is controlled by a Transistor Transistor Logic (TTL) signal delivered by the pulse generators.

#### 4.2.4 Timings

The pulse generators are controlled by the software interface (from a window that can be called from the interface shown in Fig. 4.4). The chronogram in Fig. 4.5 illustrate a complete cycle of bunching/trapping/measurement. One starts by defining the cycle time of the bunch manipulation. Then the different pulses within each cycle are defined as follow:

- The first pulse is defined by a gate width and starts at the beginning of each cycle. This pulse drives the Behlke switch of the blade deflector and thus corresponds to the time of creation of the ion bunch. Its width defines (but is not equal to) the ToF-size of the bunch.

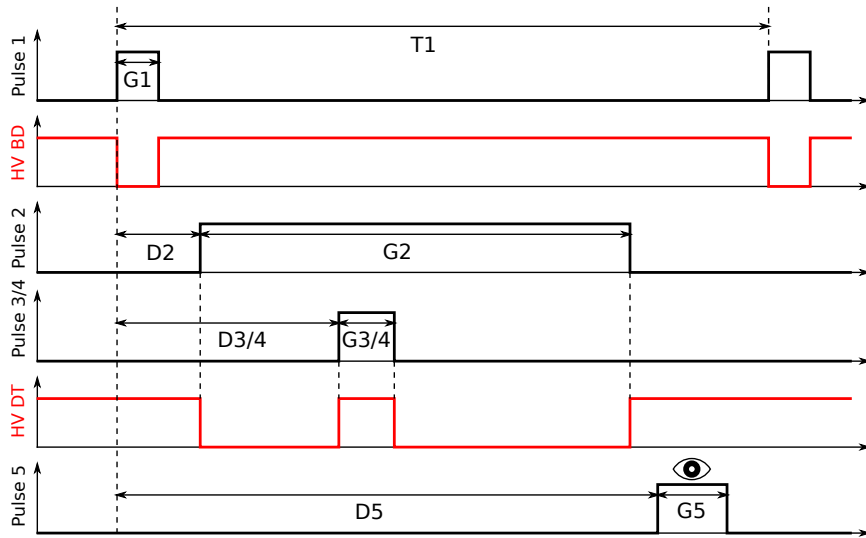


Figure 4.5 – Chronogram of bunch manipulation and observation in PILGRIM. Shows the different pulses (in black), the adjustable cycle time ( $T_1$ ), gates (G) and delays (D) as well as the potentials of the blade deflector (HV BD) and the drift tube (HV DT). See text for the explanation of the pulses.

- The second pulse controls the ion trapping via the pulsed drift tube potential. On the rising edge of this pulse, the potential of the drift tube is switched from  $\sim 1\text{ kV}$  down to  $0\text{ V}$  for capturing the ions. On the falling edge, the voltage of the drift tube is switched back to its original value and the ions are released.
- Two short pulses can also be used to control the switching of the drift tube for extraction of unwanted ions within one trapping cycle (labeled  $3/4$  in Fig. 4.5). We want to be able to eject the isotopic contaminants  $^{39/41}\text{K}$  while the ions of interest  $^{40}\text{K}/^{40}\text{Ca}$  are at the turn-around point in the mirrors, where they are insensitive to the switching of the drift tube.
- The fifth pulse is an observation gate used to synchronise the visualisation of the MCP signals on the scope or the data acquisition system with the expected time of arrival of the ions on the MCP (see next section). This gate was usually limited to  $4\ \mu\text{s}$ .
- A last pulse is used to switch the ejection E-lens to  $3\ \text{kV}$ , in order to disperse an eventual bunch of unwanted contaminant and protect the MCP (not represented in the chronogram).

#### 4.2.5 Diagnostics and acquisition

PILGRIM is equipped with a Faraday Cup (FC) and two MCPs. The FC and the first MCP are each mounted on a piston and are positioned in front of each other in the first 6-ways cross (see Fig. 4.2). The software command prevents the two diagnostics from being inserted in the beam line at the same time. The FC can be optionally powered with a low voltage to prevent the electrons that could be knocked out of the cup from escaping. The reading of the FC and its ring are done on two pico-amperes. The MCP helps determining the ToF width of the bunch

before trapping. In the third 6-ways cross, two grids can be inserted to attenuate the beam and protect the end-pipe MCP from a high beam intensity (see again Fig. 4.2). These grids have an attenuation factor of 10 and 100 respectively and can be inserted at the same time to achieve a total attenuation factor of 1000. As it intercepts 90% of the beam, the first grid is also used as a FC to qualitatively check the transmission of the beam through the MR-ToF-MS in shoot through mode.

The reading of the signals from the MCP was solely done with an oscilloscope in the first place, but was then replaced with a more elaborate setup as shown in Fig. 4.6. As described above, the pulse generator delivers signals used to control the switches of the blade deflector and of the drift tube. Another gate is used to synchronise the observation with the estimated time of arrival of the bunch on the MCP. This pulse is used as a START signal in a FASTER acquisition system. Whenever an ion hits the MCP, it generates a pulse of variable height which is amplified in a pre-amplifier. The signal is then sent to a Constant Fraction Discriminator to cancel the timing variation due to the difference in pulse height. The output signal of the CFD is used as the STOP of the FASTER acquisition. FASTER is a modular digital acquisition system developed by LPC-Caen [92]. It is triggerless: input signals are digitised and are assigned a timestamp. Correlations between input channels can be performed online or offline according to the user's wish. The time resolution is limited by the 500 MHz clock to 2 ns. The START and STOP names of the channels in Fig. 4.6 are merely here to help the reader, since the system only returns the difference between the timestamps of the two digitised signals, if this difference is within a certain pre-defined time gate. Thus in our case the observation gate and the signal from the CFD do not define the START and the STOP of a Time-to-Amplitude Converter. The data are analysed offline using ROOT, which allows us to fit the ToF profile of the bunch and have a precise measurement of the FWHM bunchwidth.

In parallel, we measure the number of counts on the MCP in and out of the observation gate by using a coincidence unit and a scaler module (see Fig. 4.6). This module helps us figuring out if the time of arrival of the bunch of interest is outside the observation gate. Also the difference between the two scalers when the bunch of interest is inside the gate indicates the amount of contamination reaching the MCP. For instance, when observing mass 40, this contamination can be due to:

- $^{23}\text{Na}$  ions which were found as contaminant alkali delivered by the source (see 4.3.4 below). If the timing is set to capture mass 40, these ions are already outside the drift tube when it is pulsed to 0V.
- $^{39}\text{K}$  and  $^{41}\text{K}$  ions if they happen to be in phase with mass 40 when it is ejected.
- contaminant ions created by the full-range gauges.

In addition, we still use an oscilloscope for fast check of the injection/ejection of the bunch and qualitative estimate of the bunchwidth

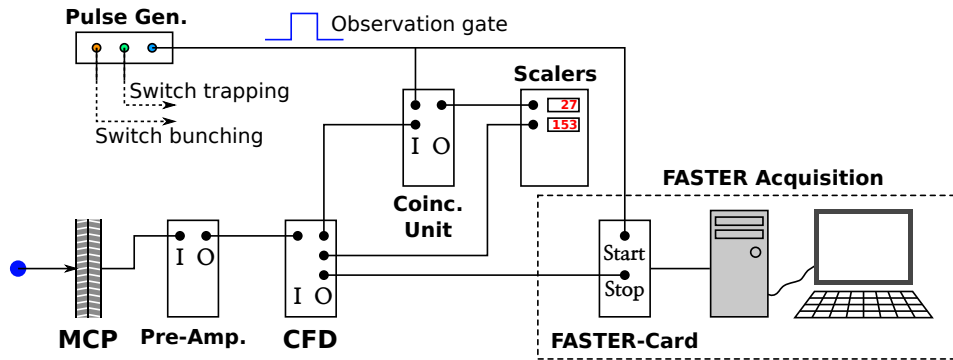


Figure 4.6 – ToF measurement setup at LPC-Caen. The START and STOP signals of the acquisition are given by an observation gate and by the modified MCP signal. The FASTER system digitises these signals, then calculates and displays their time difference. We also used scalars to measure the number of ions hitting the MCP, in coincidence or not with the observation gate.

(not shown in the figure). The oscilloscope triggers on the rising edge of the observation gate and reads the output of the coincidence unit. By averaging this last signal over a long time we can even obtain a smooth peak shape on which the FWHM can be measured, though less precisely than with the ROOT fit.

We also decided to monitor the temperature of the spectrometer to check the effect of thermal expansion on the ToF. The temperature is measured on a flat spot on one of the invar rods of the drift tube with a wide range ultra-high vacuum Pt100 resistor from Allectra.

## 4.3 EXPERIMENT AND PARALLEL SIMULATIONS

### 4.3.1 Beam tuning

The first step of the experiment was to optimise the optics of the ion source. We started the source by heating the filament at a  $\sim 8$  W power, corresponding to a heating potential of 5.3 V applied to the filament (10 V maximum). Though we knew that the ionisation rate of calcium would be very weak at this low power, we chose to keep a heating potential between 4 and 5.5 V in order to spare the source during the preliminary tests. The acceleration potential was put at 3 kV, matching the kinetic energy of the ions used in the simulations of PILGRIM, and the extraction potential at 2800 V. We used the two ammeters to measure the current from the ion source on the FC and on the ring electrode, respectively. The current on the FC was around 30 pA, or  $\sim 200$  ions per  $\mu$ s. Once the source intensity was stable, we tuned the E-lenses from the source to focus the beam on the FC. This was done by trying to maximise the current on the FC and minimise the current on the ring. However, it was only after applying a small deflecting potential on the steering electrodes that we managed to completely cancel the ring current. This indicates that the beam was probably slightly off-axis before the steering.

We had no proper way of measuring the emittance of this beam, but we tried nevertheless to deduce a rough estimate by making some assumptions. We first used the mobile slits to measure a beam profile at the position of the slits then used this beam profile to deduce an angular spread, knowing the distance between the blades and the collimator, and considered the diameter of the collimator to be roughly the size of the beam (see Fig. 4.7).

For each slit, we moved one blade by steps of 1 mm and observed the evolution of the current on the FC. A loss in intensity on the FC means that this blade intercepts a part of the beam. Since both the slits are located on one side of the collimator and the FC on the other one, the intensity loss corresponds to a part of the beam which would have gone through the collimator without the blade. In addition, the emittance of the beam after the collimator is the same as the emittance of the part of the beam before the collimator that would go through it. Thus profiling the beam with the blades, even before the collimator is equivalent to profiling the beam after it, as long as the FC is after the collimator. The dependency of the intensity to the blade position is given in Fig. 4.8 for both slits, from which we deduce the beam profile.

We use the X and Y spread at the positions of the slits to determine the root mean square (RMS) angular spread of the beam (see Fig. 4.7). We consider that the RMS angular spread in both axes should be the same and thus we average the angular spread values obtained on the two axes at  $0.48^\circ$ . We calculate the emittance on the collimator, whose aperture size is known. At the position of the aperture we expect the distribution in transverse position to be greater on the beam axis, or in the worse case scenario uniform over the 1 mm aperture. In the later case, the radius containing 95% of transverse spread distribution would be  $0.95 * 1/2 = 0.475$  mm. Thus we can estimate that the maximum emittance of the beam going through the collimator is  $15.9 \pi$ .mm.mrad.

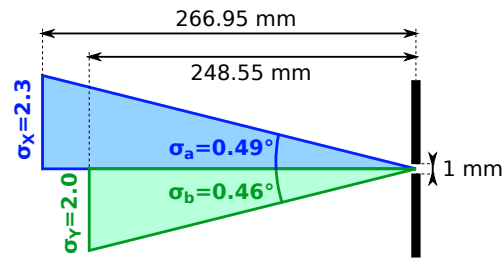


Figure 4.7 – Estimation of the emittance using the transverse beam profiles spreads.

After this we tried to increase the transmission of the beam through PILGRIM in shoot-through mode. All mirror electrodes were put at a new set of potentials optimised for this test setup (see next section). The ammeter previously used on the ring was plugged to the 10% transmission grid. We tuned again the source optics, along with the injection and ejection lenses from the PILGRIM ensemble, to maximise the current on the grid. Under these new optical conditions, the current on both the FC and the grid was around 10 pA. This beam tuning has been repeated many times since and though the intensity itself varied, depending on the source heating, the intensity on the grid was repeatedly found to be between 80% and 100% of the FC current. We should mention the fact that the **ion current** on the grid cannot be higher than 90% of the one on the

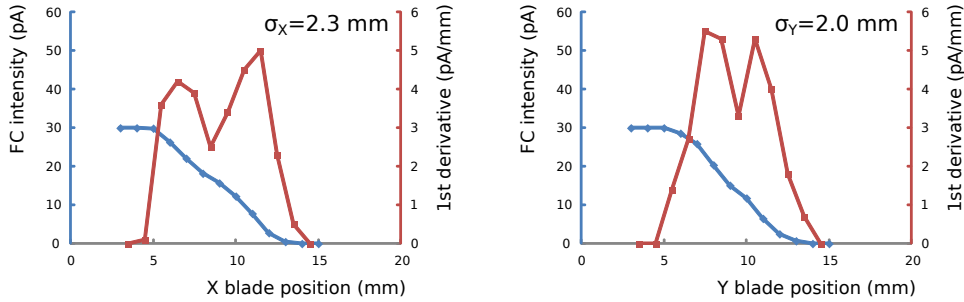


Figure 4.8 – **Blue**: intensity on the FC as a function of the position of a blade from the X-slit (left) or the Y-slit (right). **Red**: first derivative of the intensity to deduce the beam profile. The calculated spread in transverse position is given for each graph. The error on the measurement of the FC-intensity is typically 0.2 pA.

FC, but the **electronic current** that we actually measure can, if the ions knock off some electrons while impinging on the grid.

Once the bunching and the trap were operational, the source optics and the injection/ejection E-lenses were optimised again using the scalers (see Fig. 4.6) to maximise the number of counts per cycle on the MCP.

#### 4.3.2 Bunching

Simulations of the full experimental setup at LPC Caen have been performed by Y. Liu in the course of his master thesis. In particular, simulations of the bunching are crucial, as it defines the ToF size of the bunch and its occupancy of the phase space. We already stated that the performances of PILGRIM relies widely on the longitudinal and transversal emittances of the input bunch. In simulations, the lower blade of the deflector was at 150 V most of the time and was pulsed at 0 V for 1100 ns, which led to a bunchwidth of  $\simeq 100$  ns FWHM upon entering in the mirrors. At an energy of 3 keV, ions of mass 40 take  $\simeq 1 \mu\text{s}$  to fly through the length of the blade deflector. Therefore, we initially interpreted the pulse length to be simply the sum of the output bunchwidth and the time needed for an ion of mass 40 to pass next to the two grounded blade, undeflected. However, this simple interpretation hides the origins of the bunch peculiar characteristics.

Fig. 4.9 shows the effect of the blade deflector for different times of arrival of the ions in the deflector.  $t_{\text{switch}1}$  and  $t_{\text{switch}2}$  are the switch-off and switch-on times of the deflector, respectively. The **U** graphs show the deflecting potential. In all 3 cases **a**, **b** and **c**, the green ion is the earliest and the red ion is the latest (prior to the deflector, the beam is still continuous). In the **a** case, ions enter the deflector before the blade has been switched off. Thus the ions are deflected until the deflector is turned off, and the green ion experiences the deflecting field for a longer time and is thus more deflected. In the **b** case, ions are still between the blade when the deflector is turned on again. In this case, the green ion "feels" the deflecting field for a shorter time and thus is less deflected. Thus the angle of deflection decreases with the time of arrival in case **a** and increase in case **b**, indicating we are to expect a minimum angle of deflection in

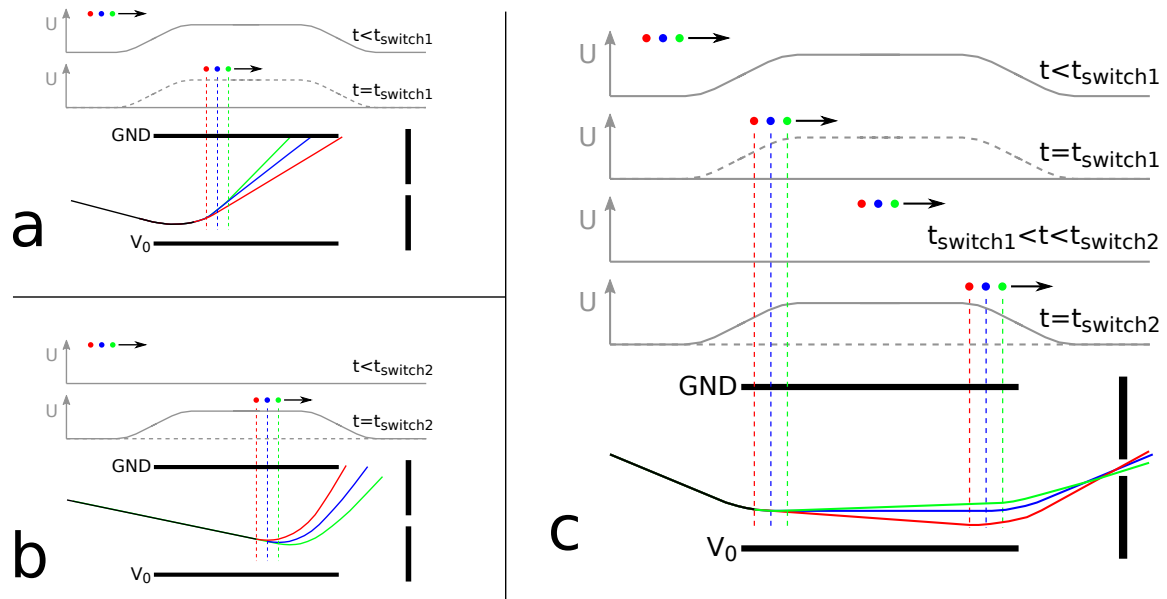


Figure 4.9 – Effect of the pulsing of the deflector blade on the ions in 3 different scenarios. The deflector blades, the collimator are schematically pictured and are not at scale. The deflection angles are exaggerated for understanding. In grey is the deflecting potential between the blades for several times. **a**: ions enter the deflector before the bottom blade has been switched to 0 V. **b**: ions enter the deflector after the blade has been switched to ground potential but do not exit the deflector before the blade is switched back to 150V. **c**: ions enter the deflector as the blade is switched off and exit while the blade is switched back on. The coloured dotted lines mark the position of the ions at the time of a switch. Details of the consequences in text.

between. The pulsing of the deflector is responsible for a back-and-forth sweeping of the deflection angle, and a bunch is created when the beam crosses the aperture of the collimator. Of course, if the deflector is "open" long enough and provided that the ions are injected along the optical axis, the minimum angle of deflection should be  $0^\circ$ . However, it was verified in simulations that the 1100 ns time window was not enough for any ion of mass 40 to pass completely undeflected, as the field of deflection is larger than the blades themselves and typically extends from the steerers to the collimator. As the minimum deflection angle is not  $0^\circ$  for mass 40, only ions making a certain angle with the optical axis before the deflection will pass through the collimator. This is the reason why the input ions make an angle with the optical axis in Fig. 4.9.

Ideally the steering potential, the deflecting potential and the gate width should be chosen so that only the ions with the minimum deflection angle can go through the aperture. If the steering potential is wrongly set and pre-constrains the beam to an angle below  $0^\circ$ , the minimum deflection angle can be lower than  $0^\circ$  as well and the beam can pass twice in front of the aperture, thereby creating two bunches. In Fig. 4.9, this would favour the transmission of the red ion in case **a** and of the green ion in case **b**, and the beam would be lost below the aperture in case **c**. Such an effect is particularly visible for long bunch durations (or equivalently faster ions), for which the end and the beginning of the bunch are well separated. This was confirmed experimentally by comparing the ToF profiles of  $^{23}\text{Na}$  and  $^{39}\text{K}$ . As the 1100 ns gate duration was optimised for producing a short bunch at mass 40, the ToF profile of  $^{39}\text{K}$  showed

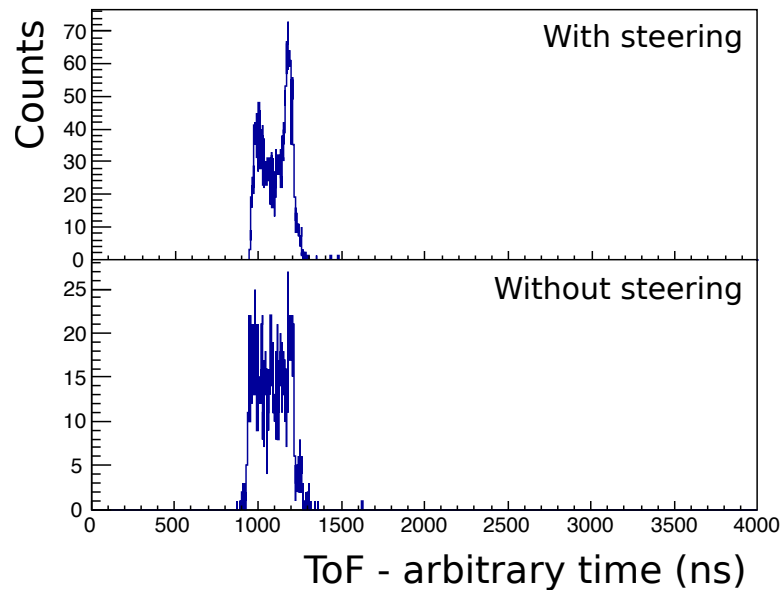


Figure 4.10 – ToF profile of  $^{23}\text{Na}$  on the end-pipe MCP after a 1100 ns bunching gate with and without steering. The flight time from the blade deflector to the MCP is  $\simeq 17.5 \mu\text{s}$ .

a single peak in shoot through mode and after a 16 ms trapping alike. However the corresponding ToF profile of  $^{23}\text{Na}$  measured on the end-pipe MCP exhibited two peaks as shown in Fig. 4.10-top. By removing the steering, we could reach a configuration where only the  $^{23}\text{Na}$  ions having the minimum deflection angle would go through the collimator and the double peak structure was reduced (see Fig. 4.10-bottom), which seem to confirm our interpretation.

Coming back to the configuration for bunching mass 40, we tried to understand the energy dispersion of the bunch in the simulations. The energy fluctuations due to the thermal energy of the ions before their acceleration should be below 1 eV. However the energy dispersion observed in simulations after bunching is 18 eV (RMS) around a mean energy of 3008 eV. Because the potentials applied to the two blades of the deflector are symmetric when the gate is opened (0V/0V) and asymmetric (150V/0V) when the gate is closed, the potential along the beam axis rises when the bottom blade is powered. Ions which are already in the deflecting field before it is switched off loose energy while ions which are still in the range of the deflector before it is switched on gain energy. The energy distribution of the simulated mass 40 bunch showed ion energies lower and higher than 3000 eV, which proves that most of the ions of this bunch are deflected twice (before the switch-off and after the switch-on) as pictured in the case c of Fig. 4.9.

The transient potential between the end of the blades and the collimator decreases almost linearly with the position on the optic axis. The ions of the mass 40 bunch are in this transient region when the bottom blade is pulsed to 150V, and thus experience a position-dependent energy kick (see Fig. 4.9), quite alike what happens during the ejection from a RFQCB. This effect is responsible for a high energy-ToF correlation after the col-



limator. This correlation is positive right after the collimator (i.e. ions of higher energy are late compared to ions of lower energy) and the bunch eventually reaches a ToF focus near the end of the exit mirror of PILGRIM in shoot-through mode. It is likely that for long bunches or light ions, the ToF would not be correlated with the energy in the middle of the bunch (because some ions would not experience the deflection field) but would still be correlated on the sides. This effect could probably accentuate the formation of the two bunches described before.

### 4.3.3 Beam characteristics and expected resolving power

The source optics and the timing of the deflector pulsing were optimised in simulations in order to reduce the transverse emittance and the ToF bunchwidth for mass 40. A realistic voltage switching on the deflector with a 70 ns rise/decay time was used. This corresponds to the performances of the switch used on the test bench. The bunch coming out of the collimator makes a rather large angle of  $\sim 1^\circ$  with the PILGRIM axis. Because of this, approximately half of the beam is lost on the first electrode of the injection E-lens. The rest of the beam trapped within PILGRIM has the following characteristics:

- a transverse emittance fluctuating between 3 and 4  $\pi$ .mm.mrad
- a high average angle of  $\sim 1.2^\circ$  just after focussing in the injection E-lens
- an energy spread of 42 eV FWHM
- a ToF bunchwidth of 64 ns FWHM, determined by simulation at the position of the external ground plate of PILGRIM on the injection side
- a theoretical minimum bunchwidth (the incompressible time) of 13 ns FWHM

The last value has been obtained by correcting offline the energy-ToF correlation of the bunch. The difference between the two values of the ToF bunchwidth is due to the fact that the bunch is still highly correlated to the energy before it reaches PILGRIM. We showed in the previous section that the performances of PILGRIM depend largely on the injection. As the bunch in these simulations is very different from the one which was considered for S3 setup, Y. Liu had to re-optimize the potentials of the different electrodes of the PILGRIM ensemble for this specific bunch. Using a new optimal set of potentials, we could obtain a 53 ns FWHM bunchwidth after a 16 ms flight (1000 revolutions inside the trap), corresponding to a resolving power of  $\simeq 150000$ . During the experiments, we used the sets of potentials and timings which were optimised in simulation. We proceeded only to minor adjustments in order to achieve the best resolving powers, as will be described below.

### 4.3.4 Shoot-through mode

Before starting to trap ions in PILGRIM, we used the setup in shoot-through mode, i.e. without switching the drift tube. We scanned the ToF

spectrum on the end-pipe MCP up to a few tens of  $\mu\text{s}$  and observed 2 bunches at 16.36 and 21.26  $\mu\text{s}$  after the rising edge of the bunching pulse, defining the time of the creation of the bunches. Knowing the approximate time of arrival for mass 40 from the simulations, and knowing that the heating power of the source was probably too low to ionise calcium, we identified the peak at 21.26  $\mu\text{s}$  as  $^{39}\text{K}$  and the one at 16.36  $\mu\text{s}$  as  $^{23}\text{Na}$ . The ratio of ToF between two ions of same energy is related to the ratio of their masses by:

$$\frac{TOF_{m_1}}{TOF_{m_2}} = \sqrt{\frac{m_1}{m_2}} \quad (4.1)$$

and thus  $TOF_{23} = 21.26\sqrt{23/39} = 16.33 \mu\text{s}$ , which is in very good agreement with what we observed. After more data was accumulated, we spotted a small peak in the ToF spectrum near the one of  $^{39}\text{K}$ , whose position and comparative height were consistent with  $^{41}\text{K}$ .

#### 4.3.5 Trapping

The first step was to find the time of injection of the bunch in PILGRIM. We focused on mass 39 as  $^{39}\text{K}$  was both highly produced (93.26% of K natural abundance) and close to the mass of interest. The  $^{39}\text{K}$  bunch is found to arrive at 23.4  $\mu\text{s}$  with the drift tube powered, but not pulsed. There is a small difference with the previous section because the ToF in shoot through mode was measured while the potential of the drift tube was 0 V. The switching time of the pulsed drift tube is then calculated to be 11.7  $\mu\text{s}$  as the position of the blade deflector and the position of the MCP happen to be almost symmetrical with respect to the centre of the drift tube. Simulations predicted a round trip time of  $\simeq 16 \mu\text{s}$ . Thus we configured the pulse controlling the drift tube with a delay of 11.7  $\mu\text{s}$  and a gate width of 16  $\mu\text{s}$ . By doing so, the  $^{39}\text{K}$  peak completely disappeared from the ToF spectrum at 23.4  $\mu\text{s}$  and could be found back at 39.4  $\mu\text{s}$ , confirming the trapping of the bunch for one turn. We then processed to increase gradually the number of turns, measuring each time the time of arrival on the MCP:

- shoot-through: 23.4  $\mu\text{s}$
- 1 revolution: 39.4  $\mu\text{s}$
- 2 revolutions: 55.4  $\mu\text{s}$
- 10 revolutions: 183.6  $\mu\text{s}$
- 60 revolutions: 983.7  $\mu\text{s}$
- 100 revolutions: 1625.0  $\mu\text{s}$

We used the ToF to measure a round trip time of 16.015  $\mu\text{s}$ . In order to tune precisely the ejection time at a high number of turns, we adopted the following strategy. Let  $t$  be the total ToF of an ion,  $t_O$  its observation time in the ToF spectrum,  $D_O$  the delay on the observation gate and  $t_E$  the ejection time. We have:

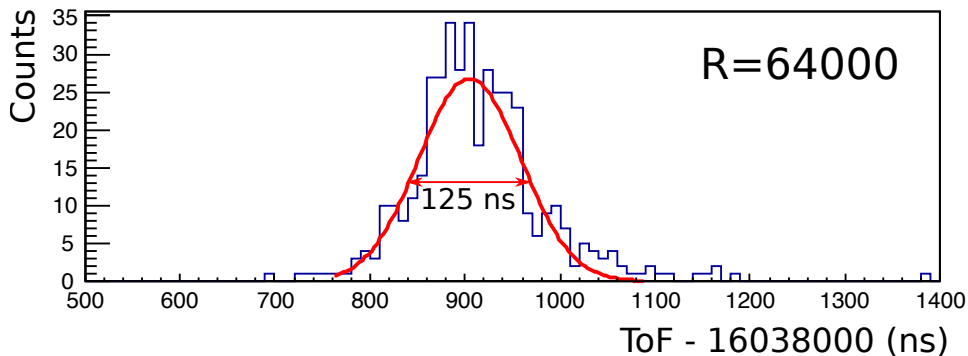


Figure 4.11 – ToF profile measured with FASTER after a 16 ms flight and measurement of the corresponding sensitivity.

$$t - t_E = t_O + (D_O - t_E) \quad (4.2)$$

For a different number of turns, we tune the observation delay  $D_O$  to keep the observation time  $t_O$  constant (i.e. to keep the peak at the same position in the time spectrum) while keeping the  $(D_O - t_E)$  difference constant. According to the previous equation, this implies that  $t - t_E$  is the same for different number of turns, which means that the ion is ejected from the same point in the drift tube.

Trapping times up to 32 ms have been achieved, but were not pursued because of the low repetition rate and thus, low statistics, of such a long trapping. We limited ourselves to 1000 turns (16 ms) and tried to optimise the resolving power. When mass 39 makes 1000 turns, mass 41 makes 975.3 turns. At this fraction of a turn the bunch of  $^{41}\text{K}$  is in one of the mirror at the time of ejection and thus is not ejected and does not contaminate the ToF spectrum of  $^{39}\text{K}$ . We used the set of potentials calculated for the LPC setup as a starting point and tuned the potentials of the mirror electrodes to reduce the bunchwidth after 1000 turns. Within two weeks from the first trapping of an ion bunch, we managed to measure precisely  $\Delta\text{ToF}_{FWHM} = 125.2(66)$  ns by fitting a gaussian curve on the ToF distribution given by the FASTER acquisition (see Fig. 4.11). This corresponds to a resolving power of  $\frac{T}{\Delta T} = 63.9(34) \cdot 10^3$ . Resolving powers around 65k have been achieved many times since. A maximum resolving power of  $\simeq 77\text{k}$  was once achieved but couldn't be maintained for more than an hour.

#### 4.3.6 Measurement stability

The round-trip time has been noticed to slowly vary from 16.013 up to 16.017  $\mu\text{s}$  over a few hours. This change in ToF was first tentatively attributed to the variation in temperature of the invar rods. However, the dependency of the relative ToF to the temperature was later estimated to be of the order of  $25 \cdot 10^{-6} \text{ K}^{-1}$  (4 ns difference over a  $\sim 10\text{K}$  temperature variation), while the expected thermal expansion coefficient for invar is  $1.2 \cdot 10^{-6} \text{ K}^{-1}$ . We then suspected that the temperature has an even more pronounced effect on the stability of the ISEG HV supplies. The data sheet of the power supplies from the ISEG DPS series indicates a dependency of the voltage to the temperature below  $5 \cdot 10^{-5} \text{ K}^{-1}$ . We measured this

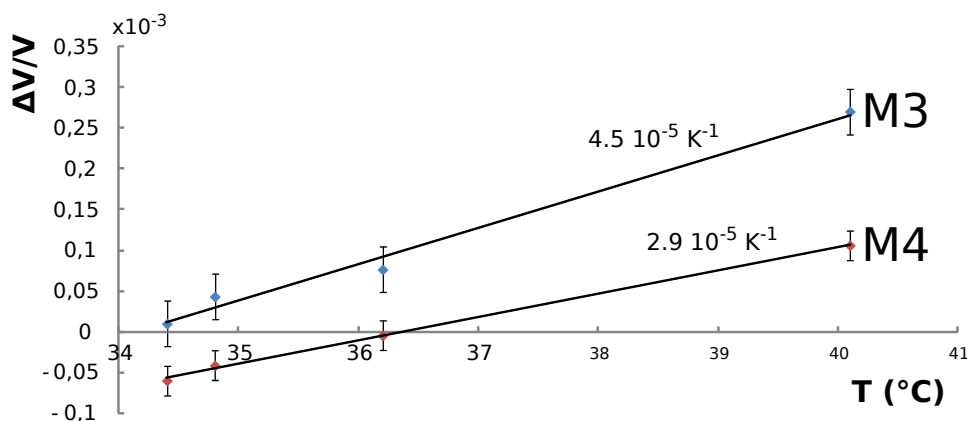


Figure 4.12 – Relative potential as a function of the temperature of the ISEG crate for mirror electrodes M3 and M4.

dependency for the mirror electrodes 3 and 4. The ToF and the bunch-width are most sensitive to the potentials of these electrodes because they define the potential at the turn-back point of the ions in the mirrors. We measured the potentials on the voltage reading of the user interface and used the temperature signal delivered by the ISEG crates. The values of the potentials on the reading were fluctuating and we considered the error on the potentials to be  $\simeq 50$  mV. Using a cooling fan, we decreased the temperature of the ISEG crate and observed the variation of the potentials on the electrodes M3 and M4. Fig. 4.12 confirms that the sensitivity of the power supply to the crate temperature is below, but in the order of,  $5 \cdot 10^{-5} \text{ K}^{-1}$ .

We then measured systematically the dependency of the ToF with respect to the potential of the different mirrors. This was done by measuring the variation of the peak position in the ToF spectrum while varying the potential of a given electrode. Tab. 4.1 gives the sensitivity of the ToF to the potential and the sensitivity of the potential to the temperature. We then deduce the sensitivity of the ToF to the temperature for all mirror electrodes. If we consider that the temperature affects all power supplies in the same way, the ToF sensitivities of each electrode to the temperature add up and the total ToF sensitivity of PILGRIM to the temperature due to the power supply instability is around  $-1.6 \cdot 10^{-5} \text{ K}^{-1}$ . This seem to explain to a good extent the observed variation of ToF during the day.

At a constant temperature, the ISEG power supplies are expected to have a precision of 10 ppm on the potential. Using the third column of Tab. 4.1, we expect a maximum precision on the ToF of 3.5 ppm, which corresponds to a maximum resolving power of  $\sim 600000$ . Thus, the voltage precision is not a limiting factor for resolving isobars on this setup, provided that the temperature can be controlled or measured to  $\sim 0.1\text{K}$ .

#### 4.3.7 Search for the mass 40 doublet

As shown in section 4.3.5, the necessary resolving power to separate  $^{40}\text{K}$  from  $^{40}\text{Ca}$  at FWHM has been exceeded by a factor greater than 2. Therefore, we tried to observe the separation of the two isobars. We chose

El.	U (V)	$S_{\text{ToF}/V}$ ( $\mu\text{s}/\text{V}$ )	$S_{\delta\text{ToF}/\delta V}$	$S_{\delta V/T}$ ( $\text{K}^{-1}$ )	$S_{\delta\text{ToF}/T}$ ( $\text{K}^{-1}$ )
IEL	-2847.86	0.2	0.036	$< 5 \cdot 10^{-5}$	$< 1.8 \cdot 10^{-6}$
M1	-2959.89	0.2	0.037	$< 5 \cdot 10^{-5}$	$< 1.8 \cdot 10^{-6}$
M2	1542.53	0.2	0.019	$< 5 \cdot 10^{-5}$	$< 0.9 \cdot 10^{-6}$
M3	1802.18	-2	-0.225	$4.5 \cdot 10^{-5}$	$-10.1 \cdot 10^{-6}$
M4	2709.18	-1.5	-0.254	$2.9 \cdot 10^{-5}$	$-7.3 \cdot 10^{-6}$
M5	2705.98	-0.2	-0.034	$< 5 \cdot 10^{-5}$	$> -1.7 \cdot 10^{-6}$

Table 4.1 – Potentials ( $U$ ) and various sensitivities ( $S$ ) for all mirror electrodes (M1 – 5) and the Inner Einzel Lens (IEL).  $S_{\text{ToF}/V}$ : measured sensitivity of the ToF to the potential;  $S_{\delta\text{ToF}/\delta V}$ : sensitivity of the relative ToF (for a 16  $\mu\text{s}$  flight) to the relative potential;  $S_{\delta V/T}$ : sensitivity of the relative potential to the temperature;  $S_{\delta\text{ToF}/T}$ : deduced sensitivity of the relative ToF to the temperature.

to set the trapping time for 500 turns to reach a higher repetition rate and thus better statistics. Instead of optimising the mirror potentials for this flight time, we kept the same set of potentials optimised for 1000 turns and tuned only the potential of the drift tube to set the ToF focus point on the MCP. This was suggested by R.N. Wolf and L. Schweikhard and is described in [58]. With this method we managed to achieve a resolving power of 64k at 500 turns for mass 39. We then extrapolated the injection and ejection times to mass 40 using Eq. 4.1. We increased the heating potential of the source to 9.5V, close to the maximum value allowed by our power supply (10V) hoping to produce Ca ions. This voltage is already well above the specification given by Heatwave (maximum 7V).

The very high amount of  $^{23}\text{Na}$ ,  $^{39}\text{K}$  and  $^{41}\text{K}$  produced for this strong heating could damage the MCP and therefore, we tried to prevent these bunches from reaching the detector. Firstly, mass 23 and mass 40 are separated during the drift time between the buncher and the middle of the trap, but they are not separated enough to allow sequential trapping of the two masses nor are they close enough to trap both at once. In order to stop the  $^{23}\text{Na}$  bunch before the MCP, we used the last pulse described in section 4.2.4 to command the switching of the output Einzel-lens at 3 kV and disperse the sodium beam. Thanks to the small aperture of PILGRIM's ground shield, this does not affect the potentials inside the trap.

Masses 39, 40 and 41 are only little separated when they reach the drift tube and we have no choice but to trap them together. Thus, we tried to find a number of turns close to 500 for which mass 40 is ejected towards the MCP and masses 39 and 41 are ejected on the injection side. This is true if we find an ejection time corresponding to an integer number of turns at mass 40 and a half-integer number of turns for the two other masses. Let us consider that the drift tube is pulsed to 0V at a time  $t_{I,1}$  when mass  $m_1 = 40$  is exactly in the middle of the trap, and pulsed up again when  $m_1$  is in the middle of the trap after  $N$  turns. Thus the time of ejection  $t_{E,1}$  is given by:

$$t_{E,1} = t_{I,1} + NT_1 \quad (4.3)$$

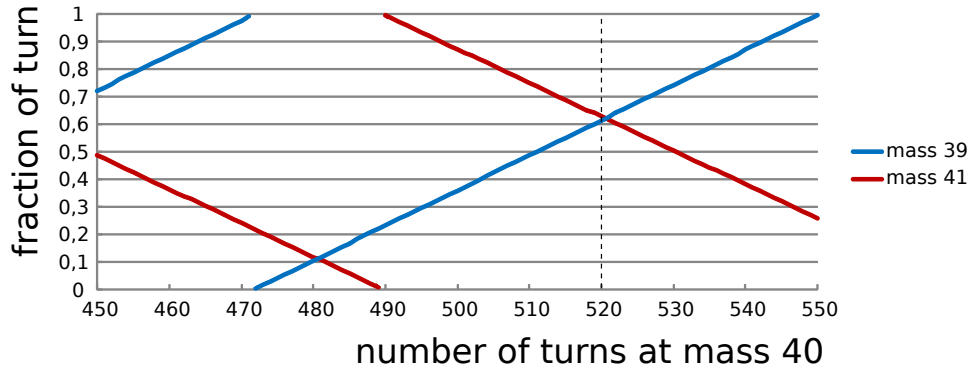


Figure 4.13 – Fractional part of  $M$  as a function of  $N$  for  $m_2 = 39$  and 41.

where  $T_1$  is the round trip time of mass  $m_1$  inside PILGRIM. If we introduce a mass  $m_2$ , the ejection time is:

$$t_{E,2} = t_{E,1} = t_{I,2} + (t_{I,1} - t_{I,2}) + NT_1 \quad (4.4)$$

where  $t_{I,2}$  is the time for which the ions of mass  $m_2$  reach the middle of the trap. The term  $(t_{I,1} - t_{I,2})$  accounts for the phase difference at injection for ions of different masses, due to the drift section between the buncher and the trap. The previous equation can be written:

$$t_{E,2} = t_{I,2} + MT_2 \quad \text{with} \quad M = \frac{t_{I,1}}{T_1} \left( 1 - \sqrt{\frac{m_1}{m_2}} \right) + N \sqrt{\frac{m_1}{m_2}} \quad (4.5)$$

where  $M$  is the number of turns traveled by mass  $m_2$  during the time taken by mass  $m_1$  to travel  $N$  turns. Thus, if  $m_1$  is the mass of interest and  $m_2$  a contaminant, we look for a half-integer  $M$  and an integer  $N$  to eject the contaminants on the injection side and the ions of interest on the MCP side. Fig. 4.13 shows the fractional part of the number of turns of  $^{39}\text{K}$  and  $^{41}\text{K}$ . The best compromise to eject  $m_2 = 39$  and 41 at once is found for 520 turns at mass 40. For this trapping time,  $^{39}\text{K}$  travels 526.62 turns and  $^{41}\text{K}$  travels 513.63 turns. For a fractional part of a turn of  $\simeq 0.6$  an ion is at the verge of the drift tube. Though we chose this configuration for the ejection of the contaminants, it is possible that some of them remain trapped after the drift tube as been switched on.

We made a few runs of rather short duration ( $\sim 30$  min) to avoid a drift in ToF due to temperature variations and to try different potentials of the drift tube. On each spectrum regrettably, a single peak could be observed at the expected position of mass 40, along with a background noise for which a possible explanation is given below (see Fig. 4.14). The ratio of the number of counts for mass 40 and 39,  $N_{40}/N_{39}$  was consistent with the ratio of natural abundances of the corresponding potassium isotopes. In addition, no peak could be found by tuning the trapping gate for mass  $^{44}\text{Ca}$ , the second most abundant isotope of calcium. Thus no evidence could be found of the presence of calcium in the spectrum, separated or not from potassium.

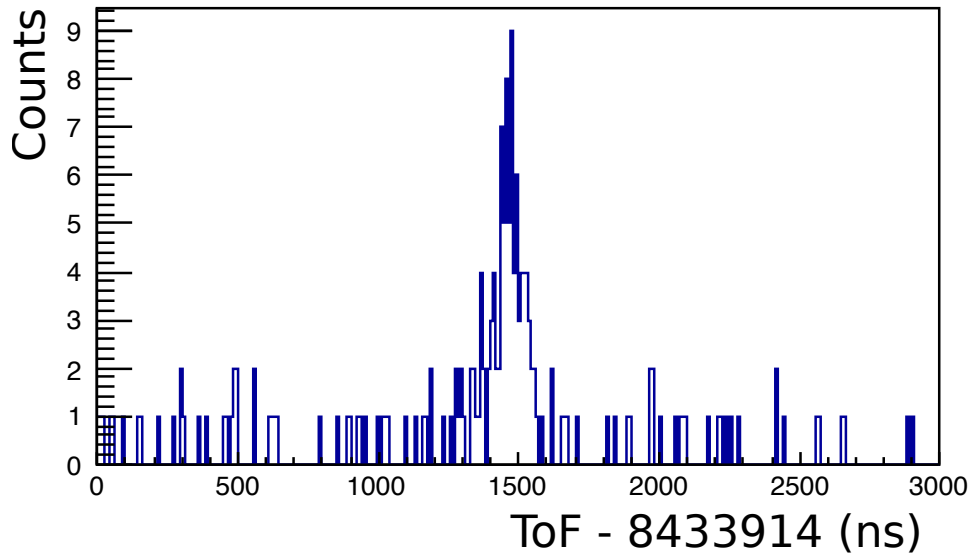


Figure 4.14 – ToF spectrum at mass 40 exhibiting low statistics and a background noise.

$^{40}\text{Ca}$  is obviously very weakly produced in our case. In [49] Schury and collaborators managed to separate the two isobars with a resolving power of  $\simeq 150000$  and observed that  $^{40}\text{K}$  was  $\sim 6$  times more abundant than  $^{40}\text{Ca}$ . It is possible to calculate that for this ratio, the actual resolving power needed so  $^{40}\text{Ca}$  is separated at FWHM from the tail of  $^{40}\text{K}$  is around 45000. Several reasons could explain why we were not able to observe  $^{40}\text{Ca}$ , some giving possible tracks for further improvements:

- I. If  $^{39}\text{K}$  and  $^{41}\text{K}$  are imperfectly ejected, a part of the contamination could remain in the trap. Because the drift tube is pulsed when the contaminants are close to the transition region, these ions might experience an important energy spread, which could result in a constant background in the ToF spectra of the next cycles.
- II. The important quantity of trapped  $^{39}\text{K}$  could create a local space charge which affects the flight path of ions of mass 40.
- III. The abundance ratio of  $^{40}\text{Ca}/^{40}\text{K}$  could be less than in [49]. As we cannot increase the heating of the source, this would require increasing the resolving power.

The first problem could both be solved by ejecting selectively  $^{39}\text{K}$  and  $^{41}\text{K}$ , while mass 40 is in one of the mirrors. Ejecting both at once towards the injection side while keeping the mass 40 inside the trap is not possible at low ToF. However, it is possible to eject  $^{39}\text{K}$  on the injection side and  $^{41}\text{K}$  on the ejection side without ejecting mass 40 from the trap. Performing a calculation of the number of turns similar to the previous one, we can find a clean ejection timing after mass 40 travelled 220.75 turns (i.e. it is in the mirror on the injection side). For this timing, the drift tube is pulsed after  $^{41}\text{K}$  travelled 218.05 turns and  $^{39}\text{K}$  travelled 223.55 turns. As a comparison, trapped ions start leaving the potential of the drift tube when the fractional part of their number of turns is around 0.12 or 0.62, meaning that both  $^{39}\text{K}$  and  $^{41}\text{K}$  are ejected. Since the contaminants would be ejected at a lower number of turns than the ions of interest ( $\sim 500$  turns), this

also partially solves the second problem. This solution would require to pulse again the ejection E-lens to disperse the  $^{41}\text{K}$  in a addition to the  $^{23}\text{Na}$ .

Increasing the resolving power would probably require deeper changes in the setup. During the tests for isobaric separation we also tried to set the trapping gate for 2000 turns at mass 39 and optimised the resolving power by tuning the ToF focus with the potential of the drift tube and we reached a resolving power of  $\simeq 65000$ . The fact that the optimal resolving power is roughly the same at 500, 1000 and 2000 turns could indicate that the ToF dispersion is almost entirely determined by the second order ToF aberration of geometric and kinetic origins and thus cannot increase for a longer ToF. The high median angle of the bunches predicted by the simulations could explain the geometric part. We mentioned earlier that the part of the incompressible time is very low in the simulated bunch (13 ns). Provided that these simulations are reliable enough, this would be consistent with the fact that the geometric and kinetic aberrations start to dominate the ToF dispersion at a rather low number of turns.

#### 4.3.8 Towards higher resolving powers

In order to achieve a better resolving power with this setup, we attempted to perform a better bunching by pulsing symmetrically the X+ and X- steering electrodes instead of pulsing asymmetrically the blades. The biggest advantage of symmetric pulsing is that the potential on the optical axis is 0 V, whether the potentials of the steerers are switched on or not. This bunching method was simulated as well and could create a bunch with an energy spread of 4.6 eV FWHM, which is almost 10 times smaller than with the previous bunching method. The observed energy dispersion is simply explained by the dispersion in transverse position at the time of the switching. The simulated bunch had also a lesser median angle than before, to the point that no ion crashed on the injection E-lens. Maybe owing to this fact, the emittance of this new bunch was higher ( $6 - 7 \pi \cdot \text{mm} \cdot \text{mrad}$ ). Like before we calculated the incompressible time. The deduced value, 14 ns, is not significantly higher than for the previous bunching. The potentials of PILGRIM were optimised again for this new method and a resolving power over 300k has been obtained in simulation, probably owing to the lesser median angle and energy dispersion.

This new method requires an additional HV switch to pulse both X+ and X-. In order to test the bunching, we used the switch previously assigned to the ejection E-lens to disperse the  $^{23}\text{Na}$ . Unfortunately, the switch from the deflecting blade broke before we could test this method. Thus we are 2 switches short to fulfil the fully operational setup that we envision for testing again the separation of  $^{40}\text{K}/^{40}\text{Ca}$ .

## CONCLUSION

In the course of a 2-months experiment on a brand new instrument, we have been able to repeatedly achieve:



- beam chopping on the continuous beam of a thermal ion source
- trapping of ion bunches for extended times above 30 ms
- resolving powers of 65000

The resolving power of the setup seems to be limited by the properties of the created bunch and the repeatability of the results for a given potential set is limited by the instability of the ISEG power supplies when facing quick temperature changes. We already plan to try a new bunching method to enhance the resolving power and hopefully reach the separation of isobars for the first time in Caen. In the future, ion bunches will be created by a dedicated RFQCB, providing a much cleaner beam. Also we plan to invest in a temperature-regulated electrical rack to maintain the stability of the power supplies over extended periods of time. When the ToF for a given mass will be stable enough, we will try to measure the mass of ions with respect to the mass of isobars or neighbouring isotopes.

# OPTIMIZATION AND DESIGN OF THE 90° ELECTROSTATIC DEFLECTOR

## CONTENTS

6.1	GOALS OF THE EXPERIMENT . . . . .	119
6.2	DESCRIPTION OF THE EXPERIMENT . . . . .	119
6.2.1	General description . . . . .	119
6.2.2	EXOGAM . . . . .	120
6.2.3	DIAMANT . . . . .	122
6.2.4	NWall . . . . .	123
6.2.5	Acquisition . . . . .	123
6.3	CALIBRATION OF THE DETECTORS . . . . .	126
6.3.1	EXOGAM . . . . .	126
6.3.2	DIAMANT . . . . .	137
6.3.3	NWall . . . . .	137
6.4	PRE-ANALYSIS . . . . .	138
6.4.1	Expected reactions and contaminations (Ar and C) . . . . .	138
6.4.2	Background reduction and scattering rejection in EXOGAM . . . . .	138
6.4.3	Neutron identification in NWall . . . . .	140
6.4.4	Scattering rejection in NWall . . . . .	141
6.4.5	Charged particles identification in DIAMANT . . . . .	141
6.5	SPIN AND POLARITY ASSIGNMENTS . . . . .	144
6.5.1	DCO ratios and polarisation asymmetries . . . . .	145
6.5.2	<sup>94</sup> Pd . . . . .	148
	CHAPTER CONCLUSION . . . . .	151

**I**N this chapter, we detail the design of the electrostatic deflector meant to precede PILGRIM in the beam line. We explain the requirements of this deflector and detail the optimization procedures that were applied to both its geometry and potentials. The performances of several types of deflector are compared. The usage of two consecutive deflectors has also been explored. The overall study helped deciding the layout of the end of the S3 Low Energy Beam line.



## 5.1 MOTIVATIONS

The necessity of designing a Multi-direction 90° deflector arose from the layouts of the S<sub>3</sub>-LEB and DESIR installations.

In S<sub>3</sub>-LEB, the beam arrives from the gas-stopping cell of S<sub>3</sub> before being deflected by a C-shaped RFQ and bunched in a RFQCB. Afterwards, it must be carried to the S<sub>3</sub> decay station or towards the DESIR facility. Thus, this must involve some kind of beam deflecting switchyard. In addition, the space available at the end of the LEB line was insufficient to fit the PILGRIM spectrometer and this multi-direction

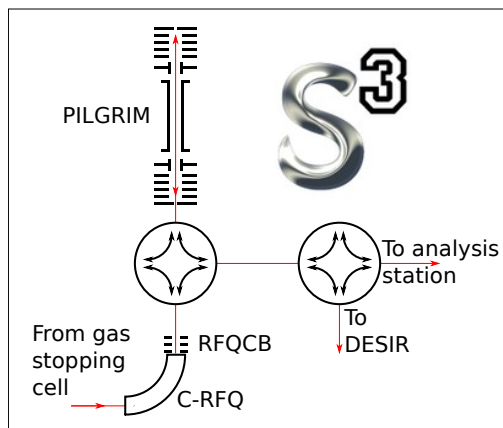


Figure 5.1 – PILGRIM layout in S<sub>3</sub> and beam distribution through 2 deflectors.

switchyard. It was therefore decided to add a second deflector and to put PILGRIM on a "side track" of the beam line as pictured in Fig. 5.1.

In DESIR the PILGRIM spectrometer and the PIPERADE double Penning trap will be on a line parallel to the input beam line. We need to be able to send the beam coming from the GPIB<sup>1</sup> either directly to PIPERADE or to PILGRIM for isobaric purification before PIPERADE. Thus two deflectors are again needed (see Fig. 5.2).

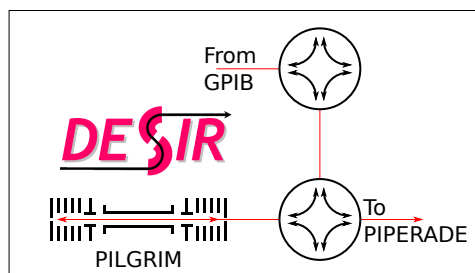


Figure 5.2 – Expected PILGRIM layout in DESIR and beam distribution using the same 2 deflectors.

As stated in Chapter 2, the deflection of charged particles is done with a magnetic field according to the  $\frac{p}{q}$  ratio and with an electric field according to the  $\frac{K}{q}$  ratio. In both S<sub>3</sub>-LEB and DESIR setups, ions are extracted and accelerated from a linear buncher Paul trap by a dipolar electric field. An ion accelerated under a potential  $U$  is deflected by a field  $\mathbf{B}$  perpendicular to the plane of deflection with a radius of curvature:

$$r_B = \frac{1}{\|\mathbf{B}\|} \sqrt{\frac{2mU}{q}} \quad (5.1)$$

The same ion, deflected this time by an electric field  $\mathbf{E}$  perpendicular to its motion follows a path of radius:

$$r_E = \frac{2U}{\|\mathbf{E}\|} \quad (5.2)$$

<sup>1</sup>General Purpose Ion Buncher

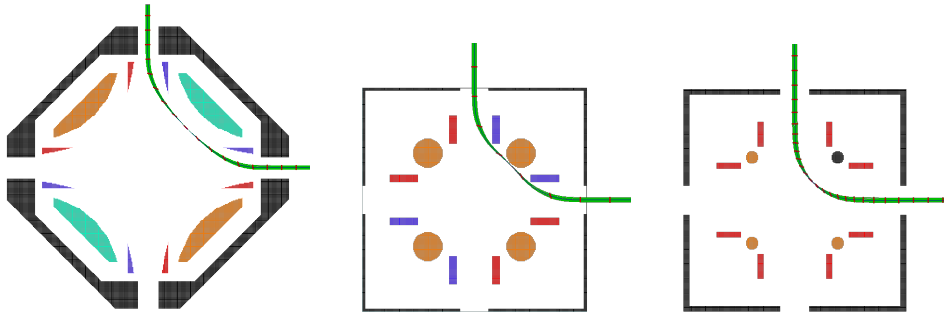


Figure 5.3 – Three different concepts of deflector and their voltage supplies. Electrodes with the same colour have the same potential (see details in text). Only the first one is true quadrupolar deflector. The green beam is an ensemble of trajectories simulated with SIMION. The first design is 700 mm wide, while the others two are 500 mm wide.

This shows simply that the ion trajectory in any electrostatic device does not depend on the  $\frac{m}{q}$  ratio as long as the ions have been accelerated with a purely electrostatic field. This fact combined with the large cost and size of magnetic dipoles advocated the study of an electrostatic beam deflector. This deflector must be able to deflect the beam at  $\pm 90^\circ$  or let it pass undeflected. Such "4-ways" switchyard is thus fundamentally different from the electrostatic deflectors mentioned in Chapter 2.

We studied in particular the case of the multidirectional quadrupole deflector. Such devices have been around for a long time [93] and are implemented in several installations [94, 95]. This kind of deflector is usually used in a small version ( $\sim 10$  cm) to deliver ion beams to short beam lines but introduces aberrations for ions far from the optical axis. In order to limit these aberration, it was decided from the beginning to design a large-sized object with a  $\sim 50$  cm edge length. The electrodes used in such devices are usually long in the direction perpendicular to the deflection plane (see e.g. the commercial deflector from [96]), in order to get rid of the edge effect due to finite size electrodes. This is of course unrealistic for the large apparatus that we are envisaging. We explain in the next section how we compensate for the edge effects.

Because MR-ToF devices are very sensitive to both transversal and longitudinal emittances, the optical design of this deflector will play a crucial role in the final performances of PILGRIM. Especially energy-related ToF-spread can be corrected in PILGRIM but ToF aberrations due to odd-order geometric terms cannot. Thus the dimensions of the electrodes and the potentials applied to it have to be optimised to reduce the optical aberrations to a minimum compatible with a subsequent injection into PILGRIM.

## 5.2 OPTIMIZATION

### 5.2.1 Deflector concepts and optimised parameters

We optimised the geometry and potential of several deflector designs with different voltage supplies, as shown in Fig. 5.3. The first design is

a conventional quadrupolar deflector and has opposite potentials on its two sets of opposite partially-cylindrical electrodes (orange and light blue on the drawing). The radius of the cylindrical electrodes is 1.13 times the radius of the circle inscribed between them, which is close to the values suggested in [97, 98]. Additionally, 4 sets of blade electrodes of opposite polarity (red and dark blue) help in defining the hyperbolic potential expected from a quadrupole field. The next two designs use fully-cylindrical electrodes and have the triangular blades replaced by rectangular ones. We deliberately simplified the geometry to ease the mechanical design. In the second concept, the cylindrical electrodes are at the same potential and thus the beam is deflected by two 45° dipolar deflectors. In the third concept the rectangular electrodes are all at the same potential and 3 of the 4 cylindrical electrodes are at high potential while the last one is grounded. In this configuration the cylindrical electrodes ensure the bending while the rectangular ones have a focussing role. The last two concepts are not considered as quadrupolar even though from an etymological point of view they do have "4 poles". A simplified geometry of the first concept was also optimised but could not match the performances of the full geometry and for this reason is not detailed here.

For each concept, two potentials corresponding to the cylindrical electrodes and the blades were optimised. The geometry of the first concept was not optimised as it was an expanded version of a deflector design installed at NSCL [99]. For the second and third designs, the dimensions and position of the cylindrical and rectangular electrodes, as well as the thickness and the opening window of the grounding electrode, were also parameters of the optimisation (see Fig. 5.4). In order to limit the space taken by the vacuum chamber it was considered for each deflector to use the grounding electrode both as an electrical shield and as the vacuum chamber itself.

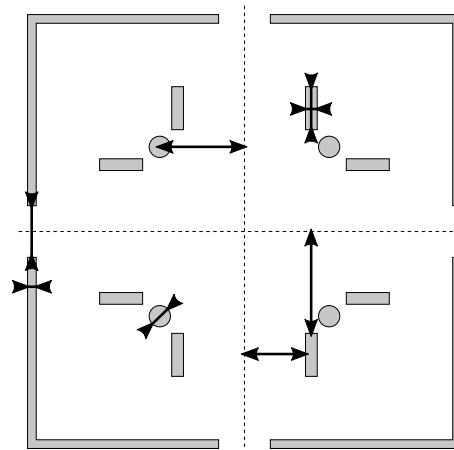


Figure 5.4 – Scheme of the third configuration showing the adjustable geometric parameters that have been optimised.

### 5.2.2 Criteria

A reference beam was chosen to optimise the deflector. The injected bunch of 11 ions had no time spread, no energy spread and was perfectly parallel to the input beam axis. The ions were initially distributed in a 10 mm line sequence in the direction perpendicular to the beam axis, in the plane of deflection. The main criterium of optimisation is to leave such a beam unchanged after passing through the deflector. As such, the output bunch should still be parallel ( $\sigma_{V_x} \simeq 0$ ), be centred around the beam axis ( $\bar{x} \simeq 0$ ), have no ToF spread ( $\sigma_{ToF} \simeq 0$ ) and remain symmetrical if injected so. For this last criterium we define an asymmetry factor  $F_{asym}$  as the root mean

square of the sum of the transverse position of ions injected symmetrically ( $x_i + x_{-i}$ ). This factor should be close to 0 as well to reduce the beam asymmetry. The goal function used for the optimisation was:

$$s = \bar{x} + 20 * \sigma_{V_x} + 30 * \sigma_{ToF} + F_{asym} \quad (5.3)$$

The coefficients in this function were initially arbitrary and were chosen after testing several goal functions and observing the results and convergence speed of a potential optimisation. Of course, the reference beam is not realistic as the transversal and longitudinal emittances are zero. Nevertheless, it is important that the emittance does not increase after deflection. The adopted strategy is therefore the optimisation of the deflector using these reference beam and goal function, followed by an *a posteriori* check with a more realistic beam. Because there are a lot of parameters to optimise, it is likely that the goal function has numerous local minima. Thus the optimal results presented next are not necessarily the very best ones, even though they are satisfactory.

### 5.2.3 Method

Like for PILGRIM, we used the SIMION 8.1 software to calculate the fields created by the electrodes and the trajectories of the ions within. We started the optimisation on the 2D geometries of the concepts which we mentioned previously in order to select the most promising one. The potentials are again optimised with the Nelder-Mead algorithm. Potentials and geometry are optimised separately, firstly because the time taken to change a geometric parameter and refine the potential map is much longer than the time needed to simply change a potential in the software and secondly because the simplex optimiser applied to the geometry would lead to electrodes size or position which are not an integer number of SIMION grid cells.

Like for PILGRIM, each potential optimisation was restarted twice after randomising the optimal set to increase the chance of finding a better optimum. After the potential optimisation, one geometric parameter was changed by one custom graduation (usually 1 or 2 mm) and the potentials were optimised again for this new geometry. After changing this parameter several times ( $\sim 10 - 20$  times), it was changed back to its initial value and the next geometric parameter started to be scanned as well. Once all parameters had been scanned, the best set of geometry and potential was used as a new starting point for the next optimisation cycle. Numerous cycles were performed until the goal function could not be minimised by changing any of the geometric parameters by one grid unit.

The geometries were then optimised again in 3D following the same procedure, with two minor differences:

- I. The third dimension and the associated edge effect were taken into account, which modified the previously optimal geometry and brought a few additional geometric parameters to optimise as well.

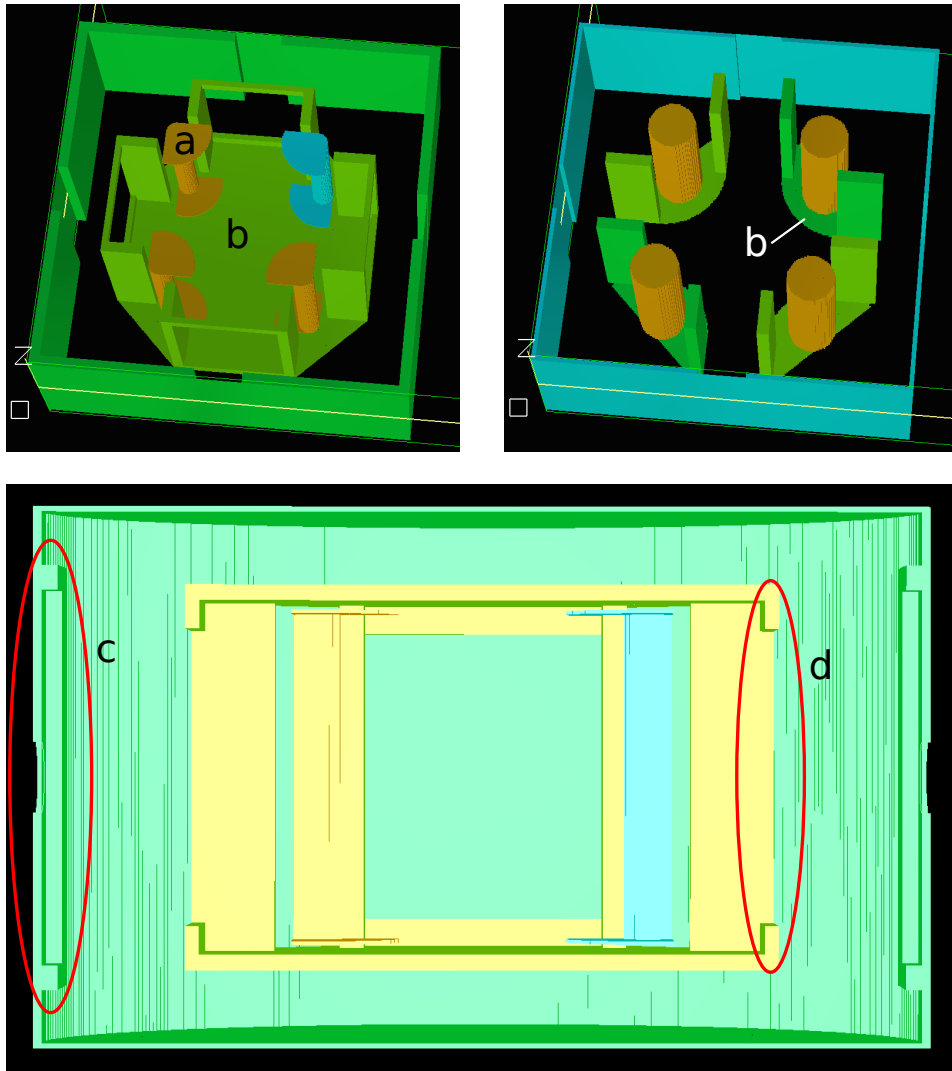


Figure 5.5 – **Top:** 3D layout of the second and third configurations. *a* and *b* mark the shields of the cylindrical and rectangular electrodes, respectively. In the second configuration, all rectangular electrodes are held together by the two octagonal shields. **Bottom:** sideview of one of the deflectors showing new geometric parameters to optimise. *c* is the input/output aperture in the grounded electrode. *d* is the aperture in the octagonal box for the second concept.

II. The deflector was then optimised with a bunch of 22 ions initially spread in a cross-like pattern along the two axes perpendicular to the beam direction.

In the 3D version, the cylindrical and rectangular electrodes are equipped with shields to reproduce the effect of infinite electrodes in the direction perpendicular to the deflection plane (see Fig. 5.5, top) and to reduce the contribution of the grounded vacuum chamber to the electric field in the middle of the deflector. The shields are separated when they belong to electrodes with different potentials. The shape of the shields was chosen so as to mimic a quadrupolar shaped field. The size and thickness of the shields, as well as the height and depth of the vertical apertures (see Fig. 5.5, bottom) have been optimised as well. Several shield shapes have been tested and optimised for each deflector concept.



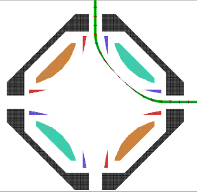
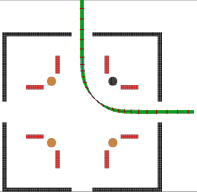
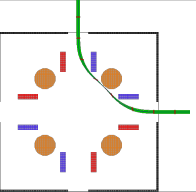
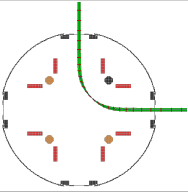
Name	Quad	NQuad	NQuad 2	NQuad Cyl.
Geometry				
$\sigma_{ToF}$ (ns)	1.06	0.40	0.78	0.59
$\sigma_{V_y}$ (mm/ns)	46.84	2.46	7.44	1.89
V1	+/- 1564.2	+ 5274.5	- 331.5	+ 5773.938
V2	+/- 1701.9	+ 2100.3	+/- 2271.2	+ 2155.349

Table 5.1 – Comparison of optimisation results from different deflectors.

### 5.3 RESULTS

Tab. 5.1 shows the results of the present optimisation. The quadrupolar deflector was only optimised in 2D as it failed to match the same performances as the others. The 2 non-quadrupolar deflectors have been optimised in 3D. Since it was mechanically advantageous to build a cylindrical chamber instead of a square one and because the second deflector was giving the best results, it was decided to change the geometry of this particular deflector (see fourth column of Tab. 5.1). All 3D non-quadrupolar configurations have better optimisation results than the 2D quadrupolar one. The NQuad concept and its cylindrical counterpart exhibit the lowest ToF and angle spreads. However, it should be noticed that the potential applied on the cylindrical electrodes is much higher for these than for the other two configurations, for which the dipolar field between the triangular/rectangular electrodes ensures most of the beam deflection. This implies that the corresponding HV sources and switches would be more expensive.

What can be observed for all optimised geometries is that the reference beam meets a focal point on the 45° plane and is also symmetric with respect to this plane. The fact that the beam is reversed and symmetric at 45° guarantees that two ions symmetric with respect to the beam axis and injected parallel to it will have travelled paths of equal length, which means that the ToF is independent of the position at first order (and all odd orders). The even orders were passively canceled out by the optimisation. However if we choose to use a non-parallel input beam, the focal point is not at 45° and the first order dependency reappears as shown in Fig. 5.6-left. In addition, ions with an energy different from the one for which the deflector was optimised end up with a final transverse position different from the initial one (Fig. 5.6-right).

Considering the beam optics notations of Chapter 2, the state of the beam after deflection (index  $d$ ) can be expressed at first order with respect to its state before (index  $i$ ) as:

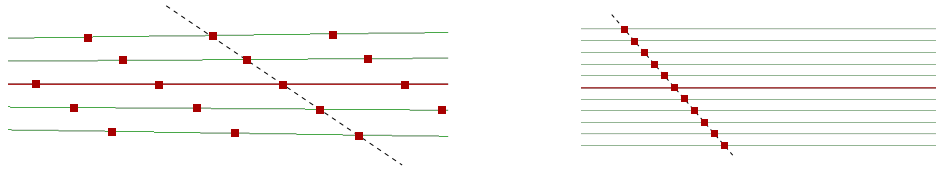


Figure 5.6 – Ions after deflection. The red line is the reference beam axis, the green lines are the ions trajectories and the red dots represent a fixed ToF. **Left:** point like source on the beam axis, angular spread. The output ToF spread is  $\sim 100$  ns/degree. **Right:** same point like source, but with energy spread. The transverse position spread is  $\sim 0.1$  mm/eV at 3 keV.

$$\begin{pmatrix} x_d \\ a_d \\ y_d \\ b_d \\ \delta_{K,d} \\ \delta_{t,d} \end{pmatrix} = D \begin{pmatrix} x_i \\ a_i \\ y_i \\ b_i \\ \delta_{K,i} \\ \delta_{t,i} \end{pmatrix} \quad (5.4)$$

With

$$D = \begin{pmatrix} -1 & (x|a) & 0 & 0 & (x|\delta_K) & 0 \\ 0 & -1 & 0 & 0 & 0 & 0 \\ 0 & 0 & 1 & (y|b) & 0 & 0 \\ 0 & 0 & 0 & 1 & 0 & 0 \\ 0 & 0 & 0 & 0 & 1 & 0 \\ 0 & (\delta_t|a) & 0 & 0 & (\delta_t|\delta_K) & 1 \end{pmatrix} \quad (5.5)$$

Where  $x$  and  $y$  are the directions perpendicular to the beam axis in the plane of deflection and perpendicular to it, respectively, and  $a$  and  $b$  are the corresponding angles. In red are shown the two matrix elements corresponding to the aforementioned effects. The first two diagonal values are negative because the beam is reversed in the  $x$  coordinate but not in the  $y$  one. This matrix is simplified for the purpose of the explanation as several "0" are actually very small finite coefficients. In the following, we write  $l_1 = -(x|a)$ ,  $l_2 = (y|b)$  and  $\tau_1 = (\delta_t|\delta_K)$ . We also write  $l_3 = +/- (x|\delta_K)$  and  $\tau_2 = +/- (\delta_t|a)$  depending if the deflector bends the beam in the **left direction** or in the **right direction**. Especially, the correlation between the ToF and the direction is harmful to the performances of PILGRIM. At this point of the study we were left with two choices: we could either send the ions in the deflector with a reduced angular spread (and thus an increased transverse position spread) to limit the ToF spread after the deflection, or combine the deflector with an other optical setup to cancel the first order contribution. We explore both the solutions in the following sections.

## 5.4 DOUBLE DEFLECTOR

### 5.4.1 U and S-configurations

By using 2 deflectors in a row it is possible to cancel the red terms in Eq. 5.5. We will call U- and S-configurations, the arrangement of two de-

flectors turning in the same direction and in different directions, respectively. The first order transfer matrices  $U$  and  $S$  can be expressed as:

$$U = \begin{pmatrix} 1 & 2l_1 & 0 & 0 & 0 & 0 \\ 0 & 1 & 0 & 0 & 0 & 0 \\ 0 & 0 & 1 & 2l_2 & 0 & 0 \\ 0 & 0 & 0 & 1 & 0 & 0 \\ 0 & 0 & 0 & 0 & 1 & 0 \\ 0 & 0 & 0 & 0 & 2\tau_1 & 1 \end{pmatrix} \quad (5.6)$$

and

$$S = \begin{pmatrix} 1 & 2l_1 & 0 & 0 & \pm 2l_3 & 0 \\ 0 & 1 & 0 & 0 & 0 & 0 \\ 0 & 0 & 1 & 2l_2 & 0 & 0 \\ 0 & 0 & 0 & 1 & 0 & 0 \\ 0 & 0 & 0 & 0 & 1 & 0 \\ 0 & \mp 2\tau_2 & 0 & 0 & 2\tau_1 & 1 \end{pmatrix} \quad (5.7)$$

the presence of a drift section between the two deflector would only increase the  $U_{1,2}$ ,  $U_{3,4}$ ,  $U_{6,5}$ ,  $S_{1,2}$ ,  $S_{3,4}$  and  $S_{6,5}$  matrix elements. Looking at the layout of S3-LEB, we have all types of deflection:

- A single deflection from the RFQCB or from PILGRIM to the analysis station. Any beam of realistic emittance will have a slight ToF after a single deflection due to  $\tau_2$ . Therefore, the Bradbury-Nielsen Gate should be placed before the deflector in order to have the best mass selection after separation in PILGRIM.
- A U-configuration from the RFQCB to DESIR, for which the only first-order contribution to the ToF dispersion is due to the kinetic energy, as it would be the case in a drift section.
- A S-configuration from PILGRIM to DESIR, for which the ToF dispersion due to the angular spread is simply twice the one for a single deflection.

In the last two cases the ToF bunchwidth matters little as the beam will be re-bunched at the beginning of the DESIR beam line. Meanwhile in the considered DESIR layout we have:

- A U-configuration from the general purpose ion buncher to PILGRIM. Thus the ToF bunchwidth is only energy-dependent at first order, which can be corrected in PILGRIM.
- A S-configuration from the GPIB to PIPERADE if no purification by PILGRIM is needed.

Note that we can also skip the S-configuration by using the U-configuration and making a single reflexion inside PILGRIM. Also we will see at the end of this chapter that it could be possible to cancel the  $S_{1,5}$  and  $S_{6,2}$  matrix element by adding an additional optical system between the 2 deflectors.

### 5.4.2 Comparison of double deflector performances

We compare here the effect of initial angle and energy spread on the deflected beam for a single deflection and the U-configuration, for each deflector concept. The idea here is to have a quantitative description of the  $D_{6,2}$  and  $D_{6,5}$  matrix elements and higher order coefficients and to see up to what extent these dependencies are suppressed in the U-configuration. Fig. 5.7 shows the ToF bunchwidth increasing with respect to the angular and energy dispersions. The input beam has a uniform transverse position distribution over 10 mm in the plane of deflection and various angle and energy spreads. The dispersions in angle and energy are also uniform, which makes the beam quite unrealistic. Simulations with realistic beams confirming the following results are detailed in the next section. In the first graph, we can confirm that the double deflection cancels the ToF increase due to the first order coefficient ( $\delta_t|a$ ). The NQuad2 configuration gives the lowest dependency for a single deflection. When using two deflectors in the U-configuration, the 3 non-quadrupolar concepts outmatch the quadrupolar one, as long as the angular spread is below 10 mrad FWHM. Under these conditions, the ToF spread can reach a few ns only, which is insignificant compared to the 50 ns expected from a RFQCB. The second graph shows that the ToF is independent of the energy in the quadrupolar case and is a linear function of the energy in the other cases. Thus in this respect, the 3 non-quadrupolar concepts are equivalent to drift sections of different lengths. The longest "drift section" is achieved by 2 cylindrical deflectors in a U arrangement. However, we mentioned in Chapters 2 and 3 that by tuning the potential of the pulsed drift tube in PILGRIM, we can control the first order coefficient ( $\delta_t|\delta_K$ ) inside the trap. The third graph makes the assumption that we could correct the linear part of the curves from the second graph, leaving only a constant bunchwidth due to the very low, and previously neglected, first order ( $\delta_t|x$ ) coefficient. The very constant behaviour of all the curves proves that the second order coefficient ( $\delta_t|\delta_K\delta_K$ ) and all subsequent even orders are extremely low. Two NQuad Cyl deflector in a U arrangement increase the bunchwidth by only 1.2 ns.

It can be noticed that the NQuad and NQuad Cyl configurations have almost the same results except for the constant part due to the transverse position spread. Regarding the ToF dependency to the angular dispersion, the Quad deflector is generally better than these last two in single deflector mode, but is easily outclassed in U configuration by all other concepts. The NQuad2 version has the lowest angular-related ToF spread in single deflector mode and has a very reasonable ToF spread in all other matters. However in this configuration, the beam passes very close to one of the cylindrical electrodes (see Fig. 5.3) which can distort or even cut the emittance profile. Thus, we decided to develop the cylindrical deflector which has very good performances in the U arrangement, in order to facilitate the mechanical design and spare the cost of a very large square vacuum chamber, which would have been the case with the other versions.

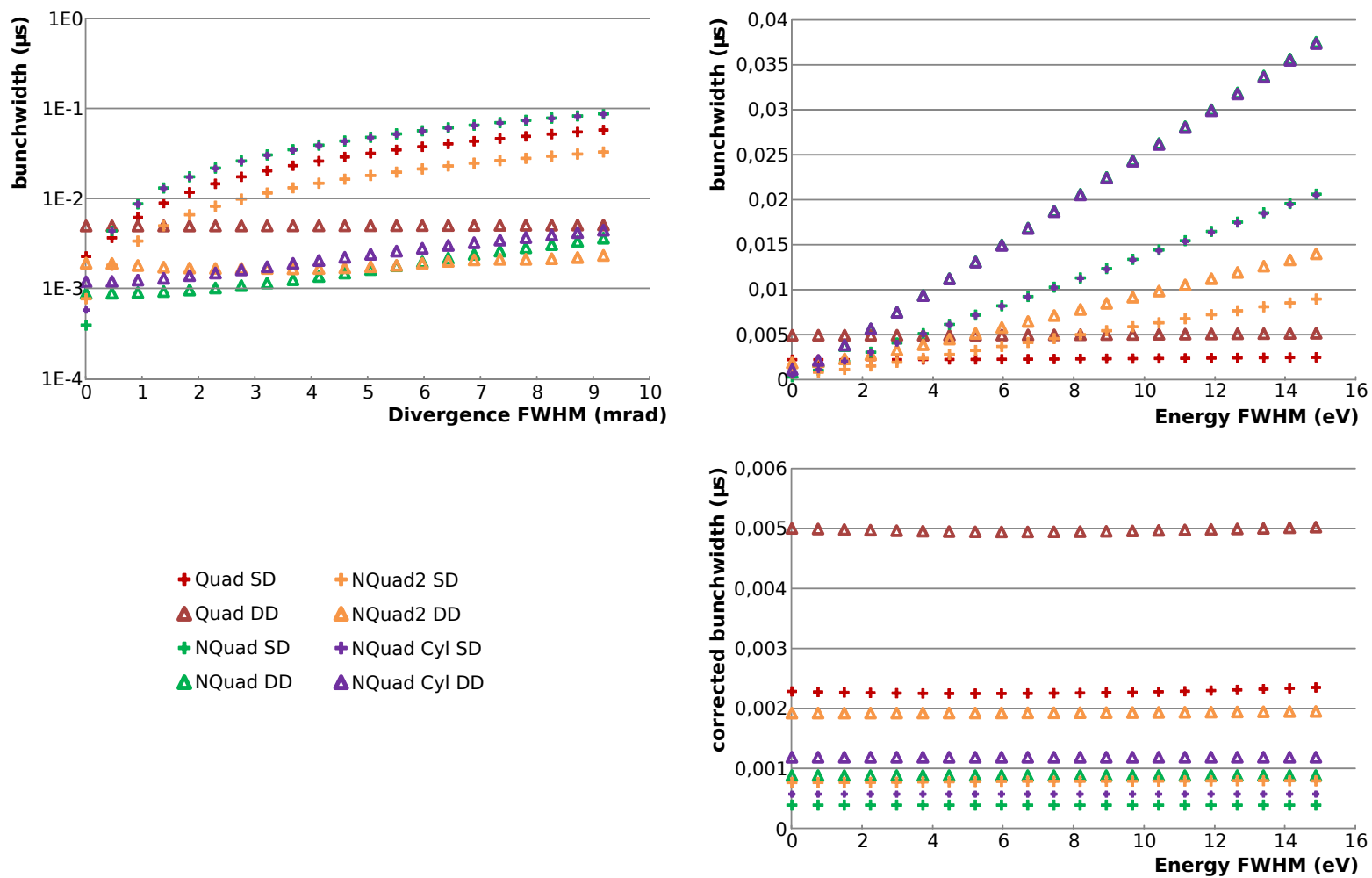


Figure 5.7 – Comparison of the ToF bunchwidth (FWHM) for several deflectors, either in the Single Deflector configuration (SD) or Double Deflector one (DD). The initial beam has a uniform distribution in transverse position and has either an angle dispersion (top left) or an energy dispersion (top right). The bottom right figure shows what the ToF bunchwidth would be if we managed to apply a first order energy dependent correction in PILGRIM up to the ToF-focus. See comments in text.

## 5.5 REALISTIC BUNCHES

We have simulated the deflection of a beam with a realistic transverse emittance, without energy or ToF dispersion, through the cylindrical deflector. The input beam had a dispersion of 0.2 mm in transverse position and  $0.5^\circ$  in angle (RMS values) for an emittance of  $7 \pi \cdot \text{mm} \cdot \text{mrad}$ . We deliberately chose a beam with a low  $x$  dispersion and a rather high  $a$  dispersion to show the difference between a close-to-parallel beam and strongly dispersive one. In Fig. 5.8 top-left, we show the resulting ToF-spread. In Fig. 5.8 top-right, the ions are made almost parallel by an Einzel lens, reducing the ToF spread after deflection. The output ToF dispersions are consistent with the results of the previous section. A high ToF spread reduces the achievable resolving power. Assuming the resolving power is ultimately limited by the incompressible time  $\Delta t_{inc}$ , the maximum resolving power achievable after one deflection would be:

$$R_{Def} \simeq \sqrt{\frac{\Delta t_{inc}^2}{\Delta t_{inc}^2 + \Delta t_{Def}^2}} R_{NoDef} \quad (5.8)$$

Where  $\Delta t_{Def}$  is the ToF spread due to the angular dispersion before the deflector. Thus, even for the roughly parallel beam mentioned before, the maximum resolving power achievable in PILGRIM would be reduced by a factor 1.07 for  $\Delta t_{inc} = 50$  ns, 1.38 for  $\Delta t_{inc} = 20$  ns and 2.89 for  $\Delta t_{inc} = 7$  ns. For a very small emittance of  $2 \pi \cdot \text{mm} \cdot \text{mrad}$  these factors become 1.006, 1.037 and 1.272, respectively. In the bottom part of Fig. 5.8 are shown the emittance figures at three positions of the beam line (case  $7 \pi \cdot \text{mm} \cdot \text{mrad}$ ). It can be seen that in the case of a non-parallel injection, the deflector distorts the emittance profile. This effect was initially attributed to the second order cross dependency ( $a|ax$ ), meaning it would cancel itself in the U-configuration (this is only true because  $(a|a) \simeq (x|x) \simeq -1$ ). However this effect does not seem to be completely canceled out by the second deflector (see Fig. 5.9 right). A possible explanation for this residual distortion is given in the next section.

This banana shaped distortion has an indirect effect on the ToF: the small change in angular spread due to the first deflector can induce an equally small change in the ToF bunchwidth in the second deflector. More importantly, this distortion might lead ions in regions of the phase space where they would become unstable or phase-shifted in the MR-ToF-MS, which would reduce the transmission or resolving power of PILGRIM, respectively. The effect of the deflector on the phase-space and the importance of the input beam profile are discussed in the next section. While using a two deflectors system we see a symmetric curvature in the longitudinal position profile at a given ToF (Fig. 5.9 left), characteristic from a second order dependency to the angle, or  $(\delta_t|aa)$ . The ToF spread after the 2 deflectors is 7 ns without using the E-lens, and only 2 ns while using it.

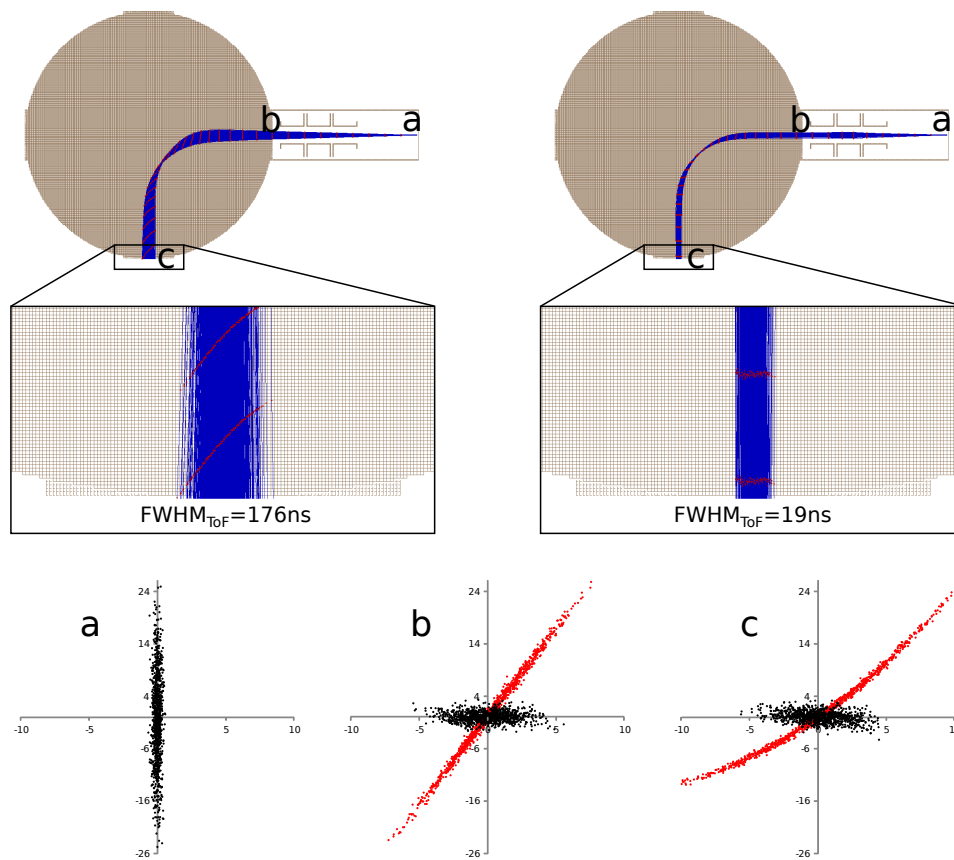


Figure 5.8 – **Top left:** injection of a beam with realistic emittance in the deflector. The Einzel lens on the drawing is at ground potential. **Top right:** Same beam, using the Einzel lens to make the beam roughly parallel before the deflection. **Bottom:** transverse emittance profiles of the beam in the plane of deflection. The profiles a, b and c refer to the state of the beam before the E-lens, after it, and after deflection, respectively. The black (resp. red) profile corresponds to an activated (resp. deactivated) E-lens. X and Y axes are in mm and mrad, respectively.

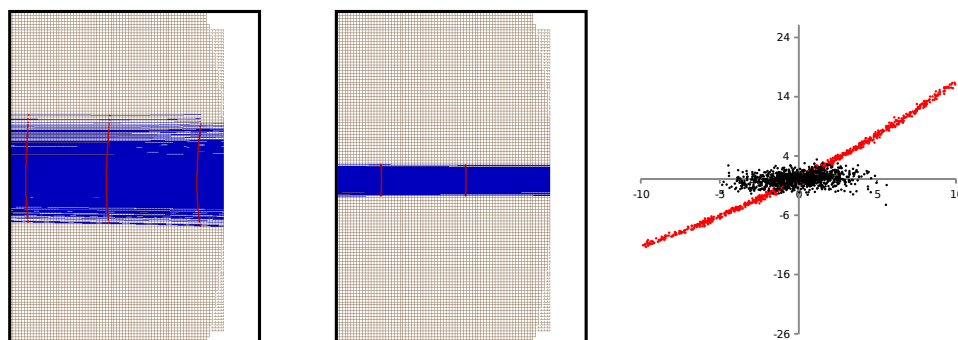


Figure 5.9 – SIMION simulations of the beam state after a double deflection in case the beam was previously focused (middle figure and black emittance profile) or not (left figure and red emittance profile).

## 5.6 PROPER USAGE OF THE DEFLECTOR.

### 5.6.1 Modelling the deflector in Mathematica

In order to have a better understanding of the cylindrical deflector we fitted the parameters of the beam after deflection, and obtained  $(x|x)$ ,  $(x|xx)$ ,  $(x|xxx)$ ,  $(x|a)$ ,  $(x|\delta_K)$ ,  $(a|a)$ ,  $(a|x)$ ,  $(a|xx)$ ,  $(a|ax)$ ,  $(a|axx)$ ,  $(\delta_t|\delta_K)$  and  $(\delta_t|a)$ . We used these values to create a simplified mathematical model of the deflector with the Wolfram Mathematica software. Fig. 5.10 shows the geometric behaviour of the deflector after one or two deflections. All plots display an output value on the colour scale as a function of the input  $x$  on the X axis and the input  $a$  on the Y axis. On the left are the output  $x$  and  $a$  after deflection on the colour axis v.s. the input  $x$  and  $a$ . The values on the colour axis are given in absolute value so that two ions of opposite  $x$  or  $a$  after deflection will have the same colour on the graphs. The green dashed lines show what the graph would be by considering  $(x|x) = (a|a) = -1$  and taking only  $(x|a)$  into account. Thus these lines show the results for an aberration-free deflector, equivalent to a drift section and the differences between the green dashed lines and the thin black ones exhibit the distortion of the emittance profile. The graphs on the right of Fig. 5.10 show the asymmetries in the output  $x$  and  $a$  profiles. The asymmetry for an output quantity  $\chi$  ( $\chi = x$  or  $a$ ) depending on the input  $x$  and  $a$  is defined here as:

$$A_\chi(x, a) = \left| \frac{\chi(x, a) + \chi(-x, -a)}{2} \right| \quad (5.9)$$

We notice that the asymmetry is the sum of the even order elements of  $\chi$ . The similarity between the  $a$  asymmetry after one deflector and the  $x$  asymmetry after two deflectors in Fig. 5.10 hints that part of the  $x$  dispersion after the second deflection (U-configuration) comes from the  $a$  dispersion after the first deflection. This would explain both the curvature of the output  $x$  and the residual distortion of the emittance profile after 2 deflectors shown in Fig. 5.9. Regions of low asymmetry, i.e. low second order aberration can be defined as regions of acceptance for the input beam. For this reason, we superimposed two realistic emittance profiles on the asymmetry graphs. The black distribution is the same as in the previous section and the red profile corresponds to the focussing of the beam at the entrance of the deflector. In a purely geometric appreciation, the second beam seems to be the best solution to minimise the geometric aberrations after a single deflection. However, it was stated earlier that a widely converging or diverging beam induces a very important ToF dispersion. Thus we cannot use a single deflector before PILGRIM unless we use a roughly parallel beam and we can spare both the small  $x$  spread and the ToF spread mentioned in the last section ( $\simeq 19$  ns). In the U arrangement, the ToF becomes independent from  $x$  and  $a$  at first order. However at high input  $a$ , the output  $a$  distortion becomes important. Thus it is still preferable to send a rather parallel beam through the two deflectors. In the light of all these considerations, the layout of S3-LEB was decided. For simplicity, and to limit the ToF aberrations before PILGRIM we chose to lead the beam in a straight line through a deactivated deflector and then pulse its electrodes to bend the beam after isobaric separation and purification. In



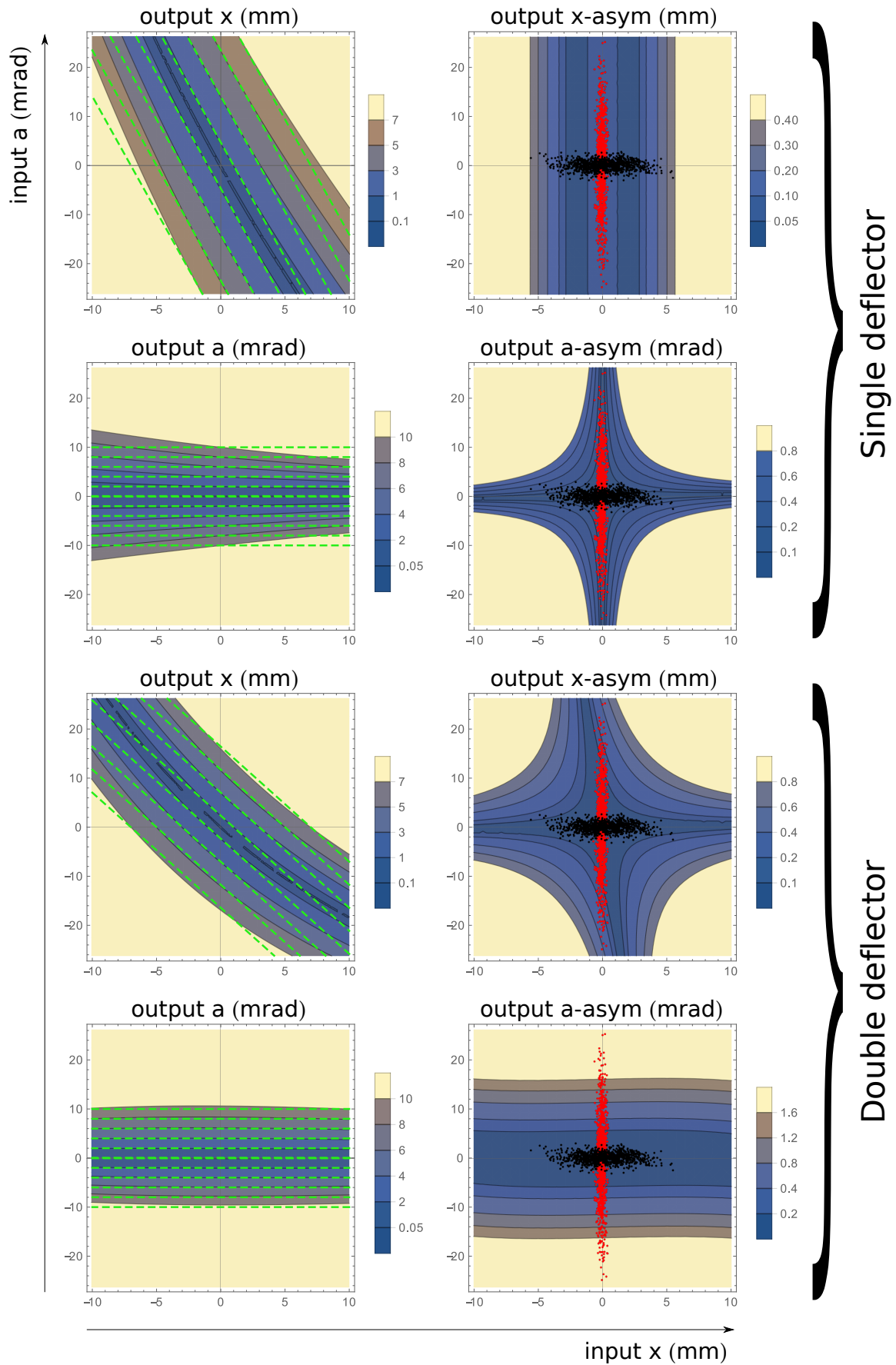


Figure 5.10 – *Left*: output transverse position  $x$  and output angle  $a$  on the colour scale as a function of the input  $x$  and  $a$  after 1 or 2 deflections. *Right*: asymmetries of these output values. Details in text.

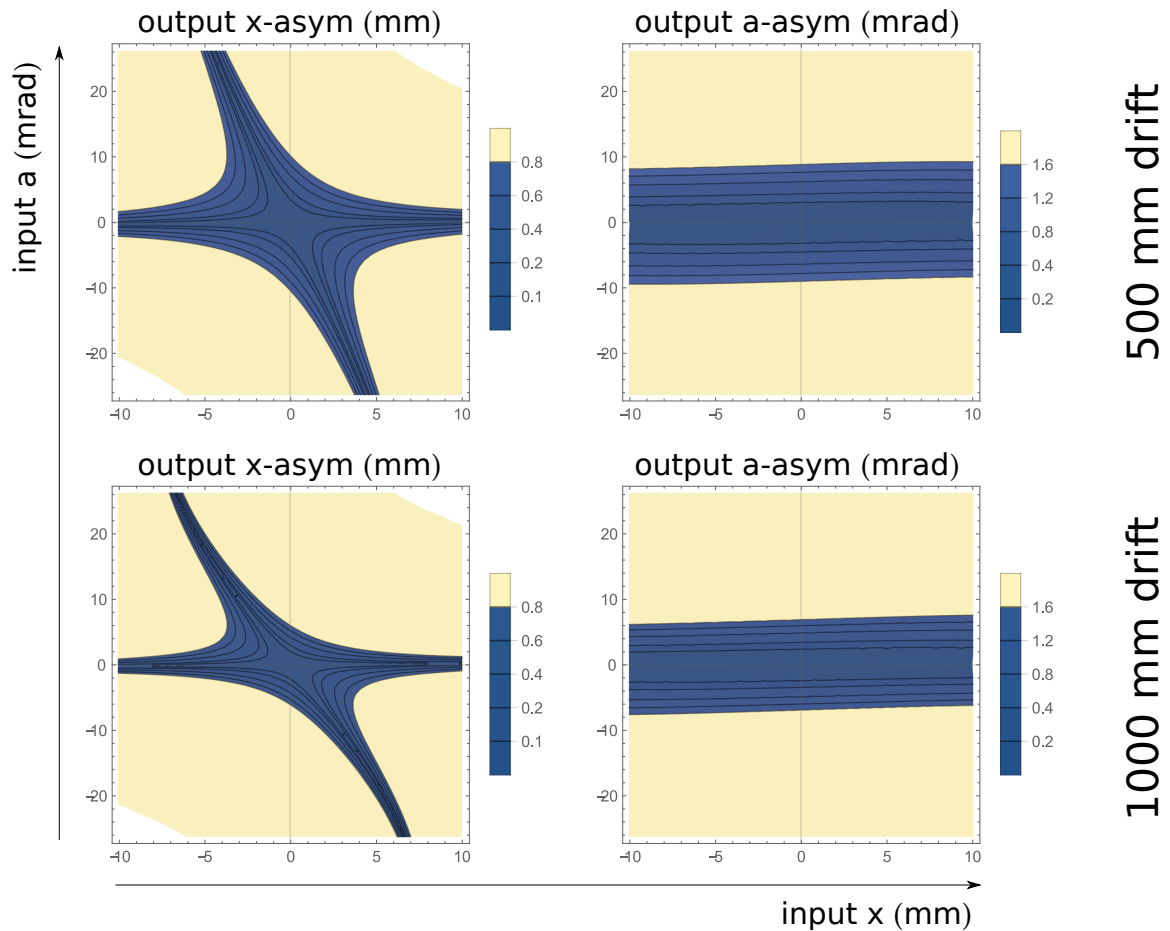


Figure 5.11 –  $x$  and  $a$  asymmetries for a 500 and a 1000 mm drift section between the deflectors.

DESIR though, the U-configuration was already part of the initial layout of the beam line. As shown above, this should conveniently match the ToF spread requirements for injection in PILGRIM without spoiling the resolving power.

### 5.6.2 Effect of the distance between deflectors

So far, we only considered the U-configuration to be two deflectors next to each others. However, because of the space taken by the different beam-lines, the deflectors will probably have to be separated by 50 cm or more in S3 and up to 2 m in DESIR. In the absence of any optical system between the deflector, the additional drift length changes the asymmetry profiles, reducing the size of the low aberration regions and thus the acceptance of the whole system, as seen in Fig. 5.11. This is simply due to the fact that the  $x$  spread increases with the angle and distance in a drift section. Therefore, the longer is the drift section, the larger are the  $x$ -dependent aberrations in the second deflector. Of course if the beam is quite parallel between the deflectors, the  $x$  spread and the subsequent aberrations are limited. In Fig. 5.11 this is shown by the fact that the asymmetries are small near  $a = 0$ , regardless of the drift length.

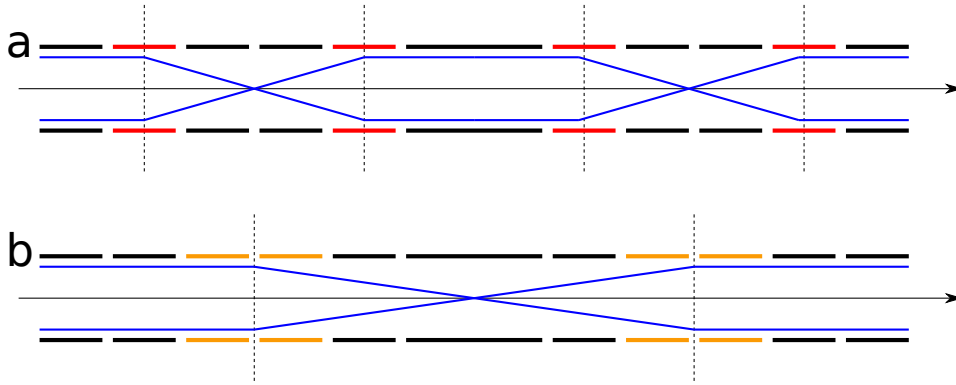


Figure 5.12 – Telescopic arrangement of electrodes with two different powerings. *a*: distance suppression. *b*: beam inversion. See details in text.

### 5.6.3 Telescopic lenses

In the light of the previous results, we proposed to solve the problem of the distance between the deflectors by inserting a telescopic arrangement of drift section and Einzel lenses (see Fig. 5.12-a). The system consists of 5 drift sections of length  $f$ ,  $2f$ ,  $2f$ ,  $2f$  and  $f$ , respectively, separated by 4 Einzel lenses of focal length  $f$ . Using a simplified model of the Einzel lens, the transfer matrix of the full optical system is:

$$ALA^2LA^2LA^2LA = I_2 \quad (5.10)$$

with

$$A = \begin{pmatrix} 1 & f \\ 0 & 1 \end{pmatrix} \quad L = \begin{pmatrix} 1 & 0 \\ -\frac{1}{f} & 1 \end{pmatrix} \quad I_2 = \begin{pmatrix} 1 & 0 \\ 0 & 1 \end{pmatrix} \quad (5.11)$$

This means that such a system is optically equivalent to no drift at all, at least at first order. If inserted between two deflectors, this device would cancel the distance between those deflectors from an optical point of view. In addition, by using segmented electrodes and appropriately changing their potentials, it would be possible to use the same setup to achieve an other telescopic system (see Fig. 5.12-b), described by:

$$A_2L_2A_2^2L_2A_2 = -I_2 \quad (5.12)$$

Reverting the  $x$  and  $y$  values between the deflectors would allow to use the S-configuration without adding the ToF-aberrations, which could give flexibility to the DESIR beam-line (see Fig. 5.2). This is very preliminary since this system has not yet been simulated: such a system could bring non-negligible second order ToF-aberrations owing to the strong focussing.

## 5.7 DEFLECTOR DESIGN

The mechanical design and assembly of the deflector has been made by the CENBG (Bordeaux) and is detailed in Fig. 5.13 and Fig. 5.14. During the optimisation phase, it was noticed that the ToF bunchwidth was very

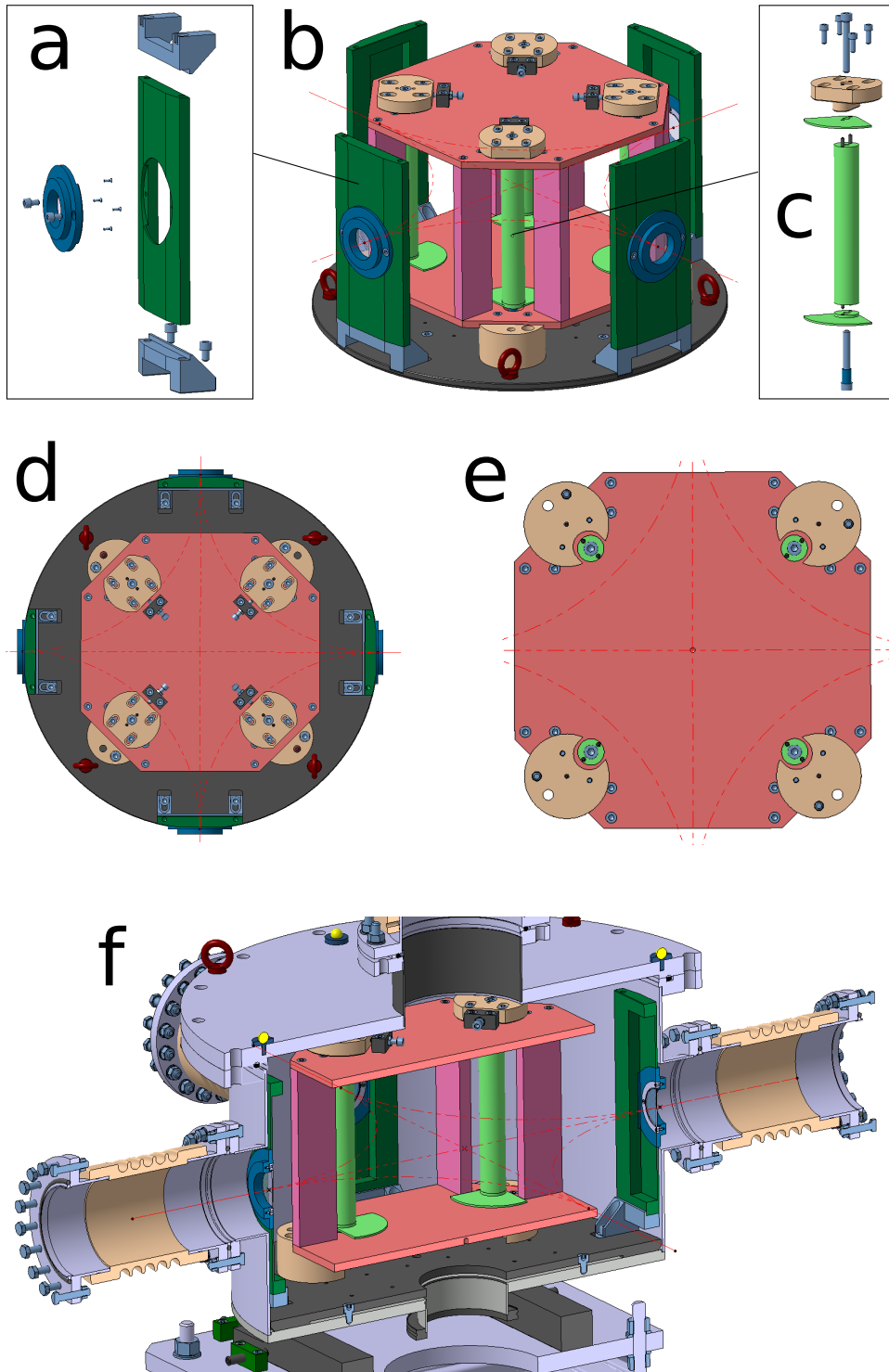


Figure 5.13 – Mechanical design of the deflector. **a:** mobile entrance/exit window, detail. **b:** deflector ensemble. **c:** cylindrical electrode, detail. **d:** top view. **e:** bottom view. **f:** vacuum chamber.

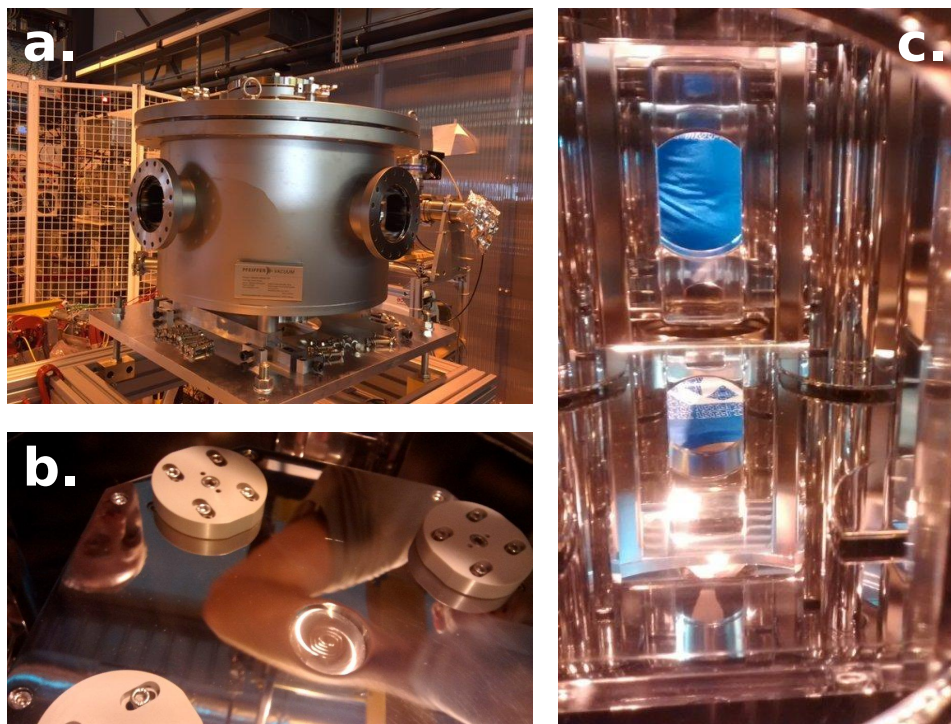


Figure 5.14 – Prototype deflector at CENBG. *a*: vacuum chamber. *b*: top octagonal plate and and cylinder PEEK supporting parts. *c*: inside of the chamber.

sensitive to the position of the cylindrical electrodes, but little sensitive to the position of the entrance aperture. Thus it was decided to use mobile cylinders (c) and to design an additional mobile entrance/exit window (a) to achieve a coarse and fine tuning of the deflection, respectively. Making other mechanical dimensions and positions adjustable was considered too difficult. A special attention has been paid to conserve the symmetry of the potential distribution with respect to the plane of deflection. For this reason, the in/out windows have a symmetric counterpart to their bottom support part. The top part has no motive but to ensure the field symmetry. The cylindrical electrodes, equipped with their shields, are held mechanically from the top side and powered by the bottom side through holes drilled into the two octagonal shield plates (d,e). The top fixing screw and the bottom powering screw have the same length for the same reason of symmetry. The cylinders are fixed to flat PolyEther Ether Ketone (PEEK) parts (in beige on the drawings), which themselves are supported by the top octagonal shield (b). The PEEK parts can slide along the diagonal axis inside a groove and can be maintained in position with 4 screws (b,d). Thanks to this system, the cylindrical electrodes, though mobile, remain very parallel to each other once fixed. The entrance windows will be equipped with grids to close the potential field map, as comparative simulations showed that it was optically advantageous. These grids have not been designed yet but should consist of an arrangement of  $20\ \mu\text{m}$  wires spaced by  $0.5\ \text{mm}$ , either welded or stuck onto a plate. The vacuum chamber (f) has a  $500\ \text{mm}$  inner diameter with 4 side flanges for the beam, one top flange for pumping and one bottom flange to bring the potentials to the different electrodes.

## CONCLUSION

A multi-direction electrostatic deflector has been studied for usage before and/or after the MR-ToF-MS PILGRIM. This deflector has been simulated and its geometry and potentials have been optimised in SIMION 8.1. A detailed optical analysis has been performed to understand the effect of such a device on the ToF and the transverse emittance, leading to practical limitations: precision ToF experiments can only be performed after 0 or 2 deflections (if the deflectors are close enough) or after a single deflection, but only for a close-to-parallel beam. A first prototype has been built and will be tested as a part of the commissioning setup of PIPERADE at CENBG [100].



# DATA ANALYSIS OF THE EXOGRAM/NWALL EXPERIMENT

# 6

**T**HIS chapter details the analysis of the data from the experiment of October 2014 on the EXOGAM/NWall/DIAMANT experiment on  $^{96}\text{Cd}$ . Though the study of this exotic  $N = Z$  nucleus will not be detailed here as it is the object of a post-doctoral work, other nuclei can be studied with the same experiment. This chapter will detail the calibration of the different detectors involved in the experiment as well as the gating procedures applied for event selection, and will propose a spectroscopic analysis of  $^{94}\text{Pd}$ .





## 6.1 GOALS OF THE EXPERIMENT

GANIL experiment E623 of October 2014 aimed to study the excited states of the  $N = Z$  nucleus  ${}^{96}_{48}\text{Cd}_{48}$ , 2 protons and 2 neutrons away from the double shell-closure  $N = Z = 50$  ( ${}^{100}_{50}\text{Sn}_{50}$ ). For  $A \lesssim 80$ , even-even nuclei are expected to exhibit an important  $T = 1$  isovector pairing which is responsible for important energy gaps whenever a pair is broken. This results in the grouping of excited levels with respect to their seniority  $\nu$  (number of unpaired nuclei). This level structure is still found for heavier nuclei far from the  $N = Z$  line as the like-nucleon ( $T = 1$ ) coupling is dominant (see Fig. 6.1,  ${}^{96}\text{Pd}$ ). On the  $N = Z$  line and for  $A \gtrsim 80$  however, a new  $T = 0$  n-p coupling arises. This so called isoscalar coupling can become dominant over the usual isovector coupling in which case it deeply modifies the shape of the level scheme (see Fig. 6.1,  ${}^{92}\text{Pd}$  and Fig. 6.2) giving it a "regular spacing" pattern.  ${}^{96}\text{Cd}$ , being an even-even nucleus on the  $N = Z$  line, is hence expected to show such a level structure. The main objective of the experiment was to measure and identify the first excited levels of this nuclei in order to constrain the isoscalar coupling model.

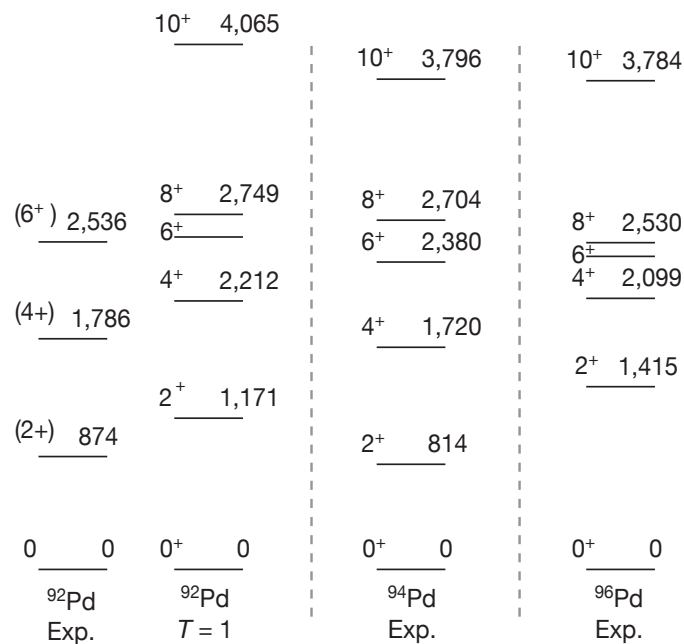


Figure 6.1 – Experimental energy levels of  ${}^{92}\text{Pd}$ ,  ${}^{94}\text{Pd}$  and  ${}^{96}\text{Pd}$ . One can witness the transition from a seniority-based level scheme to a regularly spaced one. A calculated level scheme considering a pure isovector pairing ( $T = 1$ ) for  ${}^{92}\text{Pd}$  is also displayed and highlights the importance of the isoscalar contribution. Partially reproduced from [101].

## 6.2 DESCRIPTION OF THE EXPERIMENT

### 6.2.1 General description

In order to reach excited levels of  ${}^{96}\text{Cd}$ , a beam of  ${}^{40}\text{Ca}$  was sent on a thick target of  ${}^{58}\text{Ni}$  with  $5 - 6 \text{ mg/cm}^2$  (depending on the selected target) to achieve the fusion reaction  ${}^{40}\text{Ca} + {}^{58}\text{Ni} \rightarrow {}^{98}\text{Cd}^*$ . The excited compound nucleus then evaporates various numbers of protons, neutrons

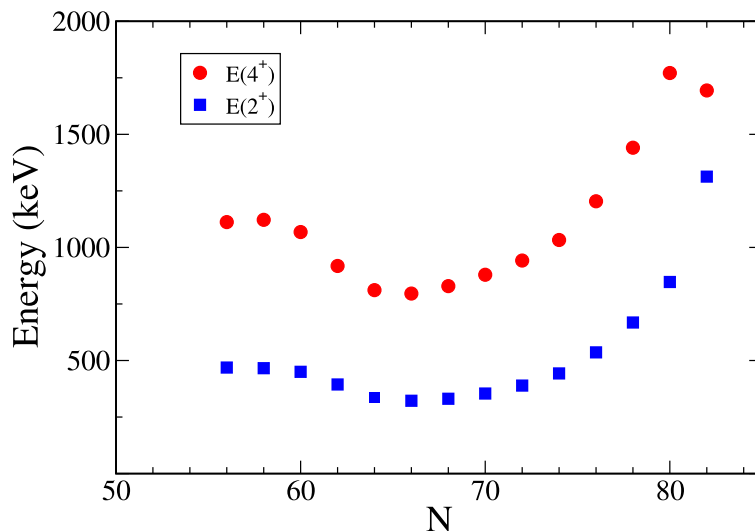


Figure 6.2 –  $2^+$  and  $4^+$  levels of the even-even isotopes of Xenon ( $Z = 54$ ). The energy difference between these levels is noticeably higher near the  $N = Z$  line. This gives a clue of the disappearance of the seniority grouping on this line. Figure from [102].

and  $\alpha$ -particles and populates several excited states in a range of a dozen nuclei beneath  $N = 50$  and  $Z = 48$ . The primary beam is accelerated at GANIL at  $\simeq 152$  MeV ( $3.7996$  MeV/ $u$ ) and is slowed through a  $1$   $\mu\text{m}$ -thick tantalum window to  $\simeq 130$  MeV.

The experimental set-up itself includes the gamma array EXOGAM [103, 104, 105], the charged-particle detector DIAMANT ([106, 107]) and the neutron detector NWall ([108, 109]). Pictures and drawings of the detectors of the experiment E623 can be found in the general figure Fig. 6.3 and a scheme of the experiment is given in Fig. 6.3(h). These last two detectors are used for particle selection, while EXOGAM is used to build the level scheme of the selected nuclei. For instance, to analyse  $^{94}\text{Pd}$ , 2 protons and 2 neutrons below the compound nucleus  $^{98}\text{Cd}$ , we will only consider  $\gamma$ -rays in coincidence with 2 protons in DIAMANT and 2 neutrons in NWall.

### 6.2.2 EXOGAM

EXOGAM is a high efficiency, highly segmented germanium detector array for  $\gamma$ -ray spectrometry designed for radioactive beam facilities (initially for SPIRAL at GANIL). EXOGAM was used for spectrometry in a variety of experiments both in stopped-beam and in-flight configuration. The full array of detectors consists in 16 clovers arranged as the square faces of a rhombicuboctahedron, except for two faces for the entrance and exit of the beam tube (see Fig. 6.3(b)). EXOGAM aims indeed to reach a geometric efficiency as close to  $4\pi$  as possible, in order to maximise the photopeak efficiency. In the case of E623, 11 of those detectors were used (Fig. 6.3(e)), including 7 detectors at  $90^\circ$  with respect to the beam and the 4 at  $135^\circ$  (backward angles). The detectors in the forward angles are dismantled to allow the installation of the neutron wall.

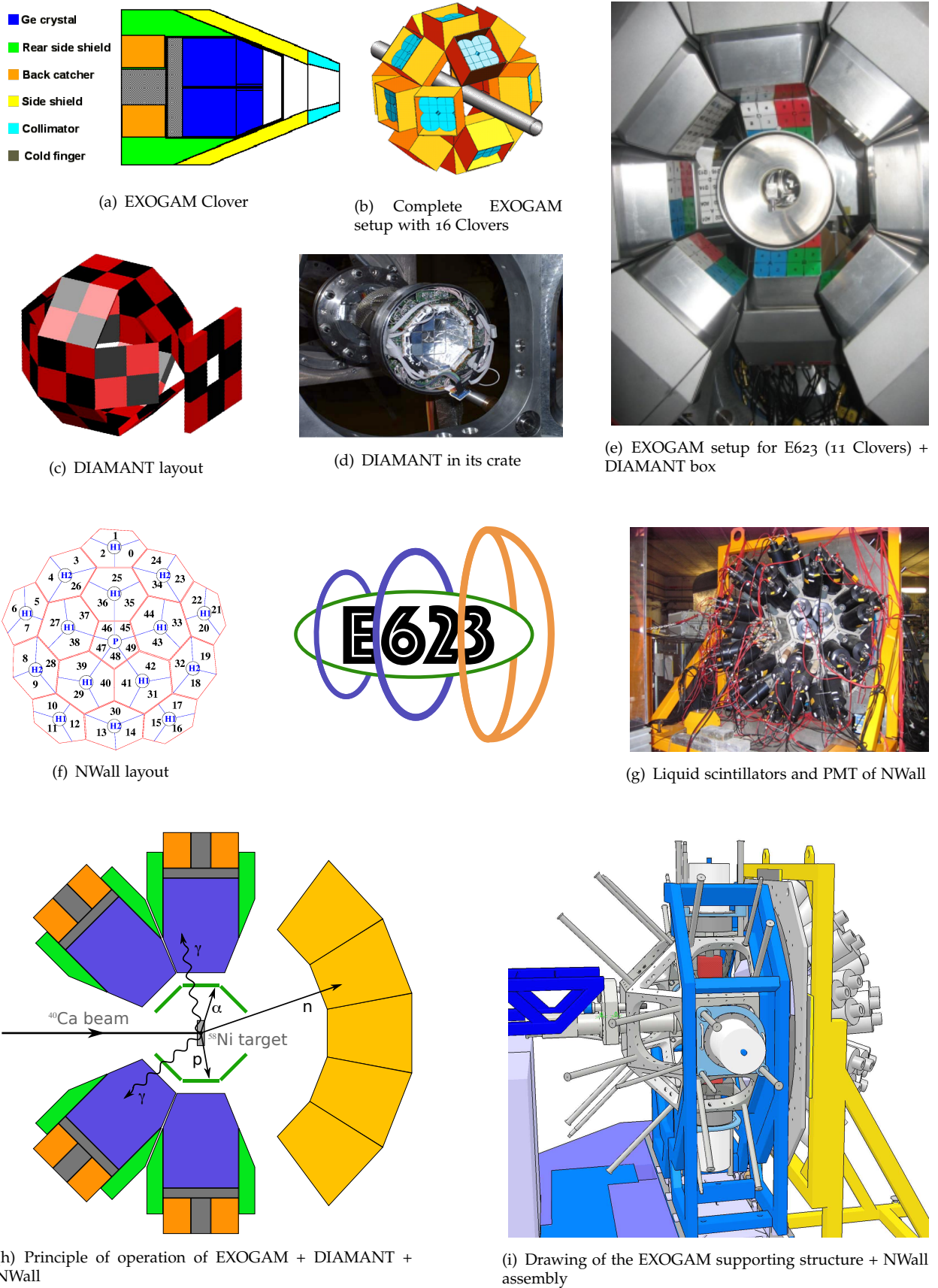


Figure 6.3 – The detectors of E623: EXOGAM (a)(b)(e), DIAMANT (c)(d)(e), NWall (f)(g) and coupling of these detectors (h)(i).

A clover detector consists of 4 germanium crystals of 60 mm diameter, each arranged in a four-leaf clover inside a same cryostat. A clover is surrounded by a bismuth germanate shield (BGO, labeled as "rear side shield" in Fig. 6.3(a)) which is used as a *veto* for Compton-scattered  $\gamma$ -rays in Ge. This allows to reduce the background (assumed to be essentially due to Compton scattering) without reducing *a priori* the photopeak efficiency. Another BGO shield, labeled "side shield" in Fig. 6.3(a) can be added to increase the peak-to-background ratio but requires the Clover to be further away from the target, which reduce the efficiency. These side-shields were not used in E623.

Each of the individual crystals is electronically segmented into four segments. This segmentation arise from the wish of the EXOGAM designers to reduce the opening angle of the smallest "brick of detection", in order to reduce the Doppler broadening. Nevertheless, as in our case the beam was stopped in the thick  $^{58}\text{Ni}$  target, the compound nucleus was at rest in the frame of the laboratory and the resolution was not widened by Doppler broadening. Therefore, the crystals were considered as whole for this experiment and no signal was acquired for the individual segment.

In such an experiment, the performances typically expected from EXOGAM are, at 1.3 MeV[104]:

- Energy resolution  $\Delta E_{FWHM} \leq 2.3$  keV.
- Photopeak efficiency  $\epsilon_{ph} \simeq 20\%$ .
- Peak-to-total ratio  $P/T \simeq 45\%$ .

### 6.2.3 DIAMANT

DIAMANT is an array of 84 scintillation detectors used for the detection of light charged-particles, in this case protons and alpha particles. Each detector consists of a CsI(Tl) scintillation crystal, a plexy-glass light guide, a PIN photodiode and a pre-amplifier. These detectors are arranged yet again in a rhombicuboctahedron configuration, with 4 crystals per square face, 2 per front triangle face, one per backward triangle face and 8 on a so-called forward wall (see Fig. 6.3(c)). In the E623 experiment, one of the square faces was removed to allow the insertion of different targets during the experiment via a small spindle, bringing the total number of detectors down to 80. A target mounted on the spindle can be seen in Fig. 6.3(e). With this arrangement, the geometrical efficiency is  $\simeq 90\%$  of  $4\pi$  and the proton and alpha detection efficiencies are expected to be approximately 70% and 50%, respectively [107]. Such large efficiencies associated to a large number of individual detectors allow to select a reaction channel with a rather high multiplicity of evaporated charged particles (e.g. 2 alpha particles, 4 protons ...).

Whenever a light particle or a  $\gamma$ -ray hit interacts with one of the scintillators, the signal from the pre-amplifier is processed to extract three different informations: energy, PID (Particle Identification) and time. These

informations are extracted from the amplified analog signal of the scintillator and are then digitised by an ADC. The energy information is deduced from the amplitude of the signal while the PID is generated by a pulse shape analysis method mixing two techniques [106]. The time information is obtained by the time of arrival of the pulse with a non-delay-line CFD (Constant Fraction Discriminator).

#### 6.2.4 NWall

NWall is a liquid scintillator array for neutron detection. In this experiment it is used in combination with the DIAMANT detector for selection of certain reaction channels, but also participates in the validation of the master trigger, as detailed in the next section. The array is composed of 15 hexagonal detector units and one central pentagonal unit, arranged as shown Fig. 6.3(f). Each hexagonal unit is divided into 3 detectors hermetically separated, while the pentagonal unit is divided into 5, for a total of 50 detectors. Each detector contains liquid scintillator BC-501A from Bicron<sup>®</sup>, a separation glass window and a PMT (Photo-Multiplier Tube).

As usual, the array is designed to achieve maximal efficiency by covering a large solid angle ( $1\pi$ ). The intrinsic efficiency of these liquid scintillators is roughly 50% for evaporation neutrons, with a total efficiency of  $\epsilon = 25 - 30\%$  (knowing that the neutrons are not emitted isotropically but mostly forward). The high granularity of the array allows to limit the number of events where a neutron and a  $\gamma$  would both hit the same detector. Indeed, NWall is a very efficient gamma detector and thus needs to be segmented to limit the number of pile-up events.

During an event, the electronics of NWall register the neutron energy, Time of Flight (ToF) and Zero Crossover time (ZCO) signals. The last is the measurement of the zero crossing time of a bipolar signal built from the output signal of one of the cells. The ToF and ZCO signals are used to distinguish the neutrons from the  $\gamma$ . Because NWall takes part in the creation of the trigger signal, a hardware neutron gate in ToF and ZCO was implemented for this experiment so as to limit the number of  $\gamma$  mistaken for neutrons in the trigger system.

#### 6.2.5 Acquisition

The three detector arrays use the VXI (VME eXtensions for Instrumentation) bus standard. Among other features, this standard defines a large sized crate chassis and additional bus lines for timing and triggering with respect to the original VME standard. The chassis gathers the circuits for analog signal processing, A/D conversion and digital treatment in one card. The trigger and readout system in EXOGAM is the same as for Euroball [103, 110]. Several modes of operation are available with this trigger system, including the "common dead-time" mode which was used for this experiment. In this mode, once an event is being treated, the acquisition is dead and does not accept a new event until the end of the readout process (or abortion if the event is refused). The trigger/readout is a two stage

process. The first stage is the creation of the FT (Fast-Trigger) signal by the master trigger card, whenever the trigger conditions are met. This FT is sent after a certain delay to each channel of EXOGAM, NWall and DIAMANT to stop the individual TAC (Time to Amplitude Converter) and to check the FT/FT-sample coincidence (see step III) and thus allow or cancel the treatment of an event. During the second stage, the master trigger card will validate or reject the event, enabling or disabling the readout, respectively. An example of a typical trigger process is illustrated by the chronogram Fig. 6.4, and can be described as follows:

- I.  $\gamma$ -rays are detected in one or several germanium detectors in EXOGAM. The local CFD outputs a signal and the local trigger immediately starts 2 programmable timers (see step 3 and 4) called "FT sample time" and "Validation sample time". After an adjustable delay (to align the CFD in time), all the signals from the different CFD are summed in the Sumbus.
- II. The Master Trigger card compares the input signal to its pre-set trigger conditions. Trigger conditions may require a certain  $\gamma$ -multiplicity (e.g.  $> i$   $\gamma$ -rays), in which case the level amplitude of the summed signal on the Sumbus is compared to a given level, or a more complex combination (e.g.  $> i$   $\gamma$ -rays AND  $> j$  particles X). Once all the conditions are met, the card generates a FT (Fast-Trigger) pulse of a given width and after a given time (called gate and delay pulse, or GD) and a Validation gate with a larger delay. The card also issues an inhibit signal which freezes the acquisition until the end of the event treatment.
- III. At the end of the FT sample time started by the local electronics of individual crystals (step 1), the local trigger will sample the FT signal to check if the conditions mentioned earlier have been met by the master trigger. If the FT signal has not been validated, the local trigger cancels the ongoing signal processing and waits for the next  $\gamma$ . This way, if a background  $\gamma$ -ray reaches a crystal of EXOGAM between 2 reactions and if the trigger conditions require 2  $\gamma$  or the detection of an additional particle, not only the local trigger of this crystal rejects the event, but it also will be ready to accept a new  $\gamma$ -ray within a few hundred nanoseconds, thus reducing the dead time of the acquisition.
- IV. After the generation of the Validation gate, the master trigger checks for its validation conditions. If these conditions are met within the time of the Validation gate, it issues a Validation pulse. As in our case there was no validation condition, the Validation pulse was issued immediately after the start of the Validation gate. At the end of the Validation sample time, the local triggers sample the Validation pulse as they did with the FT pulse. If the Validation signal is seen, A/D conversion and readout are initiated in the local VXI card.

Three main trigger conditions were used during this experiment:

- n- $\gamma$ : this is the main trigger of the experiment. The FT requires 1  $\gamma$ -ray in EXOGAM and 1 count in NWall validated by the hardware neutron gate mentioned earlier. In spite of the name, any count in NWall, neutron or  $\gamma$  is

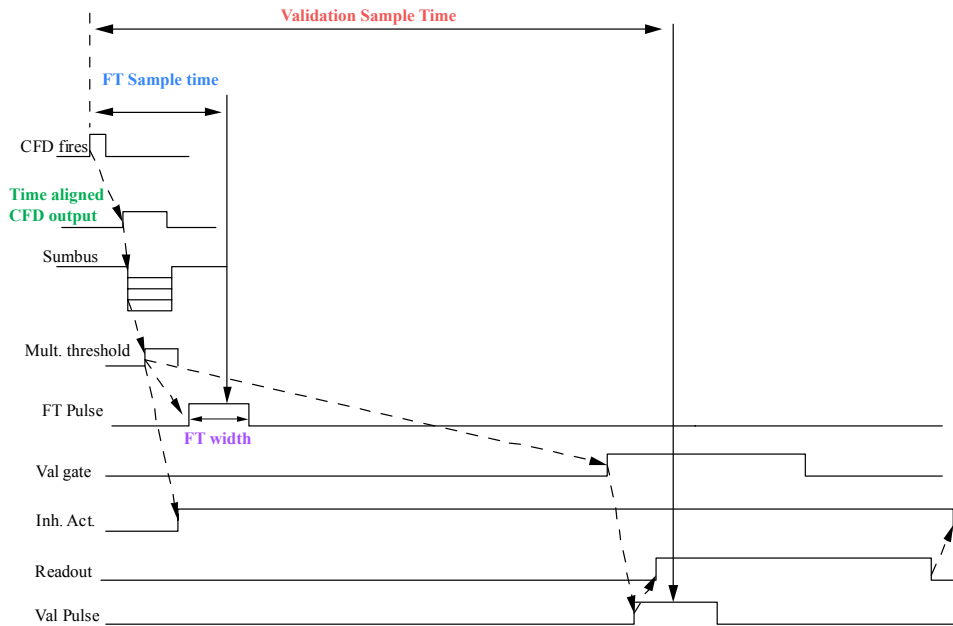


Figure 6.4 – Chronogram of a typical triggering/readout process in common dead-time mode (figure from [110]).

Trigger	$\gamma$	$2\gamma$	$n-\gamma$	$n-\gamma+\text{BaF}_2$
Run(s)	7, 9-12	16, 18	7, 13-15, 17, 57-147	19-56

Table 6.1 – Triggers and runs using them.

likely to participate to the trigger. Indeed, the overwhelming proportions of the neutron-less channels 3p and 4p (Fig. 6.14, further) leads to the number of  $\gamma$ -rays detected in NWall dwarfing this of neutrons, before and even after application of the gate. When the master trigger card receive from NWall the message that a neutron has been detected, it opens a gate, waiting for the signal of one or several  $\gamma$ -rays in the Sumbus. If a  $\gamma$ -ray is observed in coincidence with the gate, the FT signal is delivered.

- $\gamma/2\gamma$ : the trigger requires 1 or 2  $\gamma$ -rays to be detected in EXOGAM. This trigger essentially tests EXOGAM's capabilities and bring a comparison for the later calculus of the neutron detection efficiency. The  $2\gamma$  condition leads to less background contamination.
- $\text{BaF}_2$ : a Barium Fluoride ( $\text{BaF}_2$ ) scintillation detector was added in one of the backward triangle opening of EXOGAM. Such a detector is used for precision time measurement of  $\gamma$ -rays. It has a very poor energy resolution ( $\Delta E/E \simeq 10\%$ ) but a very good time resolution, typically below 1 ns. This detector was used here to monitor the energy spread of the ion bunches. During a part of the experiment, the  $\text{BaF}_2$  signal could also trigger the FT pulse.

The master trigger card could be manually set to answer to one or a combination of these conditions. Usually, a change of trigger conditions marked the start of a new run, so as to keep a unique trigger within a same run. Tab. 6.1 gives a list of the physics runs and their corresponding FT.



Source	Decay radiations energies	Activity
$^{60}\text{Co}$	<b>1173.237(4)</b> , <b>1332.501(5)</b>	10.2 kBq
$^{152}\text{Eu}$	121.7817(3), <b>244.6975(8)</b> , <b>344.2785(12)</b> , 411.1163(11), 443.965(3), <b>778.9040(18)</b> , 867.378(4), 964.079(18), 1085.869(24), <b>1112.074(4)</b> , <b>1408.006(3)</b>	20.2 kBq

Table 6.2 – Decay radiations and activities of the calibration sources. In bold are the energies of the peaks used for the calibration.

## 6.3 CALIBRATION OF THE DETECTORS

### 6.3.1 EXOGAM

The energy and time signals of the 44 crystals of EXOGAM must be calibrated. A good energy calibration is essential to the analysis as a precise value of  $\gamma$ -ray energies enables a precise knowledge of the structure of the nuclei that emitted it. As the time variable in EXOGAM is only used to differentiate the prompt  $\gamma$ -rays from the delayed ones, it is not necessary to have a very good absolute time calibration. However, a good relative calibration is very important.

#### Energy calibration

In order to calibrate EXOGAM in energy, two calibration runs have been made by installing  $^{152}\text{Eu}$  and  $^{60}\text{Co}$  sources at the target position. One calibration run has been made before the beginning of the experiment and another one after the end, to monitor any change in calibration. A list of the  $\gamma$ -energies used for the calibration is given in Tab. 6.2.

The calibration with these runs proceeds in two stages summarised in Fig. 6.5. Firstly, the two peaks of the  $^{60}\text{Co}$  at 1173 keV and 1332 keV are identified. These peaks are by far the highest in the  $\gamma$ -spectra of the different crystals and are easily identified. Their position in the spectra provides a first coarse approximation of the linear calibration coefficients. This allows to know the position of the other peaks with a 1-2 keV precision and therefore identify them as well. The peaks are then fitted by a sum of a simple gaussian and a quadratic background. The positions of all the fitted peaks are then used to determine the coefficients of a second, still linear, calibration with smaller errors. It can be noticed on Fig. 6.5 that all the peaks have not been used for this linear calibration. The reason is that because of the low statistics of this measurement, several peaks were poorly fitted by a gaussian function.

Fig. 6.6 displays the residues of the linear calibration for the crystal ECC0-A. It can be noticed that most of the residues are below 0.1 keV. The same method is applied to each of the 44 crystals with roughly the same results as in Fig. 6.6. The few peaks which are further than 0.1 keV from the calibration curve are either too small to be fitted nicely considering the background (often the case of the 121 keV peak of the  $^{152}\text{Eu}$ ), or part of a double peak. A quadratic calibration was also tried and, as expected, gave better results in terms of  $\chi^2$  and residue, including the peaks not

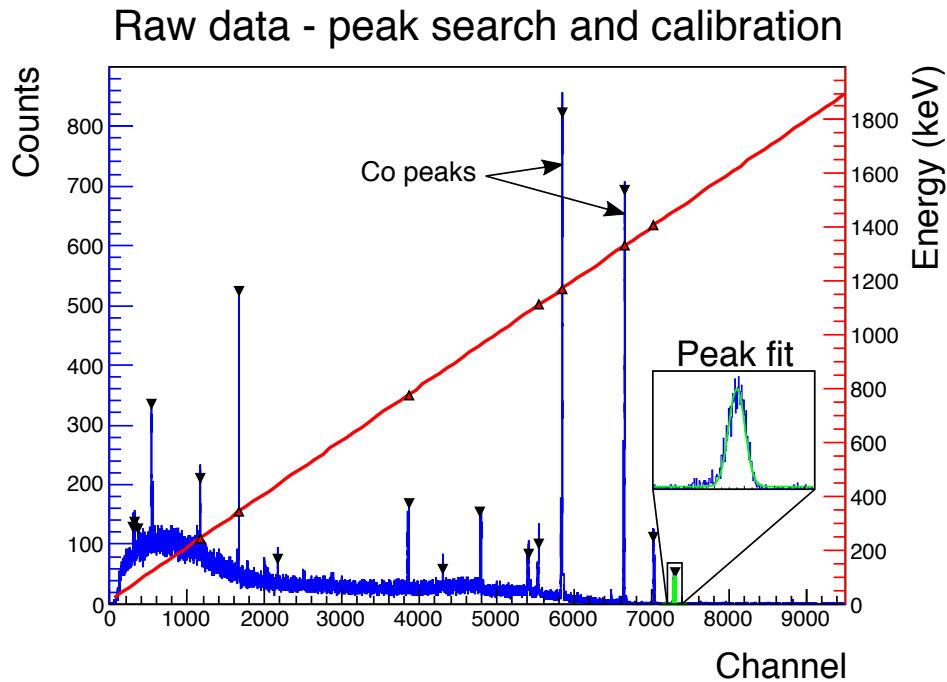


Figure 6.5 – In blue, the uncalibrated  $\gamma$ -spectrum. The peaks with black triangles above them are those found by Root's automatic Search() routine. In the inset, an example of a fitted peak. In red triangles, the energies of the mean peaks VS the electronic channels, fitted by a first degree polynomial curve.

used for the calibration.

Fig. 6.7 shows the distribution of FWHM (Full Width at Half Maximum) of all the crystals for several energies. Some crystals exhibit a higher FWHM consistently throughout the energy spectrum: 2-A and 2-B (light green), 5-A and 5-B (pink) and 13-A and 13-B (dark grey). All the crystals of clovers 2, 5 and 13 are either above or close to the limit displayed on this figure. This could be due to the cards dedicated to these clovers.

At this point we can expect a good calibration at low energies ( $\lesssim 1500$  keV) and for the first runs. Therefore it is important to check both the quality of this calibration at high energy and the consistency of the calibration throughout the experiment.

- The first point can be verified on the high energy peak of a physical run. We checked the 2790 keV peak from  $^{95}\text{Rh}_{50}$  ( $3p$  channel) in run 7 (first experimental run) and saw that this peak is shifted by more than 0.2 keV from the expected value for two thirds of the crystals, whether the calibration is linear or quadratic. We then decided to follow the 511 keV peak from  $\beta$ -decays and the 1431 keV peak from  $^{94}\text{Ru}_{50}$  ( $4p$  channel) in the same run. These  $\gamma$ -peaks are strong and rather isolated in the spectra, allowing a clean fit. We noticed that at low energy, crystals 1-C, 1-D and all the crystals of clover 6, exhibit a calibration shift (important shifts from the calibration curve at 511 and 1431 keV) which is not observed in the first calibration run, nor in the second. This grouping of crystals seems to incriminate either full clovers or the acquisition card, but the precise reason was not investigated.

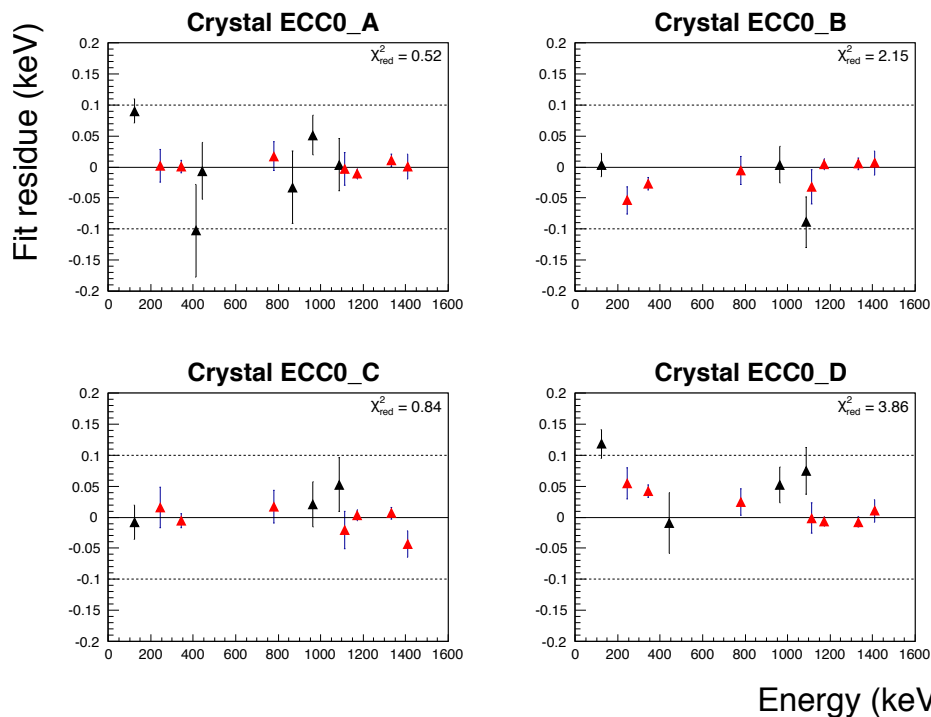


Figure 6.6 – Residues of the linear calibration for the 4 crystals of clover o. In red, the residues of the peaks used for calibration. In black, the pseudo-residues of the peaks not used in the calibration. These value are calculated both as a check of the peaks gaussian fits and of the calibration itself. The criterion for using a peak in the calibration was that it could be found by the Search() routine in each of the 44 crystals. The reduced  $\chi^2$  is plotted though it should be noticed that the error on the  $\chi^2$  itself is of the order of unity for only 7 fit-points [111]

- The second point can be checked by comparing the calibrations of the beginning and end of the experiment. Deviations of the calibration peaks ranging from 0.1 to 2.5 keV occur for one third of the crystals. This of course does not account for the possible self-cancelling variations that may occur during the experiment.

In the light of these two issues, we decided to use the three peaks mentioned previously as well as the 716 keV peak from the 3p channel and the 1898 keV peak from the 4p channel to re-fit the calibration curve several times in the middle of the runs with a quadratic function, arbitrarily, every 300,000,000 events. This procedure generated 19 energy calibration files. Fig. 6.8 shows the distribution of each peak's residue of the quadratic fit for each calibration and for each crystal.

### Efficiency calibration

The efficiency of EXOGAM is determined using the same calibration runs as before. Knowing the source activity  $A$ , exposure time  $T$ , the  $\gamma$ -intensity  $I_\gamma$  of a given decay radiation of energy  $E$ , and measuring the number of counts in a detector  $N$ , one can deduce the photopeak efficiency at this energy, following:

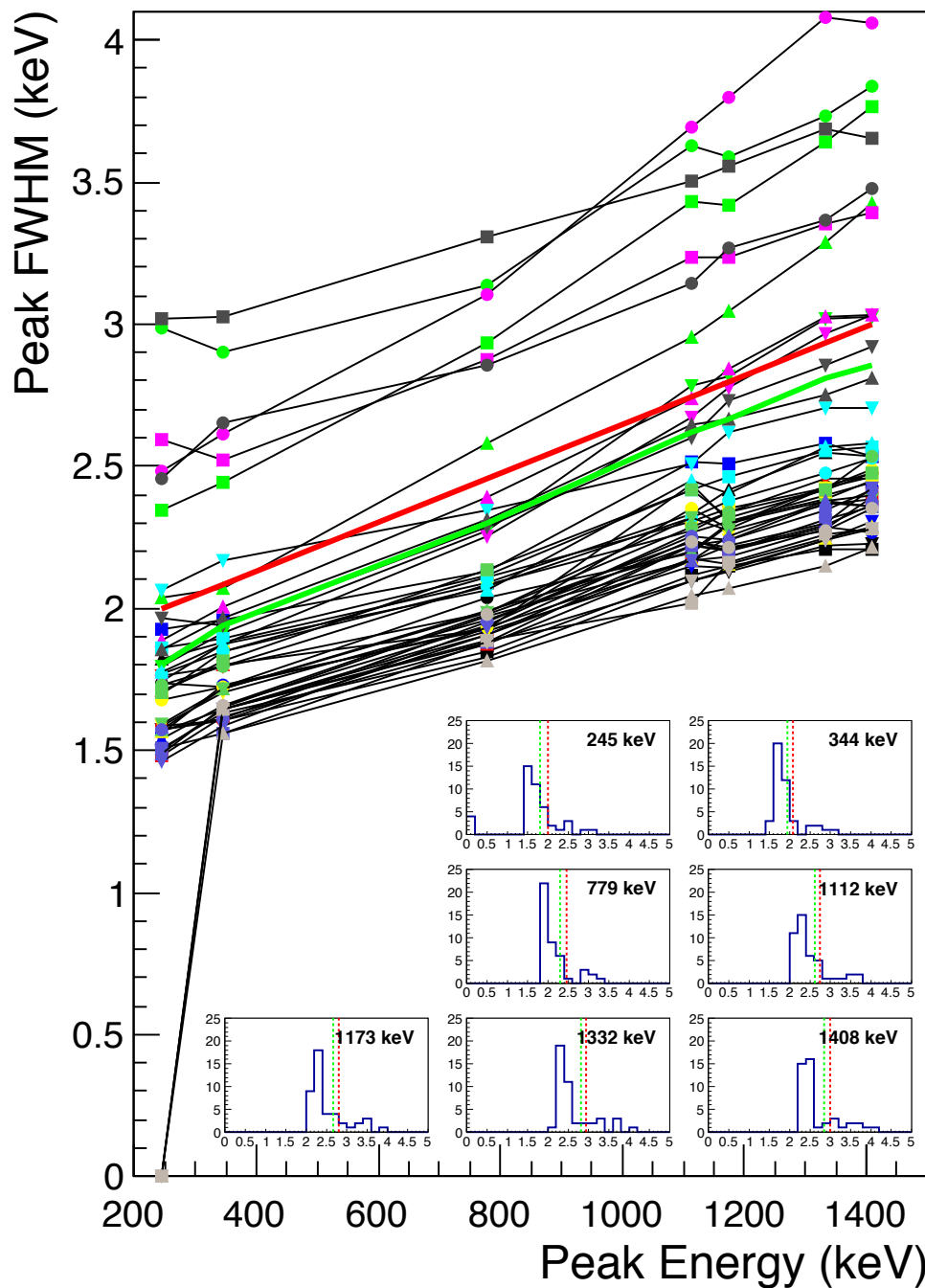


Figure 6.7 – Full Width Half-Maximum of the 7 calibration peaks for all crystals. The **bold green line** represents the FWHM of the same peaks for the summed spectrum. The **bold red line** is a linear function of the energy and an arbitrary limit above which the peak FWHM needs investigation. Clover 12 has a complete loss of efficiency at low energy, making the fit of the 245 keV peak impossible. The corresponding FWHM were zeroed to highlight this fact on the graph. The insets simply give the distribution of FWHM for a given energy, for all crystals.

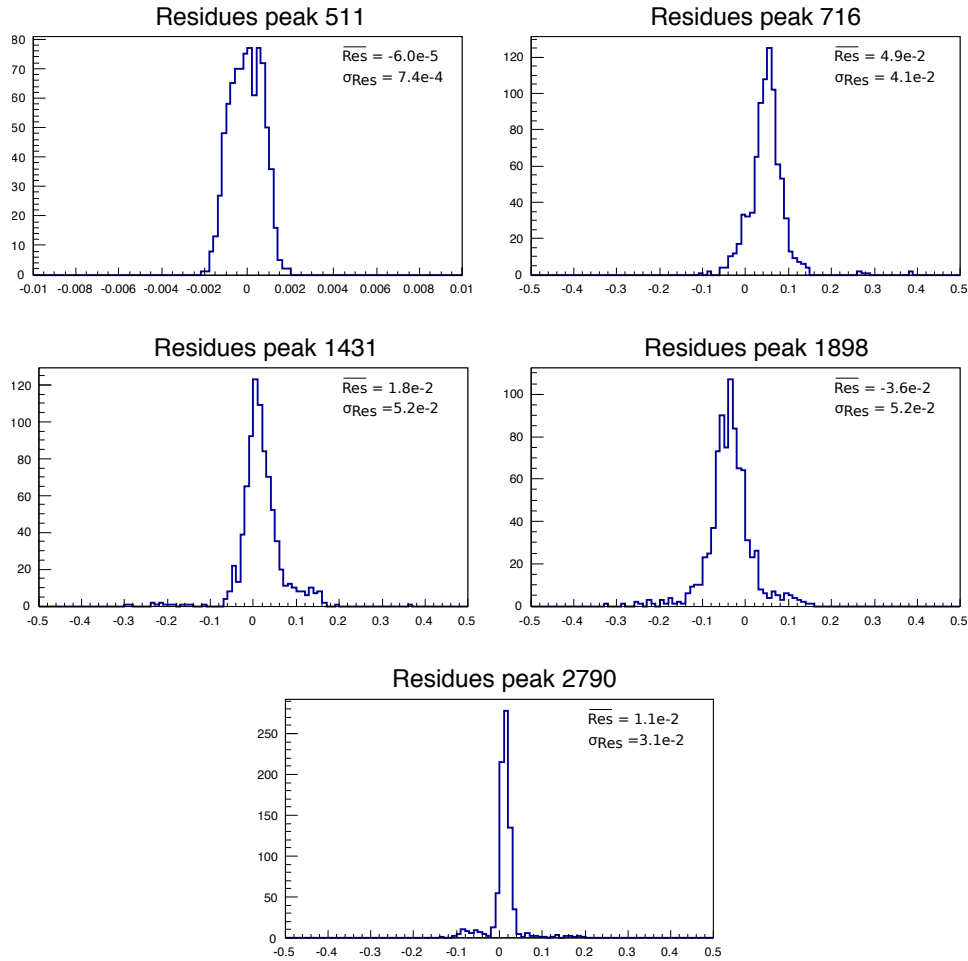


Figure 6.8 – Distributions of the residues of the post-calibrations for the fit peaks 511, 716, 1431, 1898 and 2790 keV. Each distribution gathers the residues of the 44 crystals for 19 re-fits. The high number of statistics and the precision on the energy of the 511 keV peak imposed a important weight on this peak in the fits, hence the low residues. It can be noticed that most of the residues are beneath 100 eV, and only 3 residues throughout all the calibrations were above 300 eV.

$$\epsilon_{real,calib}(E) = \frac{N(E)}{A.T.I_{\gamma}(E)} \quad (6.1)$$

In addition, the dead time  $DT$  of the acquisition changes during the experiment with respect to the activity. The ideal efficiency is considered to be the same throughout the experiment and during the calibration runs and is given by  $\epsilon_{ideal} = \epsilon_{real,calib} / (1 - DT_{calib}) = \epsilon_{real,exp} / (1 - DT_{exp})$ . The dead time during the calibration is obtained by imputing a pulsed signal in one of the crystal's electronics and counting the number of pulses detected. Emitted with a rather precise voltage, these pulses appear in the energy spectrum like any other peak and can be fitted. The live-time  $(1 - DT)$  has been measured at 72.73(2)% for  $^{152}\text{Eu}$  and 70,0(1)% for  $^{60}\text{Co}$ .

The calibration consists simply of fitting the energy-dependant ideal efficiency with one of state-of-the-art efficiency calibration curves. Several functions are mentioned and compared in [112]. For our application we choose to try the Gray [21], and Fazekas [112] functions as well as

the Radford function described in [113]. Though the Fazekas function is supposed valid on a wider range than the others (50 – 11,000 keV), the lack of high energy  $\gamma$  in our sources and the high number of parameters in this function made it virtually useless above 1500 keV. In most of the clover's efficiency plots, we observed that the  $\epsilon_{ideal}$  of  $^{60}\text{Co}$  was slightly above what was expected from the efficiency fit of the sole  $^{152}\text{Eu}$  (up to 10% more). This was still the case in the whole-EXOGAM efficiency plot. However, the efficiencies of both sources matched perfectly in the clover 8, which was the one used for  $DT$  measurement. From this we deduce that the  $DT$  is not the same for each clover.

Despite this efficiency shift between the two sources, it is possible to fit all peaks at once if we introduce an additional parameter for the two  $^{60}\text{Co}$  peaks. This parameter is a ratio of  $\sim 1.0 - 1.1$ . This two peaks are fitted aside as shown Fig. 6.9. One can notice that since we are adding one degree of freedom but two data points, we still gain in statistics by using the  $^{60}\text{Co}$  peaks. This figure displays the Gray and Radford fits for the whole EXOGAM setup, as well as the sums  $\Sigma$  of Gray and Radford fits for each individual clover. The Radford and  $\Sigma$  Radford functions are in better agreement with each other than their Gray counterparts. Moreover the Radford and Gray functions have a reduced  $\chi^2$  of 1.37 and 17.7 respectively. The second value can be explained by the fact that the Gray function fails to fit the point 121 keV. It will therefore be the one used for calibration. For greater simplicity, we will assume that the  $DT$  of EXOGAM is the  $DT$  measured on  $^{152}\text{Eu}$  in clover 8. The ratio mentioned earlier between  $^{60}\text{Co}$  and  $^{152}\text{Eu}$  fits will be considered as error on the  $DT$  and subsequently as an error on the efficiency itself.

### Time calibration of the crystal's TAC

In this part, we focus on the calibration of each crystal's TAC. It is a crucial part as the selection or rejection of a  $\gamma$ -ray in EXOGAM depends on the time of arrival of this  $\gamma$ -ray. As stated in the description of the acquisition, these TAC are started by the crystals individual CFD and are stopped by the FT<sup>1</sup>. Of course, the value and error given by a TAC depends on the type of FT (see again Tab. 6.1). It is important to have a basic understanding of the time spectra structure to understand what follows. Let's describe a few cases arising from this very simple setup:

- I. The background counts in the time spectra occur when the CFD, or the FT, or both have been triggered by a random event from the  $\gamma$  background, mostly from beta decays. The n- $\gamma$  condition is supposed to prevent the master trigger card from issuing a FT on a background radiation, but BaF<sub>2</sub> trigger still allows it.
- II. In case the FT is created by a n- $\gamma$  coincidence, a CFD signal and the FT can be both generated by the same  $\gamma$ . As the FT is validated by the  $\gamma$  (not the neutron), the start and stop of this CFD are given by the same signal travelling different routes. The time difference between a signal and

<sup>1</sup>From here, all the TAC of the experiment will be stopped by the FT, unless specified otherwise.

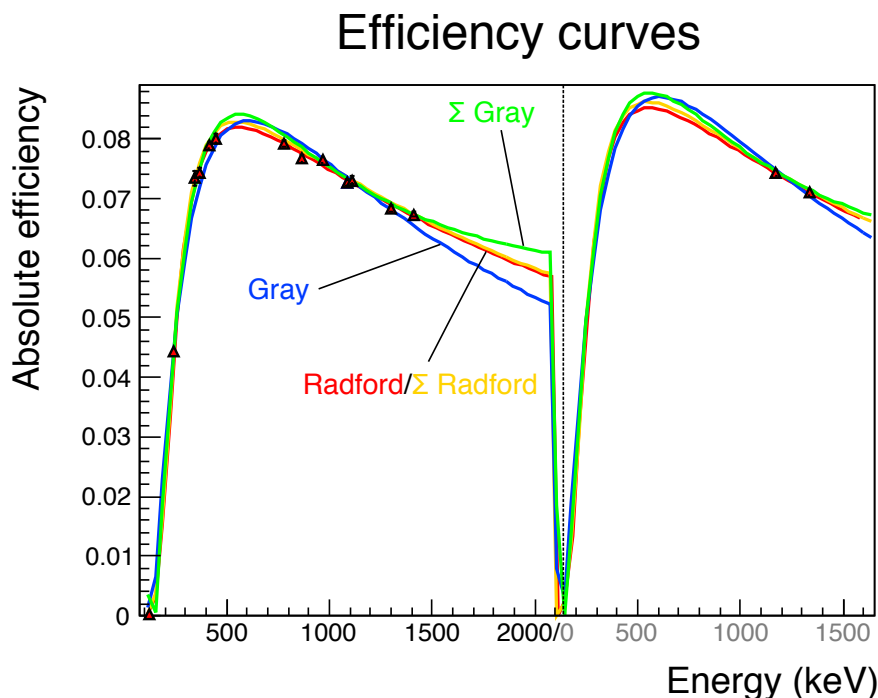


Figure 6.9 – EXOGAM efficiency fit with Gray (blue) and Radford (red) functions. Sum of all 11 Clovers efficiency fits with Gray (green) and Radford (yellow) functions. The two data points corresponding to the two  $^{60}\text{Co}$  peaks are fitted aside, but in the same fit procedure. The fit functions on both sides of the dashed line are the same, ignoring a multiplication factor.

himself is bound to have a very good resolution, and the small error on this value is only due to the electronics of the acquisition (not to the Ge crystals). This self-triggering explains the presence in each crystal's TAC spectrum of a single very sharp peak (Fig. 6.10) that we will call self-trigger peak.

III. In most cases, a TAC is initiated by a  $\gamma$  and stopped by the FT triggered by another  $\gamma$  hitting another crystal. Here, the error on the time information given by the TAC depends on the time resolution of both crystals. In the TAC spectrum of a crystal X, we will call FT-peak the peak due to the FT of a crystal Y different from X. Assuming that the time resolution  $\sigma_{t,Ge}$  is the same for all crystal, and knowing that this resolution is roughly 10 times larger than this of the electronics (given by the previous self-trigger peak), we can assume that the width of the FT-peak is  $\sqrt{2}\sigma_{t,Ge}$ . Normally, the CFD of the different crystals are time-aligned with a programmable delay (green on Fig. 6.4) so that the position of the FT in a time spectrum does not depend on the crystal which validated the FT, which is to say that the FT-peaks and the self-trigger peak should all be aligned in any of the crystals TAC spectrum. This was not the case during this experiment, as illustrated by the 4 bumps corresponding to 4 groups of crystal FT on the black histogram Fig. 6.10.

IV. When the  $\text{BaF}_2$  also triggers the FT, it acts as a 45<sup>th</sup> crystal. As this detector is not time-aligned either, it creates yet another peak in the TAC spectra (see again Fig. 6.10).

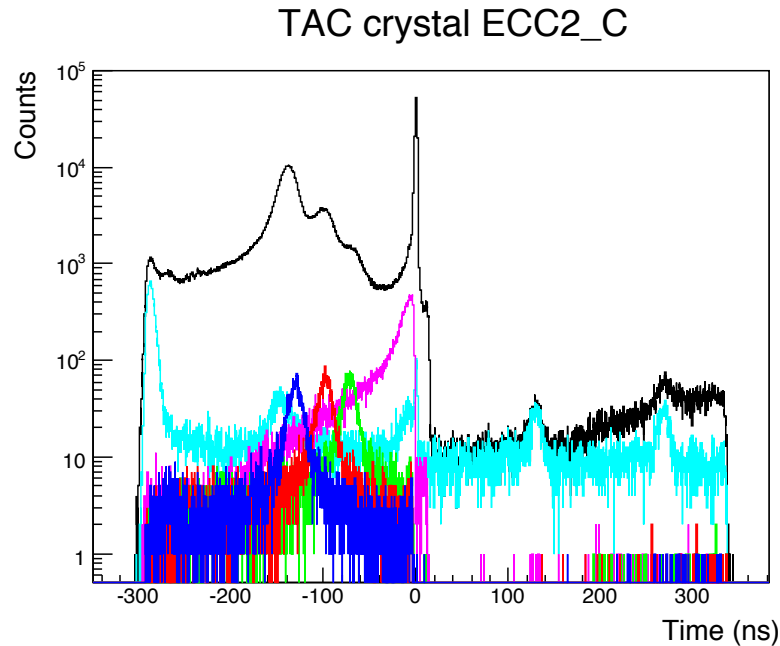


Figure 6.10 – Calibrated time spectrum of the TAC of the crystal ECC2-C for run 56. Black: all events. One can see the sharp self-trigger peak, the three bumps resulting of the crystal misalignment and a small peak on the left corresponding to the BaF<sub>2</sub> trigger. Coloured spectra: same TAC with the condition FT generated by ECC0-C (dark blue), ECC0-A (red), ECC4-A (green), ECC2-D (pink) and BaF<sub>2</sub> (light blue). HF repetitions can be observed for this last one.

These time spectra already provide us two means of calibration. Firstly, the BaF<sub>2</sub> and a crystal can be triggered by 2  $\gamma$ -rays generated by a different reaction. With a cyclotron frequency of 7.136 MHz, an ion bunch impinge on the target every  $\simeq 140$  ns. As a consequence, it is possible that a crystal and the BaF<sub>2</sub>, and for the concerned runs the FT, are triggered at different cycles. This effect is responsible for the presence of several peaks in the BaF<sub>2</sub>-triggered-only spectra (Fig. 6.10, light blue) which can be used for time-calibration. From now on we will call these secondary peaks HF repetitions<sup>2</sup>. Secondly, a count in a crystal will be read if and only if it is in coincidence with the FT pulse. Therefore the channel difference between the first and the last excited channel of a spectrum corresponds always to the size of the FT pulse, which is 651 ns. In addition to this two methods, a time shift on the FT signal occurred in the middle of the experiment though the value of the shift was unknown, it provided an occasion for a relative calibration of all crystal's TAC. It can be noted that all these methods aim to determine the gain. In the first place the offset was chosen so the self-trigger peak was centred on 0.

The second method was chosen, as it could be used for each and every run separately, in case of a brutal change of calibration. Nevertheless, for runs where both the second and third method could apply, the two were used as a check. The two methods showed to be consistent with a difference in relative gain below 1% for 75% of the crystals and maximum

<sup>2</sup>There are also HF repetitions for the normal n- $\gamma$  FT, but because of the crystal misalignment mentioned previously, it can not be exploited for a time calibration.



difference of 3.8%. As we don't understand so far the origin of this time shift, we will consider the reliability of this calibration with a bashful aloofness. Once calibrated, we also checked that the distance between the HF repetitions were indeed 140 ns. In the end 24 sets of calibration coefficients were determined, so as to frequently compensate small shifts of individual CFD or the FT. After calibration, we measured the widths of the FT-peaks at  $\simeq 8.5$  ns, and deduce the Ge detector time resolution  $\sigma_{t,Ge} \simeq 6$  ns (14 ns FWHM) and the electronic resolution (self-trigger peak) at  $\sigma_{t,el} = 1.1$  ns (2.5 ns FWHM). Finally, assuming the mid-experiment shift is instantaneous (not a drift), we can estimate that the calibration precision is roughly 1 ns and that the shift itself is  $\simeq 40$  ns.

### Time alignment of the crystals

In order to apply the same time selection/veto to every crystal, it is crucial that these are time-aligned with respect to a given reference, *e.g.* the HF of the cyclotron, the FT generated by a given crystal, the FT generated by the BaF2. . . Two solutions were tried:

- The first one was to determine the misalignments of each crystal  $Misal(crys)$  with respect to the crystal ECC2-C. If during an event 2  $\gamma$  hit crystals  $X$  and  $Y$  and the one on  $Y$  triggers the FT, the alignment of this event in the TAC of crystal  $X$  is given by  $TAC_{aligned}(X) = TAC_{unaligned}(X) + Misal(Y) - Misal(X)$ .
- Much cleaner, the second solution is to add the value of the TAC CFD-X-FT of a crystal  $X$  to the value of a TAC started by the FT and stopped by a HF pulse (which we will call TAC FT-HF). This way we can obtain a CFD-X-HF time independant of the FT. The only issue is that due to the calibration method (centering the self-trigger peak in 0) the different TAC CFD-X-FT won't be aligned. It is therefore mandatory to know the crystal misalignments for this method as well.

We will only detail the second method here, starting with the measure of the misalignments. To measure the misalignment of a crystal  $Y$  with respect to the crystal ECC2-C, we selected the events for which only these two crystals were hit. By looking at the TAC of ECC2-C (see Fig. 6.11) we can see 2 peaks: the self-trigger peak of ECC2-C and the FT-peak generated by crystal  $Y$ . The distance between these peaks is the misalignment. The FT-peaks of the different crystals are gathered in 4 groups, as seen in Fig. 6.11. The approximative misalignments are  $-140$  ns,  $-95$  ns,  $-70$  ns and  $0$  ns, for group 1, 2, 3 and 4 respectively. The reason we choose ECC2-C as a reference is that it has the longest delay of all the crystals. Indeed the FT generated by a crystal  $X$  can only appear on the TAC spectrum of a crystal  $Y$  with a longer delay. Therefore the TAC of ECC2-C is the only one for which all FT peaks appear.

A rapid check performed for 3 runs showed that these shifts change very little throughout the experiment, and only within the  $\sim 1$  ns error range of the calibration. The next step is to calibrate the TAC FT-HF. This

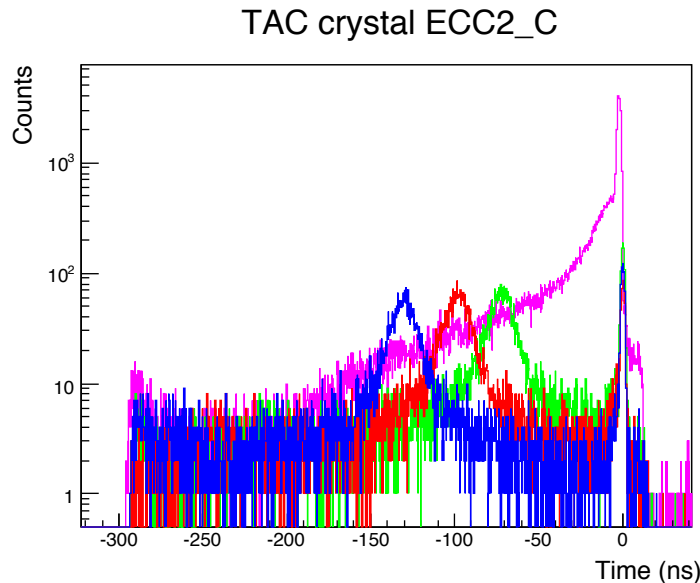


Figure 6.11 – Calibrated time spectrum of the TAC of the crystal ECC2-C when it has been triggered in coincidence with ECC0-C (group 1, dark blue), ECC0-A (group 2, red), ECC4-A (group 3, green) and ECC2-D (group 4, pink), for run 56. These graph differs from these, of the same color, of Fig. 6.10 by the presence of the self-trigger peak.

TAC is started by the FT signal and stopped by the next HF pulse. Therefore the value given by this TAC (and in general every TAC stopped by the HF) cannot exceed the HF period, 140.1 ns. Unfortunately, we cannot use this fact to calibrate the TAC, as all the events for which the start and stop are too close are counted in a sharp peak next to the origin of the spectrum (see histograms on the Y-axis of Fig. 6.12). We propose here to calibrate this TAC by comparing the distances between the FT peaks of the different crystals in the two spectra TAC FT-HF and TAC ECC2-C. We have to be cautious with this method, as the FT-HF spectrum is a "folded spectrum". Indeed the groups 1 and 4 mentioned earlier are separated by roughly one period in the crystal's TAC spectra, meaning that they are superimposed in the FT-HF spectrum. Before the calibration we have to fold up the TAC ECC2-C spectrum. The folding and the linear calibration are showed Fig. 6.12.

Like the other calibrations, this one was quite stable during the course of the experiment, within the limit of 1 ns. A small issue arises in the FT-HF spectrum: if the FT-HF peak of a given crystal is around 0 in the spectrum, the peak can be cut in two parts as illustrated bellow. We solve this problem by cutting the FT-HF spectrum with a FT generated by a crystal X at 70 ns (half a period) of the FT peak of X and shifting one of these two parts by 140 ns. As the FT peaks are rather large ( $\sigma \simeq 8.5$  ns i.e.  $\simeq 51$  ns at  $3\sigma$  on both sides), we applied this procedure to all FT peaks for good measure.

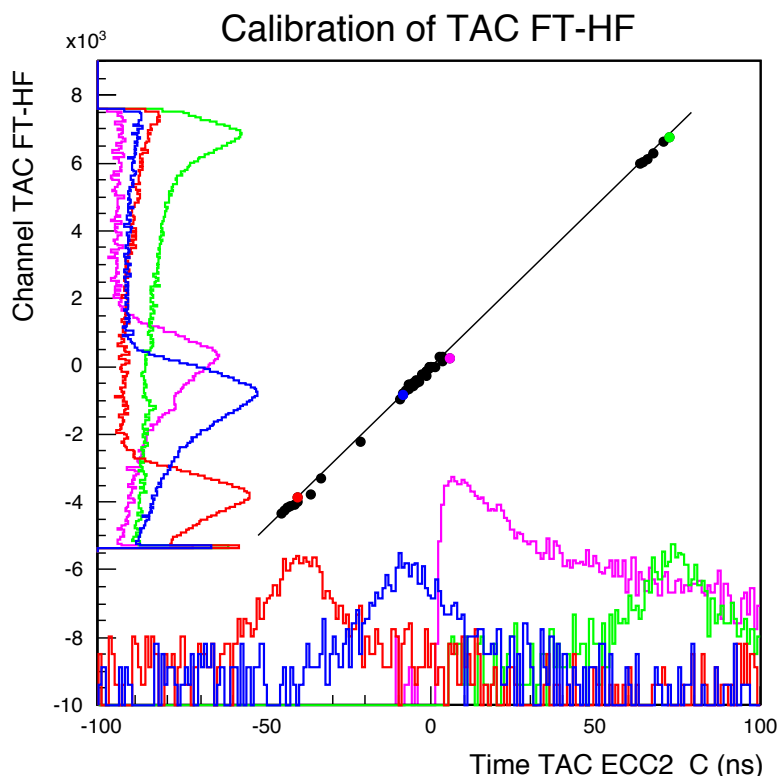
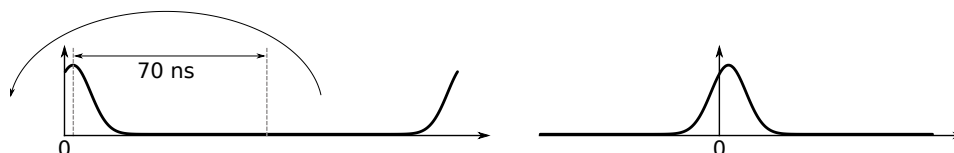


Figure 6.12 – Calibration process of the TAC FT-HF. The histogram on the Y-axis is the uncalibrated TAC FT-HF spectrum. On the X-axis, the calibrated *folded* TAC ECC2-C spectrum. Colours are the same as before. Apart from the folding the spectra on the X-axis are the same as in previous figures.



Once all crystal's TAC and the FT-HF TAC are calibrated we can build a calibrated CFD-X-HF time spectrum for which all the FT of the different crystals are aligned (Fig. 6.13, up left). Using the crystal misalignments, we can then build a global CFD-Exogam-HF time spectrum (Fig. 6.13, up right). The very last step of this time alignment is to compensate the HF drift. Depending on the tuning of the beam optics between the cyclotron and the experimental room, the time-of-flight of the ion bunch may (and does) vary during the experiment, inducing a variable CFD-HF time <sup>3</sup>. Fig. 6.13, down left shows the evolution of the HF drift throughout the experiment. This evolution was monitored every 10,000,000 events with the position of the peak in the TAC-HF-BaF spectrum. Fig. 6.13, down right displays the TAC-CFD\_Exo-HF for several runs before and after the HF drift compensation.

<sup>3</sup>Though we call this effect "HF drift", it's actually the impact time, and therefore the CFD, which moves.

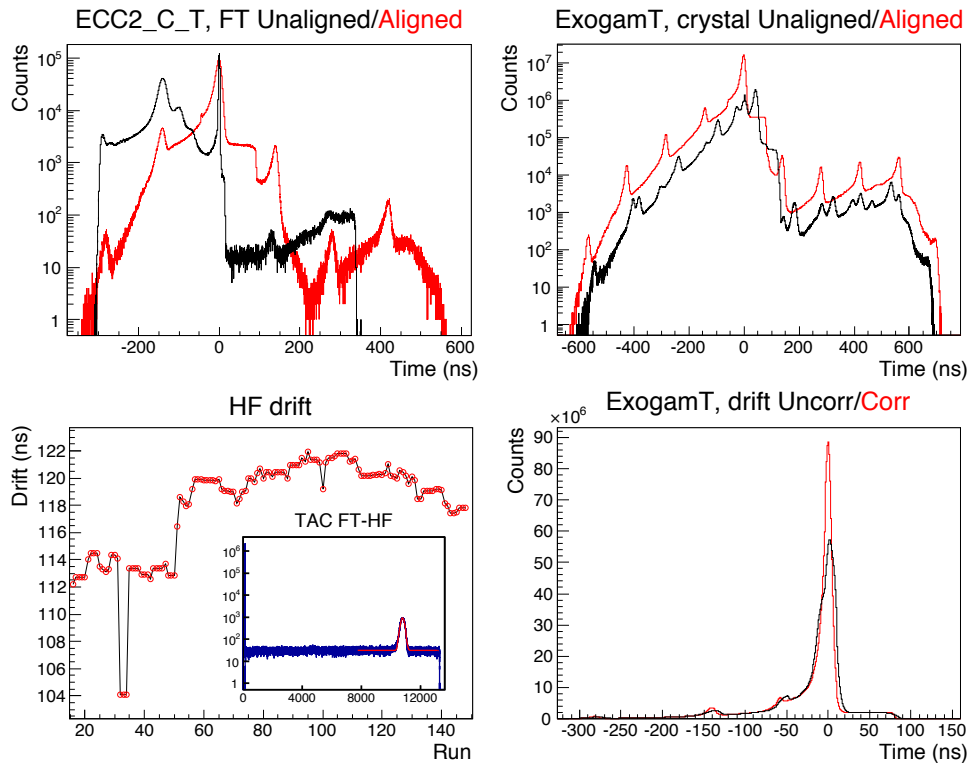


Figure 6.13 – Illustrations of the time alignment. **Up left:** alignment of the different FT in the TAC of a given crystal (here 2C), run 34. The black and red spectra are CFD-X-FT (unaligned) and CFD-X-HF (HF-aligned), respectively. The small peak in  $-50$  ns and the step in  $+90$  ns are due to the shape of the TAC-FT-HF spectrum. **Up right:** alignment of the different crystals with the calculated misalignments, run 34. **Down left:** evolution of the HF-drift during the experiment. The inset is an example of peak fitted in the TAC-FT-HF spectrum to measure the drift (run 36). **Down right:** sum of the TAC-CFD\_Exo-HF for several runs (runs 30-60) before and after HF-drift correction.

### 6.3.2 DIAMANT

The DIAMANT setup was only used for charged particle selection/rejection. It therefore did not require calibration nor alignment, but only some 2D graphical cuts on individual detectors detailed later.

### 6.3.3 NWall

The NWall setup was used for neutron selection/rejection, but unlike for DIAMANT, time-calibration and alignment are needed to differentiate the neutrons from the  $\gamma$ -rays by the ToF method. We initially used a set of ToF and ZCO linear calibration coefficients that had been used during the experiment. The ToF gain and offset were slightly corrected to align the HF repetition peaks of the ToF spectrum of each NWall cell. As for the EXOGAM, the time signals were referenced to the HF pulses and corrected from the HF drift by the simple operation:  $Time - CFDX - HF = TAC - CFDX - CFDOR + TAC - CFDOR - HF + Drift$  with CFDX being the output of the CFD of cell X and CFDOR being an OR gate on all CFDX of NWall. The TAC of the ZCO did not need HF drift correction as it is started by the cell's CFD and stopped by the zero-crossover time of the bipolar signal and thus is not referenced to the HF.

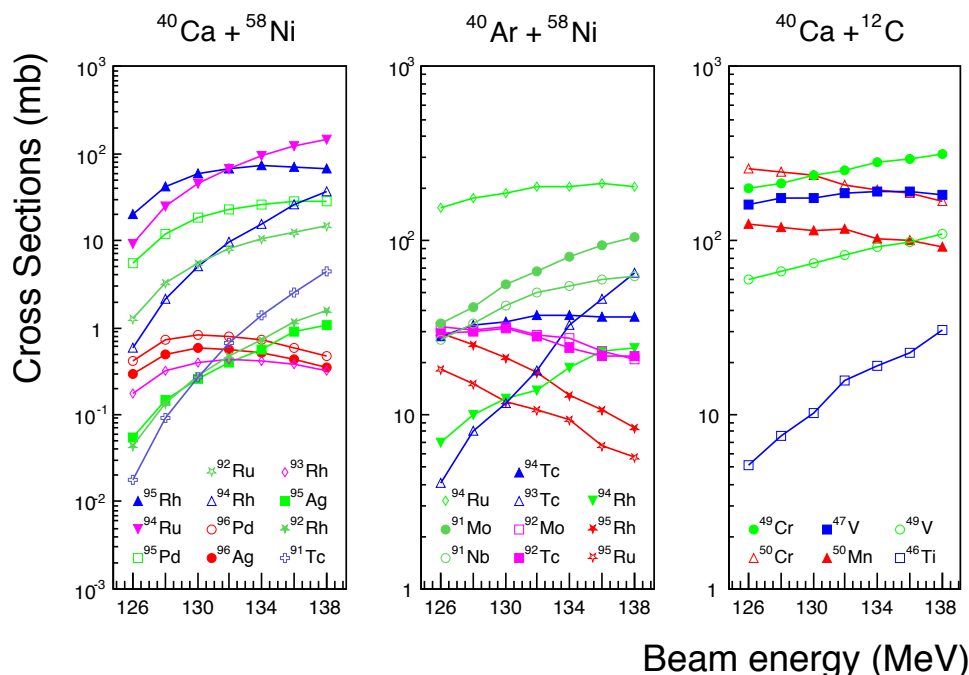


Figure 6.14 – Cross-sections of fusion-evaporation reactions for the main fusion reaction, for the beam contaminant  $^{40}\text{Ar}$  and for the target substrate  $^{12}\text{C}$ . Weaker reaction channels (like the  $^{94}\text{Pd}$ ) are not printed.

## 6.4 PRE-ANALYSIS

### 6.4.1 Expected reactions and contaminations (Ar and C)

Fig. 6.14 displays the cross-sections of several fusion-evaporation reaction, including contaminants. The calculations of these cross-sections have been made with the PACE4 fusion-evaporation code. Other calculations had been made prior to the experiment using HIVAP and though the results were different, the order of magnitude and the relative ordering of the different reaction channels are quite close. As predicted by PACE4,  $^{58}\text{Ni}(^{40}\text{Ar},2\text{p}2\text{n})^{94}\text{Ru}$ ,  $^{12}\text{C}(^{40}\text{Ca},3\text{p})^{49}\text{V}$  and  $^{12}\text{C}(^{40}\text{Ca},2\text{p}1\text{n})^{49}\text{Cr}$  have all been observed in the spectra at various rates, depending on the contamination of  $^{40}\text{Ar}$  in the beam and the contamination of  $^{12}\text{C}$  in the different targets.

### 6.4.2 Background reduction and scattering rejection in EXOGAM

The energy and time calibrations in EXOGAM enable a 2D-gate in the  $E\gamma T\gamma$  matrix. This gate cuts out a significant part of the constant  $\gamma$  background generated by  $\beta$ -decay. Also the Compton background due to scattered  $\gamma$  can be reduced either by suppression or add-back of the concerned events. The scattering of  $\gamma$ -rays in EXOGAM mostly happens between neighbouring crystals of a same clover thanks to the high absorption of anti-Compton shields. If the BGO shield of a clover and one or more of its crystals are triggered in coincidence, the energy collected in this clover is not considered. If several crystals of a same clover are triggered in coincidence but not its BGO, the energies of the different

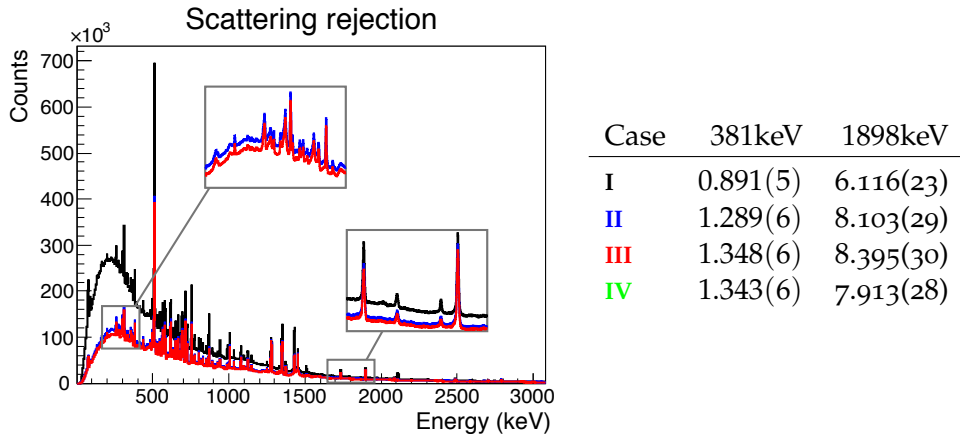


Figure 6.15 – Figure: EXOGAM spectrum, run 71, for case I, II and III (matching colors). Table: peak-to-background ratios of 381keV (3p) and 1898keV (4p) with different scattering-rejection methods. This ratio is calculated as the number of counts in a peak divided by the number of background counts per keV at the position of the peak.

crystals are added and the event is taken into account.

We also considered the possibility of scattering rejection between different clovers. By looking at the coincidence count rate for each pair of crystal in EXOGAM we noticed, as expected, that coincident hits are most likely between neighbouring crystals of a same clover. In addition, a high number of coincidences were also observed with neighbouring crystals from different clovers, proving that inter-clover scattering occurs in noticeable proportions. In the following, we try to take into account this scattering to enhance the peak-to-background ratio. First, for each crystal, we listed the neighbours from a different clover (e.g. crystal 0D is neighbour with 4A and 6B). All simultaneous events in neighbouring crystals are automatically considered as scattered events. Fig. 6.15 and its table compare the peak-to-background ratio at low and high energy in various cases:

- I. No condition.
- II. Add-back within a same clover and rejection if BGO triggers.
- III. Same as II and rejection of out-of-clover neighbouring crystals energies.
- IV. Same as II and add-back of out-of-clover neighbouring crystals energies.

The systematic rejection of the events with out-of-clover neighbouring crystals seems to work better at both low and high energy than the simple add-back between crystals of a same clover, thus we will use the condition III. At high energy, the add-back of neighbouring crystals from different clovers seems to be less effective. This seems consistent with the fact that the number of pile-up events at high energy is higher than for lower energies, for which the  $\gamma$ -rays are less likely to scatter.

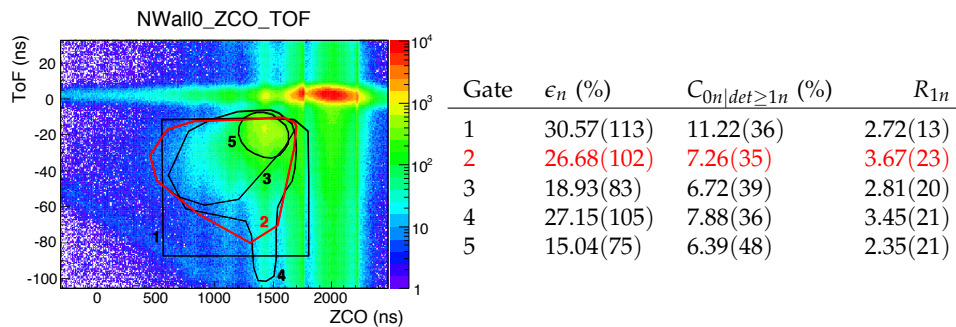


Figure 6.16 – Image: ToF v.s. ZCO matrix of cell 0, run 71. The lower left region of the matrix is populated by neutrons. The lines defined by  $ToF \simeq 0$  and  $ZCO \simeq 2000$  are due to  $\gamma$ -rays which manage to pass the hard-neutron gate. Table: comparison of different neutron gates (not exhaustive) in efficiency and  $\epsilon_n$ , contamination  $C_{0n|det \geq 1n}$  and efficiency/contamination ratio  $R_{1n}$ . See details in text.

### 6.4.3 Neutron identification in NWall

In NWall, the neutrons and  $\gamma$ -rays can be separated according to their ZCO, as well as their ToF. We do both at once by using a graphical cut in a 2D plot of ToF v.s. ZCO as shown in Fig. 6.16. Several gates were used and compared in Fig. 6.16. Since the ToF and ZCO signals of NWall have been calibrated and aligned, we can use the same gate(s) on all NWall-cells. The ToF-ZCO matrix of cell 0 was only given here to show that the ZCO structure that we observe is not due to the sum of several non-aligned matrixes. The sharp transition near  $ZCO=1800$  could be due to a reset in ZCO. Depending on the size and shape of the gate, this can induce some  $\gamma$ -contamination of the neutron-condition. In order to weight the effect of the different gates, we introduce the following variables:

- The neutron efficiency or  $\epsilon_n = I_{1n|det \geq 1n(noHNG)} / I_{1n(noHNG)}$ , where  $I_{1n|det \geq 1n(noHNG)}$  is the integral of a given  $\gamma$ -ray peak in a 1n-channel with at least 1 neutron detected and  $I_{1n(noHNG)}$  is the integral of the same peak without any neutron condition. The "noHNG" indicates that these integrals were measured for runs without the Hardware Neutron Gate trigger condition. We decided to use the 1280 keV peak of the  $^{94}\text{Rh}$  (3p1n channel) in run 16.

- The contamination 0n into 1n-conditioned spectra or  $C_{0n|det \geq 1n} = (I_{0n|det \geq 1n} \times I_{1n}) / (I_{1n|det \geq 1n} \times I_{0n})$ , with  $I_{0n|det \geq 1n}$  being the integral of peak from a 0n channel detected in coincidence with "at least 1 neutron", etc. This contamination is calculated as the ratio of the "0n" channel over the "1n" channel in the  $det \geq 1n$  conditioned spectrum. The peak intensities in this spectrum are by their intensities in the unconditioned spectrum.

We choose the 2790 keV peak from the  $^{95}\text{Rh}$  for the 0-n channel. Integrals were measured in run 71.

- The efficiency-contamination ratio or  $R_{1n} = \epsilon_n / C_{0n|det \geq 1n}$ .

We decided to choose the 2D cut that maximised the  $R_{1n}$  ratio, in red in Fig. 6.16. The table on the right hand side of the figure displays the efficiencies, contamination and  $R_{1n}$  for several gates.

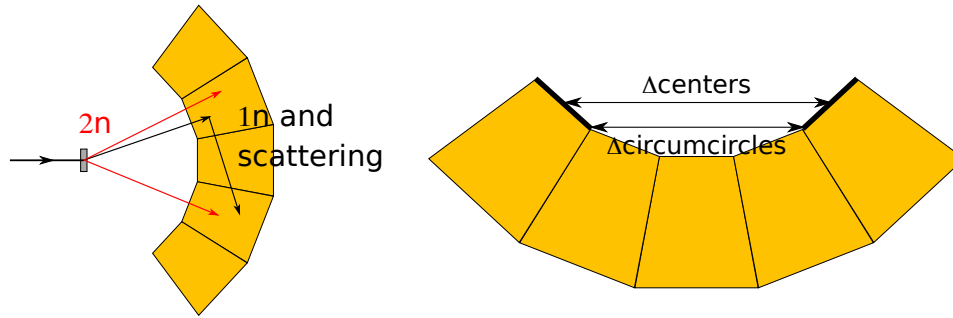


Figure 6.17 – **Left:** difference between a true "2n" event and a single scattered neutron. **Right:** different ways of measuring the distances between the different cells of NWall.

#### 6.4.4 Scattering rejection in NWall

Assuming that we are now capable of identifying a neutron, we want to be able to differentiate a true 2n event from a 1n scattering event (see Fig. 6.17-left). In order to achieve so, we applied a "time limit" condition on the event selection: if the time between the trigger of two cells is smaller than the distance between those cells divided by the estimated speed of a scattered neutron, then this time is too short to be due to one scattered neutron. Also, under a certain distance (neighbouring cells), we consider all events to be scattering. The high number of counts at low relative distance between cells as shown in Fig. 6.18 confirms it. The distance between cells was initially just the distance between their centres. Afterwards, we preferred to use the distance between the circumcircles of each cell, a more severe criterium (see Fig. 6.17-right). We initially considered 2 MeV neutrons, i.e. a speed of  $\sim 2 \cdot 10^7$  m.s<sup>-1</sup>, and tried several other speeds. As in the previous part, we define the following notations:

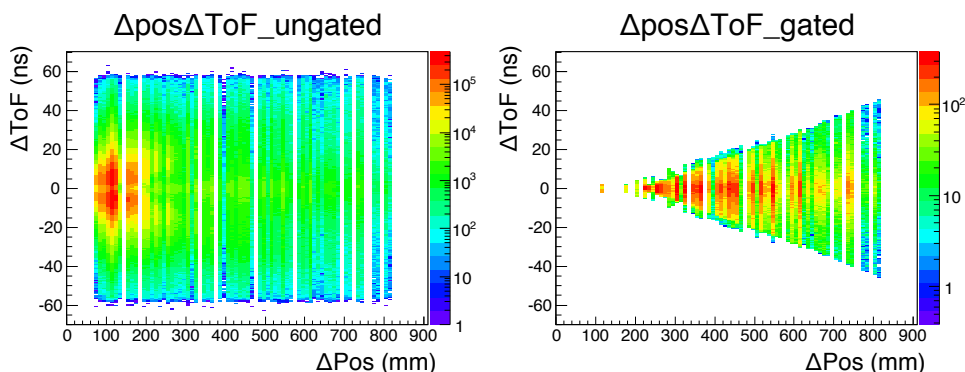
- $\epsilon_{2n} = \epsilon_{1n} \times I_{2n|det \geq 2n} / I_{2n|det \geq 1n}$ . Here we define the 2n efficiency with respect to the 1n efficiency because the intensities of the peaks from all 2n-channels were too small to be measured in the unconditioned spectrum, and only a few could be measured in both the 1n and 2n spectra.
- $C_{1n|det \geq 2n} = (I_{1n|det \geq 2n} \times I_{2n|det \geq 1n}) / (I_{2n|det \geq 2n} \times I_{1n|det \geq 1n})$ . As before we measure the ratio of 1n events counted as 2n over the true 2n events, and normalise the intensities in the 2n spectrum by the intensities of the 1n-spectrum.
- $R_{2n} = \epsilon_{2n} / C_{1n|det \geq 2n}$

Here, the 1n channel peak was still 1280 keV and the 2n was 906 keV from <sup>94</sup>Pd (2p2n channel). Again, the table next to Fig. 6.18 shows the results of the different cuts, the best in red.

#### 6.4.5 Charged particles identification in DIAMANT

The particle identification in DIAMANT was performed through 2D gates in Energy-PID matrices. Numerous gates were built to accommodate the differences in the matrices between two scintillators or for different runs. Among the reason why these matrixes change from one another we can cite:





Distance	Speed	$\epsilon_{2n}$ (%)	$C_{1n det \geq 2n}$ (%)	$R_{2n}$
circumcircle	13	2.67(34)	1.21(18)	2.21(26)
<b>circumcircle</b>	<b>15</b>	<b>2.60(33)</b>	<b>1.04(16)</b>	<b>2.51(27)</b>
circumcircle	20	2.23(30)	0.98(16)	2.27(28)
center	35	2.46(33)	1.73(25)	1.42(27)
center	45	2.16(29)	1.31(21)	1.66(28)
center	55	1.82(26)	1.25(21)	1.46(29)

Figure 6.18 – Images:  $\Delta$ Position *v.s.*  $\Delta$ ToF matrixes (one count for each pair of triggered cells). Table: comparison of different gating conditions. “Distance” indicates if the distance between cells is considered to be the distance between their center or their circumference. “Speed” refers to the estimated speed of the scattered neutrons (in  $m \cdot \mu s^{-1}$ ). The gated matrix correspond to the red set of parameters.

- the intrinsic imperfections of each scintillator.
- the fact that the PID signal is more resolved for forward angles and less for backwards angles.
- the fact that the electron-pileup in DIAMANT, impacting the resolution, depends on the beam intensity, and hence on the run.

Fig. 6.19 shows an example of graphical cut the Energy-PID matrix of a forward scintillator. As the gates change from one detector to the other and from one run to another, we have to measure the proton and  $\alpha$  efficiencies (respectively  $\epsilon_p$  and  $\epsilon_\alpha$ ) using conditioned  $\gamma$ -spectra of all the runs. As there was no 1p channel with enough data to fit a peak properly, we deduced the proton efficiency from the rates of the 3p channel  $^{95}\text{Rh}$  and the 3p1n channel  $^{94}\text{Rh}$  in 1p-, 2p- and 3p-conditioned spectra, using the expressions in the first column of Tab. 6.3. We chose these two nuclei for their high production rate through the  $^{40}\text{Ca} + ^{58}\text{Ni}$  reaction, but relatively low production rate by the contamination reaction  $^{40}\text{Ar} + ^{58}\text{Ni}$ . Tab. 6.3 shows the intensity ratios 1p/2p and 2p/3p for the 696 and 703 keV peaks of  $^{94}\text{Rh}$  and the 716 keV peak of  $^{95}\text{Rh}$ , as well as different estimates of the proton efficiency  $\epsilon_{1p}$ . The efficiency deduced from the two peaks of  $^{94}\text{Rh}$  are in remarkable agreement for a given ratio. The efficiency estimated with the  $^{95}\text{Rh}$  peak is higher, hinting the existence of an additional peak on the 716 keV position not belonging to a 3p channel (yet not identified). On each of the 2 peaks of  $^{94}\text{Rh}$ , we see a small difference between the efficiencies calculated with the first and the second ratio, which is most likely due to a contamination from  $\gamma$ -rays in the proton gate. Such a contamina-

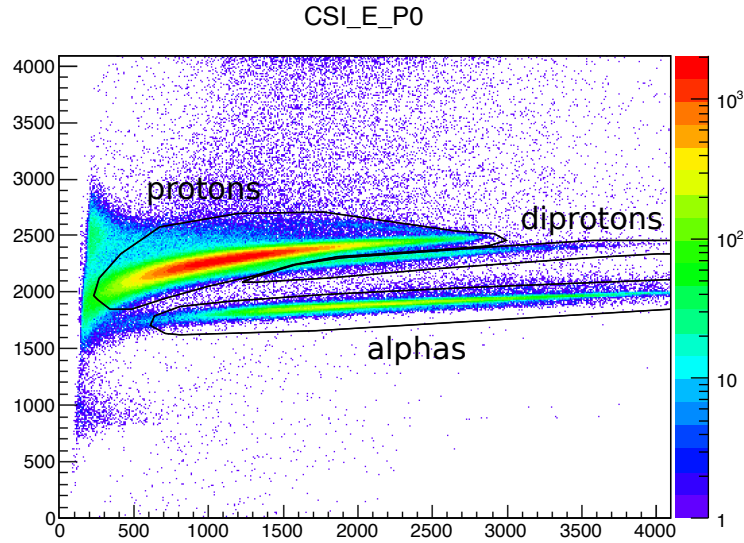


Figure 6.19 – Energy-PID matrix of the first CsI of DIAMANT. The events in the top-left corner of the proton distribution are  $\gamma$ -rays. The axes have are in channels, since the Energy and PID signals of DIAMANT have not been calibrated.

tion would indeed shift the distribution of the counts in the 1p, 2p and 3p spectra. It is possible to use this difference to calculate the contamination. If we consider a probability  $C_p$  of having a contamination in the proton gate for each event, we can write the following set of equations:

$$\frac{I_{3p|det=1p}}{n} = 3\epsilon_{1p}(1 - \epsilon_{1p})^2(1 - C_p) + (1 - \epsilon_{1p})^3C_p \quad (6.2)$$

$$\frac{I_{3p|det=2p}}{n} = 3\epsilon_{1p}^2(1 - \epsilon_{1p})(1 - C_p) + 3\epsilon_{1p}(1 - \epsilon_{1p})^2C_p \quad (6.3)$$

$$\frac{I_{3p|det=3p}}{n} = \epsilon_{1p}^3(1 - C_p) + 3\epsilon_{1p}^2(1 - \epsilon_{1p})C_p \quad (6.4)$$

Where  $\frac{I_{3p|det=ip}}{n}$  is the detection efficiency of  $i$  protons in a peak from a  $3p$  channel and  $n$  is the total number of  $\gamma$ -ray emitted at this energy during the same period.  $n$  disappears when calculating ratios of these 3 equations. The expressions of the real efficiency and contamination, are too long to be written here, and can be numerically calculated. The calculation on both peaks leads to a proton efficiency  $\epsilon_{1p} = 55.1\%$  and a contamination  $C_p \sim 5\%$  (i.e.  $\sim 1$  of 20 counts in the proton gate is actually a  $\gamma$  or an  $\alpha$ ).

The  $\alpha$  efficiency is much easier to calculate as there are several  $1\alpha$  channels that we can exploit. In the end we choose to measure it with the 804 keV  $\gamma$ -transition from  $^{92}\text{Ru}$  ( $2p1\alpha$  channel), as it is the strongest peak from the strongest  $1\alpha$  evaporation channel. As before we obtain the efficiency by comparing the photopeak intensity of this transition with or without an  $\alpha$ -condition and the contamination by measuring the effect of this condition on a  $0\alpha$  channel. For the contamination measurement, we took the 1898 keV  $\gamma$ -ray from the  $4p$  channel  $^{94}\text{Ru}$ . We define and calculate the following:

Method	Energy	Ratio	$\epsilon_{1p}(\%)$
$\frac{I_{3p det=1p}}{I_{3p det=2p}} = \frac{1-\epsilon_{1p}}{\epsilon_{1p}}$	696 keV	0.7914(12)	55.82(7)
	703 keV	0.7941(13)	55.74(7)
	716 keV	0.6709(47)	59.85(28)
$\frac{I_{3p det=2p}}{I_{3p det=3p}} = \frac{3(1-\epsilon_{1p})}{\epsilon_{1p}}$	696 keV	2.251(4)	57.14(12)
	703 keV	2.268(4)	56.95(13)
	716 keV	1.792(13)	62.60(45)

Table 6.3 – Calculation of the proton efficiency on several peaks, considering no contamination occurs.

- $\epsilon_{1\alpha} = I_{1\alpha|det \geq 1\alpha} / I_{1\alpha} = 28.13(5)\%$
- $C_{0\alpha|det \geq 1\alpha} = (I_{0\alpha|det \geq 1\alpha} \times I_{1\alpha|det \geq 0\alpha}) / (I_{1\alpha|det \geq 1\alpha} \times I_{0\alpha|det \geq 0\alpha}) = 3.17(4)\%$

## 6.5 SPIN AND POLARITY ASSIGNMENTS

In this part, we detail how the EXOGAM setup was used to measure  $\gamma$ -ray angular distributions and  $\gamma$ -ray linear polarisation in order to assign the electromagnetic nature and angular momentum of several transitions in order to deduce the parity and spin ( $J^\pi$ ) of nuclear levels. We will mostly follow here the method described in [114].

In a fusion-evaporation experiment, the spin of the compound nucleus is preferentially aligned perpendicularly to the beam axis. This is due to the fact that the incoming nuclei bring angular momentum to the pre-fusion dinuclear system, then to the compound nucleus. The spins of the target and projectile nuclei has little effect on the orientation of the compound nuclei compared to the angular momentum brought by the projectile. However evaporated particles ( $p$ ,  $n$ ,  $\alpha$ ) leave the nucleus carrying a part of its angular momentum. This results in the broadening of the spin distribution of the residual nuclei. Let us consider the beam axis as the axis of quantisation. It is usually assumed that the distribution of population of the magnetic substate is gaussian and centered in  $m = 0$  (i.e. perpendicularly to the beam axis) as in [115]. The partial alignment of the residual nuclei implies an anisotropic distribution of the decay  $\gamma$ -rays, with a symmetry with respect to the beam axis. The angular distribution depends on the multipolarity of the considered transition and can generally be expressed as a linear combination of Legendre polynomial of even order :

$$W(\theta) = \sum_{i=0}^l a_{2i} P_{2i}(\cos\theta) \quad (6.5)$$

Where  $\theta$  is the angle between the emitted  $\gamma$  and the primary beam axis,  $l$  is the quantum number of the angular momentum taken by the outgoing  $\gamma$ ,  $P_{2i}$  is the Legendre polynomial of order  $2i$  and  $a_{2i}$  is the corresponding coefficient depending on the multipolarity (and the mixing ratio of the different multiplicities) and the alignment of the residual nuclei. As multipolarity higher than 2 are quite unusual, we usually express the distribution with the first factors:

$$W(\theta) = a_0 + a_2 P_2(\cos\theta) + a_4 P_4(\cos\theta) \quad (6.6)$$

or

$$W(\theta) = A_0 [1 + A_2 P_2(\cos\theta) + A_4 P_4(\cos\theta)] \quad (6.7)$$

with  $A_0$  the intensity and  $A_2$  and  $A_4$  the dipole and quadrupole normalised factors. The dispersion of the nucleus orientation lowers these factors. Indeed  $A_i$  can be expressed as  $A_i = \alpha_i A_i^{max}$  with  $A_i^{max}$  being the normalised factor of order  $i$  for a perfectly aligned nuclei and  $\alpha_i$  being an attenuation coefficient accounting for a partial alignment (see [116, 117]). With Germanium-detector arrays like EXOGAM, it is possible to measure the distribution of a certain  $\gamma$ -transition at several given angles (in EXOGAM  $90^\circ$  and  $135^\circ$ ). By fitting Eq. 6.7 on the  $\gamma$  intensity at several angles, one can deduce the  $A_2$  and  $A_4$  factors. Though the precise determination of the multipolarity mixing ratio requires to know  $A_2^{max}$  and  $A_4^{max}$ , the knowledge of  $A_2$  and  $A_4$  is often sufficient to determine the dominant multipolarity.

### 6.5.1 DCO ratios and polarisation asymmetries

The anisotropy in the angular distribution can be exploited to reveal the multipolarity of a  $\gamma$ -transition. With a germanium array, this multipolarity can be estimated by several tests: with the  $A_2$  coefficient as in [118], the calculation of the anisotropy between 2 angles as in [119] or the calculation of DCO ratios as in many papers (e.g. [114, 118, 120]). The DCO (Directional Correlation from Oriented state) ratio is defined in EXOGAM by:

$$R_{DCO} = \frac{I(\gamma_1@90^\circ|\gamma_2@135^\circ)}{I(\gamma_1@135^\circ|\gamma_2@90^\circ)} \quad (6.8)$$

where  $I(\gamma_1@90^\circ|\gamma_2@135^\circ)$  (resp.  $I(\gamma_1@135^\circ|\gamma_2@90^\circ)$ ) is the intensity of the  $\gamma_1$  transition at  $90^\circ$  (resp.  $135^\circ$ ) gated by  $\gamma_2$  at  $135^\circ$  (resp.  $90^\circ$ ). We could argue that it is possible to extract the anisotropy information from the simple  $I(\gamma_1@90^\circ)/I(\gamma_1@135^\circ)$  ratio. Nevertheless fusion-evaporation reactions allow to reach high spin states in residual nuclei and the resulting single spectra are usually dense (without mentioning the contaminations). Thus, gating a  $\gamma - \gamma$  matrix on a transition  $\gamma_2$  feeding or decaying from  $\gamma_1$  cleans the spectrum and allows a better fit of the  $\gamma_1$  peak. Also, gating on  $\gamma_2$  at a given angle correlates the angular distribution of  $\gamma_1$  to that of  $\gamma_2$ . If we choose to gate on a well known transition, we have the remarkably simple interpretation:

- if  $R_{DCO} \simeq 1$   $\gamma_1$  and  $\gamma_2$  have the same multipolarity
- if  $R_{DCO} \neq 1$   $\gamma_1$  and  $\gamma_2$  have different multipolarities

In the case of EXOGAM,  $R_{DCO} \simeq 0.6$  (resp.  $\simeq 1.6$ ) for pure stretched dipole (resp. quadrupole) transitions gated by a pure stretched quadrupole (resp. dipole) transition [114].

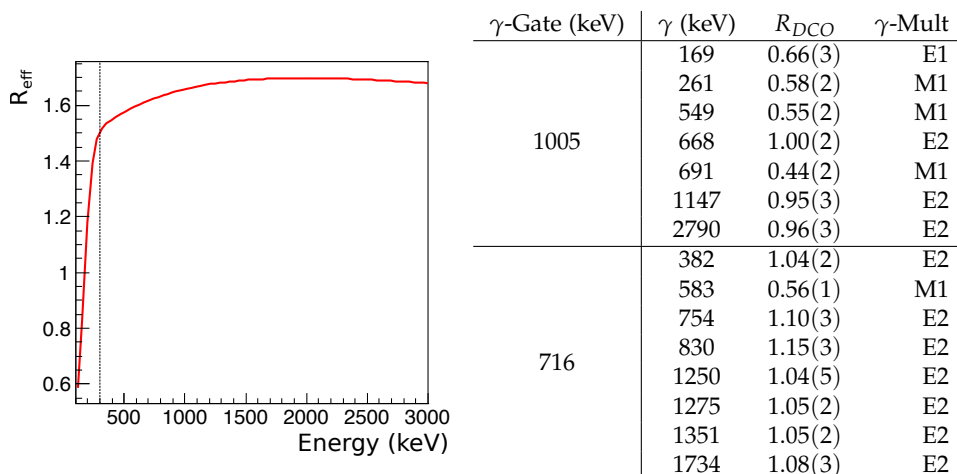


Figure 6.20 – **Picture:** evolution of  $R_{eff}$  with the  $\gamma$ -energy. The correction of the  $R_{DCO}$  is necessary of energies below 300 keV. **Table:** important transitions of the rather well known  $^{95}\text{Rh}$  and their measured  $R_{DCO}$  using two E2 transition for  $\gamma$ -gating. The last column shows the known transition multiplicities of  $^{95}\text{Rh}$ , which are consistent with the  $R_{DCO}$  values. It has been noted that the values of  $R_{DCO}$  for 717 and 1351 keV are lower when gating on 2790 keV. We attribute this difference to the 19 ns isomeric state at 2236 keV between the 2790 keV transition and the two others, during which the nucleus alignment is partially or completely lost.

The  $R_{DCO}$  depends on the efficiencies of the detectors at  $90^\circ$  and  $135^\circ$ .

$$R_{DCO} \propto \frac{\epsilon_{90^\circ}(\gamma_1)\epsilon_{135^\circ}(\gamma_2)}{\epsilon_{135^\circ}(\gamma_1)\epsilon_{90^\circ}(\gamma_2)} = \frac{R_{eff}(\gamma_1)}{R_{eff}(\gamma_2)} \quad (6.9)$$

If all the detectors had the same efficiency behaviour with respect to the  $\gamma$  energy,  $R_{eff}$  would be constant and this ratio would be equal to 1. As it is not the case, the  $R_{DCO}$  has to be corrected. Fig. 6.20 shows the evolution of  $R_{eff}$  with the energy. The table next to it gives the  $R_{DCO}$  measurements for  $^{95}\text{Rh}$ . The  $R_{DCO}$  match the known multipolarity, even at low energy, confirming that the  $R_{eff}$  is good. We also checked the validity of the  $R_{DCO}$  estimates on  $^{94}\text{Ru}$  and later in this chapter, on  $^{94}\text{Pd}$ .

Though very useful, the DCO ratio of a transition is insufficient in several respects. First a mixed quadrupole+dipole transition will have a  $R_{DCO}$  between 0.6 and 1 (or 1 and 1.6 according to the gate) depending on the multipole mixing ratio  $\delta$ . For instance a  $R_{DCO} = 0.7$  may indicate a dipole and quadrupole mixing. Secondly, in case of unstretched transitions ( $\Delta I = 0$ ) the angular momentum taken by the outgoing  $\gamma$  of lowest multipolarity (i.e. dipole) cannot be aligned with the spin of the decaying or the decayed nuclei, which mean this  $\gamma$  has a different angular distribution than an stretched dipole  $\gamma$ . An unstretched pure dipole transition has roughly the same  $R_{DCO}$  as a stretched quadrupole transition. Finally the DCO ratio depends on the multipolarity of a  $\gamma$ -ray and thus on the spin of the feeding/decaying nuclear state, but does not give any information about the electromagnetic nature of the transition. For this, one needs to determine its linear polarisation.

The EXOGAM array is also capable of performing polarisation measurements. The linear polarisation allows to sort the  $\gamma$ -transitions accord-

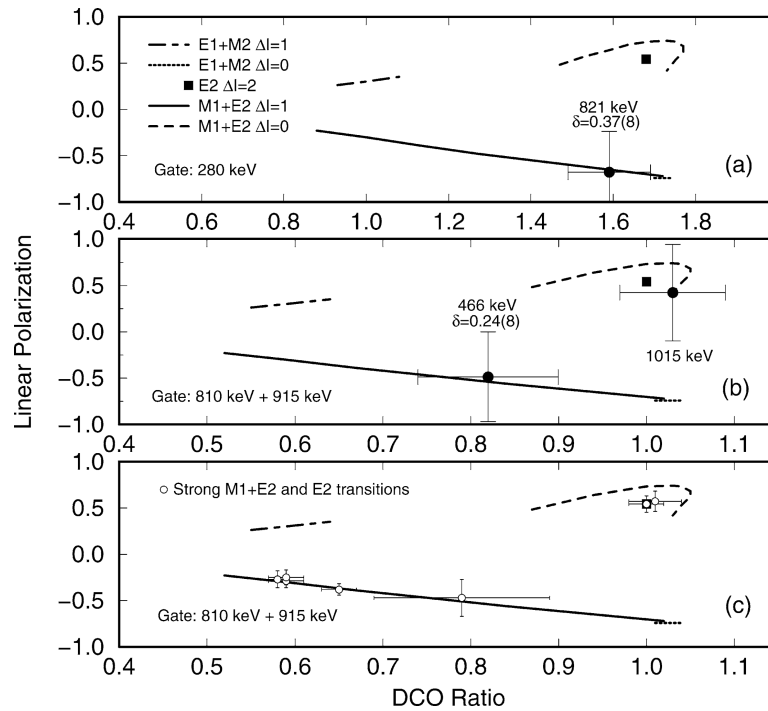
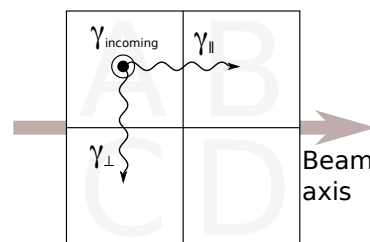


Figure 6.21 – Calculated and measured DCO ratios and polarisation for several transition types. A pure stretched E2 transition is well defined in this frame, while mixed transitions may vary in both observables according to their mixing ratio. Taken from [121].

ing to their electromagnetic nature. Knowing both the DCO ratio and the linear polarisation of a given transition is a good way to assign its multipolarity, EM nature and even know if the transition is stretched/unstretched. Fig. 6.21 shows the expected position of several types of transition in the polarisation v.s.  $R_{DCO}$  frame, while gating on a dipole (a) or quadrupole (b and c) transition. It can be noted that only the stretched M1 + E2 shows a strong dependency to the mixing ratio.

Let the emission plane be defined by the beam axis and a first  $\gamma$ -ray. In the case of a Compton event involving 2 crystals of the same clover, the scattering diminution depends on the degree of linear polarisation and the electromagnetic nature of this  $\gamma$ -ray. The polarisation is measured with the seven  $90^\circ$  clovers, as polarisation-sensitivity of the array is the greatest at this angle. If two neighbouring crystals of the same clover are triggered simultaneously and their alignment is parallel (resp. perpendicular) to the emission plane (e.g. crystals A and B in the drawing above) then the event is considered as a parallel (resp. perpendicular)  $\gamma$ -scattering. We build two  $\gamma$ - $\gamma$  matrices. The parallel (resp. perpendicular) matrix gives the coincidence between a parallel (resp. perpendicular)  $\gamma$ -scattering in a  $90^\circ$  clover and a hit on any other clover. One of the axis of these matrices is the add-back energy of the 2 crystals while the other is the add-back energy of the full



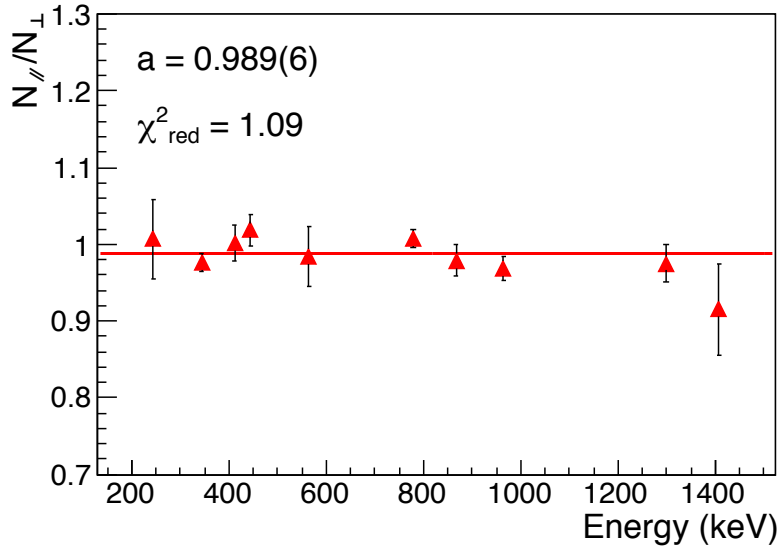


Figure 6.22 – Normalisation factor  $a$  as a function of the energy.

clover. The aim of clover gating is merely to suppress the background and contaminations. Let  $N_{||}$  and  $N_{\perp}$  be the number of counts of parallel and perpendicular scattering of a given  $\gamma$ . We define the experimental polarisation asymmetry  $A$  by:

$$A = \frac{aN_{\perp} - N_{||}}{aN_{\perp} + N_{||}} \quad (6.10)$$

where  $a$  is a normalisation factor that corrects the experimental asymmetry between the number of parallel and perpendicular scattering for non-polarised  $\gamma$ -rays. This factor is a characteristic of the EXOGAM setup and is given by :

$$a(E_{\gamma}) = \frac{N_{||}(\text{unpolarised})}{N_{\perp}(\text{unpolarised})} \quad (6.11)$$

The  $^{60}\text{Co}$  and  $^{152}\text{Eu}$  sources are used to determine this factor. In several articles,  $a$  is considered to be energy dependant and is written  $a(E_{\gamma})$ . In our case, this factor seemed to exhibit a slightly decreasing trend (see Fig. 6.22). Nevertheless a linear fit led to values of the asymmetry at high energy which were very far from what was expected. The factor was therefore fitted by a constant  $a = 0.989(6)$ . The  $N_{||}(\text{unpolarised})$  and  $N_{\perp}(\text{unpolarised})$  counts have been obtained by fitting various  $\gamma$  from the  $^{152}\text{Eu}$  source. Measures of the asymmetry  $A$  for several transitions of  $^{95}\text{Rh}$  and  $^{94}\text{Ru}$  can be found in Tab. 6.4 along with values from the literature. The values of  $A$  are generally compatible, within the error bars. Whenever they are not numerically compatible, the values have at least the same sign.

### 6.5.2 $^{94}\text{Pd}$

This nucleus has already been observed through the same fusion-evaporation reaction (see [124]), through the  $\beta$ -decay of  $^{94}\text{Ag}$  (see [125]) and through the fragmentation of heavier nuclei (see [126] and reference

Nuclei	$\gamma$ -Gate (keV)	$\gamma$ (keV)	$A$ (this work)	$A$ (reference)	$\gamma$ -Mult
$^{95}\text{Rh}$	716	382	0.105(22)	0.01(2)	E2
		583	-0.044(17)	-0.09(1)	M1
		754	0.121(30)	0.12(2)	E2
		830	0.086(35)	0.09(2)	E2
		1250	0.124(56)	0.10(2)	E2
		1275	0.066(17)	0.14(1)	E2
		1351	0.050(11)	0.012(9)	E2
		1734	0.112(28)	0.11(1)	$\Delta I = 0$
	1005	169	0.33(17)	—	$\Delta I = 0$
		261	-0.095(93)	-0.18(8)	M1
		549	-0.065(28)	-0.11(2)	M1
		667	0.117(18)	0.12(1)	E2
		691	-0.089(53)	-0.13(2)	M1
		1147	0.098(35)	0.07(2)	E2
$^{94}\text{Ru}$	725	2790	0.068(34)	0.07(2)	E2
		394	-0.110(85)	-0.08(2)	M1
		543	-0.057(28)	-0.108(5)	M1
		1347	0.090(21)	0.092(3)	E2
		1898	-0.055(23)	-0.043(3)	M1

Table 6.4 – Asymmetries measured with the corresponding gates for  $^{95}\text{Rh}$  and  $^{94}\text{Ru}$ . The last two columns are the asymmetries measured and multiplicities attributed by Ghazi Moradi *et al.* in [122] ( $^{95}\text{Rh}$ ) and [123] ( $^{94}\text{Ru}$ ). In the  $\Delta I = 0$  of the 1734 peak, no multipolarity was assigned. It could be a mixture M1+E2. Idem, the  $\Delta I = 0$  could be a mixture of E1+M2.

therein). The level scheme of  $^{94}\text{Pd}$  is rather well known up to the isomeric state  $J^\pi = 14+$  at 4883 keV and decay experiments have measured the  $\gamma$ -decays up to the level 20+. The spin-parity of the nuclear states below the isomeric 14+ has been attributed by angular distribution and analysis of the conversion coefficient of the 96 keV  $14+ \rightarrow 12+$  transition in [124]. These results can be confirmed here. The  $2p2n$ -conditioned spectra are rather highly contaminated with the  $^{58}\text{Ni}(^{40}\text{Ar},2p2n)^{94}\text{Ru}$  reaction as stated in Sect. 6.4.1. Moreover the  $2p2n$  condition is very strict as only 0.8% of the detected  $\gamma$  corresponding to a true  $2p2n$  channel match this condition. In order to have a sufficient number of counts in our spectra, we use a  $1p/2p - 2n$  condition, multiplying the number of counts of the  $2p2n$  channel by 2.6 (estimated with the proton efficiency). This of course allows the presence of  $^{95}\text{Ag}$  ( $1p2n$  channel) in the spectrum, but it is easily cut out by gating on a known  $\gamma$ -transition of  $^{94}\text{Pd}$ .

Fig. 6.23-right shows the sum of 8  $\gamma$ -spectra of the  $^{94}\text{Pd}$  with  $1p2n$  and  $2p2n$  conditions, gated on 814, 906, 660 and 324 keV. Most of the transition seen by Marginean *et al.* [124] have been seen. In this reference, all transitions but one (818 keV) have been assigned as E2 transition following their angular distribution, the internal conversion coefficient of the 96 keV transition (see Fig. 6.23-left) and shell-model calculations. We first determine the  $R_{\text{DCO}}$  of the 818 keV transition by gating on the 814 keV transition. Because of the low statistics available in the 818-transition, its peaks are fitted by maximum likelihood instead of the standard  $\chi^2$



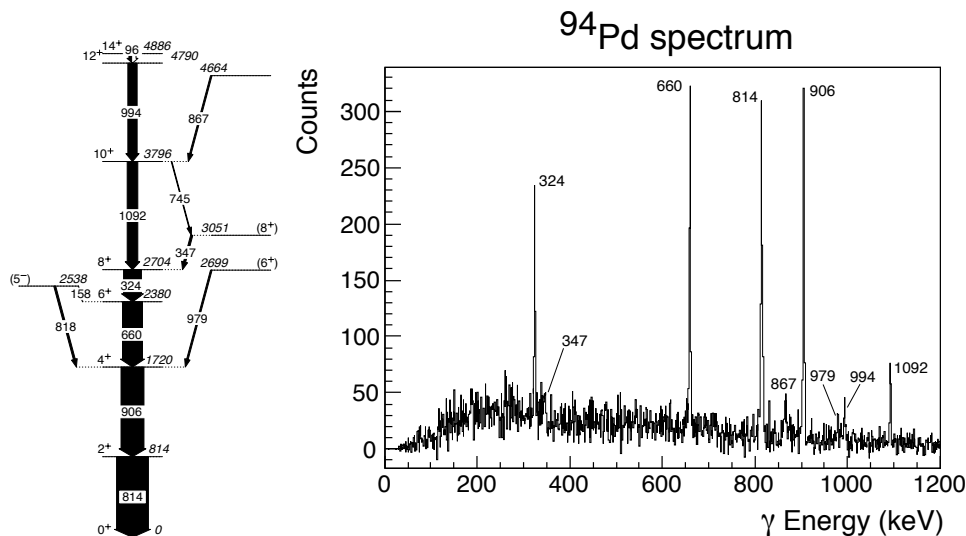


Figure 6.23 – Left: level scheme of  $^{94}\text{Pd}$  proposed in [124]. Right: energy spectrum of the  $^{94}\text{Pd}$  for several gates and particle-conditions (this work).

$\gamma$ (keV)	$R_{DCO}$	$A$	$\gamma$ -Mult/EM nature
324	1.14(13) <sup>a,b,c</sup>	–	Q
659	0.98(12) <sup>a,b</sup>	–	Q
814	1.19(19) <sup>c</sup>	0.08(18) <sup>c</sup>	E2
818	0.59(30) <sup>a</sup>	–	D
905	1.05(13) <sup>a</sup>	0.11(12) <sup>a,c</sup>	E2
1092	1.15(24) <sup>a,b,c</sup>	–	Q

Table 6.5 – Measurements of  $R_{DCO}$  and asymmetries in  $^{94}\text{Pd}$ . The letters  $a$ ,  $b$  and  $c$  label the different gates used.  $a$ : 818 keV;  $b$ : 906 keV;  $c$ : 660 keV.

method. We determine  $R_{DCO} = 0.59(30)$  which is characteristic of a stretched dipole transition gated by a stretched quadrupole transition, confirming the multipolarity of both the levels as found by Marginean *et al.* In order to ensure the nature of the 814 keV transition, we measure its asymmetry by gating on the 660 keV transition, as it is parallel to 818 keV transition which would perturb the measure. The positive asymmetry confirms the E2 nature of this  $\gamma$ -line.

We then measure the  $R_{DCO}$  of several transitions of the cascade. As the statistics are rather low, we sometimes need to gate on several quadrupole transitions at a time, but not before checking the multipolarity of the gate. For example, we gate on 814 keV to determine  $R_{DCO}(905)$ , then on 814 and 905 keV to determine  $R_{DCO}(659)$ , etc. Tab. 6.5 gives the different  $R_{DCO}$  and asymmetry measurements. We determine the nature of the first two transitions to be E2, though the estimated error for the 814 keV transition is also compatible with a negative value of the asymmetry. All  $R_{DCO}$  measurements are consistent with the spin-parity attributions from [124]. Though more populated, the 814 keV transition has a larger error on both  $R_{DCO}$  and  $A$  than the 905 keV one, as it was only gated on 660 keV.

## CONCLUSION

In the course of this chapter, we analysed nuclei close to the  $N = Z$  nucleus  $^{100}\text{Sn}$ . We calibrated the different detectors in amplitude and time and spent a great deal of effort on the time alignment of the signals from the different detectors. We estimated the efficiency of EXOGAM and the efficiencies of the different particle gates ( $p$ ,  $\alpha$ ,  $n$ ) that were applied during the analysis to increase the peak-to-background ratio. We measured the *DCO* ratios and asymmetries of several transitions of rather well known  $^{95}\text{Rh}$  and  $^{94}\text{Ru}$  nuclei as a confirmation of our method, before measuring the same experimental quantities for the transitions of  $^{94}\text{Pd}$ , confirming previous estimates of their multipolarity and, when possible, electromagnetic nature.



# THESIS CONCLUSION

The present work is part of the ongoing GANIL plan to build a next-generation nuclear physics research facility through the SPIRAL1 Upgrade and SPIRAL2 projects. The upgraded SPIRAL1 system will bring about the renewal of the current list of available radioactive beams by providing new ion sources capable of producing not only gaseous radioactive ions but also condensable ones. On the other hand, the phase 1 of SPIRAL2 features:

- stable beams of high intensity delivered by the LINAC
- new exotic or superheavy radioactive beams produced in S3 by fusion-evaporation or transfer reactions

This should open new physics cases for studying the evolution of shell-closures in the proton-rich or neutron-rich regions and the search for the island of stability of superheavy elements.

In the present report, we have detailed the optical study and off-line test of the MR-ToF-MS PILGRIM. The resolving powers optimised at rather low number of turns in the ion trap ( $\sim 250$ ) and measured on the test bench for longer trapping times are encouraging. The simulations in the S3 configuration, those in the test bench configuration and the results obtained in the actual experiment all indicated that the final resolving power and trapping efficiency of PILGRIM strongly depend on the transverse emittance characteristics of the input bunch. These include the value of the emittance but also the orientation and eventual distortion of the emittance profile. In addition, we have seen in chapter 3 that the size of the bunchwidth at ToF focus is due to both the geometric and kinetic aberrations generated during the trapping and to the initial bunchwidth due to the bunching method. We have compared the resolving powers achievable for RFQCBs with different incompressible times at ejection, highlighting the importance of creating short bunches.

In the off-line test bench at LPC we plan to increase the resolving power of PILGRIM by testing a new bunching method reducing the mean angle and energy dispersion of the input bunch, which should reduce the geometric and kinetic aberrations. We hope to take advantage of these enhanced performances to observe the first isobaric mass separation in PILGRIM on  $^{40}\text{K}/^{40}\text{Ca}$  doublet, despite their strongly unbalanced production rates. In the on-line S3 setup, the design of a dedicated RFQ Cooler Buncher will be required to achieve high resolving power and mass accuracy. A Bradbury-Nielsen gate is also yet to be designed for S3 and will be placed between an electrostatic deflector and PILGRIM or

possibly even integrated on this deflector.

We then detailed the study of the multi-direction electrostatic deflector, which was designed to induce low ToF spread after deflection if the injected beam is roughly parallel or if two of such deflectors are used in a U-configuration. In S3, the ToF dispersion induced by a deflector or a S-shaped arrangement of two deflectors does not matter much since the ToF separation in PILGRIM and the purification with a BNG will take place before any deflection. If PILGRIM comes to be installed in DESIR however, the U-arrangement will prove beneficial to its resolving power. In addition, the distance imposed between the two deflectors of DESIR will require to study a telescopic arrangement of Einzel lenses to decrease the geometric aberrations which would certainly reduce the resolving power of PILGRIM.

Though we obtained first encouraging results with PILGRIM using a rudimentary bunching setup at LPC Caen, several optical studies and technical developments thus remain to be done before PILGRIM is operational at S3-LEB for the commissioning of the S3 installation. PILGRIM will remain on the off line test bench of LPC until the end of the year. Then, it could be installed at the low-energy beam line LIRAT for the first on line tests of mass separation of radioactive ions using the new beams delivered by SPIRAL1 after its upgrade. In the first chapter, we saw that a FEBIAD ion source can ionise many different chemical elements. Owing to the non selectivity of the target ion-source system, one could test PILGRIM not only for mass separation, but also for mass measurement with one or several isobars as reference ions.

The data analysis of the E623 could also be completed with the spectroscopic analysis of other nuclei in the vicinity of  $^{94}\text{Pd}$ . Several experiments have already been carried out to study this region because of its high interest in nuclear structure. Though the DCO ratios of most  $\gamma$ -transitions of the nuclei in this region have already been calculated, leading to estimate their multipolarity, the polarisation asymmetry has not systematically been measured, as only a few  $\gamma$ -arrays around the world are capable of polarisation measurements. The polarisation asymmetry, carrying the information of the electromagnetic nature of the  $\gamma$ -transition could help to confirm or identify the spin-parity assignment of several levels of nuclei in this region. Since the calibration coefficients, particle gates and software methods have already been achieved in the present work, we could measure polarisation asymmetries for several nuclei, like  $^{95}\text{Ag}$ ,  $^{95}\text{Pd}$ ,  $^{93}\text{Rh}$  or  $^{94}\text{Rh}$ , in future.

# LIST OF FIGURES

1	Chart of nuclides showing the stable elements forming the valley of stability, the limits of the known nuclei, the estimated positions of the drip lines and path of the r-process and the magic numbers [1]. . . . .	2
2	Future layout of the SPIRAL2 facility. Phase 1: linear accelerator and NFS and S3 experimental rooms. Phase 1+: low energy experimental room DESIR receiving beams from S3 and SPIRAL1. Phase 1 + +: $A/Q = 7$ injector. Phase 2: production of radioactive ions at high intensity. The CIME cyclotron is used to post-accelerate radioactive ion beams from SPIRAL1 and will do so for the beams from SPIRAL2 as well.	3
1.1	SPIRAL1 upgrade layout. Image from [10] . . . . .	11
1.2	Principle of operation of the VD5 FEBIAD ion source. . . . .	13
1.3	Mechanical design of the FEBIAD source in SPIRAL1. . . . .	14
1.4	Identification station in SPIRAL, including a collection chamber (top) and a decay chamber (bottom). During the test of the FEBIAD source, only one of the 2 bottom HPGe was used. See description in text. . . . .	16
1.5	Fit of the $\gamma$ -efficiency at 85 mm (blue), 260 mm (green) and 590 mm (red). The error bars are not represented here since they are typically smaller than the dots. . . . .	17
1.6	<b>Top:</b> fitting a $\gamma$ -peak in time-gated energy spectrum. <b>Bottom:</b> fitting a saturation curve in an energy-gated time spectrum. The green and red areas are the peak and background gates, respectively. . . . .	18
1.7	$\gamma$ spectrum of run 47, for mass 33. . . . .	19
1.8	$\gamma$ spectrum of run 90, for mass 30. . . . .	20
1.9	Calculated 511 keV bias for several isotopes and several runs at a distance of 590 mm from the implantation point. . . . .	22
1.10	Colored elements of the periodic table (top) and isotopes of the nuclide chart (bottom) have been observed during the commissioning of the FEBIAD TISS. The colors of the chart only account for the half-life of the isotopes (from [22]). . . . .	23
1.11	Release efficiencies of aluminium as a function of the half-life of the isotope, fitted by the empirical equation Eq. 1.9 (in red). . . . .	26

2.1	Left: parabolae of neon and other elements printed on a photographic plate [26]. Right: mass spectrum sorting several elements and molecules. The abscissae are the values of the magnetic field used to deflect the ions, while the ordinates are the values of the deflection of the foils of an electroscope used to measure the current [27]. . . . .	30
2.2	Mathieu stability diagram. Mathieu's equations define regions in the $a_u$ vs $q_u$ plane in which the motion of the charged particle along the X or Y axes is stable. The intersections of X- and Y-stable regions are circled in green. Drawing from [38] . . . . .	36
2.3	Principle of operation of the reflectron. . . . .	39
2.4	Several types of low energy folded path ToF spectrometer. In trap ToF spectrometers (c,d), there is no real limit to the flight path, but the mass range that can be analysed in one cycle is limited by the opening time-window of the trap, and the trapping time itself. This problem is solved in open path spectrometers (e,f) at the expense of the maximum flight path. See [41] and reference therein for more details. . . . .	41
2.5	Schematic overview of a RFQCB and a pulsed drift tube for bunch preparation with the associated voltage pulsing. <b>a:</b> cooling of the ion in the buffer gas. <b>b:</b> ejection of the bunch. <b>c:</b> Increasing the energy in a pulsed drift tube. . . . .	43
2.6	<b>Top:</b> typical layout and operation of an MR-ToF-MS apparatus. <b>1:</b> end mirror. <b>2:</b> mirror electrodes. <b>3:</b> Einzel-lens (to keep the bunch focused in the trap). <b>4:</b> Pulsed drift-tube. <b>5:</b> Bradbury-Nielsen Gate. <b>6:</b> Micro-Channel Plate. <b>Bottom:</b> the two injection principles are represented by the two potential curves. The colors represent the potentials that are switched, both before and after the switch. The grey lines represent the total mechanical energy (kinetic + potential) of the ions, normalised by $q$ . <b>a:</b> trapping. <b>b:</b> separation. <b>c:</b> ejection. . . . .	44
2.7	Principle of operation of a Bradbury-Nielsen Gate. Shows the trajectories of the ions when the gate is off (dashed lines, green potential) or on (full lines, red potential). . . . .	45
2.8	Schematic example of the relative ToF dependency to the relative energy for one revolution. The first order $(\delta_t \delta_K)$ coefficient can be tuned by changing the energy of the ions inside the trap. Figure from [58]. . . . .	51
2.9	The MR-ToF-MS worldwide. See text for citations and details.	53
3.1	Several geometries simulated by B. Kansal. <b>a:</b> Greifswald-like lenses and mirrors. <b>b:</b> hollow mirrors. <b>c:</b> hollow mirrors and lenses. . . . .	60
3.2	Early mechanical design of the mirror. The bottom-right figure is a SIMION view. The red ellipses pinpoint the region of highest potential gradient. . . . .	62

- 3.3 3D models of the interface between the inner Einzel lens and the inner ground plate. The left (resp. right) figure shows the model without (resp. with) a small collar shield. . . . . 63
- 3.4 **Top:** mechanical design of the separator ensemble and its parts. **Middle:** SIMION version used for simulations. **Bottom:** mechanical design of PILGRIM showing the vacuum chambers and the turbo-pumps. The mirrors can be taken out and, if needed, exchanged without removing the drift tube from its chamber. . . . . 66
- 3.5 Comparative resolving powers as a function of the number of turns for 4 different beams (4 colours in the graphs and the table) and for 3 different incompressible times  $\Delta t_{inc}$  at the ejection from the RFQ.  $\epsilon_{90\%}$  is the 90% emittance. At mass 133, the ions make one revolution in  $\simeq 29.2 \mu s$ . . . . . 68
- 3.6 Emittance plots for the bunches 1, 2 and 3. X axis is the transverse position  $x$  in mm and Y the transverse angle  $a$  in mrad. We compare the shape of the emittance profile at the creation of the bunch (top, black) to the profile in the middle of the MR-ToF-MS, just before switching the in-trap lift (bottom, red). . . . . 69
- 3.7 Resolving powers as a function of the number of turns for an incompressible time of 50 ns (light blue), 20 ns (dark blue) and for no incompressible time (black). The dashed lines show  $R_{FWHM}$  for a ToF focus at 250 turns. The full lines show  $R_{FWHM}$  after changing the ToF focus by changing the potential of the drift tube. The red line show the 100k limit. . . . . 70
- 3.8 **Left:** shape of the  $\Delta t$  vs  $\Delta K$  dependency after one revolution in the MR-ToF-MS. The points **a** and **c** are isochronous configuration for which PILGRIM does not induce any dispersion or correction of the ToF correlated to the energy. The point **b** is an inflexion point for which the ToF depends quasi linearly on the energy with very little contribution of the higher orders. **Right:** ToF (in  $\mu s$ ) as a function of the energy inside the trap (in eV) for two different energy spreads. All 3 curves have been drawn by considering a bunch without transverse emittance ( $x = a = 0$ ) to simplify the interpretation. . . . . 71
- 4.1 Mechanical drawing of the source. (1) Ca/K pellet, (2) acceleration electrode, (3) extraction electrode, (4) Einzel lenses, (5) and (6) mobile slits, (7) X-Y deflectors, (8) blade deflector, (9) collimator, (10) first vacuum chamber of the PILGRIM ensemble. . . . . 76



4.2	Vacuum setup of the PILGRIM test. The drawing is part of the software interface for monitoring and control of the vacuum system. It shows the scroll pump (SP), the turbo-molecular pumps (TP), the valves, primary and secondary gauges as well as their respective readings. The pressure values read are the real measurements performed after $\sim 4$ weeks of pumping. This interface is also used to control the insertion of the diagnostics in the beam-line (see section 4.2.5).	77
4.3	Control and monitoring user interface for the high voltage power supplies and the pulse generation. . . . .	78
4.4	All non-pulsed power supplies of PILGRIM (left) and the source (right). . . . .	78
4.5	Chronogram of bunch manipulation and observation in PILGRIM. Shows the different pulses (in black), the adjustable cycle time ( $T_1$ ), gates (G) and delays (D) as well as the potentials of the blade deflector (HV BD) and the drift tube (HV DT). See text for the explanation of the pulses. . .	79
4.6	ToF measurement setup at LPC-Caen. The START and STOP signals of the acquisition are given by an observation gate and by the modified MCP signal. The FASTER system digitises these signals, then calculates and displays their time difference. We also used scalers to measure the number of ions hitting the MCP, in coincidence or not with the observation gate. . . . .	81
4.7	Estimation of the emittance using the transverse beam profiles spreads. . . . .	82
4.8	<b>Blue:</b> intensity on the FC as a function of the position of a blade from the X-slit (left) or the Y-slit (right). <b>Red:</b> first derivative of the intensity to deduce the beam profile. The calculated spread in transverse position is given for each graph. The error on the measurement of the FC-intensity is typically 0.2 pA. . . . .	83
4.9	Effect of the pulsing of the deflector blade on the ions in 3 different scenarii. The deflector blades, the collimator are schematically pictured and are not at scale. The deflection angles are exaggerated for understanding. In grey is the deflecting potential between the blades for several times. <b>a:</b> ions enter the deflector before the bottom blade has been switched to 0 V. <b>b:</b> ions enter the deflector after the blade has been switched to ground potential but do not exit the deflector before the blade is switched back to 150V. <b>c:</b> ions enter the deflector as the blade is switched off and exit while the blade is switched back on. The coloured dotted lines mark the position of the ions at the time of a switch. Details of the consequences in text. . . . .	84
4.10	ToF profile of $^{23}\text{Na}$ on the end-pipe MCP after a 1100 ns bunching gate with and without steering. The flight time from the blade deflector to the MCP is $\simeq 17.5 \mu\text{s}$ . . . . .	85
4.11	ToF profile measured with FASTER after a 16 ms flight and measurement of the corresponding sensitivity. . . . .	88

4.12	Relative potential as a function of the temperature of the ISEG crate for mirror electrodes M3 and M4. . . . .	89
4.13	Fractional part of $M$ as a function of $N$ for $m_2 = 39$ and 41. . . . .	91
4.14	ToF spectrum at mass 40 exhibiting low statistics and a background noise. . . . .	92
5.1	PILGRIM layout in S3 and beam distribution through 2 deflectors. . . . .	97
5.2	Expected PILGRIM layout in DESIR and beam distribution using the same 2 deflectors. . . . .	97
5.3	Three different concepts of deflector and their voltage supplies. Electrodes with the same colour have the same potential (see details in text). Only the first one is true quadrupolar deflector. The green beam is an ensemble of trajectories simulated with SIMION. The first design is 700 mm wide, while the others two are 500 mm wide. . . . .	98
5.4	Scheme of the third configuration showing the adjustable geometric parameters that have been optimised. . . . .	99
5.5	<b>Top:</b> 3D layout of the second and third configurations. $a$ and $b$ mark the shields of the cylindrical and rectangular electrodes, respectively. In the second configuration, all rectangular electrodes are hold together by the two octagonal shields. <b>Bottom:</b> sideview of one of the deflectors showing new geometric parameters to optimise. $c$ is the input/ouput aperture in the grounded electrode. $d$ is the aperture in the octagonal box for the second concept. . . . .	101
5.6	Ions after deflection. The red line is the reference beam axis, the green lines are the ions trajectories and the red dots represent a fixed ToF. <b>Left:</b> point like source on the beam axis, angular spread. The output ToF spread is $\sim 100$ ns/degree. <b>Right:</b> same point like source, but with energy spread. The transverse position spread is $\sim 0.1$ mm/eV at 3 keV. . . . .	103
5.7	Comparison of the ToF bunchwidth (FWHM) for several deflectors, either in the Single Deflector configuration (SD) or Double Deflector one (DD). The initial beam has a uniform distribution in transverse position and has either an angle dispersion (top left) or an energy dispersion (top right). The bottom right figure shows what the ToF bunchwidth would be if we managed to apply a first order energy dependent correction in PILGRIM up to the ToF-focus. See comments in text. . . . .	106

5.8	<p><b>Top left:</b> injection of a beam with realistic emittance in the deflector. The Einzel lens on the drawing is at ground potential. <b>Top right:</b> Same beam, using the Einzel lens to make the beam roughly parallel before the deflection. <b>Bottom:</b> transverse emittance profiles of the beam in the plane of deflection. The profiles a, b and c refer to the state of the beam before the E-lens, after it, and after deflection, respectively. The black (resp. red) profile corresponds to an activated (resp. deactivated) E-lens. X and Y axes are in mm and mrad, respectively. . . . .</p>	108
5.9	<p>SIMION simulations of the beam state after a double deflection in case the beam was previously focused (middle figure and black emittance profile) or not (left figure and red emittance profile). . . . .</p>	108
5.10	<p><b>Left:</b> output transverse position <math>x</math> and output angle <math>a</math> on the colour scale as a function of the input <math>x</math> and <math>a</math> after 1 or 2 deflections. <b>Right:</b> asymmetries of these output values. Details in text. . . . .</p>	110
5.11	<p><math>x</math> and <math>a</math> asymmetries for a 500 and a 1000 mm drift section between the deflectors. . . . .</p>	111
5.12	<p>Telescopic arrangement of electrodes with two different powerings. a: distance suppression. b: beam inversion. See details in text. . . . .</p>	112
5.13	<p>Mechanical design of the deflector. <b>a:</b> mobile entrance/exit window, detail. <b>b:</b> deflector ensemble. <b>c:</b> cylindrical electrode, detail. <b>d:</b> top view. <b>e:</b> bottom view. <b>f:</b> vacuum chamber. . . . .</p>	113
5.14	<p>Prototype deflector at CENBG. <b>a:</b> vacuum chamber. <b>b:</b> top octagonal plate and and cylinder PEEK supporting parts. <b>c:</b> inside of the chamber. . . . .</p>	114
6.1	<p>Experimental energy levels of <math>^{92}\text{Pd}</math>, <math>^{94}\text{Pd}</math> and <math>^{96}\text{Pd}</math>. One can witness the transition from a seniority-based level scheme to a regularly spaced one. A calculated level scheme considering a pure isovector pairing (<math>T = 1</math>) for <math>^{92}\text{Pd}</math> is also displayed and highlights the importance of the isoscalar contribution. Partially reproduced from [101]. . . . .</p>	119
6.2	<p><math>2^+</math> and <math>4^+</math> levels of the even-even isotopes of Xenon (<math>Z = 54</math>). The energy difference between these levels is noticeably higher near the <math>N = Z</math> line. This gives a clue of the disappearance of the seniority grouping on this line. Figure from [102]. . . . .</p>	120
6.3	<p>The detectors of E623: EXOGAM (a)(b)(e), DIAMANT (c)(d)(e), NWall (f)(g) and coupling of these detectors (h)(i). . . . .</p>	121
6.4	<p>Chronogram of a typical triggering/readout process in common dead-time mode (figure from [110]). . . . .</p>	125
6.5	<p>In <b>blue</b>, the uncalibrated <math>\gamma</math>-spectrum. The peaks with black triangles above them are those found by Root's automatic <i>Search()</i> routine. In the inset, an example of a fitted peak. In <b>red triangles</b>, the energies of the mean peaks VS the electronic channels, fitted by a first degree polynomial curve. . . . .</p>	127

- 6.6 Residues of the linear calibration for the 4 crystals of clover o. In **red**, the residues of the peaks used for calibration. In black, the pseudo-residues of the peaks not used in the calibration. These value are calculated both as a check of the peaks gaussian fits and of the calibration itself. The criterion for using a peak in the calibration was that it could be found by the *Search()* routine in each of the 44 crystals. The reduced  $\chi^2$  is plotted though it should be noticed that the error on the  $\chi^2$  itself is of the order of unity for only 7 fit-points [111] . . . . . 128
- 6.7 Full Width Half-Maximum of the 7 calibration peaks for all crystals. The **bold green line** represents the FWHM of the same peaks for the summed spectrum. The **bold red line** is a linear function of the energy and an arbitrary limit above which the peak FWHM needs investigation. Clover 12 has a complete loss of efficiency at low energy, making the fit of the 245 keV peak impossible. The corresponding FWHM were zeroed to highlight this fact on the graph. The insets simply give the distribution of FWHM for a given energy, for all crystals. . . . . 129
- 6.8 Distributions of the residues of the post-calibrations for the fit peaks 511, 716, 1431, 1898 and 2790 keV. Each distribution gathers the residues of the 44 crystals for 19 re-fits. The high number of statistics and the precision on the energy of the 511 keV peak imposed a important weight on this peak in the fits, hence the low residues. It can be noticed that most of the residues are beneath 100 eV, and only 3 residues throughout all the calibrations were above 300 eV. . . . . 130
- 6.9 EXOGAM efficiency fit with Gray (blue) and Radford (red) functions. Sum of all 11 Clovers efficiency fits with Gray (green) and Radford (yellow) functions. The two data points corresponding to the two  $^{60}\text{Co}$  peaks are fitted aside, but in the same fit procedure. The fit functions on both sides of the dashed line are the same, ignoring a multiplication factor. . . 132
- 6.10 Calibrated time spectrum of the TAC of the crystal ECC2-C for run 56. Black: all events. One can see the sharp self-trigger peak, the three bumps resulting of the crystal misalignment and a small peak on the left corresponding to the  $\text{BaF}_2$  trigger. Coloured spectra: same TAC with the condition FT generated by ECC0-C (dark blue), ECC0-A (red), ECC4-A (green), ECC2-D (pink) and  $\text{BaF}_2$  (light blue). HF repetitions can be observed for this last one. . . . . 133
- 6.11 Calibrated time spectrum of the TAC of the crystal ECC2-C when it has been triggered in coincidence with ECC0-C (group 1, dark blue), ECC0-A (group 2, red), ECC4-A (group 3, green) and ECC2-D (group 4, pink), for run 56. These graph differs from these, of the same color, of Fig. 6.10 by the presence of the self-trigger peak. . . . . 135

- 6.12 Calibration process of the TAC FT-HF. The histogram on the Y-axis is the uncalibrated TAC FT-HF spectrum. On the X-axis, the calibrated **folded** TAC ECC2-C spectrum. Colours are the same as before. Apart from the folding the spectra on the X-axis are the same as in previous figures. . . . . 136
- 6.13 Illustrations of the time alignment. **Up left:** alignment of the different FT in the TAC of a given crystal (here 2C), run 34. The black and red spectra are CFD-X-FT (unaligned) and CFD-X-HF (HF-aligned), respectively. The small peak in  $-50$  ns and the step in  $+90$  ns are due to the shape of the TAC-FT-HF spectrum. **Up right:** alignment of the different crystals with the calculated misalignments, run 34. **Down left:** evolution of the HF-drift during the experiment. The inset is an example of peak fitted in the TAC-FT-HF spectrum to measure the drift (run 36). **Down right:** sum of the TAC-CFD\_Exo-HF for several runs (runs 30-60) before and after HF-drift correction. . . . . 137
- 6.14 Cross-sections of fusion-evaporation reactions for the main fusion reaction, for the beam contaminant  $^{40}\text{Ar}$  and for the target substrate  $^{12}\text{C}$ . Weaker reaction channels (like the  $^{94}\text{Pd}$ ) are not printed. . . . . 138
- 6.15 Figure: EXOGAM spectrum, run 71, for case **I**, **II** and **III** (matching colors). Table: peak-to-background ratios of 381keV (3p) and 1898keV (4p) with different scattering-rejection methods. This ratio is calculated as the number of counts in a peak divided by the number of background counts per keV at the position of the peak. . . . . 139
- 6.16 Image: ToF v.s. ZCO matrix of cell 0, run 71. The lower left region of the matrix is populated by neutrons. The lines defined by  $\text{ToF} \simeq 0$  and  $\text{ZCO} \simeq 2000$  are due to  $\gamma$ -rays which manage to pass the hard-neutron gate. Table: comparison of different neutron gates (not exhaustive) in efficiency and  $\epsilon_n$ , contamination  $C_{0n|det \geq 1n}$  and efficiency/contamination ratio  $R_{1n}$ . See details in text. . . . . 140
- 6.17 **Left:** difference between a true "2n" event and a single scattered neutron. **Right:** different ways of measuring the distances between the different cells of NWall. . . . . 141
- 6.18 Images:  $\Delta\text{Position}$  v.s.  $\Delta\text{ToF}$  matrixes (one count for each pair of triggered cells). Table: comparison of different gating conditions. "Distance" indicates if the distance between cells is considered to be the distance between their center or their circumcircle. "Speed" refers to the estimated speed of the scattered neutrons (in  $\text{m} \cdot \mu\text{s}^{-1}$ ). The gated matrix correspond to the red set of parameters. . . . . 142
- 6.19 Energy-PID matrix of the first CsI of DIAMANT. The events in the top-left corner of the proton distribution are  $\gamma$ -rays. The axes have are in channels, since the Energy and PID signals of DIAMANT have not been calibrated. . . . . 143

- 6.20 **Picture:** evolution of  $R_{eff}$  with the  $\gamma$ -energy. The correction of the  $R_{DCO}$  is necessary of energies below 300 keV. **Table:** important transitions of the rather well known  $^{95}\text{Rh}$  and their measured  $R_{DCO}$  using two E2 transition for  $\gamma$ -gating. The last column shows the known transition multipolarities of  $^{95}\text{Rh}$ , which are consistent with the  $R_{DCO}$  values. It has been noted that the values of  $R_{DCO}$  for 717 and 1351 keV are lower when gating on 2790 keV. We attribute this difference to the 19 ns isomeric state at 2236 keV between the 2790 keV transition and the two others, during which the nucleus alignment is partially or completely lost. . . . . 146
- 6.21 Calculated and measured DCO ratios and polarisation for several transition types. A pure stretched E2 transition is well defined in this frame, while mixed transitions may vary in both observables according to their mixing ratio. Taken from [121]. . . . . 147
- 6.22 Normalisation factor  $a$  as a function of the energy. . . . . 148
- 6.23 Left: level scheme of  $^{94}\text{Pd}$  proposed in [124]. Right: energy spectrum of the  $^{94}\text{Pd}$  for several gates and particle-conditions (this work). . . . . 150



# BIBLIOGRAPHY

- [1] The EURISOL report. Rapport technique, GANIL, 2003. (cited in pages 2 and 155.)
- [2] P. Jardin, O. Bajeat, C. Couratin, P. Delahaye, M. Dubois, C. Feierstein, F. Pellemoine, P. Lecomte, P. Lehérissier, L. Maunoury, M. G. Saint-Laurent et E. Traykov. Status of the SPIRAL I upgrade at GANIL. *Review of Scientific Instruments* 83(2): 02A911, 2012. (cited in pages 2 and 12.)
- [3] What is SPIRAL2 ? URL <http://pro.ganil-spiral2.eu/spiral2/what-is-spiral2>. (cited in page 2.)
- [4] The Scientific Objectives of the SPIRAL 2 Project. Scientific report, GANIL, June 2006. (cited in page 2.)
- [5] LINAG Phase 1. Technical report, GANIL, June 2002. (cited in page 2.)
- [6] S3 : The Super Separator Spectrometer for LINAG Beams. Technical proposal, GANIL, 2008. (cited in page 2.)
- [7] DESIR: the SPIRAL2 low-energy beam facility. Technical proposal, GANIL, December 2008. (cited in page 3.)
- [8] F. Wienholtz, D. Beck, K. Blaum, C. Borgmann, M. Breitenfeldt, R. Cakirli, S. George, F. Herfurth, J. Holt, M. Kowalska, S. Kreim, D. Lunney, V. Manea, J. MeneÁndez, D. Neidherr, M. Rosenbusch, L. Schweikhard, A. Schwenk, J. Simonis, J. Stanja, R. Wolf et K. Zuber. Masses of exotic calcium isotopes pin down nuclear forces. *Nature* 498(7454): 346 – 349, 2013. (cited in pages 4 and 53.)
- [9] Y. Ito, P. Schury, M. Wada, S. Naimi, T. Sonoda, H. Mita, F. Arai, A. Takamine, K. Okada, A. Ozawa et H. Wollnik. Single-reference high-precision mass measurement with a multi-reflection time-of-flight mass spectrograph. *Physical Review C* 88: 011306, 2013. (cited in pages 4 and 53.)
- [10] P. Jardin, O. Bajeat, P. Delahaye, M. Dubois, R. Frigot, V. Kuchi, C. Leboucher et L. Maunoury. New target ion source systems at GANIL/SPIRAL1: Prospective. *Nuclear Instruments and Methods in Physics Research B* 376: 64 – 67, 2016. (cited in pages 11 and 155.)
- [11] N. Lecesne. On-line {ECR} ion sources: Present and future. *Nuclear Instruments and Methods in Physics Research B* 266(19–20): 4338 – 4345, 2008. (cited in page 12.)



- [12] M. Dubois, P. Delahaye, P. Jardin, L. Maunoury, O. Bajeat, R. Frigot, C. Leboucher et B. Rannou. SPIRAL 1 Upgrade at GANIL: status. Congress communication at EMIS XVII - International Conference on Electromagnetic Isotope Separators and Related Topics. (cited in page 12.)
- [13] L. Penescu, R. Catherall, J. Lettry et T. Stora. Development of high efficiency Versatile Arc Discharge Ion Source at CERN ISOLDE. *Review of Scientific Instruments* 81(2): 02A906, 2010. (cited in pages 12 and 23.)
- [14] C. Couratin. *Mesures de précision avec LPC-Trap et développements techniques à GANIL : corrélation angulaire beta neutrino ( $a_{\beta\nu}$ ) et probabilité de shakeoff dans la décroissance de  $l^6\text{He}^+$ , étude de la production de nouveaux faisceaux à SPIRAL*. Thèse de doctorat, Université de Caen Basse-Normandie, 2013. (cited in pages 12 and 22.)
- [15] O. Bajeat *et al.* Development of target ion source systems for radioactive beams at GANIL. *Nuclear Instruments and Methods in Physics Research B* 317: 411–416, 2013. (cited in pages 12 and 13.)
- [16] P. Delahaye, C. Couratin, E. Liénard, O. Bajeat, G. Ban, D. Durand, X. Fléchar, O. Naviliat-Cuncic, M. G. Saint Laurent, T. Stora, J. C. Thomas et E. Traykov. Production and Separation of  $T = 1/2$  Nuclides for  $\beta - \nu$  angular correlation measurements. *AIP Conference Proceedings* 1409(1): 165 – 170, 2011. (cited in pages 13 and 22.)
- [17] G. F. Grinyer *et al.* Upgrade of the SPIRAL identification station for high-precision measurements of nuclear  $\beta$  decay. *Nuclear Instruments and Methods in Physics Research A* 741: 18–25, 2014. (cited in page 15.)
- [18] P. Chauveau, P. Delahaye, M. Babo, H. Bouzomita, O. Bajeat, M. Dubois, R. Frigot, G. Grinyer, J. Grinyer, P. Jardin, C. Leboucher, L. Maunoury, C. Seiffert, T. Stora, J. Thomas et E. Traykov. A new FEBIAD-type ion source for the upgrade of SPIRAL<sub>1</sub> at GANIL. *Nuclear Instruments and Methods in Physics Research B* 376: 35 – 38, 2016. (cited in page 15.)
- [19] J. Grinyer, G. F. Grinyer, M. Babo, H. Bouzomita, P. Chauveau, P. Delahaye, M. Dubois, R. Frigot, P. Jardin, C. Leboucher, L. Maunoury, C. Seiffert, J. C. Thomas et E. Traykov. High-precision half-life measurement for the isospin  $T=1/2$  mirror  $\beta^+$  decay of  $^{21}\text{Na}$ . *Physical Review C* 91(3): 032501, 2015. (cited in pages 15 and 22.)
- [20] J. Grinyer, G. Grinyer, M. Babo, H. Bouzomita, P. Chauveau, P. Delahaye, M. Dubois, R. Frigot, P. Jardin, C. Leboucher, L. Maunoury, C. Seiffert, J. Thomas et E. Traykov. High-precision half-life measurements of the  $T=1/2$  mirror  $\beta$  decays  $^{17}\text{F}$  and  $^{33}\text{Cl}$ . *Physical Review C* 92(4): 045503, 2015. (cited in pages 15 and 22.)
- [21] P. Gray et A. Ahmad. Linear classes of Ge(Li) detector efficiency functions. *Nuclear Instruments and Methods in Physics Research A* A237(3): 577 – 589, 1985. (cited in pages 16 and 130.)

- [22] Nuclide chart from the National Nuclear Data Center, Brookhaven National Laboratory, 2016. URL <http://www.nndc.bnl.gov/chart/>. (cited in pages 23 and 155.)
- [23] S. Lukic, F. Gevaert, A. Kelic, M. Ricciardi, K.-H. Schmidt et O. Jordanov. Systematic comparison of ISOLDE-SC yields with calculated in-target production rates. *Nuclear Instruments and Methods in Physics Research A* 565(2): 784 – 800, 2006. (cited in page 25.)
- [24] S. Maher, F. P. M. Jjunju et S. Taylor. *Colloquium* : 100 years of mass spectrometry: Perspectives and future trends. *Review of Modern Physics* 87(1): 113–135, 2015. (cited in page 29.)
- [25] 2015. URL [http://www.nature.com/milestones/milemasspec/full/nmeth1015-3.html](http://www.nature.com/milestones/milemassspec/full/nmeth1015-3.html). (cited in page 29.)
- [26] J. J. Thomson. Bakerian Lecture: Rays of Positive Electricity. *Proceedings of the Royal Society of London A: Mathematical, Physical and Engineering Sciences* 89(607): 1–20, 1913. ISSN 0950-1207. doi:10.1098/rspa.1913.0057. URL <http://rspa.royalsocietypublishing.org/content/89/607/1>. (cited in pages 30 and 156.)
- [27] J. J. Thomson. *Rays of positive electricity and their application to chemical analyses*. Longmans, Green London ; New York, 1913. (cited in pages 30 and 156.)
- [28] W. Bartky et A. J. Dempster. Paths of Charged Particles in Electric and Magnetic Fields. *Physical Review* 33(6): 1019–1022, 1929. (cited in pages 31 and 34.)
- [29] W. Stephens. A pulsed mass spectrometer with time dispersion. *Physical Review* 69(674), 1946. (cited in page 31.)
- [30] B. Mamyrin, V. Karataev, D. Shmikk et V. Zagulin. The mass-reflectron, a new nonmagnetic time-of-flight mass spectrometer with high resolution. *Soviet Journal of Experimental and Theoretical Physics* 37(1): 45–48, 1973. (cited in pages 31 and 39.)
- [31] M. Comisarow et A. Marshall. Fourier transform ion cyclotron resonance spectroscopy. *Chemical Physics Letters* 25(2): 282–283, 1974. (cited in page 32.)
- [32] A. Makarov. Electrostatic Axially Harmonic Orbital Trapping: A High-Performance Technique of Mass Analysis. *Analytical Chemistry* 72(6): 1156–1162, 2000. (cited in page 32.)
- [33] J. J. Thomson. *Recollections and Reflections*. Cambridge: Cambridge University Press, 1937. (cited in page 32.)
- [34] R. Anne, D. Bazin, A. Mueller, J. Jacmart et M. Langevin. The achromatic spectrometer LISE at GANIL. *Nuclear Instruments and Methods in Physics Research A* 257(2): 215–232, 1987. (cited in page 34.)

- [35] H. Geissel, P. Armbruster, K. Behr, A. Brunle, K. Burkard, M. Chen, H. Folger, B. Franczak, H. Keller, O. Klepper, B. Langenbeck, F. Nickel, E. Pfeng, M. Pfutzner, E. Roeckl, K. Rykaczewski, I. Schall, D. Schardt, C. Scheidenberger, K.-H. Schmidt, A. Schroter, T. Schwab, K. Summerer, M. Weber, G. Munzenberg, T. Brohm, H.-G. Clerc, M. Fauerbach, J.-J. Gaimard, A. Crewe, E. Hanelt, B. Knodler, M. Steiner, B. Voss, J. Weckermann, C. Ziegler, A. Magel, H. Wollnik, J. Dufour, Y. Fujita, D. Vieira et B. Sherrill. The GSI projectile fragment separator (FRS) a versatile magnetic system for relativistic heavy ions. *Nuclear Instruments and Methods in Physics Research B* 70(1): 286–297, 1992. (cited in page 34.)
- [36] I. Wiedenhover, M. Steiner, D. Morrissey, B. Sherrill, D. Bazin, J. Stetson, A. Stolz, O. Tarasov et J. Yurkon. Commissioning of the new A1900 high resolution high acceptance fragment separator at the Coupled Cyclotron Facility. *AIP Conference Proceedings* (610): 937–941, 2002. (cited in page 34.)
- [37] T. Kubo, M. Ishihara, N. Inabe, H. Kumagai, I. Tanihata, K. Yoshida, T. Nakamura, H. Okuno, S. Shimoura et K. Asahi. The RIKEN radioactive beam facility. *Nuclear Instruments and Methods in Physics Research B* 70(1): 309–319, 1992. (cited in page 34.)
- [38] Theory of quadrupole instrumentation. URL [http://www.chromacademy.com/Mass\\_Analyzers\\_Traps\\_and\\_TOFs\\_The\\_Essential\\_Guide.html](http://www.chromacademy.com/Mass_Analyzers_Traps_and_TOFs_The_Essential_Guide.html). (cited in pages 36 and 156.)
- [39] X. Fléchar, P. Velten, E. Liénard, A. Méry, D. Rodríguez, G. Ban, D. Durand, F. Mauger, O. Naviliat-Cuncic et J. C. Thomas. Measurement of the  $\beta - \nu$  correlation coefficient  $a_{\beta\nu}$  in the  $\beta$ -decay of trapped  $6\text{ He}^+$  ions. *Journal of Physics G: Nuclear and Particle Physics* 38(5): 055101, 2011. URL <http://stacks.iop.org/0954-3899/38/i=5/a=055101>. (cited in page 36.)
- [40] G. Savard, S. Becker, G. Bollen, H.-J. Kluge, R. Moore, T. Otto, L. Schweikhard, H. Stolzenberg et U. Wiess. A new cooling technique for heavy ions in a Penning trap. *Physics Letters A* 158(5): 247–252, 1991. (cited in page 37.)
- [41] W. R. Plaß, T. Dickel et C. Scheidenberger. Multiple-reflection time-of-flight mass spectrometry. *International Journal of Mass Spectrometry* 349-350(100 years of Mass Spectrometry): 134 – 144, 2013. (cited in pages 40, 41, and 156.)
- [42] H. Savajols. The SPEG Mass Measurement Program at GANIL. *Hyperfine Interactions* 132(1): 243–252, 2001. ISSN 1572-9540. doi: 10.1023/A:1011964401634. URL <http://dx.doi.org/10.1023/A:1011964401634>. (cited in pages 40 and 51.)
- [43] B. Franzke. The heavy ion storage and cooler ring project ESR at GSI. *Nuclear Instruments and Methods in Physics Research Section B: Beam Interactions with Materials and Atoms* 24: 18 – 25, 1987. ISSN 0168-583X. doi:<http://dx.doi.org/10.1016/>

- 0168-583X(87)90583-0. URL <http://www.sciencedirect.com/science/article/pii/0168583X87905830>. (cited in page 40.)
- [44] H. Wollnik et M. Przewloka. Time-of-flight mass spectrometers with multiply reflected ion trajectories. *International Journal of Mass Spectrometry* 96(3): 267 – 274, 1990. (cited in pages 40, 45, and 47.)
- [45] R. Wolf, D. Beck, K. Blaum, C. Böhm, C. Borgmann, M. Breitenfeldt, F. Herfurth, A. Herlert, M. Kowalska, S. Kreim, D. Lunney, S. Naimi, D. Neidherr, M. Rosenbusch, L. Schweikhard, J. Stanja, F. Wienholtz et K. Zuber. On-line separation of short-lived nuclei by a multi-reflection time-of-flight device. *Nuclear Instruments and Methods in Physics Research A* 686: 82 – 90, 2012. (cited in pages 42, 45, and 57.)
- [46] A. Piechaczek, V. Shchepunov, H. Carter, J. Batchelder, E. Zganjar, S. Liddick, H. Wollnik, Y. Hu et B. Griffith. Development of a high resolution isobar separator for study of exotic decays. *Nuclear Instruments and Methods in Physics Research B* 266(Proceedings of the XVth International Conference on Electromagnetic Isotope Separators and Techniques Related to their Applications): 4510 – 4514, 2008. (cited in pages 42, 43, 45, and 53.)
- [47] P. Schury, M. Wada, Y. Ito, S. Naimi, T. Sonoda, H. Mita, A. Takamine, K. Okada, H. Wollnik, S. Chon, H. Haba, D. Kaji, H. Koura, H. Miyatake, K. Morimoto, K. Morita et A. Ozawa. A multi-reflection time-of-flight mass spectrograph for short-lived and super-heavy nuclei. *Nuclear Instruments and Methods in Physics Research B* 317(Part B): 537 – 543, 2013. (cited in pages 42, 43, and 75.)
- [48] T. Dickel, W. Plaß, J. Lang, J. Ebert, H. Geissel, E. Haettner, C. Jesch, W. Lippert, M. Petrick, C. Scheidenberger et M. Yavor. Multiple-reflection time-of-flight mass spectrometry for in situ applications. *Nuclear Instruments and Methods in Physics Research B* 317(Part B): 779 – 784, 2013. (cited in page 42.)
- [49] P. Schury, M. Wada, Y. Ito, F. Arai, S. Naimi, T. Sonoda, H. Wollnik, V. Shchepunov, C. Smorra et C. Yuan. A high-resolution multi-reflection time-of-flight mass spectrograph for precision mass measurements at RIKEN/SLOWRI. *Nuclear Instruments and Methods in Physics Research B* 335: 39 – 53, 2014. (cited in pages 42, 47, 52, 67, 75, and 92.)
- [50] H. Wollnik. History of mass measurements in time-of-flight mass analyzers. *International Journal of Mass Spectrometry* 349-350(100 years of Mass Spectrometry): 38 – 46, 2013. (cited in page 42.)
- [51] F. Herfurth, J. Dilling, A. Kellerbauer, G. Bollen, S. Henry, H.-J. Kluge, E. Lamour, D. Lunney, R. Moore, C. Scheidenberger, S. Schwarz, G. Sikler et J. Szerypo. A linear radiofrequency ion trap for accumulation, bunching, and emittance improvement of radioactive ion beams. *Nuclear Instruments and Methods in Physics Research Section A: Accelerators, Spectrometers, Detectors and Associated Equipment* 469(2): 254 – 275, 2001.

- ISSN 0168-9002. doi:[http://dx.doi.org/10.1016/S0168-9002\(01\)00168-1](http://dx.doi.org/10.1016/S0168-9002(01)00168-1). URL <http://www.sciencedirect.com/science/article/pii/S0168900201001681>. (cited in page 42.)
- [52] T. Dickel, W. Plaß, A. Becker, U. Czok, H. Geissel, E. Haettner, C. Jesch, W. Kinsel, M. Petrick, C. Scheidenberger, A. Simon et M. Yavor. A high-performance multiple-reflection time-of-flight mass spectrometer and isobar separator for the research with exotic nuclei. *Nuclear Instruments and Methods in Physics Research A* 777: 172 – 188, 2015. (cited in pages 42, 43, 52, and 53.)
- [53] E. Traykov, M. Beck, M. Breitenfeldt, P. Delahaye, V. De Leebeek, P. Friedag, A. Herlert, N. Geeraert, W. Heirman, P.-I. Lønne, J. Mader, S. Rocca, G. Soti, M. Tandecki, M. Timmermans, J. Thiboud, S. Van Gorp, F. Wauters, C. Weinheimer, D. Zákoucký et N. Severijns. A compact radio frequency quadrupole for ion bunching in the WITCH experiment. *Nuclear Instruments and Methods in Physics Research A* 648: 1–14, 2011. (cited in page 42.)
- [54] W. Plaß, T. Dickel, S. Ayet San Andres, J. Ebert, F. Greiner, C. Horning, C. Jesch, J. Lang, W. Lippert, T. Majoros, D. Short, H. Geissel, E. Haettner, M. Reiter, A.-K. Rink, C. Scheidenberger et M. Yavor. High-performance multiple-reflection time-of-flight mass spectrometers for research with exotic nuclei and for analytical mass spectrometry. *Physica Scripta T* 2015(T166): 014069, 2015. (cited in pages 42 and 67.)
- [55] W. C. Wiley et I. H. McLaren. Time-of-Flight Mass Spectrometer with Improved Resolution. *Review of Scientific Instruments* 26(12): 1150–1157, 1955. (cited in page 43.)
- [56] J. Yoon, Y.-H. Park, S. Park, G. Kim et Y. Kim. Design of the multi-reflection time-of-flight mass spectrometer for the RAON facility. *EPJ Web conference* 66: 11042, 2014. (cited in pages 43 and 52.)
- [57] H. Wollnik et A. Casares. An energy-isochronous multi-pass time-of-flight mass spectrometer consisting of two coaxial electrostatic mirrors. *International Journal of Mass Spectrometry* 227(2): 217 – 222, 2003. (cited in pages 43 and 45.)
- [58] R. Wolf, G. Marx, M. Rosenbusch et L. Schweikhard. Static-mirror ion capture and time focusing for electrostatic ion-beam traps and multi-reflection time-of-flight mass analyzers by use of an in-trap potential lift. *International Journal of Mass Spectrometry* 313: 8 – 14, 2012. (cited in pages 44, 50, 51, 67, 70, 90, and 156.)
- [59] N. E. Bradbury et R. A. Nielsen. Absolute Values of the Electron Mobility in Hydrogen. *Physical Review* 49(5): 0388–0393, January 1936. (cited in page 45.)
- [60] W. Plaß, T. Dickel, U. Czok, H. Geissel, M. Petrick, K. Reinheimer, C. Scheidenberger et M. Yavor. Isobar separation by time-of-flight mass spectrometry for low-energy radioactive ion beam facilities.

- Nuclear Instruments and Methods in Physics Research B* 266(19): 4560 – 4564, 2008. (cited in page 45.)
- [61] C. Jesch, T. Dickel, W. R. Plaß, D. Short, S. Ayet San Andres, J. Dilling, H. Geissel, F. Greiner, J. Lang, K. Leach, W. Lippert, C. Scheidenberger et M. Yavor. The MR-TOF-MS isobar separator for the TITAN facility at TRIUMF. *Hyperfine Interaction - Proceedings of TCP2014* pages 1 – 10, 2015. (cited in pages 45 and 52.)
- [62] T. Y. Hirsh, N. Paul, M. Burkey, A. Aprahamian, F. Buchinger, S. Caldwell, J. A. Clark, A. F. Levand, L. L. Ying, S. T. Marley, G. E. Morgan, A. Nystrom, R. Orford, A. P. Galván, J. Rohrer, G. Savard, K. S. Sharma et K. Siegl. First operation and mass separation with the CARIBU MR-TOF. *Nuclear Instruments and Methods in Physics Research B* 2015. (cited in pages 45, 50, and 52.)
- [63] A. Casares, A. Kholomeev et H. Wollnik. Multipass time-of-flight mass spectrometers with high resolving powers. *International Journal of Mass Spectrometry* 206(3): 267 – 273, 2001. (cited in page 45.)
- [64] A. N. Verentchikov, M. I. Yavor, Y. I. Hasin et M. A. Gavrik. Multireflection planar Time-of-Flight Mass Analyzer. II: The High-Resolution Mode. *Technical Physics* 50(1): 82 – 86, 2005. (cited in page 45.)
- [65] M. I. Yavor, W. R. Plaß, T. Dickel, H. Geissel et C. Scheidenberger. Ion-optical design of a high-performance multiple-reflection time-of-flight mass spectrometer and isobar separator. *International Journal of Mass Spectrometry* 381-382: 1 – 9, 2015. (cited in pages 45, 47, 48, and 50.)
- [66] M. Yavor, A. Verentchikov, J. Hasin, B. Kozlov, M. Gavrik et A. Trufanov. Proceedings of the Seventh International Conference on Charged Particle Optics (CPO-7) Planar multi-reflecting time-of-flight mass analyzer with a jig-saw ion path. *Physics Procedia* 1(1): 391 – 400, 2008. ISSN 1875-3892. doi:<http://dx.doi.org/10.1016/j.phpro.2008.07.120>. URL <http://www.sciencedirect.com/science/article/pii/S1875389208001302>. (cited in page 45.)
- [67] B. Schultz, J. Kelly, C. Nicoloff, J. Long, S. Ryan et M. Brodeur. Construction and simulation of a multi-reflection time-of-flight mass spectrometer at the University of Notre Dame. *Nuclear Instruments and Methods in Physics Research Section B: Beam Interactions with Materials and Atoms* 376: 251 – 255, 2016. ISSN 0168-583X. doi:<http://dx.doi.org/10.1016/j.nimb.2016.02.043>. URL <http://www.sciencedirect.com/science/article/pii/S0168583X16001737>. Proceedings of the {XVIIth} International Conference on Electromagnetic Isotope Separators and Related Topics (EMIS2015), Grand Rapids, MI, U.S.A., 11-15 May 2015. (cited in pages 47, 52, and 75.)
- [68] R. Wolf, F. Wienholtz, D. Atanasov, D. Beck, K. Blaum, C. Borgmann, F. Herfurth, M. Kowalska, S. Kreim, Y. Litvinov, D. Lunney,

- V. Manea, D. Neidherr, M. Rosenbusch, L. Schweikhard, J. Stanja et K. Zuber. ISOLTRAP's multi-reflection time-of-flight mass separator/spectrometer. *International Journal of Mass Spectrometry* 349-350: 123 – 133, 2013. (cited in pages 50 and 52.)
- [69] L. Chen, W. Plaß, H. Geissel, R. Knöbel, C. Kozhuharov, Y. Litvinov, Z. Patyk, C. Scheidenberger, K. Siegień-Iwaniuk, B. Sun, H. Weick, K. Beckert, P. Beller, F. Bosch, D. Boutin, L. Caceres, J. Carroll, D. Cullen, I. Cullen, B. Franzke, J. Gerl, M. Górská, G. Jones, A. Kishada, J. Kurcewicz, S. Litvinov, Z. Liu, S. Mandal, F. Montes, G. Münzenberg, F. Nolden, T. Ohtsubo, Z. Podolyák, R. Propri, S. Rigby, N. Saito, T. Saito, M. Shindo, M. Steck, P. Walker, S. Williams, M. Winkler, H.-J. Wollersheim et T. Yamaguchi. New results on mass measurements of stored neutron-rich nuclides in the element range from Pt to U with the FRS-ESR facility at 360–400 MeV/u. *Nuclear Physics A* 882: 71 – 89, 2012. ISSN 0375-9474. doi:<http://dx.doi.org/10.1016/j.nuclphysa.2012.03.002>. URL <http://www.sciencedirect.com/science/article/pii/S0375947412001005>. (cited in page 51.)
- [70] P. Schury, K. Okada, S. Shchepunov, T. Sonoda, A. Takamine, M. Wada, H. Wollnik et Y. Yamazaki. Multi-reflection time-of-flight mass spectrograph for short-lived radioactive ions. *European Physical Journal A* 42(3): 343 – 349, 2009. (cited in page 52.)
- [71] V. Kolhinen, M. Bussmann, D. Habs, J. Neumayr, U. Schramm, C. Schürmann, M. Sewtz, J. Szerypo et P. Thiof. MLLTRAP: A Penning trap facility for high-accuracy mass measurements. *Nuclear Instruments and Methods in Physics Research Section B: Beam Interactions with Materials and Atoms* 266(19–20): 4547 – 4550, 2008. ISSN 0168-583X. doi:<http://dx.doi.org/10.1016/j.nimb.2008.05.100>. URL <http://www.sciencedirect.com/science/article/pii/S0168583X08007738>. Proceedings of the {XVth} International Conference on Electromagnetic Isotope Separators and Techniques Related to their Applications. (cited in page 52.)
- [72] R. Wolf, M. Eritt, G. Marx et L. Schweikhard. A multi-reflection time-of-flight mass separator for isobaric purification of radioactive ion beams. *Hyperfine Interactions* 199(1): 115 – 122, 2011. (cited in pages 52, 57, and 59.)
- [73] C. Nicoloff et M. Brodeur. Simulating a Multi-Reflection Time-of-Flight Mass Spectrograph for the Purification of Radioactive Isobars, 2014. APS Division Nuclear Physics Hawaii Meeting Poster. (cited in page 52.)
- [74] R. Wolf, D. Atanasov, K. Blaum, S. Kreim, D. Lunney, V. Manea, M. Rosenbusch, L. Schweikhard, A. Welker, F. Wienholtz et K. Zuber. Background-free beta-decay half-life measurements by in-trap decay and high-resolution MR-ToF mass analysis. *Nuclear Instruments and Methods in Physics Research Section B: Beam Interactions with Materials and Atoms* 376: 275 – 280,

2016. ISSN 0168-583X. doi:<http://dx.doi.org/10.1016/j.nimb.2016.01.045>. URL <http://www.sciencedirect.com/science/article/pii/S0168583X16001063>. Proceedings of the {XVIIth} International Conference on Electromagnetic Isotope Separators and Related Topics (EMIS2015), Grand Rapids, MI, U.S.A., 11-15 May 2015. (cited in page 53.)
- [75] R. Wolf, D. Beck, K. Blaum, C. Böhm, C. Borgmann, M. Breitenfeldt, N. Chamel, S. Goriely, F. Herfurth, M. Kowalska, S. Kreim, D. Lunney, V. Manea, E. Minaya Ramirez, S. Naimi, D. Neidherr, M. Rosenbusch, L. Schweikhard, J. Stanja, F. Wienholtz et K. Zuber. Plumbing Neutron Stars to New Depths with the Binding Energy of the Exotic Nuclide  $^{82}\text{Zn}$ . *Physical Review Letters* 110(4): 041101, 2013. (cited in page 53.)
- [76] D. Atanasov, P. Ascher, K. Blaum, R. B. Cakirli, T. E. Cocolios, S. George, S. Goriely, F. Herfurth, H.-T. Janka, O. Just, M. Kowalska, S. Kreim, D. Kisler, Y. A. Litvinov, D. Lunney, V. Manea, D. Neidherr, M. Rosenbusch, L. Schweikhard, A. Welker, F. Wienholtz, R. N. Wolf et K. Zuber. Precision Mass Measurements of  $^{129}\text{--}^{131}\text{Cd}$  and Their Impact on Stellar Nucleosynthesis via the Rapid Neutron Capture Process. *Physical Review Letters* 115(23): 232501, 2015. (cited in page 53.)
- [77] M. Rosenbusch, P. Ascher, D. Atanasov, C. Barbieri, D. Beck, K. Blaum, C. Borgmann, M. Breitenfeldt, R. B. Cakirli, A. Cipollone, S. George, F. Herfurth, M. Kowalska, S. Kreim, D. Lunney, V. Manea, P. Navrátil, D. Neidherr, L. Schweikhard, V. Somà, J. Stanja, F. Wienholtz, R. N. Wolf et K. Zuber. Probing the  $N = 32$  shell closure below the magic proton number  $Z = 20$ : Mass measurements of the exotic isotopes  $^{52,53}\text{K}$ . *Physical Review Letters* 114(20): 202501, 2015. (cited in page 53.)
- [78] F. Wienholtz, D. Atanasov, S. Kreim, V. Manea, M. Rosenbusch, L. Schweikhard, A. Welker et R. Wolf. Towards ultrahigh-resolution multi-reflection time-of-flight mass spectrometry at ISOLTRAP. *Physica Scripta T* 2015(T166): 014068, 2015. (cited in page 53.)
- [79] P. Schury, Y. Ito, M. Wada et H. Wollnik. Wide-band mass measurements with a multi-reflection time-of-flight mass spectrograph. *International Journal of Mass Spectrometry* 359: 19 – 25, 2014. (cited in page 53.)
- [80] T. Dickel, W. Plaß, S. Ayet San Andres, J. Ebert, H. Geissel, E. Haettner, C. Hornung, I. Miskun, S. Pietri, S. Purushothaman, M. Reiter, A.-K. Rink, C. Scheidenberger, H. Weick, P. Dendooven, M. Diwisch, F. Greiner, F. Heiße, R. Knoßel, W. Lippert, I. Moore, I. Pohjalainen, A. Prochazka, M. Ranjan, M. Takechi, J. Winfield et X. Xu. First spatial separation of a heavy ion isomeric beam with a multiple-reflection time-of-flight mass spectrometer. *Physics Letters B* 744: 137 – 141, 2015. (cited in page 53.)



- [81] D. Dahl. SIMION for the personal computer in reflection. *International Journal of Mass Spectrometry* 200(1): 3 – 25, 2000. (cited in pages 57 and 58.)
- [82] D. Manura et D. Dahl. *SIMION Version 8.0/8.1 User Manual*. Scientific Instrument Services, Inc., revision 5 édition, November 2011. (cited in page 57.)
- [83] Notes on trajectory calculation in SIMION. URL [http://simion.com/info/particle\\_trajectory\\_calculation.html](http://simion.com/info/particle_trajectory_calculation.html). (cited in page 58.)
- [84] A. Vallette. *Dynamics of highly charged ions in a electrostatic ion beam trap*. Thèse de doctorat, Université Pierre et Marie Curie - Paris VI, 2011. (cited in page 58.)
- [85] M. Rosenbusch, P. Chauveau, P. Delahaye, G. Marx, L. Schweikhard, F. Wienholtz et R. N. Wolf. Delayed Bunching for Multi-Reflection Time-of-Flight Mass Separation. *AIP Conference Proceedings* 1668(1): 1 – 9, 2015. (cited in page 59.)
- [86] B. Kansal. *Design study of a Time-of-Flight spectrometer for GANIL/SPIRAL2*. Thèse de maître, ENSTA-PariTech, 2013. (cited in page 59.)
- [87] J. Nelder et R. Mead. A Simplex Method for Function Minimization. *The Computer Journal* 7(4): 308–313, 1965. (cited in page 59.)
- [88] P. Chauveau. SIMION's Simplex optimizer applied to electrode's potential and geometry, 2015. URL [http://simion.com/docs/ganil-2015/paper\\_pierre\\_chauveau.pdf](http://simion.com/docs/ganil-2015/paper_pierre_chauveau.pdf). (cited in page 59.)
- [89] R. Wolf. private communication. (cited in page 67.)
- [90] J. Blicke, X. Fléchar, A. Cassimi, H. Gilles, S. Girard et D. Hennecart. A new magneto-optical trap-target recoil ion momentum spectroscopy apparatus for ion-atom collisions and trapped atom studies. *Review of Scientific Instruments* 79(10): 103102, 2008. (cited in page 75.)
- [91] HeatWave Labs website. URL <http://www.heatwavelabs.com/>. (cited in page 75.)
- [92] Introduction to the faster acquisition system. URL <http://faster.in2p3.fr/index.php/about-faster>. (cited in page 80.)
- [93] H. D. Zeman. Deflection of an ion beam in the two-dimensional electrostatic quadrupole field. *Review of Scientific Instruments* 48(8): 1079 – 1085, 1977. (cited in page 98.)
- [94] E. Gartzke, V. S. Kolhinen, D. Habs, J. Szerypo et P. G. Thiolf. Implementing a 4-way-90° Quadrupole Beam-Deflector into the MLL-TRAP System. Annual report, MLL, 2008. (cited in page 98.)

- [95] F. Martinez, G. Marx, L. Schweikhard, A. Vass et F. Ziegler. The new ClusterTrap setup. *The European Physical Journal D - Atomic, Molecular and Optical and Plasma Physics* 255(2), 2011. (cited in page 98.)
- [96] URL <http://www.beamimaging.com/quad.html>. (cited in page 98.)
- [97] J. R. Gibson et S. Taylor. Numerical investigation of the effect of electrode size on the behaviour of quadrupole mass filters. *Rapid Commun. Mass Spectrom.* 15: 1960–1964, 2001. (cited in page 99.)
- [98] D. Denison. Operating parameters of quadrupole in a grounded cylindrical housing. *Journal of Vacuum Science and Technology* 8(1): 266 – 269, 1971. (cited in page 99.)
- [99] S. Schwarz. private communication, May 2015. (cited in page 99.)
- [100] E. M. Ramirez, P. Alfaut, M. Aouadi, P. Ascher, B. Blank, K. Blaum, J.-F. Cam, P. Chauveau, L. Daudin, P. Delahaye, F. Delalee, P. Dupré, S. E. Abbeir, M. Gerbaux, S. Grévy, H. Guérin, D. Lunney, F. Metz, S. Naimi, L. Perrot, A. de Roubin, L. Serani, B. Thomas et J.-C. Thomas. Conception of PIPERADE: A high-capacity Penning-trap mass separator for high isobaric contamination at {DESIR}. *Nuclear Instruments and Methods in Physics Research Section B: Beam Interactions with Materials and Atoms* 376: 298 – 301, 2016. ISSN 0168-583X. doi:<http://dx.doi.org/10.1016/j.nimb.2016.01.044>. URL <http://www.sciencedirect.com/science/article/pii/S0168583X16001051>. Proceedings of the {XVIIth} International Conference on Electromagnetic Isotope Separators and Related Topics (EMIS2015), Grand Rapids, MI, U.S.A., 11-15 May 2015. (cited in page 115.)
- [101] B. Cederwall, F. G. Moradi, T. Bäck, A. Johnson, J. Blomqvist, E. Clément, G. de France, R. Wadsworth, K. Andgren, K. Lagergren, A. Dijon, G. Jaworski, R. Liotta, C. Qi, B. M. Nyakó, J. Nyberg, M. Palacz, H. Al-Azri, A. Algora et G. de Angelis. Evidence for a spin-aligned neutron-proton paired phase from the level structure of  $^{92}\text{Pd}$ . *Nature* 469(7328): 68 – 71, 2011. (cited in pages 119 and 160.)
- [102] M. Sandzelius, B. Hadinia, B. Cederwall, K. Andgren, A. Khaplanov, R. Wyss, E. Ganioglu, I. G. Darby, M. R. Dimmock, D. T. Joss, L. Nelson, R. D. Page, E. S. Paul, M. Petri, S. Eeckhaudt, T. Grahn, P. T. Greenlees, P. M. Jones, R. Julin et S. Juutinen. Identification of Excited States in the  $T_z = 1$  Nucleus  $^{110}\text{Xe}$ : Evidence for Enhanced Collectivity near the  $N = Z = 50$  Double Shell Closure. *Physical Review Letters* 99(2): 022501, 2007. (cited in pages 120 and 160.)
- [103] J. Simpson, F. Azaiez, G. de France, J. Fouan, J. Gerl, R. Julin, W. Kortzen, P. Nolan, B. Nyako, G. Sletten et P. Walker. The EXOGAM array: a radioactive beam gamma-ray spectrometer. *Heavy Ion Physics* 11(1): 159 – 188, 2000. (cited in pages 120 and 123.)

- [104] F. Azaiez. EXOGAM: a  $\gamma$ -ray spectrometer for radioactive beams. *Nuclear Physics, Section A* 654(Supp. 1): 1003c – 1008c, 1999. (cited in pages 120 and 122.)
- [105] EXOGAM detector description. URL <http://pro.ganil-spiral2.eu/laboratory/detectors/exogam>. (cited in page 120.)
- [106] J. Gál, G. Hegyesi, J. Molnár, B. Nyakó, G. Kalinka, J. Scheurer, M. Aléonard, J. Chemin, J. Pedroza, K. Juhász et V. Pucknell. The VXI electronics of the DIAMANT particle detector array. *Nuclear Instruments and Methods in Physics Research A* 516: 502 – 510, 2004. (cited in pages 120 and 123.)
- [107] B. M. Nyakó. Performance of the DIAMANT detector at GANIL and plans for improvements. Presentation for the DIAMANT collaboration. (cited in pages 120 and 122.)
- [108] Ö. Skeppstedt, H. Roth, L. Lindström, R. Wadsworth, I. Hibbert, N. Kelsall, D. Jenkins, H. Grawe, M. Górska, M. Moszyński, Z. Sujkowski, D. Wolski, M. Kapusta, M. Hellström, S. Kalogeropoulos, D. Oner, A. Johnson, J. Cederkäll, W. Klamra, J. Nyberg, M. Weiszflog, J. Kay, R. Griffiths, J. Garces Narro, C. Pearson et J. Eberth. The EUROBALL neutron wall – design and performance tests of neutron detectors. *Nuclear Instruments and Methods in Physics Research A* 421: 531 – 541, 1999. (cited in page 120.)
- [109] Neutron Wall website, Nuclear Structure Group at Uppsala University, Sweden. URL <https://nsg.physics.uu.se/nwall>. (cited in page 120.)
- [110] I. Lazarus. Overview of the Euroball Trigger System. Rapport technique, Nuclear Physics Group - Daresbury Laboratory, 2001. (cited in pages 123, 125, and 160.)
- [111] R. Andrae, T. Schulze-Hartung et P. Melchior. Dos and don'ts of reduced chi-squared. 2010. (cited in pages 128 and 161.)
- [112] Z. Kis, B. Fazekas, J. Ostor, Z. Revay, T. Belgya, G. Molnar et L. Koltay. Comparison of efficiency functions for Ge gamma-ray detectors in a wide energy range. *Nuclear Instruments and Methods in Physics Research A* 418(2): 374 – 386, 1998. (cited in page 130.)
- [113] D. Radford. Notes on the Use of the Program gf3. URL <http://radware.phy.ornl.gov/gf3/>. (cited in page 131.)
- [114] Y. Zheng, G. de France, E. Clément, A. Dijon, B. Cederwall, R. Wadsworth, T. Bäck, F. G. Moradi, G. Jaworski, B. M. Nyakó, J. Nyberg, M. Palacz, H. Al-Azri, G. de Angelis, A. Atac, Ö. Aktaş, S. Bhattacharyya, T. Brock, P. J. Davies, A. Di Nitto, Z. Dombradi, A. Gadea, J. Gal, P. Joshi, K. Juhasz, R. Julin, A. Jungclaus, G. Kalinka, J. Kownacki, G. La Rana, S. M. Lenzi, J. Molnar, R. Moro, D. R. Napoli, B. S. N. Singh, A. Persson, F. Recchia, M. Sandzelius, J. N. Scheurer, G. Sletten, D. Sohler, P. A. Söderström, M. J. Taylor,

- J. Timar, J. J. Valiente-Dobon et E. Vardaci.  $\gamma$ -ray linear polarization measurements and  $(g_{9/2})^{-3}$  neutron alignment in  $^{91}\text{Ru}$ . *Physical Review C* 87(4): 1 – 10, 2013. (cited in pages 144 and 145.)
- [115] R. M. Diamond, E. Matthias, J. O. Newton et F. S. Stephens. Nuclear Alignment in Heavy-Ion Reactions. *Physical Review Letters* 16(26): 1205–1207, 1966. (cited in page 144.)
- [116] E. D. Mateosian et A. Sunyar. Tables of attenuation coefficients for angular distribution of gamma rays from partially aligned nuclei. *Atomic Data and Nuclear Data Tables* 13(4): 391 – 406, 1974. (cited in page 145.)
- [117] T. Yamazaki. Tables of coefficients for angular distribution of gamma rays from aligned nuclei. *Nuclear Data Sheets. Section A* 3(1): 1 – 23, 1967. (cited in page 145.)
- [118] R. Mărginean, C. Rusu, N. Mărginean, D. Bucurescu, C. A. Ur, G. de Angelis, M. Axiotis, D. Bazzacco, E. Farnea, A. Gadea, M. Ionescu-Bujor, A. Iordăchescu, W. Krolas, T. Kröll, S. M. Lenzi, S. Lunardi, D. R. Napoli, C. R. Alvarez et J. Wrzesinski. High-spin structure of  $^{95}\text{Pd}$ . *Physical Review C* 86(3): 034339, 2012. (cited in page 145.)
- [119] K. Pohl, P. Regan, J. Bush, P. Raines, D. Balamuth, D. Ward, A. Galindo-Uribarri, V. Janzen, S. Mullins et S. Pilotte. High-spin states in  $^{107}\text{Pd}$ ,  $^{108}\text{Pd}$ , and  $^{109}\text{Ag}$ . *Physical Review C* 53(6): 2682 – 2700, 1996. (cited in page 145.)
- [120] K. Lagergren, B. Cederwall, A. Johnson, J. Blomqvist, D. Sohler, G. de Angelis, P. Bednarczyk, T. Back, T. Claesson, O. Dorvaux, E. Farnea, A. Gadea, M. Gorska, L. Milechina, L.-O. Norlin, A. Odahara, M. Palacz, I. Stefanescu, O. Thelen et J. Vivien. Evidence for excited states in  $^{95}\text{Ag}$ . *European Physical Journal A* 14(4): 393 – 396, 2002. (cited in page 145.)
- [121] J. Timár, P. Joshi, K. Starosta, V. Dimitrov, D. Fossan, J. Molnár, D. Sohler, R. Wadsworth, A. Algora, P. Bednarczyk, D. Curien, Z. Dombrádi, G. Duchene, A. Gizon, J. Gizon, D. Jenkins, T. Koike, A. Krasznahorkay, E. Paul, P. Raddon, G. Rainovski, J. Scheurer, A. Simons, C. Vaman, A. Wilkinson, L. Zolnai et S. Frauendorf. Experimental evidence for chirality in the odd-A  $^{105}\text{Rh}$ . *Physics Letters B* 598(3 - 4): 178 – 187, 2004. (cited in pages 147 and 163.)
- [122] F. Ghazi Moradi, B. Cederwall, C. Qi, T. Bäck, A. Ataç, R. Liotta, M. Doncel, A. Johnson, G. de France, E. Clément, J. Nyberg, A. Gengelbach, B. Nyakó, J. Gal, G. Kalinka, J. Molnár, J. Timár, D. Sohler, Z. Dombrádi, I. Kuti, K. Juhász, D. Napoli, A. Gottardo, V. Modamio, R. Wadsworth, T. Henry, A. Nichols, H. Al-Azri, M. Palacz, E. Ideguchi, O. Aktas, A. Di Nitto, A. Dijon, T. Hüyük, G. Jaworski, P. John et B. Yilmaz. Spectroscopy of the neutron-deficient  $N=50$  nucleus  $^{95}\text{Rh}$ . *Physical Review C* 89(4): 044310, 2014. (cited in page 149.)

- [123] F. Ghazi Moradi, C. Qi, B. Cederwall, A. Ataç, T. Bäck, R. Liotta, M. Doncel, A. Johnson, G. de France, E. Clément, A. Dijon, R. Wadsworth, T. Henry, A. Nichols, H. Al-Azri, J. Nyberg, A. Gengelbach, T. Hüyük, B. Nyakó, J. Timár, D. Sohler, Z. Dombrádi, I. Kuti, K. Juhász, M. Palacz, G. Jaworski, S. Lenzi, P. John, D. Napoli, A. Gottardo, V. Modamio, A. Di Nitto, B. Yilmaz, O. Aktas et E. Ideguchi. Character of particle-hole excitations in  $^{94}\text{Ru}$  deduced from  $\gamma$ -ray angular correlation and linear polarization measurements. *Physical Review C* 89(1): 014301, 2014. (cited in page 149.)
- [124] N. Marginean, D. Bucurescu, C. Rossi Alvarez, C. Ur, L. Skouras, L. Johnstone, D. Bazzacco, S. Lunardi, G. de Angelis, M. Axiotis, E. Farnea, A. Gadea, M. Ionescu-Bujor, A. Iordachescu, W. Krolas, T. Kroll, S. Lenzi, T. Martinez, R. Marginean, R. Menegazzo, D. Napoli, P. Pavan, M. De Poli, B. Quintana, C. Rusu, P. Spolaore et J. Wrzesinski. Yrast isomers in  $^{95}\text{Ag}$ ,  $^{95}\text{Pd}$ , and  $^{94}\text{Pd}$ . *Physical Review C* 67(6): 61301, 2003. (cited in pages 148, 149, 150, and 163.)
- [125] C. Plettner, H. Grawe, I. Mukha, J. Döring, F. Nowacki, L. Batist, A. Blazhev, C. Hoffman, Z. Janas, R. Kirchner, M. La Commara, C. Mazzocchi, E. Roeckl, R. Schwengner, S. Tabor et M. Wiedeking. On the  $\beta$ -decaying (21+) spin gap isomer in  $^{94}\text{Ag}$ . *Nuclear Physics, Section A* 733: 20 – 36, 2004. (cited in page 148.)
- [126] T. Brock, B. Nara Singh, P. Boutachkov, N. Braun, A. Blazhev, Z. Liu, R. Wadsworth, M. Górska, H. Grawe, S. Pietri, C. Domingo-Pardo, D. Rudolph, S. Steer, A. Ataç, L. Bettermann, L. Cáceres, T. Engert, K. Eppinger, T. Faestermann, F. Farinon, F. Finke, K. Geibel, J. Gerl, R. Gernhäuser, N. Goel, A. Gottardo, J. Grebosz, C. Hinke, R. Hoischen, G. Ilie, H. Iwasaki, J. Jolie, A. Kaskas, I. Kojuharov, R. Krücken, N. Kurz, E. Merchán, C. Nociforo, J. Nyberg, M. Pfützner, A. Prochazka, Z. Podolyák, P. Regan, P. Reiter, S. Rinta-Antila, H. Schaffner, C. Scholl, P.-A. Söderström, N. Warr, H. Weick, H.-J. Wollersheim et P. Woods. Observation of a new high-spin isomer in  $^{94}\text{Pd}$ . *Physical Review C* 82(6): 061309, 2010. (cited in page 148.)

# NOTATIONS AND ACRONYMS

CENBG	Centre d'Etudes Nucléaires de Bordeaux-Gradignan
CFD	Constant Fraction Discriminator
DESIR	Desintégration, excitation and stockage d'ions radioactifs
FC	Faraday cup
FWHM	Full Width at Half Maximum
GANIL	Grand accélérateur national d'ions lourds
LPC	Laboratoire de Physique Corpusculaire
MCP	Micro-channel plate
MR-ToF-MS	Multi-reflection time of flight mass spectrometer
RFQ	RadioFrequency Quadrupole
RFQCB	RFQ Cooler and Buncher
RMS	Root Mean Square
S3	Super separator spectrometer
S3-LEB	S3 Low Energy Branch
SPIRAL	Système de production d'ions radioactifs en ligne
TAC	Time-to-Amplitude Converter
ToF	Time of flight







## Summary

The new generation of nuclear facilities calls for new technological developments to produce, accelerate, manipulate and analyse exotic nuclei. The main topic of this thesis work was the simulation, design and test of a Multi-Reflection Time-of-Flight Mass spectrometer (MR-ToF-MS) for fast mass separation and fast mass measurement of radioactive ions in the installations S3 and DESIR at SPIRAL2. Such a device could separate isobaric nuclei and provide SPIRAL2 with high purity beams. Also, its mass measurement capabilities would help to determine binding energies of exotic and superheavy nuclei with a high precision. This apparatus has been simulated with the SIMION 8.1 software and designed accordingly. First offline tests have been performed with a stable ion source at LPC Caen. In addition a low-aberration electrostatic deflector has been simulated and designed to operate with this MR-ToF-MS without spoiling its performances. This work also describes the analysis and results of the first online tests of a FEBIAD-type ion source intended to provide SPIRAL1 and SPIRAL2 radioactive beams of competitive intensities. Finally, we describe the analysis of a nuclear physics experiment, including the calibration of the different detectors and the gamma-spectroscopy of nuclei in the vicinity of the doubly magic  $^{100}\text{Sn}$ .

*Keywords: time-of-flight mass spectrometry, mass measurement, electrostatic deflector, ion sources, gamma spectrometry*

## Résumé

La nouvelle génération d'installations nucléaires nécessite un renouveau technologique pour produire, accélérer, manipuler et analyser des noyaux exotiques. L'objectif principal de ce travail de thèse était de simuler, concevoir et tester un spectromètre de masse par temps de vol à multi-réflexions (MR-ToF-MS) dédié à la séparation en masse et la mesure de masse rapide d'ions radioactifs auprès des installations S3 et DESIR de SPIRAL2. Ce dispositif pourrait séparer des noyaux isobares et fournir à SPIRAL2 des faisceaux très purs. De plus ses capacités de mesure de masse permettraient de déterminer très précisément l'énergie de liaison de certains noyaux exotiques ou super-lourds. Cet instrument a été simulé à l'aide du logiciel SIMION 8.1 et conçu en fonction de ces simulations. Les premiers tests hors-lignes ont été faits avec une source d'ions stable au LPC Caen. Ce travail de thèse comprend également la simulation et la conception d'un déflecteur électrostatique censé être utilisé avant ou après le MR-ToF-MS et n'introduisant que peu d'aberrations optiques pour ne pas gâcher les performances de ce dernier. Ce travail décrit aussi l'analyse et les résultats des premiers tests en ligne d'une source d'ions de type FEBIAD censée fournir des faisceaux radioactifs d'intensités compétitives aux installations SPIRAL1 et SPIRAL2. Enfin, nous décrivons l'analyse d'une expérience de physique nucléaire, ce qui inclue la calibration des différents détecteurs et la spectroscopie gamma de noyaux au voisinage du noyau doublement magique  $^{100}\text{Sn}$ .

*Mots clés : spectrométrie de masse à temps de vol, mesure de masse, déflecteur électrostatique, sources d'ions, spectrométrie gamma*

**Grand Accélérateur National d'Ions Lourds (CEA/DRF - CNRS/IN2P3)**  
Boulevard Henri Becquerel, BP 55027 - 14067 CAEN Cedex 05, France